Calibration of the Double Chooz detector and cosmic background studies

Leonidas Kalousis

UNIVERSITÉ DE STRASBOURG

École Doctorale de Physique et Chimie-Physique

THÈSE DE DOCTORAT

Spécialité : Physique des particules

Calibration of the Double Chooz detector and cosmic background studies

Présentée et

soutenue publiquement par

Leonidas N. Kalousis

le 27 Septembre 2012 devant le jury composé de:

Marcos Dracos	Directeur de thèse
Dominique Duchesneau	Examinateur
Urlich Goerlach	Examinateur
Sonia Kabana	Rapporteur
Imad Laktineh	Rapporteur

Contents

Thank you !

It is always a rare pleasure and a special privilege to write the acknowledgements section of a scientific document. Not only because at that certain moment most of the difficult part is probably accomplished. Nonetheless, in this particular case, the task required is more demanding than the usual. I know that I have to delve deep into three of the most difficult but fascinating years of my life. Looking back this long road that brought me from Athens to Strasbourg a feeling of nostalgia never fails to appear. How many lovely memories ? How many new friends and colleagues entered my life ? Destiny and fate were so generous that it is my sole duty to express, even from this standpoint, my gratitude to those that without their friendship and their support this journey would never had come to its end.

First of all I would like to thank the big family of CNRS/in2p3 and IPHC where I had the good fortune to conduct research. There are so many people that helped me in one way or the other. I would like, though, to mention in particular J.-P. Engel and J.-P. Froberger. Jean-Pierre (Froberger) provided me most of the assistance necessary to overcome the hardware and software problems of my computer equipment while Jean-Pierre (Engel) was extremely helpful in the field of photomultipliers' monitoring and calibration; a subject that he masters. Much of the ideas discussed in Chapter 5 flourished from various discussions with him.

My thesis advisor, Marcos Dracos, needs to be separately acknowledged. I would like to thank him for accepting me in his group, giving me the opportunity to pursue this Ph.D. and chasing a long-standing dream. In these years I had the chance to profit from his experience and his understanding of physics. I really enjoyed the various discussions we had during our common shifts at Chooz and I know that I will miss his excellent sense of humor.

The first office-mate I had in Strasbourg was C. Bobeth. With Christoph we shared the same office for almost a year. It is perhaps difficult to explain you and give fair justice to the support that he kindly offered me. He did so much to aid me get use to this new environment, learning the regulations of the laboratory or acclimatize myself with Strasbourg and France. His advices

and his encouragement were very valuable to me. I was very touched when he decided to leave the group and return to Germany with his family, but life is always like this ... thanks so much Christoph.

Nicholas Vassilopoulos joined our group in my second year, replacing the void that Christoph left behind him. We worked in different projects but between us a strong relationship developed. We had a wonderful time exchanging opinions, talking about physics or the ruthless situation in Greece. I delighted to hear his beautiful stories from LEP, the old searches for the Higgs boson or the early days of CNGS. I am very happy to know him and I hope that we will keep in touch in the years to come.

Much of the motivation and stamina to carry on this effort was provided by my (then) fellow Ph.D. candidates (and now most Drs.): M. Bachaalany, C. Dritsa, M. Moukaddam and Y. Voustinas. Christiana and Yiorgos were the first to introduce me to Strasbourg. We spent many coffee-breaks at Christiana's office talking about our concerns and our work. I remember the nights after hours of work that we ended up for a glass of beer at Taverne Française or Expats having endless discussions and lots of fun. Truth be told I will really miss these days.

My friend Yiorgos deserves an extra credit since he stood beside me when I really needed someone... I wish to wish him nothing. I know he is a survivor, a fact that he proved in many circumstances.

From the Double Chooz-ers I could not forget to thank A. Meregaglia and A. Tonazzo. Anselmo's office was right next to mine. We begun to work together inside the European Analysis Cluster on neutron captures. That was a study done for the Second Comparison stage and you will not find it in this document. Since then, we continued working together contributing equally to the first concise treatment of the correlated fast neutron and stopping muon background. This is a study presented in Chapter 6 and it forms essentially the core of the fast neutron/stopping muon estimation done for the first analysis publication. He was also kind enough to read and correct most of this manuscript.

Alessandra was the one that helped me start my first analysis studies in the muon working group that she is coordinating. In the beginnings I was merely reproducing hers results and hers plots sending her long chains of e-mails with questions and points that had to be clarified. She was always very helpful and very kind with me. Beyond that, she was one of the first to credit the initial steps of my approach on the Inner Detector muon rates (Chapter 8) a study that she encouraged me to continue and complete.

Those "Bloody Victorians": Akis Bikos and Christine Skatzouris. What could I possibly remember from these guys ? They had been more than a family for me, especially in the first year, extinguishing all of my loneliness

and every sense of nostalgia. We all lived at Victoria Garden and hence Victorians. We share the same mentality but as of characters we're still miles apart. But heteronymous attract ! Being scattered into different parts of Greece we would never had the chance to meet each other if it was not for Strasbourg. I cannot remember how many evenings and nights we spend together, discussing, drinking soft wine and enjoying that lovely plates that Christine was most of the times preparing.

Akis was the "elephant in the glass store". The counterpart of my calm and quiet character. He would come every afternoon outside my door shouting and screaming, scratching my door with his keys, so that the whole neibourhood would know that I returned home. I would then let him pass. We would then talk about the day past or various shorts of things concerning France or Greece. I am very lucky to meet him in the first place and it really sads me to know that life brought us to different shores. But one day, who knows ? We might meet again... and I anticipate for this moment.

Christine was the little sister that I never had. My Professor in cooking, the best I've ever had and the best I could ever imagine. She was always there, next to me, to advise me, teaching me how to organize my apartment, how to combine clothes in the washing machine or confront my wildest nightmare: go shopping ! I will really miss her laughter and her gifted character that won my respect so many times in those years. I will always remember the big dinner she prepared with Dimitri upon my arrival at Strasbourg after my Christmas holidays in Athens. I was mesmerized... did I really left home or have I just returned ?

This work would never come into fruition if it was not for my life-long friends back in Athens and Leonidion: J. Bougioukas, A. Georgitsis, G. Zafeiriou, M. Zervas, B. Kiousis, Alexandros and Fedon Nenedakis, C. Roumeliotis, A. Vynias, Stavros Touralias and M. Kastrioti. The space left in this section is too short to express what they mean to me all these years.

To my friend John Bougioukas I would like to say in particular:

Bougiouka ! Bougiouka ! Bougiouka ! Bouougiououkaaa!!!1

(OK! I did my therapy, I feel more relaxed now). Additionally, I would like to let him know that my theory of bougioukons will soon find its way to Phys. Rev. Letters and I will immortalize his surname as we have already agreed that night at Aerides.

Also, a big "Thank you !" to my friend and Professor Nicholas Tracas back in the Technical University of Athens. You know better than me that without your trust and your support this work would have never been possible and a big part of my life would have been radically different. A simple thank you is only the least I can do to express you my respect and my gratitude.

Last (but not least) comes E. Boucquerel. Elian entered my life (or maybe evaded my office) during my last year in Strasbourg. It was a tough and a stressful period for me. In him I found a good friend and well-hearted personality. How can I forget the tons of laughter we had together in the short coffee-breaks talking about various shorts of things but mostly: Angra, Kamelot, Stratovarious, Edguy, Amorphis, Threshold, Riverside, Lunatic Soul, Tool, Kyuss, Queens of the Stone Edge, Metallica, Slayer, Anthrax, Judas Priest, Iron Maiden, Helloween, Manowar, Sepultura, Led Zeppelin (LEEED ZEPPELIN !), Deep Purple, AC-DC, Diamond Head, Black Sabbath, Rush, Camel and so on and so forth ...

He is now one more of those many reasons I have to scream : "Vive la France !"

⋆⋆⋆

Finally I could not fail to acknowledge my parents Anna and Nikos and my sister Georgia for their love and their devotion. They were the driving force behind this effort. The way that they value science and education had always been a source of inspiration and a fountain of encouragement. Naturally I dedicate all this to ...

στους γονείς μου Άννα και Νίκο και
στην αδερφή μου Γεωργία για την
αγάπη τους και την γλυκύτητα τους

Summary

Double Chooz is a short-baseline, reactor experiment designed to observe the disappearance of reactor electron anti-neutrinos. Note that this will be the clear evidence of a third mode of neutrino oscillations[1] driven by the third, less known, lepton mixing angle θ_{13}. In the past, single detector experiments like CHOOZ or Palo Verde put tight constraints on θ_{13} pointing towards a small, or even zero, θ_{13} scenario. Double Chooz (DC) is a second generation effort, using two identical detectors to reduce the reactor systematics and unveil the oscillation patterns governed by θ_{13} in the atmospheric mass square splitting, Δm^2_{atm}. The experiment has started stable data taking with a single, far detector since April 2011. Currently in the world there are two more reactor experiments searching for θ_{13}. These are Daya Bay in China and RENO in Korea.

In the course my doctoral research, I was actively involved in the DC experiment. The IPHC Neutrino group, which I worked for, is responsible for the construction, the optimization and the maintenance of the Inner Veto (IV) calibration systems of both the far and near detectors. Part of my research focused on the development of the software required for the IV calibration and the analysis the associated data. I was also strongly involved in the analysis of physics data relevant for background studies.

In the first chapter of the thesis the notions of massless neutrinos within the Standard Model (SM) of particle physics are being presented. The first historical hints of lepton flavour violation in solar (Homestake) and atmospheric (IMB, Kamiokande) neutrinos are also presented. Particle mixing and neutrino oscillations are put forward as the natural interpretation of these important experimental observations. The basic physical concepts and formulae of neutrino oscillations in vacuum and in matter are given and the chapter concludes with a brief discussion on the possible neutrino mass models.

In the second chapter we elaborate on the current experimental status; that is on the most recent data. We discuss the modern experiments that

[1]The other two are dictated by the well-understood atmospheric and solar parameters.

confirmed the early oscillation signals observed in the 1960's and 80's. The most accurate measurements on the oscillation parameters phenomenology are also reported together with the next important steps necessary for Neutrino Physics. The end of the chapter contains a short discussion on those quantities not determined by oscillation measurements (absolute neutrino mass, neutrino nature) and a brief summary on sterile neutrinos and the MiniBooNE observations is also given.

DC is the issue of Chapter 3. Here we present all the material relevant to the θ_{13} oscillation analysis conducted for the first DC publication. The double detector concept is put forward through the notion of the cross-section per fission that makes the associated systematics reduction more transparent. The production and detection of reactor electron anti-neutrinos is also demonstrated and the flux calculation, as performed by the DC collaboration, is also discussed at some extent. The detector four-layer concept, most of the hardware systems, the DAQ and calibration systems are also presented. Finally the background estimations and the extraction of θ_{13} from the fit to the positron spectrum is shown. The chapter is self-consistent in the sense that in the case of important omissions we direct the reader to the relevant bibliography, so that one could clearly follow the important steps necessary for the measurement conducted.

In Chapter 4 the Inner Veto Light Injection (IV-LI) system utilized for the calibration and monitoring of the IV photomultiplier tubes (PMTs) is presented. The basic role and requirements of IV-LI are clearly stated along with some additional informations relevant for the IV and its calibration. The whole design of the IV-LI and the main parts of its hardware are demonstrated in details. The data taking procedures and running configurations are also explained. In the next chapter (Chapter 5) we present the analysis of data taken with the IV-LI. As carefully shown, these data sets are performed for the PMT gain extraction and thus are taken with low-intensity light. Central to the gain determination method is a parametrization model, developed by the author, for this purpose. We then present the analyses of data taken for the tuning of the IV PMTs High Voltage and the PMT gain monitoring in time. The proper understanding of the IV performance as extracted by the IV-LI runs is crucial for the experiment.

The rest part of the thesis is devoted to the analysis of physics data. Chapter 6 is concerned with the estimation of the fast neutron background. In this part the author played a leading role. As it is clearly demonstrated the high-energy originating background consists in two contributions: fast neutrons and chimney stopping muons. The signatures and patterns of these two components are also clearly shown. A first estimation of these backgrounds

is also given. The techniques put forward in this chapter were instrumental to the first DC θ_{13}-analysis publication.

In Chapter 7 we treat a very special background relevant for the Double Chooz detector. This is not a physics background but an instrumental effect. In particular, some photomultipliers bases emit spontaneously light that sporadically triggers the detector. This contribution has a high trigger rate in the level of natural radioactivity. A new novel scheme is developed that can help to identify and reject these pathological events. The algorithms were based on the geometrical orientation of the charge inside the detector. For this we used the sphericity tensor. Exploiting two variables, sphericity and aplanarity, we show that we can isolate an extra class of background events in the high energy regime that is passing the official selection criteria. We also use this edifice in the low energy region validating parts of the already existing treatments. That was an extremely important cross-check, helping DC to further comprehend the behavior of this difficult to treat background.

The last chapter is dedicated to muon tagging. Techniques to identify cosmic ray muons based on sharp charge cuts are given. The neutrino rates in the Inner Detector (ID) and the IV are calculated based on this strategy. Furthermore, two additional approaches to isolate the cosmic muon events that activate the ID are presented. This is a very important work in understanding and study the background itself. The first approach was based on a shape analysis of the pulses' time-profiles. In particular, we show that after some preliminary selection, the pulses that correspond to muons have a very specific shape and this property can be used to isolate them. We also provide another method to attack muon selection leaning on the geometrical characteristics of the events' hit patterns. The results of all these approaches agree to an astonishing level. This is an important result showing that we understand satisfactory the cosmic ray muon flux.

Μας προσμένουν σαν στοιχειά που ξυπνάνε απ΄ τη στάχτη
οι πιο άγριες χαρές, τα πιο υπέροχα πάθη
νυσταγμένες μελωδίες στου μυαλού μας τα βάθη
οι παλιές μας ουτοπίες τα πιο υπέροχα λάθη

Μας προσμένουν οι μεγάλοι, οι απέραντοι δρόμοι
μας προσμένουν όλα αυτά που δεν ήρθαν ακόμη
μας προσμένουν σαν στοιχειά που ξυπνάνε απ΄ τη στάχτη
οι πιο άγριες χαρές, τα πιο υπέροχα πάθη

Διάφανα Κρίνα

They wait for us like ghosts, they rise from the ashes
the wildest joys, the most wonderful passions
sleeping melodies into the depths our souls
our old utopiae and the brand new mistakes

Ahead us they lie, the wide, the glorious highways
since time is yet to come
they wait for us like ghosts, they stalk in the ashes
the wildest joys, the most wonderful passions

Part I

Introduction

Chapter 1

Neutrinos and neutrino oscillations

In this first introductory chapter, we will lay down the current understanding of neutrino phenomenology and oscillations. The established notions of left-handed, massless neutrinos within the minimal Standard Model (SM) of particle physics physics will be presented, along with the first experimental evidence of neutrino masses and oscillations that came from the observation of solar and atmospheric neutrinos. The concept of lepton mixing and the associated oscillation formulae, in vacuum and in matter, will also be presented. Finally, we will review some of the possible models that can account for the observed neutrino masses.

This chapter is meant to be a brief and complete summary to the subject of neutrinos and neutrino oscillations, presenting some basic concepts and introducing our notation concerning the theoretical conventions. In the case of important omissions we will direct the reader to some of the standard references.

1.1 Neutrinos in the Standard Model

1.1.1 Theoretical prediction and experimental discovery

Neutrinos have a long-standing history dating back to 1930 when W. Pauli first postulated their existence on purely theoretical grounds. The need for another particle came from the interpretation of data coming from the newly discovered field of nuclear physics. At that time the only "elementary" particles known were the electron and the proton, while the exact details of nuclear

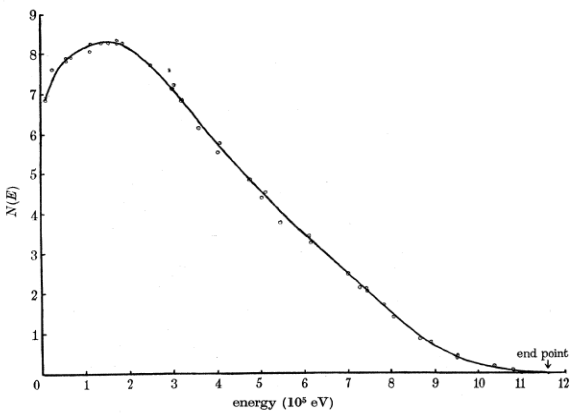

Figure 1.1: β-spectrum of RaE [1].

structure were still obscure. The idea of Pauli was an important attempt to confront the current experimental observations with the sole introduction of a light, neutral particle.

Natural radioactivity was elucidated by H. Becquerel and the Curies, while pioneering steps towards its understanding and classification were made by Sir E. Rutherford. In the 1920's a sufficient qualitative, and sometimes even quantitive, understanding of this phenomenon had been achieved. What was still mysterious, was the observed continuous spectrum of the electrons emitted by the slow processes of nuclear transmutation. In striking contrast to the observed spectra from alpha decays or gamma emission, electrons from beta disintegration seemed to have a continuous spectrum that contradicted the expected kinematics. For instance, in Fig. 1.1 we show the spectrum of electrons arising from the decay of RaE [1]. This continuum curve should be contrasted with the sharp peaks seen, for example, in the alpha disintegration spectrum of Po isotopes, Fig. 1.2.

The first accurate measurement of the electron spectrum from beta decays was made by J. Chadwick in 1914 [3]. But still, at that time, it was not fully clear whether this spectrum was primary or the artifact of some secondary processes that caused the energy losses of the emitted electrons. After some controversy, it was finally shown, mainly by the experiments of C. D. Ellis [4], that the root of the beta spectrum is indeed of primary origin. In this respect, it was still puzzling why the β-spectrum appeared to have a sharp cut-off at a maximum energy that would correspond to the allowed value assuming that beta decay is a two-body process.

The solution that Pauli offered to the problem was radical. Unable to attend a meeting of physicists at the University of Tubingen, he send a

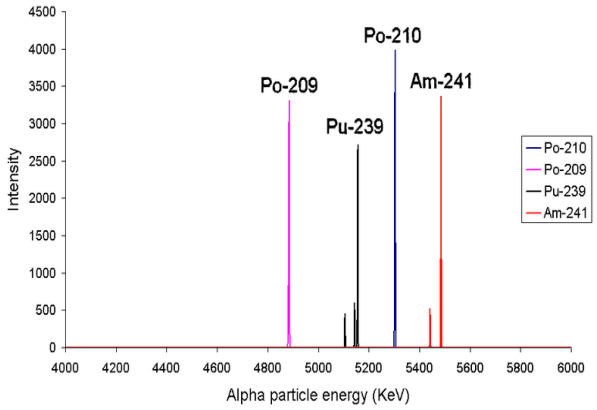

Figure 1.2: Alpha decay spectra of a few alpha emitters. The peaks corresponding to the energy lines of alpha particles are clearly visible. Figure adapted from [2].

letter[1] explaining the idea of a new particle that carries away the missing energy and momentum[2]. To account for the experimental data, neutrinos should have been neutral, to preserve the law of charge conservation, and massless or, at least, near massless to respect the energy balance. The merit of Pauli's idea was that it could easily restore energy conservation while the introduction of another fermion inside the atomic nucleus could account for the apparent anomalies related with the statistics of specific nuclei [6, 7]. Since this particle had to be neutral, Pauli baptized it the neutron, using a name already proposed by Rutherford for a hypothetical composite nuclear element.

The first mathematical theory of beta decay was put forward by E. Fermi in 1934. He was the one that finally coined the term neutrino, to distinguish this light particle from the heavier one that constitutes the nucleus and was, in the meantime, found and named by Chadwick in 1932 [8]. His theory of beta decay was modeled in the language of quantum field theory, replicating the quantization methods of Quantum Electrodynamics (QED) that he mastered [9]. The electron and neutrino were created at the moment of interaction and there was no need to preexist inside the nucleus.

[1] Addressed to the "Dear, Radioactive Ladies and Gentlemen".

[2] Pauli originally called this idea a "desperate remedy". For the original letter along with some personal recollections of Pauli one could have a look at his historical article included in [5].

For the interaction term, Fermi chose a four vector vertex between a proton, a neutron, an electron and a neutrino, relying on simplicity grounds (Occam's razor). Working the mathematics, Fermi was soon able to reproduce the energy spectrum, the Kurie Plots and many other features of beta decay. The impressive success of his theory further supported the neutrino idea of Pauli. In the 1950's, muon and pion were discovered and both their decay modes seemed to need the neutrino concept. It should be emphasized that Fermi's hamiltonian, with some small modifications, is still the correct low energy limit that can describe many spin-conserving β^- and β^+ decays.

But, despite its very success, neutrino still left a part of skepticism to the physics community, being the phantom that carried away the required missing energy, while its direct observation seemed impossible due to its small interaction cross-section. This situation was best summarized by Pauli in his famous quote: "I have done a terrible thing today, something which no theoretical physicist should ever do. I have suggested something that can never be verified experimentally" [10]. It was this reason that made Pauli to bet a bottle of champagne that the neutrino would never be discovered in a free state.

The challenge of detecting the free neutrino was finally taken by F. Reines and C. Cowan in the 1950's [11]. Their first ideas focused on the possibility to observe free neutrinos from the explosion of a fission bomb. Their experience with nuclear weapons made them confident that they could construct and house a detector close to the detonation point that could withstand the outgoing shock waves and the mechanical vibrations. The bomb was certainly a rich source of electron antineutrinos ($8\ 10^{23}\ \bar{\nu}_e$ per kton) but it was still very difficult to decide the best way to protect this detector from other backgrounds originating from the bomb; as for instance the high intensity gamma ray irradiation.

After many elaboration and public exchange, they finally realized that they could perform the same experiment near a nuclear reactor. The channel they decided to exploit was the inverse beta decay (IBD) reaction on free protons:

$$\bar{\nu}_e + p^+ \rightarrow e^+ + n^0 \tag{1.1}$$

The cross-section for this process had been calculated within the Fermi theory and it was known to be small [12], but they planned to use a huge volume ($\simeq$ 1 ton) of liquid scintillator for the target of the detector. The positrons would be detected from the signal corresponding to the positron thermalization and subsequent annihilation (prompt signal), while the neutron would be captured in a nucleus releasing a number of secondary gammas

(delayed signal). Cowan and Reines used cadmium as the element that would induce the neutron captures. It was this prompt-delayed coincidence technique that allowed them to suppress the various backgrounds and actually perform this experiment.

The first attempts to detect neutrinos happened on the Hanford reactor; a plutonium reactor constructed during the World War II. They observed a signal of 0.4 ± 0.2 events per minute above background but their results were not decisive. The experiment was repeated in 1956 at the Savannah River reactor complex with an improved detector design. Then they finally succeeded in observing a clean signal of 3.0 ± 0.2 events per hour while all their cross-checks were consistent with the assumption that they detect reactor neutrinos [13].

The result of the Savannah River experiment was posted to Pauli at CERN, Switzerland. When Pauli learned about the neutrino discovery he finally kept his promise.

1.1.2 Lepton families

In the fifties, when more weakly interacting particles begun to be discovered, mainly in the investigations of cosmic rays, a tentative study of the weak force was put forward. Among the various physical models that were starting to appear one thing seemed to be the most prominent: the evident universal character of weak interactions as manifested, for instance, in the muon decays and nuclear pion capture. An example of these theories includes the so-called Tiomno-Wheeler triangle, while other possibilities included the add of intermediate bosons to mediate the weak forces.

A common feature of some of these theories, was the prediction of the muon transmutation to an electron with the parallel emission of a gamma ray, Fig. 1.3. That was a process first predicted by G. Feinberg in 1958 [14]. The absence of this muon decay mode, as seen in the experimental data, made B. Pontecorvo to theorize that another neutrino associated with the muon should exist. According to his ideas the decay of a muon released a neutrino of a different character than those involved in the normal beta decays. Subsequently he motivated experimentalists to test this idea with a high energy neutrino beam.

This experiment was finally successfully performed in 1962 at the Alternate Gradient Synchrotron (AGS) at Brookhaven Laboratory, by L. Lederman, M. Schwartz and J. Steinberger [16]. These investigators exploited the neutrinos originating by the decay of pions created by the collisions of high energy protons in a beryllium target. In particular, they were able to show that these neutrinos produced preferentially muon leptons while the Fermi

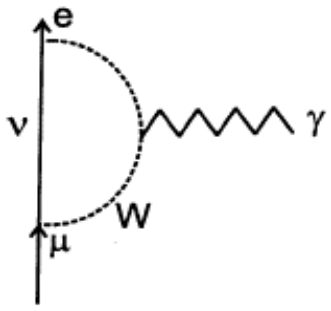

Figure 1.3: A Feynman diagram contributing to the amplitude of the hypothetical $\mu \to e + \gamma$ decay [15].

hamiltonian predicted also the production of electrons in an equal rate. The absence of these electrons decisively demonstrated that another neutrino associated with the muon exists; this was called the muon neutrino ν_μ. Soon, after the two-neutrino experiment, many theoretical models appeared that incorporated naturally the two neutrinos in their abstract formalism.

Years ago, after the advent of gauge symmetries and the SM it was more or less established that with every new, weakly interacting particle, there should be another one with the appropriate quantum numbers to form an $\mathcal{SU}(2)_\mathcal{L}$ doublet under weak isospin. It was then, when τ lepton discovered in the SPEAR facility by M. Perl and collaborators [17] that the need for a third neutrino became immediately evident. Further evidence for the presence of ν_τ was seen in tauonic decays at LEP, while the first decisive observation of ν_τ reported in 2000 by the DONUT collaboration [18].

In Table 1.1 we summarize the lepton content of the SM. The neutrinos form doublets with the associated charged leptons. It should be emphasized that after the experiments at LEP we now know that only three neutrinos exist; those in the three generations [19]. Since this conclusion is obtained from the invisible decay width of the Z^0 boson the possibilities of heavy or sterile neutrinos are still open.

1.1.3 Helicity and mass

Parity violation in the realm of weak interactions was first theorized by T. D. Lee and C. N. Yang in 1956 [21] to account for the τ - θ puzzle: the fact

First generation	Second generation	Third generation
ν_e	ν_μ	ν_τ
e^-	μ^-	τ^-

Table 1.1: Lepton content of the Standard Model.

that one particle[3] seemed to have two decay modes of different parity [22]. This possibility seemed very radical, according to the established dogmae, but was not fully excluded by the experimental observations. One year after, parity violation was confirmed by the experiment of Madame C. S. Wu [20]. Subsequently many groups verified the same patterns of parity violation in pion and muon decays [23, 24].

The maximal parity violation, observed by Wu, seemed to suggest that the weak interaction couplings involved predominantly only one of the two chirality states of the participating fermions. The experimental challenge to measure directly the neutrino handedness was taken by M. Goldhaber, Lee Grodzins and A. Sunyar in 1958 [25]. In an ingenious experiment conducted at the Brookhaven National Laboratory in the USA they investigated the gamma disexcitation of ^{152}Sm that originates from the electron capture (EC) of ^{152}Eu. According to the kinematics of the processes the outgoing gamma should have the same helicity with the electron neutrino released in the primary EC. The results of the experiment showed unequivocally that neutrinos are left-handed.

In the early 1960's all the experimental informations concerning neutrinos and weak interactions were best incorporated in the V - A theory put forward by E. C. G. Sudarshan and R. E. Marshak [26], R. P. Feynman and M. Gell-Mann [27], and J.J. Sakurai [28]. In this model the neutrino was massless and solely left-handed, ν_L. The theory of a specific neutrino polarization had been initiated by A. Salam, L. Landau and Lee and Yang in the fifties leaning on theoretical arguments [29, 30, 31]. Experiments performed at CERN had confirmed the V – A character of weak interactions, but it has to be remarked that the underlying theory had been already constructed on symmetry grounds.

In the sixties, during the construction of the SM the absence of right-chirality neutrino components served as the proof that neutrinos are massless.

[3]Now known as K^0

Within the Higgs mechanism no Yukawa couplings of the form:

$$\sim y \; (\; \bar{\nu} \; \bar{e} \;)_L \; \tilde{\phi} \; \nu_R \tag{1.2}$$

could be added to the SM lagrangian that could form a neutrino mass term after the spontaneous symmetry breaking. The observations of neutrino masses through neutrino oscillations by the Super-Kamiokande collaboration in 1998 require a modification of this section of the SM. As of now, May 2012, no experiment has been able to measure directly the masses of neutrinos but new experiments plan to start data taking in the near future [32]. Current limits for the electron antineutrino mass come from the Troitzk and Mainz experiments; $m_\nu < 2.3$ eV at 90% C.L. [33].

1.1.4 Charged and Neutral Current interactions

After the spontaneous breaking of the electroweak symmetry, the mass diagonalization of the SM Lagrangian creates two interaction terms sensitive to all neutrinos, regardless of their flavour. The first term:

$$\mathcal{L}^{(CC)} = -\frac{g}{\sqrt{2}} \sum_{\alpha} \; \bar{\ell}_{\alpha,L} \gamma^\mu \nu_{\alpha,L} \; W^-_\mu + h.c. \tag{1.3}$$

is known as the charged current (CC) interaction and arises from $W^\pm$ boson exchanges. It is responsible for the neutrino transformation into its charged-partner lepton as shown in Fig. 1.4 (left). Of course, the charge conjugate channel of Fig. 1.4 (left) also exists. The second term:

$$\mathcal{L}^{(NC)} = -\frac{g}{2\cos\theta_W} \sum_{\alpha} \; \bar{\nu}_{\alpha,L} \gamma^\mu \nu_{\alpha,L} \; Z_\mu \tag{1.4}$$

is called the neutral current (NC) interaction. It involves exchanges of Z^0 bosons and it affects in the same way all neutrinos and anti-neutrinos. The existence of neutral currents was a firm prediction of the SM. The first observation of neutral current interactions in the Gargamelle bubble chamber [34] was a brilliant confirmation of the prevailing notions of Particle Physics.

1.2 The Solar and Atmospheric Neutrino Anomalies

In the 1960's and 80's several experiments with solar and atmospheric neutrinos revealed that the measured neutrino rates are significantly smaller than the theoretical expectations. Solar neutrinos were first detected by R. Davis

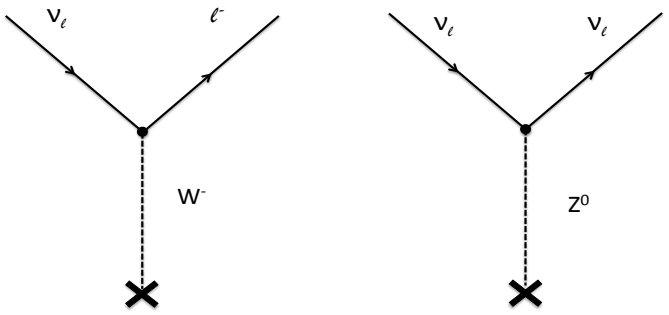

Figure 1.4: Charged current (left) and neutral current (right) weak interactions.

in his pioneering Homestake experiment [35] and the atmospheric neutrino flux was most accurately surveyed by IMB [36] and KamiokaNDE [37]. These experiments reported deficits in the counted neutrinos as compared to the established models of solar and atmospheric neutrino production. These observations raised the so-called Solar and Atmospheric anomalies.

In the early days, a lot of theoretical ideas were put forward to account for the aforementioned discrepancies. These included the modification of the neutrino properties or the reevaluation of the processes responsible for their production. Others just criticized these results arguing that the experimental setups and the measurements were very complicated and difficult to trust the outcome. As we now know, both these deficits are consistently explained by the mechanism of neutrino oscillations. In this section we will give a brief historical account on the pathbreaking experiments that led to these timely observations. A more detailed account on the current status of oscillation measurements will be given in the next chapter.

1.2.1 Solar neutrino flux

Sir A. Eddington was the first to theorize that the Sun and the rest of the stars pump up their energy from helium fusion reactions. The first in depth quantitive theories regarding the star energy production sequences were put forward by C. F. von Weizsacker [38, 39] and H. A. Bethe [40]. Briefly, the mechanisms proposed were the proton-proton (pp) chain reactions and the Carbon-Nitrogen-Oxygen (CNO) cycle. Both these branches include the emission of low energetic electron neutrinos. In Fig. 1.5 we summarize the reactions responsible for neutrino production. We should also add, that at the current temperature of the Sun, the pp-chain reactions contribute to the 99% of the solar ν_e flux. In Fig. 1.6 we show the spectrum of solar neutrinos.

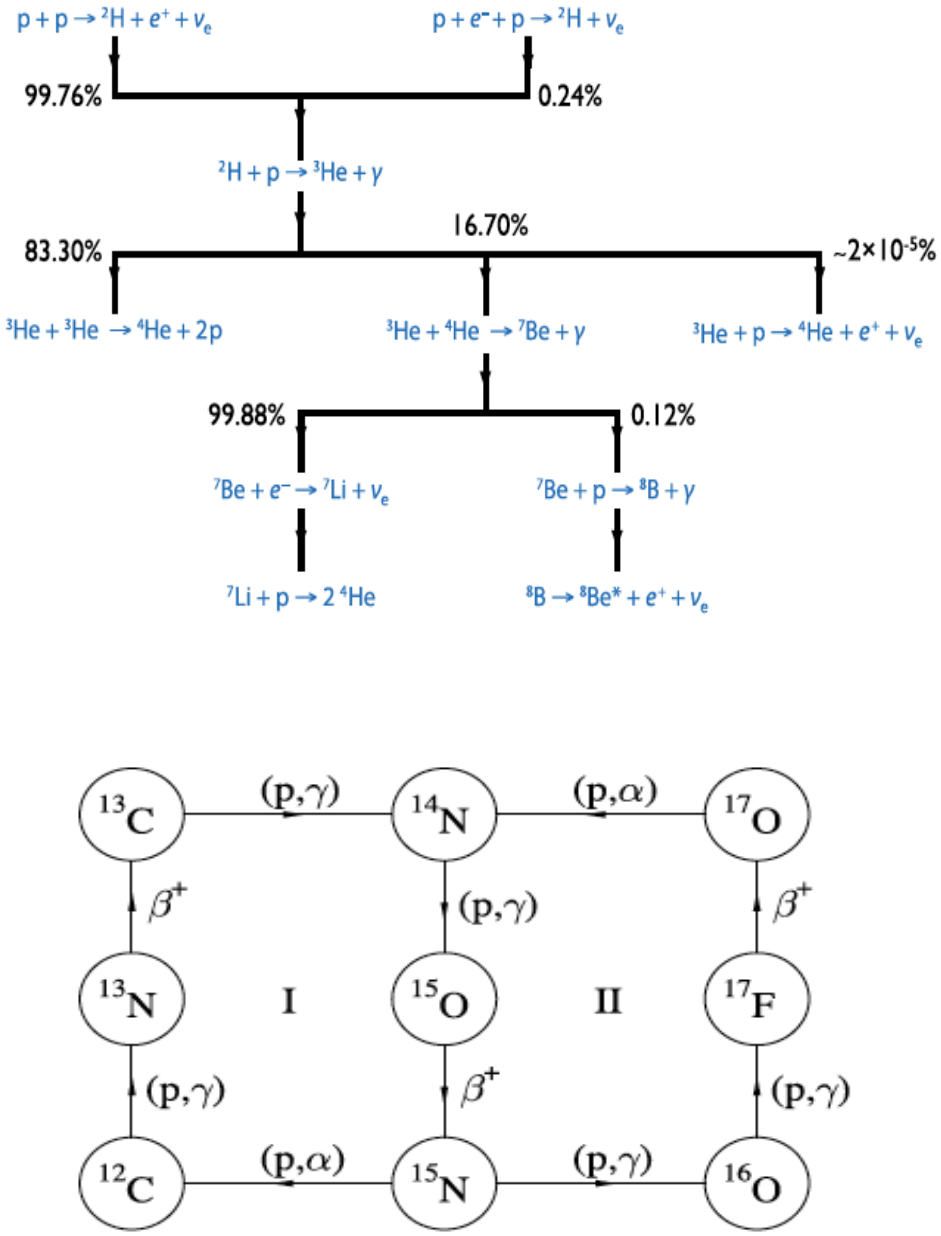

Figure 1.5: The two categories of nuclear reactions that that stimulate the Sun's burning. The pp-chain (top) and the CNO-cycle (bottom) [41].

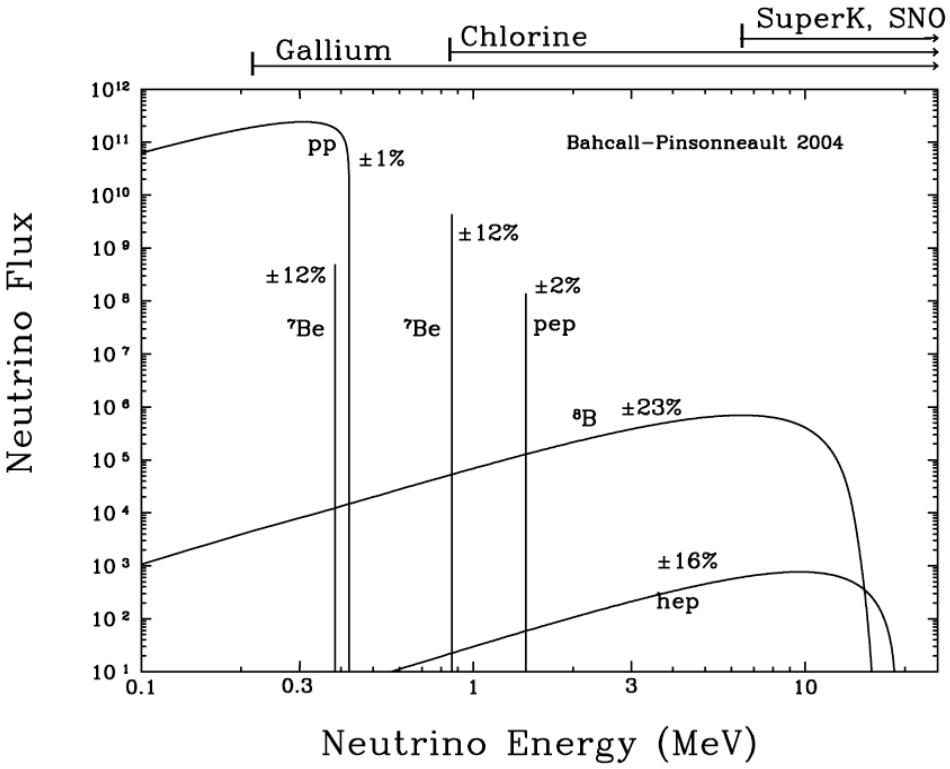

Figure 1.6: The solar neutrino spectrum [42].

In 1949, the future Nobel laureate L. Alvarez suggested the detection of solar neutrinos using their interaction on ^{37}Cl:

$$\nu_e \; + \; {}^{37}Cl \; \rightarrow \; e^- + \; {}^{37}Ar \tag{1.5}$$

but he never pursued this experiment. This is actually a reaction first proposed by B. Pontecorvo in 1946 to detect the neutrino itself. The challenge to observe neutrinos from the Sun using Cl was finally taken by R. Davis in 1964. Davis was a trained chemist working on neutrino physics for several years. In the fifties he conducted many unsuccessful experiments to observe neutrinos. His negative results combined with the Reines-Cowan observation of reactor neutrinos suggested that neutrinos and antineutrinos are not identical[4].

To trap the neutrinos originating from the sun, Davis placed a gigantic detector of 615 tons in the Homestake mine, South Dakota (USA). The detec-

[4]Note thought, that this question is not fully understood.

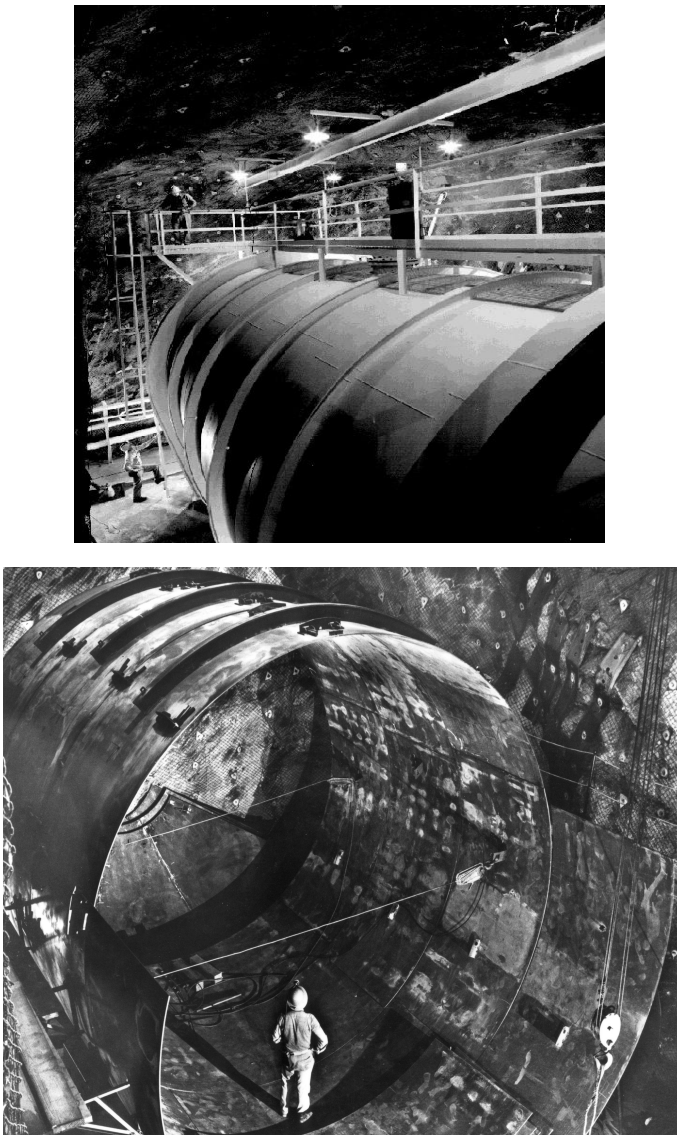

Figure 1.7: Some pictures of the Homestake detector.

tor was filled with perchloroethylene (C_2Cl_4), a common dry-cleaning fluid, and utterly placed in water pool to reduce the external cosmic background. Pictures of the detector are shown in Fig. 1.7. Crucial for the Homestake experiment was the calculation of the solar neutrino flux expected in the detector made by John Bahcall. As a matter of fact, Davis' experimental proposal and Bahcall's theoretical work were published back to back in Physical Review Letters [43, 44]. The project gain the support of many important figures like W. A. Fowler, R. W. Dodson and M. Goldhaber.

The first results from the Homestake experiment were published in 1968 [35]. The rate found was only about the one third of the predicted value. Most of the scientific community accepted this result with skepticism. In the subsequent years Davis upgraded his detector and scrutinized his results but the deficit still remained. The experiment run for many years and finally provided the result [45]:

$$\Phi_{\nu_e}(\text{Homestake}) = 2.56 \pm 0.16(stat.) \pm 0.16(syst.) \text{ SNU} \tag{1.6}$$

while the anticipated value from the Standard Solar Model (SSM) is [46]:

$$\Phi_{\nu_e}(\text{solar model}) = 7.6^{+1.3}_{-1.1} \text{ SNU}. \tag{1.7}$$

SNU is a unit equivalent to 10^{-36} captures per atom and per second.

In the eighties a real-time measurement of the solar neutrino flux was performed by the Kamiokande-II experiment [47]. Kamiokande-II was an upgrade of the prior, proton decay KamiokaNDE experiment. The solar neutrino signal was monitored in a 4500 tons detector, filled with purified water, via the neutrino - electron elastic scattering:

$$\nu_e \ + \ e^- \ \rightarrow \ \nu_e \ + \ e^- \tag{1.8}$$

The outgoing electrons were detected through the Čerenkov photon emission signal. Water Čerenkov detectors are excellent in discriminating electrons from muons. Also, the scattered neutrino momentum is strongly correlated with the incoming neutrino direction helping to reduce dangerous sources of background. This channel is sensitive to other neutrino flavours, ν_μ, ν_τ, albeit with a smaller cross-section. Kamiokande-II measured a flux of:

$$\Phi_{\nu_e}(\text{Kamiokande-II}) = 2.8 \pm 0.14 \ 10^6 \text{ cm}^{-2} \text{ s}^{-1} \tag{1.9}$$

0.55 ± 0.13 times smaller than the expectation from SSM [46].

To complete the picture, in the 1990's three more radiochemical experiments, SAGE, GALLEX and its extension GNO, measured solar neutrino fluxes lower than expectations. SAGE was a Russian-American experiment located at the Baskan Neutrino Observatory in South Caucasus (Russia). GALLEX and GNO detectors were installed at the "Laboratori Nazionali del Gran Sasso" (LNGS). All these experiments exploited the neutrino interactions on Gallium:

$$\nu_e \ + \ {}^{71}Ga \ \rightarrow \ e^- \ + \ {}^{71}Ge \tag{1.10}$$

This is a reaction that has low energy threshold at 0.233 MeV and it is ideal for the detection of the low energetic pp neutrinos. Germanium is extracted

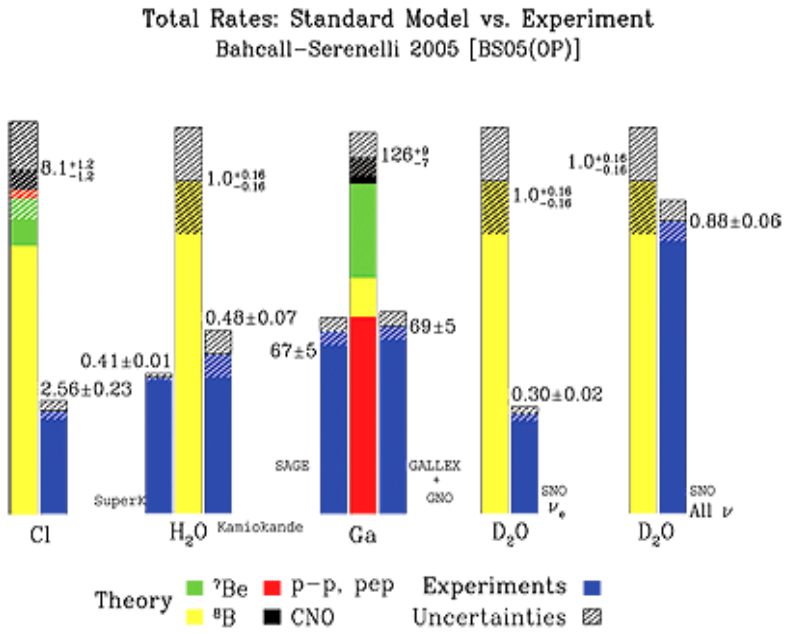

Figure 1.8: Summary of the measured solar neutrino rates.

through a complicated chemical technique and afterwards its electron capture decay is observed with low background proportional chambers.

SAGE measured a rate of [48]:

$$\Phi_{\nu_e}(\text{SAGE}) = 67.2^{+7.2}_{-7.0}(stat.)^{+3.5}_{-3.0}(syst.)\ \text{SNU}, \tag{1.11}$$

GALLEX gave [49]:

$$\Phi_{\nu_e}(\text{GALLEX}) = 77.5 \pm 6.2(stat.)^{+4.3}_{-4.7}(syst.)\ \text{SNU} \tag{1.12}$$

and GNO [50]:

$$\Phi_{\nu_e}(\text{GNO}) = 65.8^{+10.2}_{-9.6}(stat.)^{+3.4}_{-3.6}(syst.)\ \text{SNU}. \tag{1.13}$$

The predicted value according to the Standard Solar Model (SSM) is:

$$\Phi_{\nu_e}(\text{SSM}) = 128^{+9}_{-7}(stat.)^{+4.3}_{-4.7}(syst.)\ \text{SNU} \tag{1.14}$$

and so only about the 54% of the expected rate was utterly measured. The results of all these experiments are summarized in Fig. 1.8 taken from Ref. [51]. These observations formed the famous Solar Neutrino Anomaly or Problem.

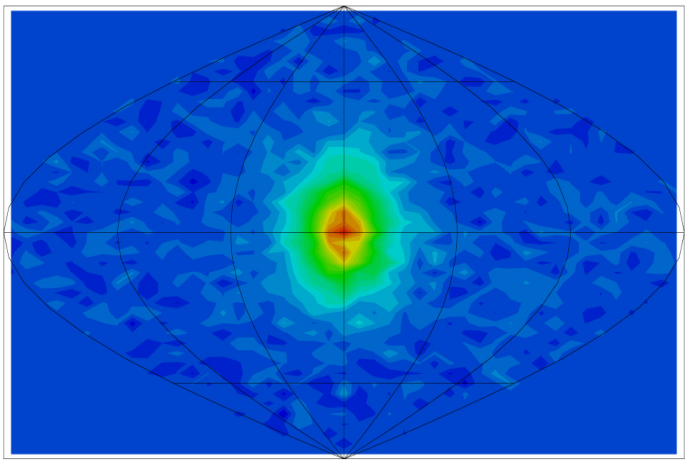

Figure 1.9: The Sun as viewed by Super-Kamiokande [53].

In the nineties the same deficit was further confirmed by the Super-Kamiokande collaboration [52]. In Fig. 1.9 we show a picture of the Sun as observed by Super-Kamiokande using solar neutrinos. The problem was finally conjured in 2001 by the Sudbury Neutrino Observatory (SNO) in a model independent way and some years after the same effect was observed by KamLAND using reactor antineutrinos. Recently, the BOREXINO low-background experiment have made some very important discoveries concerning solar neutrino spectroscopy. More about the modern solar neutrino experiments together with an up-to-date review of the solar neutrino sector will be given in Chapter 2.

1.2.2 Neutrinos from the atmosphere

When the high energetic particles of cosmic rays interact with atoms in the atmosphere, neutrinos are created, mostly through the decay of pions and muons.

$$\pi^{\pm} \rightarrow \mu^{\pm} + \nu_{\mu}(\bar{\nu}_{\mu}) \tag{1.15}$$

$$\searrow$$

$$e^{\pm} + \nu_{\mu}(\bar{\nu}_{\mu}) + \bar{\nu}_{e}(\nu_{e}) \tag{1.16}$$

Both muon and electron neutrinos and antineutrinos are produced depending on the charge of the parent pion [54]. Atmospheric neutrinos were first detected in 1965 by F. Reines et al. in a gold mine in South Africa [55] and by G. Menon et al. in the Kolar Gold Fields in India [56].

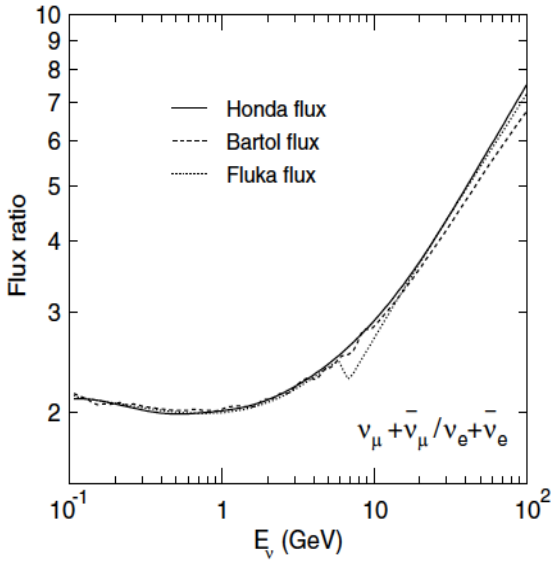

Figure 1.10: The atmospheric neutrino $(\nu_\mu + \bar{\nu}_\mu)/(\nu_e + \bar{\nu}_e)$ ratio [59].

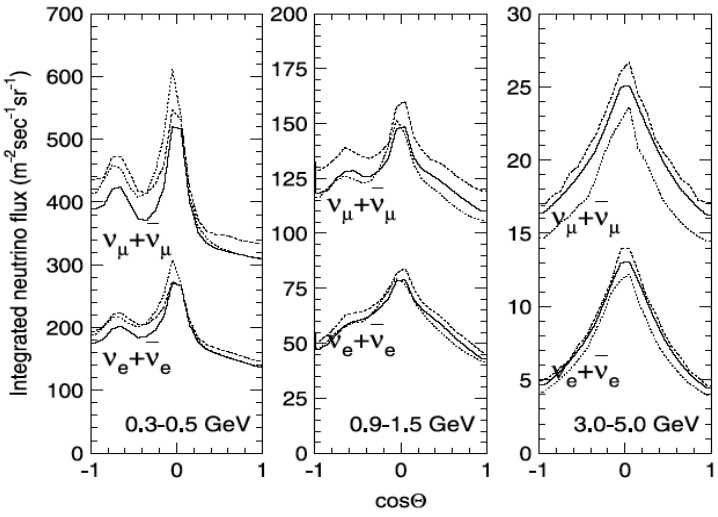

Figure 1.11: Atmospheric neutrino angular distributions [59].

To calculate the flux of atmospheric neutrinos one needs to know the primary cosmic ray flux and content. Subsequently, other phenomena like the hadron production or the earth's geomagnetic effect are taken into account in the calculation [57, 58]. Very briefly, the main characteristics of the flux are the ratio of $(\nu_\mu + \bar{\nu}_\mu)$ over $(\nu_e + \bar{\nu}_e)$ that is roughy equal to 2.0 for a vast range of energies in the sub-GeV region or the zenith angle distributions

that are almost symmetric for upward- and downward-going neutrinos. Both these effects are shown in Fig. 1.10 and 1.11.

In the 1980's two high-scale water Čerenkov detectors were built, IMB and Kamiokande. Primary objective of these instruments was the observation of proton decay suggested by many Grand Unified Theories (GUT) in the 1970's and 80's. Both IMB and Kamiokande were able to observe neutrinos originating from the atmosphere. Note that atmospheric neutrinos were a background for proton decay searches. In the course of these investigations, they reported smaller $(\nu_\mu+\bar{\nu}_\mu)/(\nu_e+\bar{\nu}_e)$ ratios from expectations (abbreviated as ν_μ/ν_e from now on).

More precisely, Kamiokande found the double ratio between the measured $(\nu_\mu/\nu_e)_{data}$ and that provided by theory and simulations $(\nu_\mu/\nu_e)_{MC}$ to be:

$$(\nu_\mu/\nu_e)_{data}/(\nu_\mu/\nu_e)_{MC} = 0.60^{+0.07}_{-0.06} \pm 0.05 \tag{1.17}$$

in the sub-GeV [60] and:

$$(\nu_\mu/\nu_e)_{data}/(\nu_\mu/\nu_e)_{MC} = 0.57^{+0.08}_{-0.07} \pm 0.07 \tag{1.18}$$

in the multi-GeV region [61]. This double ratio was formed to further reduce systematical errors. In the absence of hidden physics $(\nu_\mu/\nu_e)_{data}/(\nu_\mu/\nu_e)_{MC}$ should equal to one. One the other hand, IMB found:

$$(\nu_\mu/\nu_e)_{data}/(\nu_\mu/\nu_e)_{MC} = 0.54^{+0.05}_{-0.11} \tag{1.19}$$

in the sub-GeV region but no abnormality was found in the upward-going muon events [62] and the partially contained events above 1 GeV [63] . Furthermore, Kamiokande observed a clear dependence of the ν_μ and $\bar{\nu}_\mu$ flux on the zenith angle in high contrast with the predictions, Fig. 1.12.

These observations, formed in the early 1990's, the Atmospheric Neutrino Anomaly. Kamiokande reported in the multi-GeV range a 2.5 σ deviation. This deficit was further elaborated by the Super-Kamiokande Collaboration in the ninties and finally in 1998 the effect was unravelled with a more than 5 σ statistical significance. The same effect was seen afterwards with accelerator neutrino beams on experiments in Japan and USA.

1.3 Neutrino oscillations

Both Solar and Atmospheric Neutrino Anomalies can be consistently explained within the neutrino oscillations scenario. Especially the zenith angle dependence seen by Kamiokande (Fig. 1.12) is very characteristic of the patterns predicted by particle oscillations. In this section we will put forward

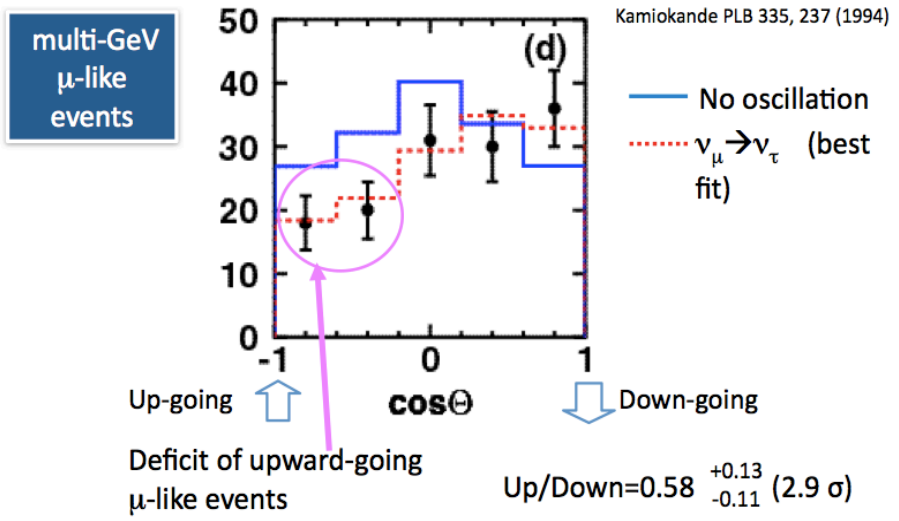

Figure 1.12: Deficit of upward-going μ-like events in Kamiokande [64].

the mathematical machinery and formulae of neutrino oscillations in vacuum and matter. As we shall see, neutrino oscillations require neutrino masses and mixing; that is Physics currently not implemented in the Standard Model. We will first review neutrino mixing.

1.3.1 Neutrino mixing

Particle mixing was first devised by M. Gell-Mann and A. Pais in connection with the strangeness scheme [65]. The way that mixing fits in the quark sector was developed by N. Cabibbo [66], S. L. Glashow, J. Iliopoulos and L. Maiani [67] and M. Kobayashi and T. Maskawa [68]. In general, particle mixing refers to the fact that the particles flavour eigenstates, those produced during the interactions, can be different from the energy eigenstates that govern the particles dynamical evolution.

In the language of neutrinos, the flavour eigenstates $|\nu_a\rangle$, $\alpha = e,\ \mu,\ \tau$, are not identical with the mass eigenstates $|\nu_i\rangle$ and, instead, they are related through a unitary matrix U. In the minimal 3×3 scenario this translates to the formula:

$$|\nu_\alpha\rangle \ = \sum_{i=1}^{3} U^*_{\alpha i} \ |\nu_i\rangle \tag{1.20}$$

The unitarity of the U matrix is important to ensure the conservation of

probabilities. U has in general complex elements, but the unitarity condition:

$$\sum_{i=1}^{3} U^*_{\alpha i}\, U_{\beta i} \;= \delta_{\alpha\beta} \tag{1.21}$$

constrains many of them. For example, the conditions imposed by Eq. (1.21) form nine independent relations that can eliminate nine free parameters. This leaves still nine parameters on U. Relying on a strict correspondence between the complex matrix U and a real matrix that would correspond to rotations in the three Euclidean space, one can see that U must have three real components (angles) and six imaginary phases.

In terms of the mass fields ν_i the charge current (CC) interaction lagrangian can be written as:

$$\mathcal{L}^{(CC)} = -\frac{g}{\sqrt{2}} \sum_{\alpha,i} U_{\alpha i}\; \bar{\ell}_{\alpha,L} \gamma^\mu \nu_{i,L}\; W^-_\mu + h.c. \tag{1.22}$$

which implies that the mixing changes the coupling of lepton current to the charged weak bosons. Nonetheless, the interaction term shows that additional complex phases could be further removed by a redefinition of the leptons phases. For the case of the charged leptons a redefinition of the form:

$$\ell_{\alpha,L} \to e^{i\phi_\alpha} \ell_{\alpha,L} \tag{1.23}$$

suffices to abolish three more complex phases. Like this the neutrino mixing matrix can be parametrized through three mixing angles and three phases in the standard form:

$$\begin{aligned} U \;=\; & \begin{pmatrix} 1 & 0 & 0 \\ 0 & \cos\theta_{23} & \sin\theta_{23} \\ 0 & -\sin\theta_{23} & \cos\theta_{23} \end{pmatrix} \times \begin{pmatrix} \cos\theta_{13} & 0 & e^{-i\delta_{CP}}\sin\theta_{13} \\ 0 & 1 & 0 \\ -e^{i\delta_{CP}}\sin\theta_{13} & 0 & \cos\theta_{13} \end{pmatrix} \\ & \times \begin{pmatrix} \cos\theta_{12} & \sin\theta_{12} & 0 \\ -\sin\theta_{12} & \cos\theta_{12} & 0 \\ 0 & 0 & 1 \end{pmatrix} \times diag\{e^{i\alpha_1/2}, e^{i\alpha_2/2}, 1\} \end{aligned} \tag{1.24}$$

Other conventions on this parametrization could be followed; we used the standard one used also in [33].

Note that, assuming that neutrinos are not represented by real fields, that means that neutrinos and antineutrinos correspond to physically different particles, some more phases can be eliminated by the action:

$$\nu_{i,L} \to e^{i\phi_i} \nu_{i,L} \tag{1.25}$$

Only two such phases can be erased from U since a total phase-change would lead to the same lagrangian. Normally phases α_1 and α_2 are cut out through (1.25) and that's why they are often called Majorana phases.

1.3.2 Oscillation formula in vacuum

Assuming that neutrinos mix,

$$U_{\alpha i} \neq 0, \tag{1.26}$$

and that a non-degenerate mass spectrum of neutrinos exists,

$$m_1 \neq m_2 \neq m_3, \tag{1.27}$$

it only requires some elementary knowledge of quantum mechanics, to show that these concepts predict the flavour transmutation of neutrinos, spontaneously as they travel along the vacuum. The quantum mechanical amplitude for this flavour change can be shown to follow an oscillatory pattern; this is the reason that this phenomenon is called neutrino oscillations.

We will derive the standard oscillation formula trying to avoid as much as possible various technicalities that underneath the full computation. For this we will lean on a semi-plane-wave approximation to the localized neutrino states. It has to be understood that this elementary approach will avoid some intricate points leading at the end to the correct formula. The completely rigorous derivation of the oscillation probability can be found in some standard references [69, 70].

Assume a neutrino of flavour α localized at x. This is described by the state ket[5]:

$$e^{-i\hat{p}x} \left|\nu_\alpha\right\rangle . \tag{1.28}$$

We employ the use of natural units. After the elapse of a ΔT time-interval this state vector will evolve to:

$$e^{-i\hat{H}\Delta T} e^{-i\hat{p}x} \left|\nu_\alpha\right\rangle \tag{1.29}$$

so that there is a non-zero probability amplitude to observe the neutrino flavour β at the x' space point.

$$e^{-i\hat{p}x'} \left|\nu_\beta\right\rangle \tag{1.30}$$

The probability for flavour transmutation is given by:

$$p(\ \nu_\alpha \to \nu_\beta\ ) = |\left\langle\nu_\beta\right| e^{i\hat{p}x'} e^{-i\hat{H}\Delta T} e^{-i\hat{p}x} \left|\nu_\alpha\right\rangle|^2 \tag{1.31}$$

which becomes:

$$p(\ \nu_\alpha \to \nu_\beta\ ) = |\sum_i U^*_{\alpha i}\ U_{\beta i}\ e^{ip_iL - iE_i\Delta T}|^2 \tag{1.32}$$

[5] I repeat that a concise treatment can only be obtained with the use of wave-packets.

through the introduction of the completeness condition:

$$\sum_i |\nu_i\rangle \langle\nu_i| = 1 \tag{1.33}$$

and the obvious relations:

$$\langle\nu_i|\ \nu_\alpha\rangle = U^*_{\alpha i} \text{ and } \langle\nu_\beta|\ \nu_i\rangle = U_{\beta i}. \tag{1.34}$$

Using the approximations valid for relativistic neutrinos:

- L = ΔT and,

- $E_i = p_i - \frac{m_i}{2E}$, where E the energy of the otherwise massless neutrinos

the $p(\ \nu_\alpha \to \nu_\beta\ )$ formula becomes:

$$\begin{aligned} p(\ \nu_\alpha \to \nu_\beta\ ) &= |\sum_i U^*_{\alpha i}\ U_{\beta i}\ e^{-i\frac{m_i L}{2E}}|^2 \\ &= \sum_{i,j} U^*_{\alpha i}\ U_{\beta i}\ U_{\alpha j}\ U^*_{\beta j}\ e^{-i\frac{\Delta m_{ij} L}{2E}} \end{aligned} \tag{1.35}$$

In a two flavour approximation the indices $i,\ j$ run from 1 to 2 and (1.35) simplifies to the formula:

$$p(\ \nu_\alpha \to \nu_\beta\ )\ =\ \sin^2 2\theta\ \sin^2 \frac{\Delta m^2 L}{4E} \tag{1.36}$$

when $\alpha \neq \beta$. The ν_β appearance probability is shown in Fig. 1.13 for some generic values of θ and Δm^2. In the x-axis the ratio L/E is plotted in arbitrary units and in logarithmic scale. The aforementioned oscillatory behavior is obvious. It should be noted that the oscillation amplitude and length are $\sin^2(2\theta)$ and $4\pi/\Delta m^2$ respectively.

The possibility of neutrino oscillations was first theorized by B. Pontecorvo in 1957, in an early model of $\nu \leftrightarrow \bar{\nu}$ oscillations [71]. Z. Maki, M. Nakagawa and S. Sakata discussed oscillations between different neutrino flavours in 1962 [72]. Stimulated by the results of the Homestake experiment Pontecorvo and Gribov proposed neutrino oscillations as the solution to the Solar Neutrino Problem in 1967 and '69 [73, 74].

1.3.3 Matter induced oscillations

The oscillation formula worked out in the previous section, is drastically altered when neutrinos travel through matter. Ordinary matter is usually

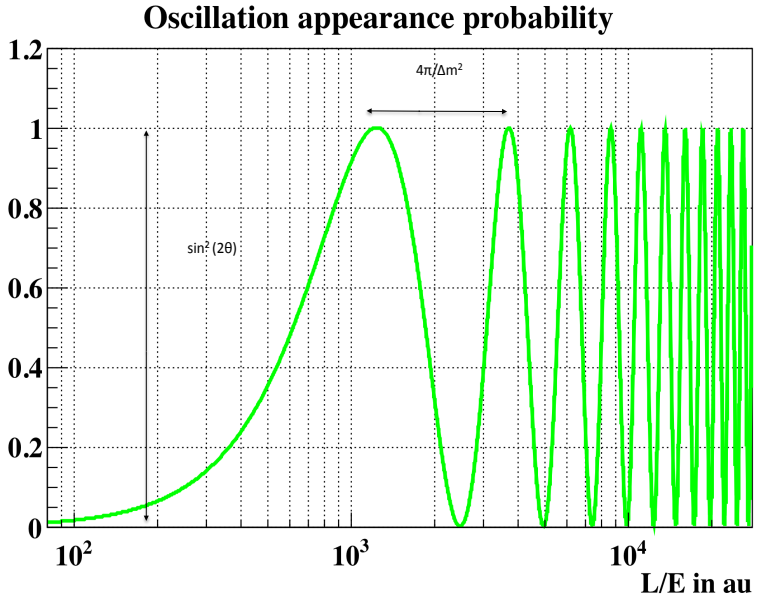

Figure 1.13: $p(\ \nu_\alpha \to \nu_\beta\ )$ appearance probability in the two-flavor approximation.

non-relativistic, neutral and non-polarized, while its main components are electrons, protons and neutrons ($e,\ p,\ n$). The weak interactions of the different neutrino flavours with the particles of matter, modify their energies and change the interference patterns that control oscillations. Given the fact that neutral current interactions influence in the same way all the neutrino generations, neutral currents contribute only a common phase that finally does not appear in the oscillation formulae. It is only the Charge Current (CC) interactions that are responsible for this phenomenon.

In a low-energy approximation, the weak interaction hamiltonian takes the form of the four-point vertex interaction:

$$\mathcal{H}_{int} = \frac{G_F}{2}(\ \bar{\nu}_\alpha \gamma^\mu \nu_\alpha\ ) \sum_f \bar{f} \gamma_\mu (\ g_V^{\alpha,f} - g_A^{\alpha,f} \gamma^5\ ) f. \tag{1.37}$$

The index f runs over the $e,\ p,\ n$ that constitute matter and $g_V^{\alpha,f}$, $g_A^{\alpha,f}$ are the effective vector and axial-vector weak couplings. The values of $g_V^{\alpha,f}$ and $g_A^{\alpha,f}$ for $\alpha = e$, μ and τ and $f = e$, p and n can be found in [75]. It is a rather

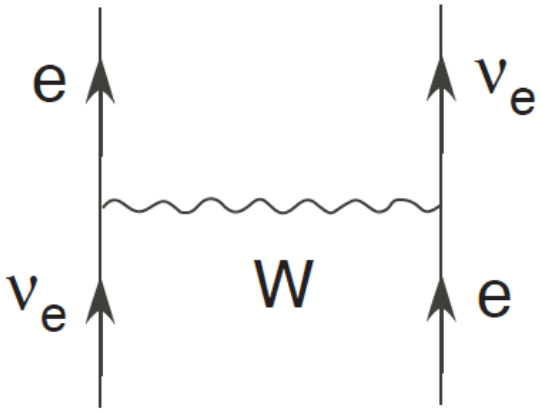

Figure 1.14: The Feynman diagram of the ν_e - e forward scattering that modifies oscillation patterns [76].

simple exercise to calculate the final interaction potentials for the various neutrino flavours. The results are:

$$\sqrt{2}G_F N_e - \frac{1}{2}G_F N_n, \; -\frac{1}{2}G_F N_n \text{ and } -\frac{1}{2}G_F N_n \tag{1.38}$$

for ν_e, ν_μ and ν_τ respectively. G_F is the Fermi weak interaction coupling constant, N_e is the electron density of matter and N_n the density of neutrons. Note that for normal, neutral matter we have $N_p = N_e$. Note also that the common -1/2 $G_F N_n$ arises from the Z^0 induced weak interactions and drops out as long as we consider neutrino oscillations. The first term $\sqrt{2}G_F N_e$ that affects only electron neutrinos corresponds to the diagram of Fig. 1.14.

The presence of these extra neutrino-matter interaction terms, modify both the neutrino energy eigenvalues and eigenvectors. In a two flavour approximation the mixing is altered according to the matrix:

$$U = \begin{pmatrix} \cos\theta_m & \sin\theta_m \\ -\sin\theta_m & \cos\theta_m \end{pmatrix} \tag{1.39}$$

where θ_m is given by:

$$\sin^2(2\theta_m) = \frac{\sin^2(2\theta)}{\sin^2(2\theta) + (\cos(2\theta) - A)^2} \tag{1.40}$$

with:

$$A = \frac{2EV}{\Delta m^2} \text{ and } V = \sqrt{2}G_F N_e. \tag{1.41}$$

Also, the oscillation probability formula in matter is modified accordingly:

$$p(\ \nu_\alpha \to \nu_\beta\ )\ =\ \sin^2 2\theta_m\ \sin^2 \frac{\Delta m_m^2 L}{4E} \tag{1.42}$$

where:

$$\Delta m_m^2 = \Delta m \sqrt{\sin^2(2\theta) + (\cos(2\theta) - A)^2} \tag{1.43}$$

It is, of course, evident that when $V = 0$ all these formulae reduce to the simpler ones related to vacuum oscillations. For antineutrinos one simply changes V with $-V$. For more details on matter driven oscillations one might consult Ref. [76].

In the special case where A equals to $\cos(2\theta)$ an enhancement of oscillations takes place. This can be seen from Eq. (1.40) since when $A \approx \cos(2\theta)$ the oscillation amplitude maximizes, $\sin^2(2\theta_m) \approx 1$. This resonant effect is very important in the understanding of the solar neutrino flux composition. Historically the modification of the oscillation probability formula due to neutrino interactions was first published by L. Wolfenstein [77]. He worked out most of the mathematical formulae that describe the phenomenon. The resonance character of matter oscillations was unveiled by S. P. Mikheyev and A. Yu. Smirnov [78, 79, 80, 81]. They were the first to conceive the importance of this effect to the Solar Neutrino Problem.

1.4 Possible mass models

In the old days of quantum field theory, a mass term, say for the electron or the muon, would enter the free lagrangian according to the recipe:

$$\mathcal{L}_m = -m\bar{\psi}\psi \tag{1.44}$$

$\mathcal{L}_m$ mixes the left and right chirality ψ components and it's called Dirac mass term since it is identical to the mass term present in the langrangian that leads to the relativistic Dirac equation. Splitting ψ in left- and right-handed parts,

$$\psi = \psi_R + \psi_L \tag{1.45}$$

$\mathcal{L}_m$ becomes:

$$\mathcal{L}_m = -m(\ \bar{\psi}_L\psi_R + \bar{\psi}_R\psi_L\ ). \tag{1.46}$$

In the Standard Model lagrangian, Dirac mass terms could not be introduced just "by hand" because they break the underlying gauge symmetries. Fermions obtain Dirac masses after spontaneous symmetry breaking through Yukawa coupling terms with the Higgs boson. Since no right-handed neutrino states ν_R exist, no neutrino Dirac masses can be generated. On the other hand, Majorana mass terms of the form:

$$\mathcal{L}_m \sim \bar{\nu}_L^c \nu_L \tag{1.47}$$

could not either created, since they generally have hypercharge $Y = -2$ and gauge invariance would require a Higgs $Y = 2$ component. For this a Higgs triplet would be necessary. For neutrino masses, one needs to extent the minimal SM in one way or the other.

The easiest way to create neutrino masses would be to introduce right chirality neutrino components and lean on the Higgs mechanism, as it is done for the rest of the SM fermions. This can always be done, but then in order to reproduce the expected neutrino spectrum a very small Yukawa coupling y_ν should be introduced. For a neutrino mass of 1 eV^2 one would need a y_ν of the order of 10^{-20}. Particle physicists are usually against theories that such a careful cancellation takes place. A structure that would explain naturally the smallness of y_ν as compared to the rest of the Yukawa couplings must be invented.

A prominent theory to address these questions is the so-called see-saw mechanism [82]. In see-saw models one assumes the existence of ν_R and allows the presence of both Dirac and Majorana mass terms.

$$\mathcal{L}_m = -m_D(\bar{\nu}_R \nu_L + \bar{\nu}_L \nu_R) - \frac{m_R}{2}(\bar{\nu}_R^c \nu_R + \bar{\nu}_R \nu_R^c) \tag{1.48}$$

A Majorana mass term made up by left-handed Weyl spinors was avoided since it would have been problematic assuming only the common SM Higgs doublet. $\mathcal{L}_m$ can be written in the form:

$$\mathcal{L}_m = -\frac{1}{2}\left(\bar{\nu}_L^c \;\; \nu_R \right) \begin{pmatrix} 0 & m_D \\ m_D & m_R \end{pmatrix} \begin{pmatrix} \nu_L \\ \nu_R^c \end{pmatrix} + h.c. \tag{1.49}$$

where M is the mass matrix:

$$M = \begin{pmatrix} 0 & m_D \\ m_D & m_R \end{pmatrix} \tag{1.50}$$

See-saw models let m_D to be at the same order of magnitude as the masses of the rest charged leptons and quarks, generated by the Higgs mechanism,

while m_R is constrained to be extremely heavy; probably related to a higher energy scale, $m_R >> m_D$.

To derive the mass spectrum corresponding to this lagrangian one needs to diagonalize M. This is just an elementary calculation. Then, the neutrino masses are given by the M eigenvalues. The result of this calculation is:

$$m_1 = m_D^2/m_R \quad \text{and} \quad m_2 = m_R \tag{1.51}$$

We see that owning to m_R the masess of light neutrinos are wildly suppressed in accordance with the experimental evidence, while another type of heavy neutrino exists. It should be noted that in this scheme the two physical neutrinos are naturally Majorana particles.

See-saw mechanism offers an attractive solution to the neutrino mass puzzle. It explains in a neat approach the smallness of neutrino masses while it makes the direct prediction that they are Majorana-type particles. Nonetheless, we should emphasize that an established model concerning these questions is not yet available. For a more detailed account on the possible neutrino mass mechanisms one could have a look at Ref. [83].

Chapter 2

Present experimental status

In this short chapter, we will try to give a full account on the current status of oscillation measurements and experiments. Emphasis will be given on the main modern experiments elucidating oscillations, after the 1998 Super-Kamiokande epochal observations, since most of the prehistory was covered in the previous chapter. We will also sketch forth-coming experiments and future projects to address the important questions of neutrino mass hierarchy, CP-violation in the leptonic sector or sterile oscillations modes.

2.1 Atmospheric parameters

Super-Kamiokande started operation in 1996. It is an imaging water Čerenkov detector, just like Kamiokande, albeit with a larger fiducial volume (22.5 kt). Main motivation for its construction was the search for proton decay and the observations of solar and atmospheric neutrinos. It is a joint Japanese-American project located 1000 m underground in the Mozumi Mine, 186 miles west of Tokyo in the Japanese Alps. Of course, part of the motivation to built Super-Kamiokande was to elaborate on the observations of IMB and Kamiokande regarding the Atmospheric Neutrino Anomaly.

The Super-Kamiokande collaboration presented in 1998, at the Neutrino conference at Takayama (Japan), their first analysis of atmospheric neutrino events [84]. The data set used for this study, consisted in 33.0 kiloton-year (535 days) exposure of the Super-Kamioknade detector and provided the first direct evidence of neutrino oscillations. The results were, again, formulated in terms of the ν_μ/ν_e data - MC double ratio, and confirmed the earlier observations on the deficit of upward-going $\bar{\nu}_\mu$ and ν_μ. The effect was pined down with a statistical significance greater than 5 σ erasing the possibility to explain it in terms of experimental biases or statistic errors.

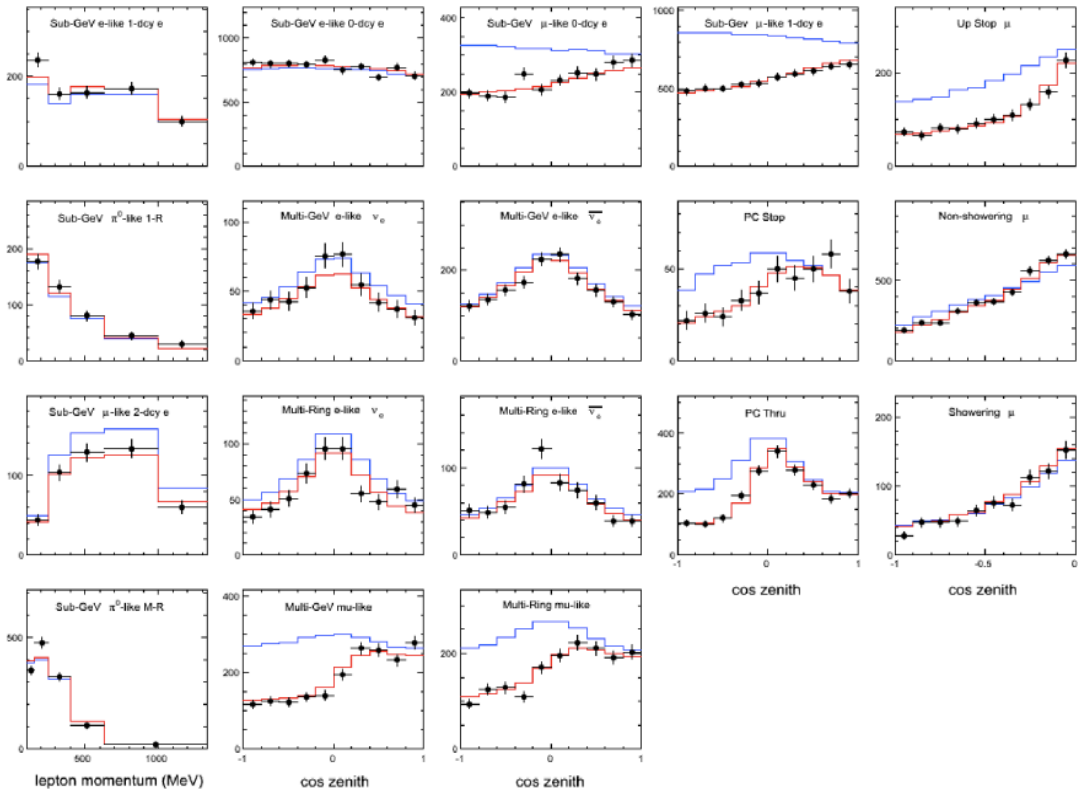

Figure 2.1: Zenith angle distributions of e-like and μ-like events in Super-Kamiokande. Blue lines denote the MC expectation in the non-oscillation scenario and red lines the best fit curves [85].

In particular, Super-Kamiokande measured the ratio of,

$$(\nu_\mu/\nu_e)_{data}/(\nu_\mu/\nu_e)_{MC} = 0.63 \pm 0.03 \text{ (stat.)} \pm 0.05 \text{ (syst.)} \qquad (2.1)$$

in the sub-GeV and,

$$(\nu_\mu/\nu_e)_{data}/(\nu_\mu/\nu_e)_{MC} = 0.65 \pm 0.05 \text{ (stat.)} \pm 0.08 \text{ (syst.)} \qquad (2.2)$$

in the multi-GeV energy ranges. The result, interpreted as two flavour neutrino oscillations between ν_μ and ν_τ, $\nu_\mu \leftrightarrow \nu_\tau$, suggested a neutrino mixing angle and mass square splitting of:

$$\sin^2(2\theta_{23}) > 0.82 \text{ and } 5\ 10^{-4} eV^2 < \Delta m^2 < 6\ 10^{-3}\ eV^2 \qquad (2.3)$$

All these observations were fully consistent with the early findings of IMB and Kamiokande. In the subsequent years, Super-Kamiokande further scrutinized

its results with the accumulation of more statistics elucidating the up-down asymmetry with "infinite", more than 13 σ, significance. In Fig. 2.1 we show the azimuthal angle distributions for electron- and muon-like events; the deficit of the upward-going μ-like events, suggesting the oscillation of ν_μ as they travel inside earth, is clearly visible. Furthermore, Super-Kamiokande has also presented a dedicated analysis showing that the L/E disappearance patterns, favour strongly neutrino oscillations over the other possible models that reproduce this zenith angle dependence [86].

With the objective to investigate independently the oscillation signal seen with atmospheric neutrinos, many long base-line oscillation experiments with high energetic $\nu_\mu(\bar{\nu}_\mu)$ beams were put forward. The first of them, that ever took data was K2K (KEK to Kamioka) in 1999. In these projects, narrow beams of muon neutrinos or anti-neutrinos are produce artificially from the collision of high-energy protons on a fixed target, in a way that resembles closely the production of neutrinos from cosmic rays in the upper levels of the atmosphere. These primary, high intensity proton beams are produced in particle accelerators and that's why these initiatives are widely known as "accelerator experiments".

In K2K experiment [87], the beam of neutrinos was produced at the Japanese National Accelerator Facility KEK through the collisions of 12 GeV proton bunches to a hadron production target. Subsequently, a set of horn magnets was used to focus the secondary charged particles, mainly pions, created in the target. The polarity of the horns was such that only positive pions were focused; negative charged particles were deflected away. The charged pions were then let to decay in a 200 m long tunnel filled with helium at 1 Atm pressure. Muon neutrinos were produced predominantly by the pion decay:

$$\pi^+ \rightarrow \mu^+ + \ \nu_\mu \tag{2.4}$$

while a small and calculable fraction of electron neutrinos (roughly 1%) were produced by the muon decay:

$$\mu^+ \rightarrow e^+ + \bar{\nu}_\mu + \nu_e. \tag{2.5}$$

$\bar{\nu}_\mu$ and $\bar{\nu}_e$ were also produced, albeit with a smaller rate. The main ingredients of the K2K beam focusing system are summarized in Fig.2.2.

The ν_μ flux and energy spectrum can be calculated by complicated simulation packages. Nonetheless, the uncertainties on these parameters are quite significant. To evade this, K2K built another detector, 294 m away from the pion production target, to monitor the beam profile and the neutrino production. This near detector was a 1 kton water Čerenkov device constructed

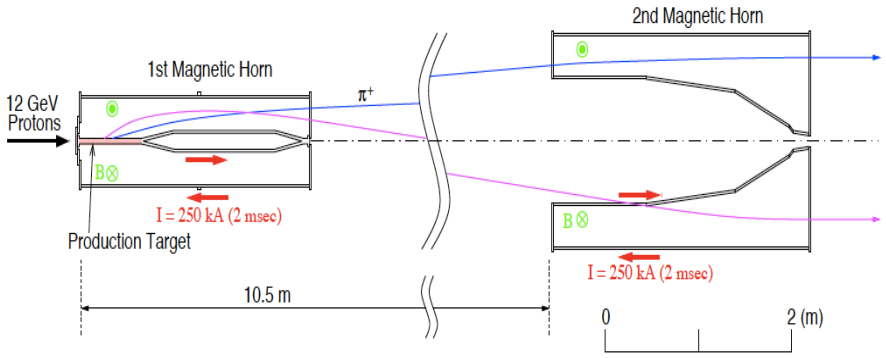

Figure 2.2: The K2K beam focusing magnetic horns [87].

in the standards of Super-Kamiokande in order to have the same neutrino interaction cross-sections. Super-Kamiokande, on the other hand was located in a 250 km distance away from KEK with the purpose to search for the signature of particle oscillations. This two detector scheme was able to reduce the beam systematics and enhance the sensitivity on θ_{23} and Δm^2_{23}.

K2K took data for three years. In the analysis of the whole data sample, one hundred and twelve beam-originated neutrino interactions were detected in the Super-Kamiokande fiducial volume. Leaning both on simulations and near detector measurements, $158.1^{+9.2}_{-8.6}$ events were expected in the absence of neutrino oscillations. In addition, a clean spectral distortion was seen in 58 single-ring muon-like events that was fully consistent with neutrino oscillations (Fig. 2.3). A likelihood analysis based on the normalization and shape informations yielded the results for a two flavour analysis:

$$\sin^2(2\theta_{23}) = 1 \text{ and } \Delta m^2_{23} = 2.8\ 10^{-3}\ eV^2 \tag{2.6}$$

The non-oscillation hypothesis was excluded at 4.3 σ and the results were in excellent agreement with those of Super-Kamiokande. The allowed regions of oscillations parameters for K2K and Super-Kamiokande are shown in Fig. 2.4.

The muon neutrino disappearance channel has been investigated also by the MINOS experiment (Main Injector Neutrino Oscillation Search). The neutrino beam for MINOS is produced at the NuMI facility at Fermilab. The beam is peaked around 3 GeV (tunable in a certain energy range) and the flux composition can change from ν_μ to $\bar{\nu}_\mu$ depending on the focusing magnets current polarity. More details on the MINOS beam-line can be found elsewhere [88]. MINOS experiment uses two detectors of the magnetized iron-

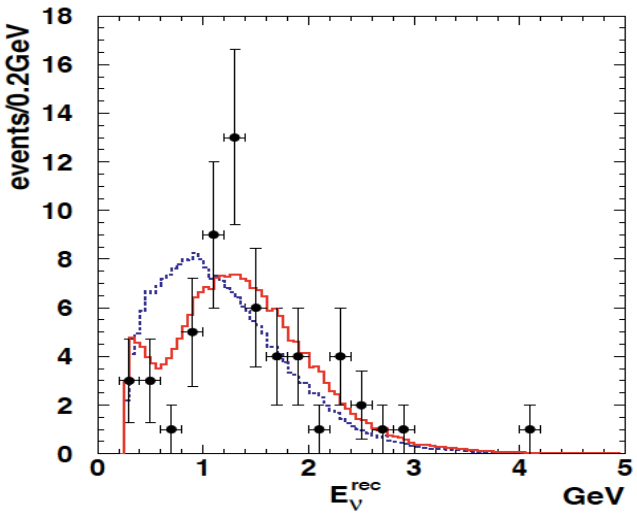

Figure 2.3: Energy spectrum of one-ring μ-like events (data points) in Super-Kamiokande. The expectation in the absence of oscillations (blue line) is also shown.

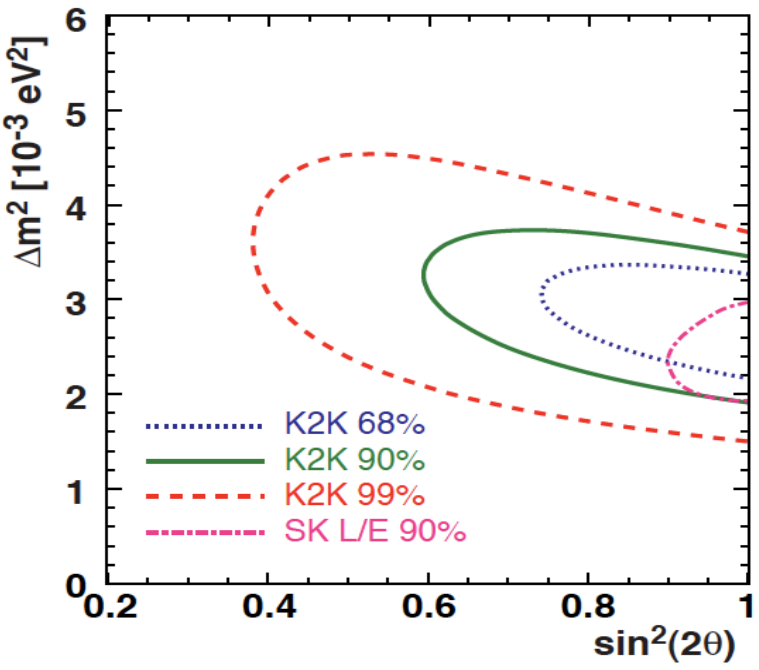

Figure 2.4: Allowed regions of oscillation parameters for the K2K at 68, 90 and 99 % confidence level. Overlapped the results of Super-Kamiokande are also shown.

Figure 2.5: The MINOS near (top) and far (bottom) detectors.

calorimeter technique to trace the signature of neutrino charge- and neutral-current interactions. The near detector, Fig. 2.5(top), is placed at a 1 km distance away from the target while the far detector, Fig. 2.5(bottom), is 734 km away from the near in the Soudan mine, 710 m underground. Both detectors have large fiducial volume masses (1kton the near and 5.4 kton the far detector) to induce neutrino interactions and there are functionally identical.

MINOS has published analyses both for the ν_μ and $\bar{\nu}_\mu$ runs. In all cases, the results were those anticipated from the oscillation patterns established by Super-Kamiokande and K2K. For instance, in the muon neutrino runs a clear reduction on the flux has been observed, combined with a distortion of the reconstructed energy spectrum, Fig. 2.6 [89]. The detected energy

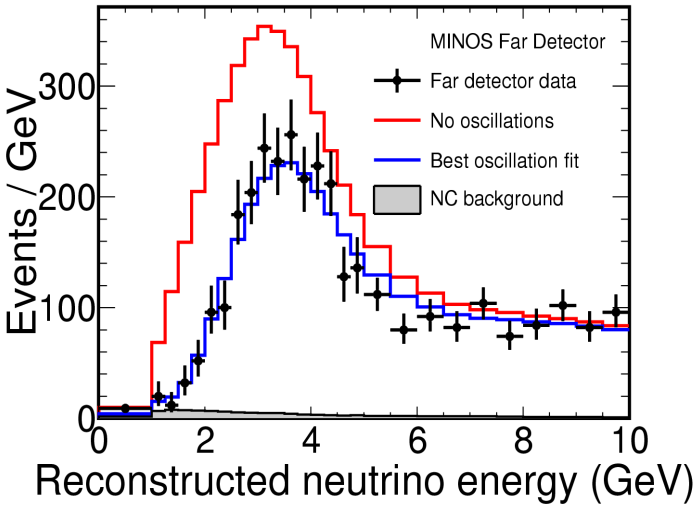

Figure 2.6: The reconstructed ν_μ energy at the MINOS far detector, data are shown in black points. In red the non-oscillation scenario curve is shown and in blue the best fit.

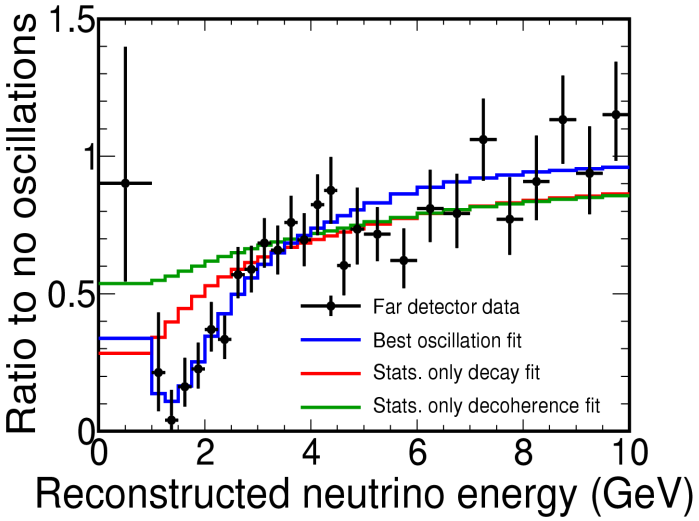

Figure 2.7: Ratio of the reconstructed ν_μ energy at the MINOS far detector with respect to the non-oscillation scenario expectation.

shape was fully consistent with the oscillation mechanism as it can be seen in Fig. 2.7 where the ratio of the energy spectrum to the non-oscillation prediction is shown. Neutrino oscillations were uncovered with a more than 6 σ significance while other possible explanations, like quantum decoherence and neutrino decay models were strongly disfavored. The final MINOS results, presented at the Neutrino 2012 conference, are [90]:

$$\sin^2(2\theta_{23}) = 0.96^{+0.04}_{-0.04} \text{ and } \Delta m^2_{23} = 2.39^{+0.09}_{-0.10}\ 10^{-3}\ eV^2 \tag{2.7}$$

for the atmospheric neutrino parameters and

$$\sin^2(2\bar{\theta}_{23}) = 0.97^{+0.03}_{-0.08} \text{ and } \Delta \bar{m}^2_{23} = 2.48^{+0.22}_{-0.27}\ 10^{-3}\ eV^2 \tag{2.8}$$

for the antineutrino parameters. It is important to emphasize the accuracy on the mass square splitting determination achieved by the MINOS collaboration.

Very recently, T2K experiment (Tokai to Kamioka) reported a measurement of the atmospheric parameters based also on the disappearance of ν_μ. T2K is the first implementation of the off-axis technique in a long-baseline neutrino oscillation experiment [91]. It exploits a neutrino beam, of roughly 0.6 GeV energy, produced at the J-PARK Accelerator Complex at Tokai and directed 200 km away at Super-Kamiokande. The L/E ratio is tuned to the first oscillation maximum. To monitor the neutrino flux T2K uses a sophisticated configuration of near on- and off-axis detectors. Details on the T2K experimental setup can be found elsewhere [92]. The first analysis of ν_μ disappearance gave the results [93] for the best fit values:

$$\sin^2(2\theta_{23}) = 0.98 \text{ and } \Delta m^2_{23} = 2.65\ 10^{-3}\ eV^2. \tag{2.9}$$

The picture of oscillations in the atmospheric region is finally completed with the OPERA experiment (Oscillation Project with Emulsion tRacking Apparatus) [94]. The OPERA detector consists of parallel walls of bricks made by lead and nuclear emulsions, interleaved with plastic scintillator counters. This high-granularity detector provides the necessary spatial resolution to search for the appearance of tau neutrinos created through the oscillation $\nu_\mu \to \nu_\tau$. OPERA started data taking in 2008; on the analysis of the first data sets two ν_τ events were detected in accordance with expectations [95].

2.2 Solar sector

To investigate independently the puzzle of missing solar neutrinos, that persisted up until the early 1990's, many experiments were put forward.

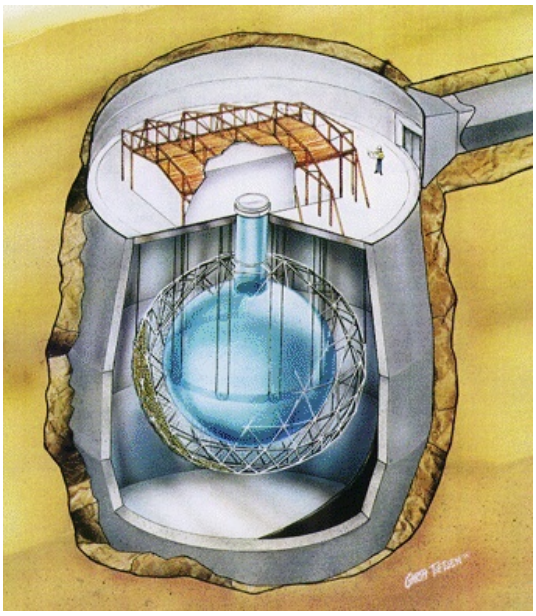

Figure 2.8: The Sudbury Neutrino Observatory.

The first important effort towards that direction was SNO (Sudbury Neutrino Observatory). SNO was located deep underground (6800 feet) in the INCO's Creighton mine, near Sudbury, Canada. It was a heavy water (D_2O) Čerenkov detector with a total target volume of 1000 tons. The target was totally contained in a spherical, acrylic vessel of 12 m diameter and was monitored by 9600 photomultipliers mounted on a support structure, offering a 4π coverage. A sketch of the SNO detector is shown in Fig. 2.8. More details on the detector's components and functioning can be found elsewhere [96].

A heavy water detector is an ideal instrument to test the Solar Neutrino Anomaly, as realized by H. H. Chen as early as 1984 [97]. In heavy water, three types of neutrino interactions can take place:

i. First, elastic scattering (ES) with electrons is possible, exactly in the same way that it happens in a light water detector.

$$\nu_x \; + \; e^- \; \rightarrow \; \nu_x \; + \; e^- \tag{2.10}$$

The e^- recoil is observed through the Čerenkov radiation rings. This is a reaction sensitive to all neutrino flavours, although ν_e dominate this channel; the cross-section for ν_μ and ν_τ is about six times smaller than that for ν_e

ii. Charge current (CC) neutrino interactions on deuterium are also induced.

$$\nu_e \ + \ D \ \rightarrow \ p \ + \ p \ + \ e^- \tag{2.11}$$

The outgoing electron is, again, detected from the emitted Čerenkov radiation.

iii. Finally, neutral current (NC) interactions can occur in the following manner:

$$\nu_x \ + \ D \ \rightarrow \ p \ + \ n \ + \ \nu_x \tag{2.12}$$

The reaction is detected through the subsequent neutron capture in an atomic nucleus. During its first phase SNO relied on the deuterium neutron absorptions to identify neutral currents. The reaction is sensitive to all neutrino flavours with the same cross-section and it is appropriate to trace a possible non-electron component in the solar neutrino flux.

SNO operated in three distinct phases from 1999 to 2006. In each phase a different technique to track the NC component was employed [98]. Even from the analysis of the first phase data alone, SNO was able to observe a clear non-electron component to the solar neutrino flux at 5.3 σ [99]. In particular, the folowing fluxes (ϕ) for the three detection channels were measured:

$$\phi_{CC}^{SNO} = 1.76^{+0.06}_{-0.05}(stat.)^{+0.09}_{-0.09}(syst.) \tag{2.13}$$

$$\phi_{ES}^{SNO} = 2.39^{+0.24}_{-0.23}(stat.)^{+0.12}_{-0.12}(syst.) \tag{2.14}$$

$$\phi_{NC}^{SNO} = 5.09^{+0.44}_{-0.43}(stat.)^{+0.46}_{-0.43}(syst.) \tag{2.15}$$

All results are expressed in 10^6 cm^{-2} s. The difference between the ES and CC measurements is evident. The standard solar model (SSM) prediction for the total neutrino flux is:

$$\phi^{SSM} = 5.05^{+1.01}_{-0.81}(stat.) \tag{2.16}$$

in accordance with the NC measurement. Furthermore, Super-Kamiokande measurements using the electron elastic scattering only, found [100]:

$$\phi = 2.32^{+0.03}_{-0.03}(stat.)^{+0.08}_{-0.07}(syst.) \tag{2.17}$$

The Super-Kamiokande and SNO ϕ_{NC} values are totally consistent. The combination of the two results provides additional evidence towards the oscillation scenario as shown in Ref. [99]. A combined analysis of the all data, from the three phases of SNO can found in Ref. [101].

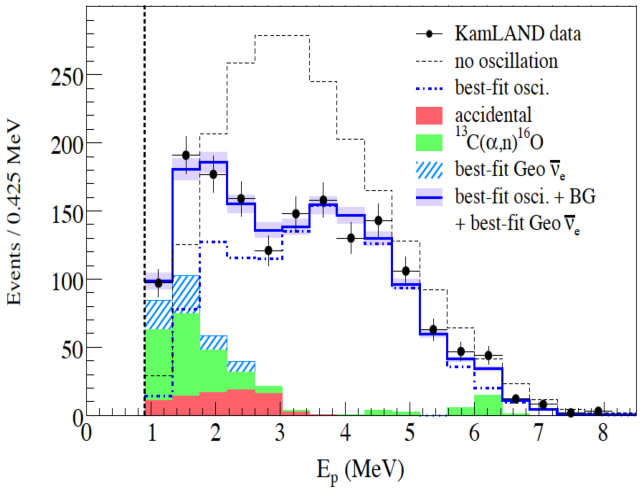

Figure 2.9: The electron anti-neutrino spectrum, measured in KamLAND is shown in black points. In the black, dashed curve the the expected spectrum in absence of oscillations is also shown.

To further investigate the Solar Neutrino Anomaly in a model independent way, without the additional complications arising from solar neutrino flux calculations, KamLAND experiment (Kamioka liquid Scintillator Anti-Neutrino detector) was designed [102]. KamLAND was located at the Kamioka Observatory, in the same place of the old Kamiokande experiment. It exploited the anti-neutrino flux emitted from all the Japanese nuclear reactors, to search for neutrino oscillations in the $\bar{\nu}_e$ disappearance channel. The KamLAND detector consisted of 1 kton of liquid scintillator contained in a light transparent acrylic vessel. Since the $\bar{\nu}_e$ detection principle is the essentially identical to the one used in Double Chooz we will not cover it here. More details on reactor anti-neutrinos and their detection will be given in the next chapter. Further information regarding the KamLAND experiment can be found in the reference above.

KamLAND started data taking, in stable conditions, in January 2002. From the analyses of its data [103, 104] a clear deficit of reactor anti-neutrinos was found, when compared with the null expectation, computed with reactor simulation packages. The deficit was accompanied with a spectral distortion consistent with oscillations, Fig 2.9. The ratio of the observed $\bar{\nu}_e$ L/E spectrum over the theoretical prediction, assuming no oscillations, revealed the

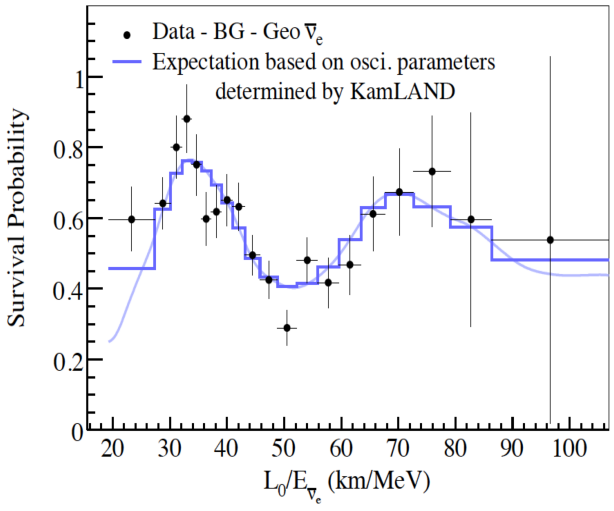

Figure 2.10: The electron anti-neutrino survival probability as measured by KamLAND.

modulation patterns characteristic of particle oscillations, Fig. 2.10. One should never fail to admire the beauty of this plot. An oscillation analysis output the values:

$$\Delta m^2_{12} = 7.58^{+0.14}_{-0.13}(stat.)^{+0.15}_{-0.15}(syst.)\ 10^{-5}\ eV^2 \tag{2.18}$$

and

$$\tan^2(2\theta_{12}) = 0.56^{+0.10}_{-0.07}(stat.)^{+0.10}_{-0.06}(syst.) \tag{2.19}$$

for the solar mass square splitting and mixing angle respectively. It should be noted that these values are consistent with the Large Mixing Angle (LMA) solution of the solar neutrino puzzle [105]. Global fits using all solar neutrino experiments and KamLAND results give [104]:

$$\Delta m^2_{12} = 7.59^{+0.21}_{-0.21}(stat.)\ 10^{-5}\ eV^2 \text{ and } \tan^2(2\theta_{12}) = 0.47^{+0.06}_{-0.05} \tag{2.20}$$

Finally, important measurements on the solar neutrino flux and energy spectrum have been performed by the BOREXINO collaboration. BOREXINO is an detector of 270 tons of ultra pure liquid scintillator located at the LNGS (Laboratori Nazionali del Gran Sasso) [106]. It takes advantage of the electron-neutrino elastic scattering to identify solar neutrinos, owing to

the large scintillator light yield. This low radioactivity environment allows the observation of the low energetic part of the solar neutrino spectrum in a real-time process. BOREXINO has started data taking in 2007 and since then has presented many interesting results, including measurements of the pp, ^{8}B, ^{7}Be and pep solar neutrino fluxes. All data are now consistent with the Standard Solar Model and the LMA scenario of solar neutrino oscillations. For a recent review of the BOREXINO status and achievements one might consult Ref. [107].

2.3 The hunt for θ_{13}

When this thesis begun[1], no decisive evidence in favour of a non-zero θ_{13} value existed. Many important endeavors have set severe limits on the third mixing angle, but yet a conclusive measurement was still missing. The most tight constrains were coming from the CHOOZ [109] and Palo Verde [110] experiments performed in the 1990's. In these efforts, the disappearance of reactor electron anti-neutrinos, $\bar{\nu}_e$, was probed at a baseline of roughly 1 km. Data from Super-Kamiokande and IMB were suggesting a neutrino mass-square difference of $\Delta m^2 \sim 10^{-3}\ eV^2$, and the low energetic reactor anti-neutrinos was an excellent source to test this possibility [111].

CHOOZ was mostly a european collaboration, centered around the French nuclear power-plant of Chooz (Ardennes, France)[2] [112]. On the other hand, Palo Verde was a U.S. effort installed at the homonymous nuclear station in Tonopah, Arizona [113]. Both projects leaned on the delayed-coincidence technique, to isolate neutrino interactions in large-mass target volumes of Gadolinium (Gd) doped liquid scintillator. CHOOZ was a large detector of 5 tons target mass contained in an acrylic vessel. This central volume was embedded in a region of liquid scintillator monitored by 192 eight-inches photomultipliers (PMTs) that offered a total 15 % photocathode coverage. A final scintillation region, instrumented with 24 PMTs, that surrounded the inner detector served as an active muon veto. A simple sketch of the CHOOZ detector is shown in Fig. 2.11 (top).

Palo Verde, on the other hand, was a segmented detector, Fig. 2.11 (bottom). It consisted of 66, 9 m long, acrylics cells containing Gd loaded liquid scintillator. Each cell was inspected by two 5-inches PMTs attached at its long edges. The central detector was surrounded by a 1 m thick water shield

[1] That was in October 2009.

[2] CHOOZ experiment took his name, just like the power-plant, from the nearby French village of Chooz. The now prevailing nomenclature is to write CHOOZ with capitals not because it is acronym but because people thought that it was [114].

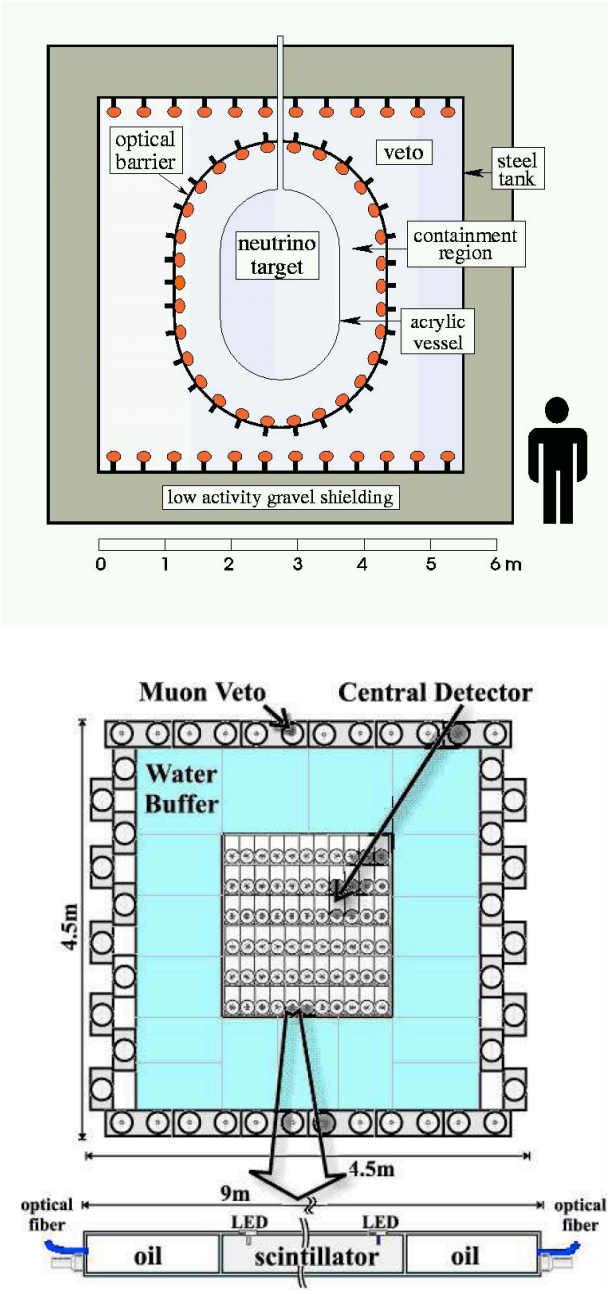

Figure 2.11: The CHOOZ (top) and Palo Verde (bottom) detectors.

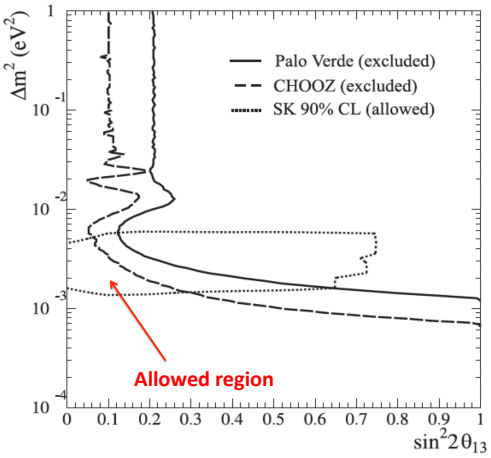

Figure 2.12: The allowed region of θ_{13} and m_{13} after the combined CHOOZ, Palo Verde and Super-Kamiokande observations.

to moderate fast neutrons, while additional scintillation counters, outside the water tank, identified cosmic muons. Both experiments exploited the inverse beta decay:

$$\bar{\nu}_e + p^+ \rightarrow e^+ + n \tag{2.21}$$

on free protons of the scintillator to tag reactor anti-neutrinos, although the selection decisions were unlike owing to the different detector designs. We will not elaborate any further on the detection procedure of reactor neutrinos since that will be the subject of Chapter 3. Besides the original publications, additional information on the CHOOZ and Palo Verde detectors can be found in Ref. [115].

Both CHOOZ and Palo Verde failed to observe an unambiguous deficit of reactor electron anti-neutrinos; their results [109, 110] were consistent with the absence of neutrino oscillations within experimental errors. Nonetheless, these findings were vital to the 1998 Super-Kamiokande discovery [84] of neutrino masses and oscillations, suggesting that $\nu_e \leftrightarrow \nu_\mu$ flavour transmutations cannot account for the anomalous observed $(\nu_\mu/\nu_e)_{data}/(\nu_\mu/\nu_e)_{MC}$ atmospheric ratio. This left out $\nu_e \rightarrow \nu_\tau$ oscillations as the only solution to the Atmospheric Neutrino Anomaly. The data of CHOOZ and Palo Verde when combined with Super-Kamionde further constrain the θ_{13} allowed region (Fig. 2.12) as showed in Ref. [110]. Lower bounds were also obtained from three flavour analyses to Solar and Atmospheric data. For an authoritative summary of the early era one could have a look at Ref. [116, 117].

That was the situation before 2010. The first important result beyond these observations came from the MINOS experiment [118]. MINOS collaboration, searching for the appearance of electron neutrinos in the Soudan mine far detector, was able to further constrain θ_{13} beyond the previous established limits. Nonetheless, the first storming indication in favour of a third mode of neutrino oscillations controlled by θ_{13} came from the T2K experiment in June 2011 [119]. Even though the catastrophic earthquake of 2011 in Japan, had suspended normal data taking, the analysis of the already existing runs revealed the presence of 6 ν_e events in the Super-Kamiokande detector.

In the absence of oscillations the expected number was 1.5 ± 0.3 ν_e, signaling a 2.5 σ excess over background. Interpreted in terms of $\nu_\mu \to \nu_e$ oscillations the data were consistent with:

$$0.03 < \sin^2(2\theta_{13}) < 0.28 \tag{2.22}$$

in the normal hierarchy (that is if $\Delta m^2_{23} > 0$, NH) and

$$0.04 < \sin^2(2\theta_{13}) < 0.34 \tag{2.23}$$

in the inverted hierarchy ($\Delta m^2_{23} < 0$, IH) scenarios at 90 % C.L. [119, 120]. The $\nu_\mu \to \nu_e$ oscillation formula can be found in [121], here we only remark that the appearance probability in this channel depends heavily on δ_{CP} and $\mathrm{sgn}(\Delta m^2_{23})$. The above results were obtained assuming $\delta_{CP} = 0$; for different δ_{CP} values the confidence intervals change in sigma-like patterns.

T2K results were presented in June 2011 at KEK (Ibaraki, Japan). Some weeks after, almost simultaneously, MINOS presented an improved analysis on the ν_e appearance [122, 123]. It was a thrilling moment for Neutrino Physics. MINOS best fit values were:

$$2\sin^2(\theta_{23})\sin^2(2\theta_{13}) = 0.041^{+0.047}_{-0.031} \tag{2.24}$$

for normal and

$$2\sin^2(\theta_{23})\sin^2(2\theta_{13}) = 0.079^{+0.071}_{-0.053} \tag{2.25}$$

for inverted hierarchy respectively; again $\delta_{CP} = 0$ was assumed. MINOS data disfavored $\theta_{13} = 0$ at 89 % C.L. Subsequently, global fits to the world data pointed towards a $\theta_{13} > 0$ scenario, albeit with a weak statistical significance. See for instance Ref. [124, 125].

The next thread in this tapestry came from the Double Chooz experiment. Double Chooz will be the issue of Chapter 3. It is a reactor experiment, like CHOOZ or Palo Verde, but with a different experimental layout and an improved detector design. It is located at the Chooz power-plant just

like CHOOZ. The analysis of the first 101 days of data taking supported oscillations at 94.6 % C.L. For this result Double Chooz operated with a single detector and the reactor $\bar{\nu}_e$ spectrum was inferred by computer simulations. A combined rate plus shape analysis output the best fit value:

$$\sin^2(2\theta_{13}) = 0.086 \pm 0.041(\text{stat.}) \pm 0.030(\text{syst.}). \tag{2.26}$$

It should be remarked that Double Chooz was the first, second generation reactor experiment that reported on θ_{13} [126]. More details on Double Chooz will be given in Chapter 3.

The first unambiguous measurement of θ_{13} came from the Daya Bay collaboration in March 2011 [127]. Daya Bay utilized a multi-detector setup of three experimental sites, located close to the Daya Bay and Ling Ao nuclear power-plants [128]. These are two of the most powerful nuclear stations in operation worldwide. The high $\bar{\nu}_e$ reactor flux permitted the determination of θ_{13} at 5.2 σ in only 55 days of running with all detectors simultaneously. The result, obtained with a rate-only analysis, was:

$$\sin^2(2\theta_{13}) = 0.092 \pm 0.016(\text{stat.}) \pm 0.005(\text{syst.}). \tag{2.27}$$

A month after, RENO collaboration popularized another independent measurement of θ_{13} [129]. For this result, RENO used two massive detectors installed at the Yonggwang Nuclear Power Plant in Korea. The observed $\bar{\nu}_e$ deficit was consistent with neutrino oscillations with a significance of 4.9 standard deviations. The best fit value:

$$\sin^2(2\theta_{13}) = 0.113 \pm 0.013(\text{stat.}) \pm 0.019(\text{syst.}). \tag{2.28}$$

confirmed early indications and Daya Bay. Both Daya Bay and RENO used a multi-detector setup to reduce the dominant reactor systematics in a way that we will explain later on. Double Chooz on the other hand operated with a single detector. The addition of the a second detector to the Double Chooz configuration is expected to elevate the θ_{13} extraction. The combination of all three reactor experiments will elevate also the determination of Δm^2_{13} as shown very recently [130]. The positron spectra measured by Double Chooz, Daya Bay and RENO are shown in Fig. 2.13. A first combination of the recent θ_{13} accelerator and reactor measurements can be found in Ref. [131].

2.4 Open questions and further perspectives

Having determined all three mixing angles ($\theta_{12},\ \theta_{23},\ \theta_{13}$) and the different neutrino mass square splittings ($\Delta m^2_{12},\ |\Delta m^2_{23}|$) the next step would be to

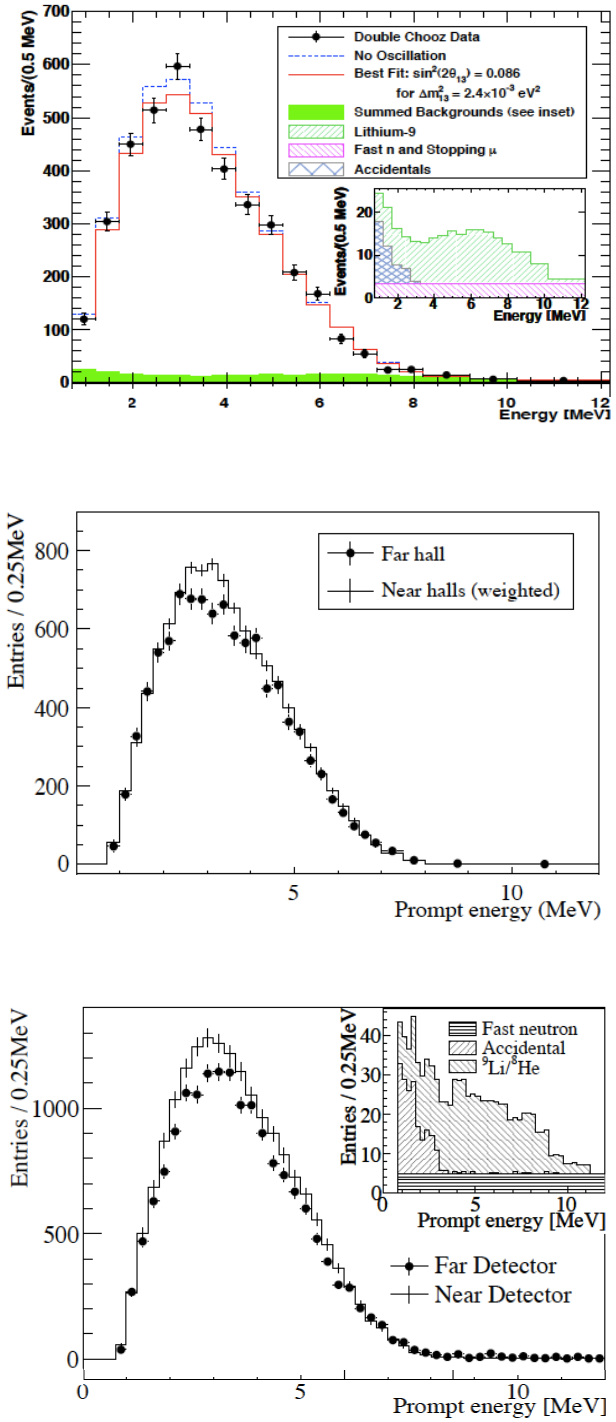

Figure 2.13: The positron spectra measured by Double Chooz (top), Daya Bay (middle) and RENO (bottom) reactor experiments. Daya Bay and RENO overlap the Far and Near detector weighted spectra. Double Chooz shows in red line the best fit curve.

perform even more accurate measurements and further scrutiny the prevailing oscillation paradigm. If not for no other reason, "precision measurements at one energy scale allows us to guess New Physics at the next scale" as it has been emphasized in many circumstances[3]. Of the open questions that tantalizing, Neutrino Physics those that can be explored with oscillation experiments include:

- Is $\sin^2(2\theta_{23})$ maximal ?
- What is the neutrino mass hierarchy ?
- What is the value of δ_{CP} ?

The value of $\sin^2(2\theta_{23})$ has been probed by many experiments with natural and artificial neutrino sources as explained in Sec. 2.1. All available data are now consistent with an almost maximal θ_{23} scheme, $\sin^2(2\theta_{23}) \simeq 1$. The natural question would be: is θ_{23} exactly 45 degrees ? In this connection, we should mention that the final results from the MINOS accelerator experiment [90] favour the non-maximal θ_{23} possibility. Certainly, additional information from currently running and future experiments will shed more light on this important issue.

Oscillation experiments are only sensitive to the absolute values of the mass square differences unless matter effects become significant. The oscillation formula (Eq. 1.36) in vacuum is invariant under the substitution:

$$\Delta m^2 \leftrightarrow -\Delta m^2. \tag{2.29}$$

Matter effects break this redundancy. The observation of matter induced oscillations in solar experiments helped us unveil the sign of Δm^2_{21} that would otherwise remained unknown. We now know that m_1 is the lightest of the two mass eigenstates, $\Delta m^2_{21} > 0$. Matter oscillations have not been observed yet in the atmospheric sector and the sign of Δm^2_{32} is still deluding us. The two possible scenarios are termed with the notorious names: normal ($\Delta m^2_{32} > 0$) and inverted ($\Delta m^2_{32} < 0$) hierarchy[4]. In Fig. 2.14 we show schematically the two possibilities.

Mass hierarchy could be designated in accelerator experiments like T2K or the future project Noνa [133, 134]. An interesting possibility to tackle $sgn(\Delta m^2_{32})$ with a large-scale reactor experiment was very recently proposed [135]. Note also that, in principle, this question could be answered by precise measurements of the mass square differences [136].

[3] A quote borrowed from John Iliopoulos [132]

[4] Note that the word hierarchy stems partly for the Greek word $\iota\epsilon\rho\acute{o}\varsigma$ that means sacred or saint. We still don't know how this adjective finally made it to the physics vocabulary.

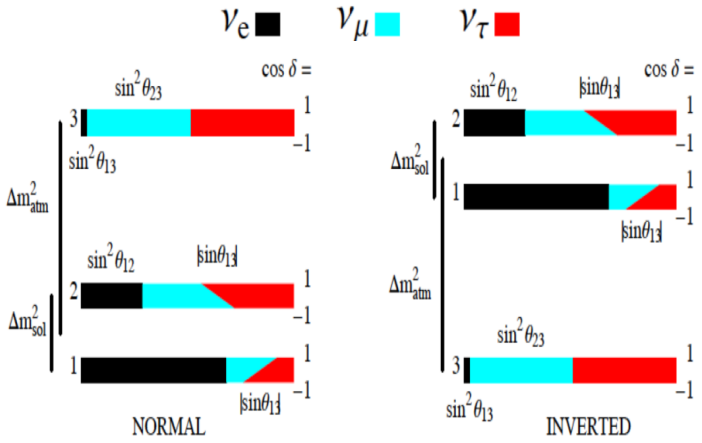

Figure 2.14: The normal (left) and inverted (right) hierarchy possibilities [137].

The exact value of the CP-violating phase δ_{CP} is important for Particle Physics and Cosmology. If $\delta_{CP} \neq 0$ then CP-violation in the leptonic sector could explain matter-antimatter asymmetry through the leptogenesis mechanism [138]. A simple way to address leptonic CP-violation would be to compare the oscillations probabilities:

$$p(\ \nu_\mu \rightarrow \nu_e\ ) \quad \text{and} \quad p(\ \bar{\nu}_\mu \rightarrow \bar{\nu}_e\ ) \tag{2.30}$$

in an accelerator experiment. In light of the relative high θ_{13} value, Noνa experiment could have a good chance to find out δ_{CP}. Other options to measure δ_{CP} include high intensity neutrino sources from super-beams, beta-beams and neutrino factories [139]. Finally, a novel approach to attack δ_{CP} through the interference between solar and atmospheric oscillations has been proposed [140].

Of those questions that cannot be answered by oscillation experiments the most important are:

- What is the absolute neutrino mass scale ?
- Are neutrinos their own anti-particles ?

Direct measurements of neutrino masses have, thus far, only set upper limits on this question. This situation could change soon with the next generation

tritium beta decay experiment KATRIN [141]. KATRIN is a precision spectrometer that could quantify m_{ν_e} if this lies in the sub-eV region. On the hand, the Majorana or Dirac nature of neutrinos can be most appropriately tested with the observation of neutrinoless double beta ($0\nu\beta\beta$) decay [142]. This is a process allowed for certain elements only for identical neutrinos and anti-neutrinos. Note that neutrinos are the only chargeless elementary fermions and a Majorana mass term is not prohibited by $\mathcal{U}(1)_{em}$ invariance. As a rule of thumb "every process that is not ruled out by a symmetry principle should be allowed"[5]. Nonetheless, this is always a matter of the experiment to decide.

Double beta decay has been investigated by countless experiments in the past. Reviews of those efforts could be found in Ref. [143, 144]. From these experiments lower limits on the $0\nu\beta\beta$ decay half-life of many elements have been published. Additionally, there is a highly controversial claim that the $0\nu\beta\beta$ decay signature has been observed with Germanium [145, 146]. Recently, important results on the $0\nu\beta\beta$ decay half-life of Xenon were published by EXO [147] and KamLAND-Zen [148]. For an excellent, modern treatment of present and future experiments in search of double beta decay one might turn to Ref. [149].

The last, acknowledged question that Neutrino Physics must address is related to the existence of sterile neutrinos.

- Are there any species of sterile neutrinos ?

Measurements at LEP have constrained the number of light neutrinos that couple the Z^0 boson to be exactly equal to three. This result leaves still open the possibility for heavy-mass active neutrinos or sterile ones.

Light sterile neutrinos have a long-standing history. The most significant evidence for sterile neutrino oscillations comes from the LSND experiment (Liquid Scintillator Neutrino Detector) in the 1990's [150, 151, 152]. LSND was a π^+ decay in flight and μ^+ decay at rest experiment that conducted oscillation searches, predominantly, in the $\bar{\nu}_e$ appearance channel:

$$\bar{\nu}_\mu \to \bar{\nu}_e \tag{2.31}$$

After five years of operation, LSND observed a 3.8 σ excess of $\bar{\nu}_e$-like events, Fig. 2.15, consistent with two-flavour neutrino oscillations at $\Delta^2 m \simeq 1$ eV^2 and $\sin^2 2\theta \simeq 0.005$. It is evident that a such high $\Delta^2 m$ value demands a fourth mass eigenstate.

KARMEN experiment, performed at ISIS, was not able to confirm or reject the LSND oscillation claims [153]. There were different regions in the

[5] A quote often related to E. P. Wigner.

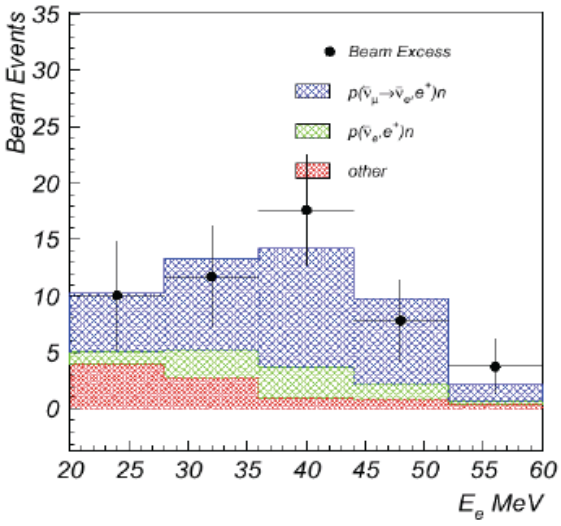

Figure 2.15: The LSND observed $\bar{\nu}_e$ excess.

$\sin^2 2\theta$ - $\Delta^2 m$ plane that the two data sets were consistent. To settle down this debate MiniBOONE experiment was designed [154]. MiniBOONE's objective was to test independently and unequivocally the LSND observation. The decided strategy was to keep the same L/E as LSND but change L and E separately. The neutrino detection technique and detector are also different to offer different backgrounds and systematics. As previously said, a totally independent test.

MiniBOONE has presented results in the appearance channel:

$$\nu_\mu \to \nu_e \tag{2.32}$$

that refute oscillations as the source of the LSND signal at 98 % C.L. [155]. In parallel, an unexplained 3.0 σ excess has been observed in the low energy region (E<475 MeV) [156]. Its shape is not consistent with two-flavour neutrino oscillations and its origins are still undetermined. On the other, an oscillation search on the conjugate channel:

$$\bar{\nu}_\mu \to \bar{\nu}_e \tag{2.33}$$

seems to favour oscillations [157]. Note that this mode offers a direct check of the LSND result. A comparison of the LSND and MiniBOONE reconstructed L/E distributions (Fig. 2.16) finds them in good agreement. Additionally, a low energy excess of $\bar{\nu}_e$ events has been identified.

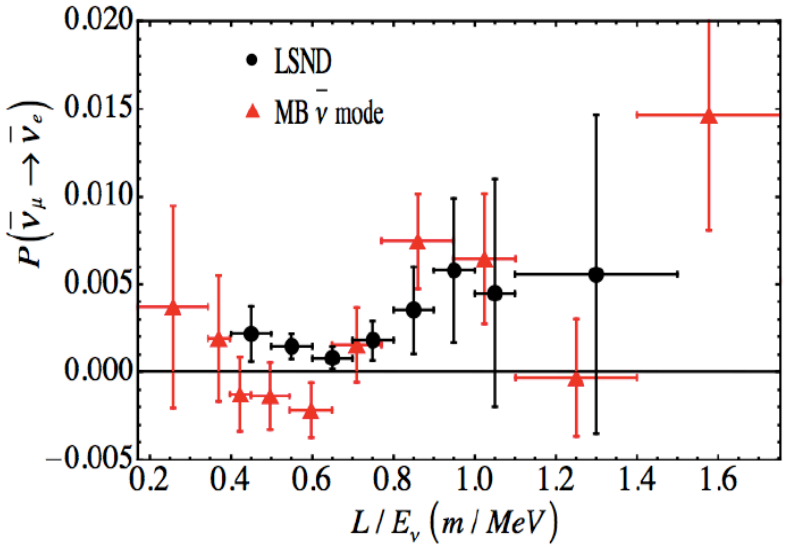

Figure 2.16: The LSND (black) and MiniBOONE anti-neutrino (red) L/E distributions.

To interpret simultaneously LSND and MiniBOONE findings, many hypotheses have been put forward [158, 159]. Perhaps the most radical is to introduce an additional, fifth sterile neutrino. Models with three active and two sterile neutrinos are preferable since they can accommodate naturally CP-violation. More details on sterile neutrinos and future projects can be found in Ref. [160]. In Chapter 3 we will elaborate again on sterile neutrinos in connection with the Reactor Antineutrino Anomaly.

Chapter 3

The Double Chooz experiment

3.1 Introduction

Double Chooz (DC) is a short-baseline reactor experiment designed to measure or further constrain, in the case of negative signal, the neutrino mixing angle θ_{13} [161, 162, 163]. It employs a scintillator-based detector technique, in the spirit of CHOOZ, incorporating in parallel, additional improvements critical to go below the previous θ_{13} limits. DC has started stable data taking since April 2011 and its first results were presented at the 2011 LowNu conference [164] almost simultaneously with the first publication from the DC collaboration [126]. There are in the world three more reactor experiments searching for neutrino oscillations in the same channel; these are RENO at Korea [165] and Daya Bay at China [166] that are currently running and the future second generation Brazilian project Angra [167].

DC was designed to observe the disappearance of electron antineutrinos, $\bar{\nu}_e$, emitted from the nuclear cores of the Chooz-B power plant located at Ardennes, France (Fig. 3.1). Chooz-B has two pressurized water reactors (PWR) of the quite recent N4 technology. Both of them operate at a thermal power of 4.27 GW, while each reactor is off roughly for one month every year. Chooz-B started running with only one reactor in May 1997 while the second reactor began operating in September of the same year.

DC exploits the already existing laboratory constructed by Électricité de France (EDF) and used in the 1990's for the first CHOOZ experiment. The already existence of an underground facility with an important rock overburden of 300 meters of water equivalent (m.w.e.) was an important reason for choosing this specific location minimizing thus the civil engineering expenses and construction time. The laboratory has a mean distance of 1.05 km from the reactor cores that makes it ideal for oscillations searches at

Figure 3.1: Location of Chooz village at the map of France and a panoramic picture of the Chooz power plant.

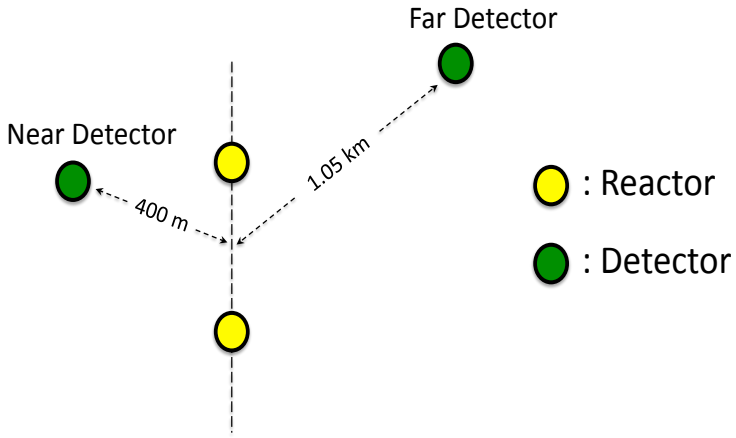

Figure 3.2: A pictorial representation of the Double Chooz two-detector concept.

square mass differences of the order of 10^{-3} eV^2. The importance of this baseline in reactor oscillation experiments was realized during the 90's in connection with the Atmospheric Neutrino Anomaly.

In contrast to CHOOZ, DC shall use two detectors to look for the signature of θ_{13} driven oscillations. The first detector is located in the existing old laboratory and it is referred as the far detector, while the second detector will be installed in a new laboratory closer to the Chooz-B cores at a mean distance of 400 m and a 120 m.w.e. shielding from cosmic rays. This second detector (called the near detector) will monitor the neutrino flux and spectrum coming from the reactors while the far one is going to search for deviations from what it is expected. A simple sketch of the DC two-detector configuration is shown in Fig. 3.2.

The major advantage of this choice is the reduction of the systematic errors associated with the production and the detection of reactor neutrinos; the main source of systematics to experiments like CHOOZ and Palo Verde. For this to happen it is imperative for the two detectors to be as much identical as possible. To this end careful calibration and monitoring systems for both detectors are imperative.

Additionally, a huge improvement in the reduction of the statistical errors is expected from the increase of the target mass and the elongation of the data taking period. Remember that the CHOOZ experiment run only for a few months with various periods recording data with only one reactor operating. In contrast, DC is expected to take data constantly for three years with two detectors. For the first DC results only the far detector was operating. The civil construction of the Chooz far detector laboratory began in 2009. First excavations for the near detector laboratory started in April 2011 and the near detector is scheduled to start data taking in late 2013.

3.2 Antineutrino detection

Reactor electron antineutrinos can be detected through many interaction modes including both the charge (CC) and neutral current (NC) terms of the electroweak lagrangian. Nowadays, all experimental efforts exploit the inverse beta decay (IBD) reaction on free protons for low energy reactor $\bar{\nu}_e$ oscillation searches.

$$\bar{\nu}_e + p^+ \rightarrow e^+ + n \tag{3.1}$$

This mode has the major advantage that large Liquid Scintillator (LS) detectors can be built using the free scintillator's protons for IBD interactions to happen. In this way, the neutrino target and the detection material are one and the same. Note that the same recipe was also used in the legendary Reines and Cowan experiment that detected the free neutrino for the first time. More recently the KamLAND experiment exploits the same signature to detect $\bar{\nu}_e$ coming from the Japanese nuclear reactors probing the solar oscillation sector. In contrast, the Borexino experiment uses the elastic scattering on free electrons (NC mode) to detect low energy solar neutrinos.

IBD reactions have an energy threshold at 1.8 MeV. This endothermic character could be easily understood from the proton-neutron conversion. The value of 1.8 MeV accounts for the difference in the nucleon masses as well as the positron mass. The $\bar{\nu}_e$ - e^+ energies and momenta are of course strongly correlated. In the static approximation the $\bar{\nu}_e$ and e^+ energies, $E_{\bar{\nu}_e}$

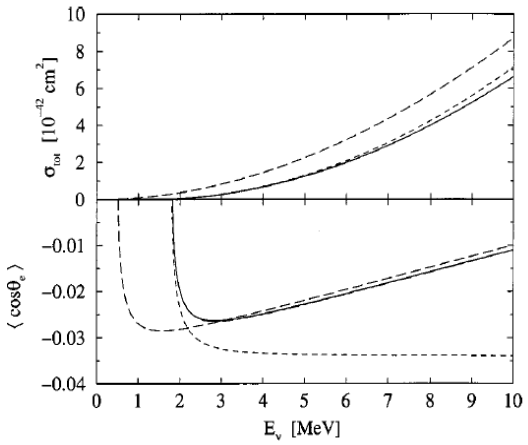

Figure 3.3: IBD cross-section as a function of $E_{\bar{\nu}_e}$. Also the $p_{\bar{\nu}_e}$ - p_{e^+} mean angle versus $E_{\bar{\nu}_e}$ is shown. Both figures adapted from [168].

and E_{e^+}, are related through the formula:

$$E_{\bar{\nu}_e} = E_{e^+} + (m_n - m_p) + \mathcal{O}(2) \tag{3.2}$$

where m_n and m_p refer to the neutron and proton masses respectively and the the dots denote second order corrections arising from the proton recoil treatment. The full formula can be found at [163] Sec. 2.1.

The cross section for the IBD reaction (3.1) can be derived through the CC weak interaction lagrangian. The result parametrized through the positron energy E_{e^+} is:

$$\sigma(E_{e^+}) = \frac{2\pi^2\hbar^3}{m_e^5 f \tau_n} p_{e^+} E_{e^+} (1 + \delta_{rad} + \delta_{w.m.}) \tag{3.3}$$

where:

- E_{e^+} and p_{e^+} are the positron energy and momentum,
- m_e the electron/positron mass,
- τ_n is the neutron lifetime,
- f is the free neutron decay phase factor,
- and δ_{rad}, $\delta_{w.m.}$ second order contributions originating from radiation corrections and the weak magnetism term.

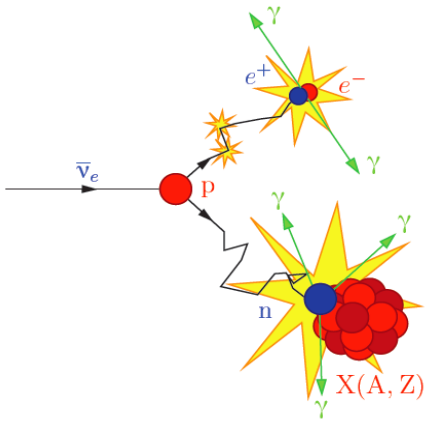

Figure 3.4: Inverse beta decay detection principle in Double Chooz [169].

A representative plot of the integrated IBD cross-section as a function of $E_{\bar{\nu}_e}$ is given in Fig. 3.3. A more rigorous discussion on the theory and the derivation of (3.3) including the numerical values of many factors that we omitted to mention could be found in the paper of Beacom and Vogel [168]. It is also important to add that the IBD has the highest cross-section in the energy range of reactor electron antineutrinos.

The detection of IBD signals in LS detectors like DC usually follows a two step procedure. First the outgoing positron thermalizes inside the liquid and annihilates with an electron producing, most of the times, two 511 keV gammas pointing on opposite directions. This gives a prompt signal with maximum energies around 10 MeV. Subsequently the IBD-created neutron thermalizes but without triggering the detector and it is absorbed in the detector releasing a second delayed signal. Neutron absorptions can happen on hydrogen (H) giving characteristic 2.2 MeV delayed pulses. In the specific case of DC, the LS has been doped with a gadolinium (Gd) compound to enhance the neutron absorption. Neutron absorptions on Gd produce a number of gammas with a mean energy of 8 MeV. The whole IBD decay mode and its prompt-delayed detection recipe is depicted in Fig. 3.4.

The expected energy distribution of the delayed signals originating from neutron captures on Gd are shown in Fig. 3.5. The 8 MeV peak corresponding to Gd neutron absorptions is more than evident. The plot was prepared with the data and the neutrino selection cuts decided for the first DC publication. Looking at the energy spectrum of singles coming from the DC detector one could identify the peaks corresponding to natural radioactivity originating from elements like K and Th, Fig. 3.36. One can also see the 8 MeV that

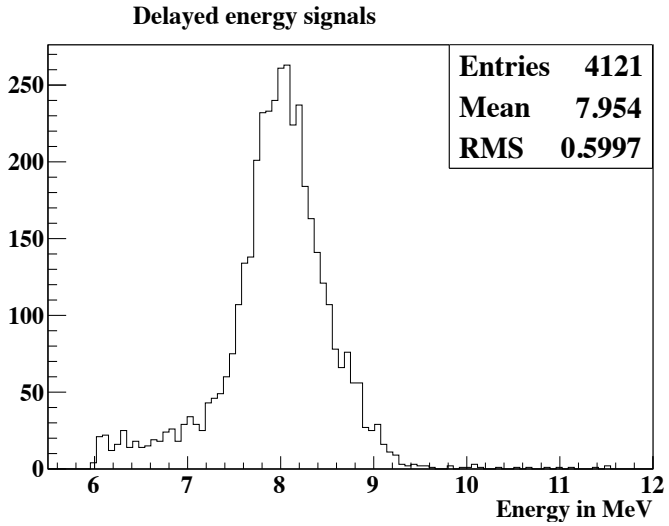

Figure 3.5: Delayed signal energy spectrum for the neutrino candidates of the DC first publication sample.

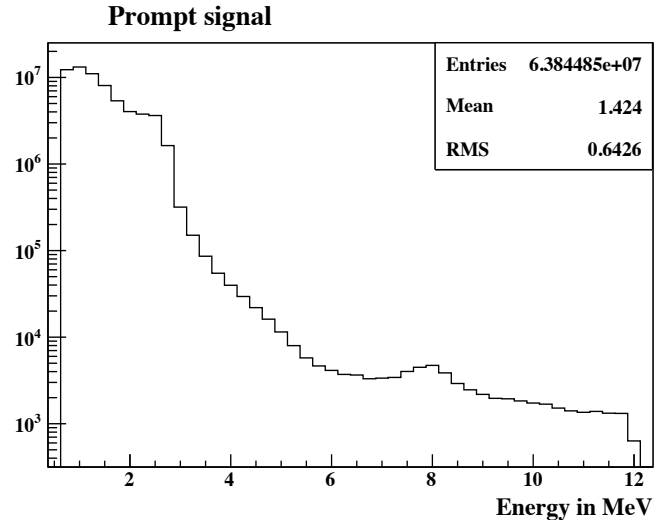

Figure 3.6: Singles spectrum in the prompt signal energy window from the data sample of the first publication.

corresponds to neutron captures on Gd. The background population below 3 MeV is obvious higher than that existing beyond 6 MeV and close to the Gd peak. The decision to dope the detector with Gd was deliberately taken for this purpose: to reduce the accidental background originating from low energy radioactivity and rock gammas that could otherwise pollute the

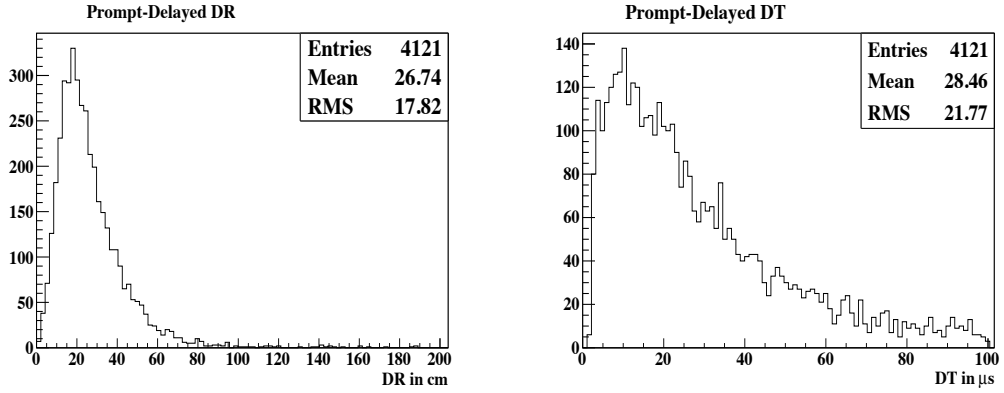

Figure 3.7: Prompt and delayed space (left) and time (right) correlation distributions.

selected neutrino sample. Nonetheless, it should be noted, that additional efforts to detect neutrinos through the H absorption peak are also being pursued within the DC collaboration [170].

The absorption mean life-time of neutrons on Gd is around 30 μs. The prompt and delayed signals are also strongly correlated in space. This clean prompt-delayed signature makes easy to detect neutrinos reducing significantly the expected accidental background that unavoidably contamine the signal. The time and space correlation distributions for the first publication selected neutrino candidates are shown in Fig. 3.7. For this analysis, no fiducial volume cut was used owing to the low rate of accidental background.

3.3 Reactor antineutrino flux and spectrum

A typical commercial reactor emits 2 10^{20} $\bar{\nu}_e$ core^{-1} sec^{-1} for 1 GW of thermal power in a totally isotropic manner. These are produced from the β–decays of neutrons and fission fragments inside the reactor cores. This intense antineutrino flux permitted the experimental discovery of neutrino in the 1950's and latter on allowed precise tests of the V - A nature of weak interactions. The first experiments looking for neutrino oscillation modes with reactor antineutrinos began in the decade of 1970.

Before the 1980's the knowledge of the antineutrino flux and spectrum coming from nuclear reactors was only poor understood. That was a limiting factor to the sensitivity available to oscillation searches. It was only after the pioneering experiments at the Institute of Laue-Langevin (ILL) at Grenoble that a more precise understanding of the reactor neutrino yield could be achieved [171, 172, 173].

To predict the neutrino output from a nuclear reactor the information necessary could be categorized in the following manner:

- the fissile isotope contribution,
- the number of fissions and,
- the neutrino yield.

A brief elaboration on these items is given subsequently. A detailed treatment of the reactor flux theory can be found in more specialized references; see for instance [115, 174, 175].

Fissile isotope contribution.
The main fissile isotopes that contribute to the reactor neutrino output are ^{235}U, ^{239}Pu, ^{241}Pu and ^{238}U. Other isotopes contribute also to the neutrino flux but this component is only sub-leading. In DC, for the calculation of the contribution for each isotope separately two reactor simulation packages were used: the Monte-Carlo analytical package MURE [176, 177] and the deterministic DRAGON computer simulation code [178].

For the numerical simulations a lot of input was given by EDF. This included the geometry of the cores, the initial fuel composition, the boron concentration and the running conditions of the power plant among others. The results of the two simulations were found to be in a very good agreement. Furthermore both results agreed with calculations made by EDF and past benchmark measurements [179]. The systematic errors were assigned from the differences between the two simulations and the uncertainties on these parameters are quite small. A more detailed exposition to the reactor simulation tools and techniques used in DC can be found elsewhere [180].

Number of fissions.
To determine the number of fissions inside the core one must first know the fissile isotope contribution. Having this done, as we explained above, we can then write down the number of fissions $\sec^{-1}$ with the knowledge of the thermal power output of the power plant, W_{th}. This quantity is very significant for the operation of the nuclear station and many ways to measure it have been developed by the reactor authorities. The most accurate method is through the total thermal power measured as the heat balance of the steam generator. The uncertainty on W_{th} is indeed negligible. In Fig. 3.8 we show the evolution of the reactors thermal power versus time for the period relevant for the first phase of DC. The periods where one detector is down are clearly visible.

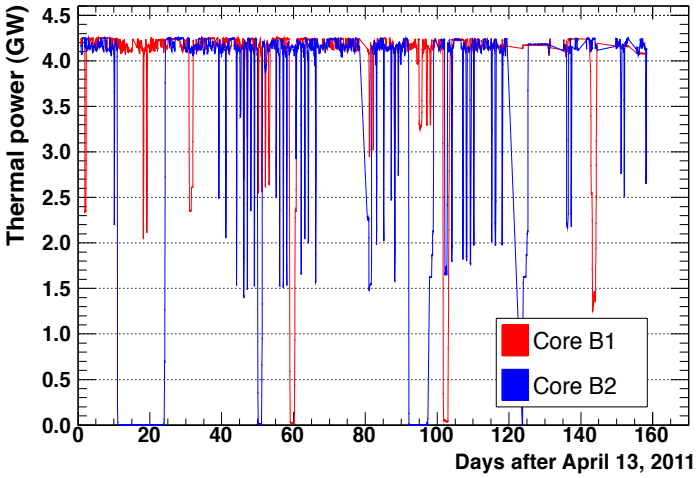

Figure 3.8: The power plant's thermal output W_{th} versus time separately for each reactor core.

In the strict mathematical language, the number of fissions per sec is given by the ratio:

$$(\text{ no. of fissions sec}^{-1}) = \frac{W_{th}}{< E_f >} \tag{3.4}$$

W_{th} is the thermal power and $< E_f >$ is the mean energy realased per fission. $< E_f >$ accounts for the contributions of the four main fissile isotopes:

$$< E_f >= \sum_k f_k E_k, \tag{3.5}$$

where f_k are the fissile isotope contribution previously mentioned and E_k the energies released by the fissions of each isotope separately. The energies per fission are those computed by Kopeikin [181]. Nuclear data evaluated from the JEFF3.1 database [182] were used. The results concerning the fission rates in the days relevant for the data sample of the first DC publication are shown in Fig. 3.9.

Neutrino yield.

To complete the calculation one needs to know also the number of $\bar{\nu}_e$ per fission emitted by each isotope and the neutrino energy distribution. This is the factor that drives the main uncertainty of the calculation. In the past, as already mentioned, experiments at ILL irradiating with thermal neutrons pure fissile isotopes did precise measurements on the resulting electron β–decay spectra. Then the antineutrino output can be calculated through the

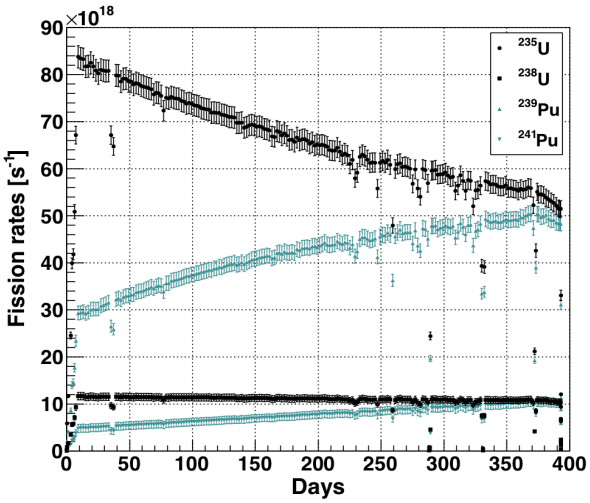

Figure 3.9: Fission rates as calculated for the first DC publication.

so-called inversion method to the reference ILL electron measurements. Note that this works only for decaying elements with small life-times ($\sim$ 1 day). Contributions for β–decay branches with lifetimes longer than 1 day need to be separately calculated.

For the calculation of the neutrino spectrum, a new improved conversion method to the old ILL reference spectrum was developed from DC collaborators of Saclay/Irfu (Paris) and Subatech (Nantes). Without entering the technicalities of the subject that could be found in their full glory in [183], we mention that the new spectrum results in a 3% net increase of the new predicted flux as compared to the old predictions. A full account of the improved method, together with a clear exposition of the various contributions modeled in the conversion technique, could be found in the aforementioned reference. It is remarkable that the results of this calculations were confirmed by the independent work of P. Huber [184].

An interesting by-product of the new improved reactor spectra is the so-called "Reactor Antineutrino Anomaly" [185]: the fact that all reactor experiments with baselines smaller than 100 m recorded signals slightly smaller from the new prediction. Even though other explanations could be invented the most interesting would be to attribute this almost 3.0 σ deficit to the presence of a new oscillation mode due to a forth sterile neutrino. It is hard to overestimate the revival that this work brought to oscillation searches with reactor antineutrinos and to the field of sterile neutrinos in general.

Important the subject might be, we decided not to cover it here since it is not essential for the remaining part of this thesis. For more information

besides the initial publication [185] one could also consult the following references [186, 159, 187]. For a discussion on the possible experiments to test similar sterile oscillation modes one could have a look at [188, 189, 190].

3.4 Reactor uncertainties

A convenient way to discuss the observed antineutrino signal in reactor experiments like DC is through the concept of the cross-section per fission σ_f. This quantity has the advantage of encrypting the main uncertainty relevant to single detector experiments like CHOOZ or Palo Verde. It also gives us a beautiful way to explain the multi-detector idea towards reactor neutrino oscillations first discussed by L. A. Mikaelyan and V. V. Sinev [191]. Since for the first phase of DC only one detector was operating, σ_f is an important factor not only for the θ_{13} extraction but also for the oscillation analysis interpretation.

σ_f is interaction the probability per hydrogen atom for IBD to happen assuming that one fission happened in the reactor cores. Without including the fine details (which otherwise could be found at [109]) the number of neutrino events detected by a single detector at a distance L from the reactor is formulated with the aid of σ_f like this:

$$n = \frac{1}{4\pi L^2} \frac{W_{th}}{< E_f >} N_p \, \sigma_f \, \epsilon. \tag{3.6}$$

N_p is the the number of protons available for IBD and ϵ the antineutrino detection efficiency. The ratio $W_{th}/< E_f >$ gives us the number of fissions and $1/4\pi L^2$ accounts for the reduction in the flux as a result of the distance between reactor and detector.

The importance of (3.6), as modeled through σ_f, is that all the significant factors needed for the calculation of the expected antineutrino rate are transparent and that the main source of errors is deliberately enclosed in σ_f. All the other quantities can be found with an accuracy better than 1 % while according to theory [109]:

$$\sigma_f^{(pred)} = 5.824 \; 10^{-19} \text{ b/fission} \pm 2.7 \; \% \tag{3.7}$$

Note also that the most accurate measurement of σ_f comes from the Bugey-4

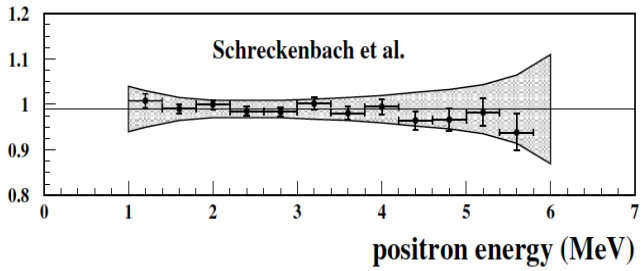

Figure 3.10: Data/MC ratios for the reactor $\bar{\nu}_e$ spectra. Data points taken from the Bougey-3 experiment [109].

experiment [192]:

$$\sigma_f^{(obs)} = 5.752\ 10^{-19}\ \text{b/fission} \pm 1.4\ \%. \tag{3.8}$$

The close agreement between theory and experiment is overwhelming while the final error achieved by Bugey-4 is almost two times better than the corresponding error from direct calculations.

The theory and experimental predictions on the antineutrino spectrum are also consistent, as shown in fig. 3.10, where the ratios between the values of the normalized $\bar{\nu}_e$ spectra for theory and experiment are plotted. The theoretical values are taken from K. Schreckenbach et *al.* [171, 172, 173]. For other reactor models the consistency is not that perfect.

The calculation of the antineutrino spectrum totally built from theory and simulations was done for the first phase of DC. The results concerning the total errors on the different parameters are shown in fig. 3.11. We see that only the reactor induced uncertainties produce an error of 2.7 %. The main uncertainty is driven by σ_f. In the past, since the value of θ_{13} is quite small, this insufficient knowledge was limiting the search for the disappearance of reactor $\bar{\nu}_e$.

To further minimize the reactor uncertainties two paths could be followed. The first, originally taken by CHOOZ, is to use the Bougey-4 σ_f value to attack the reactor systematics. As it has been seen, the measurement of σ_f as claimed from the Bougey-4 experiment was better than the predicted by Schreckenbach et al. by a factor of two. Anchoring σ_f to the Bougey-4 nominal point and correcting for the differences in the reactor burn-up the reactor systematics can be further ameliorated. This technique has been verified in the past with the same detector in two different sites [193, 194] and it was also employed in the CHOOZ experiment [109]. With this recipe the reactor uncertainties for DC can be as low as 1.7 %. The whole error diagram is shown in fig. 3.12.

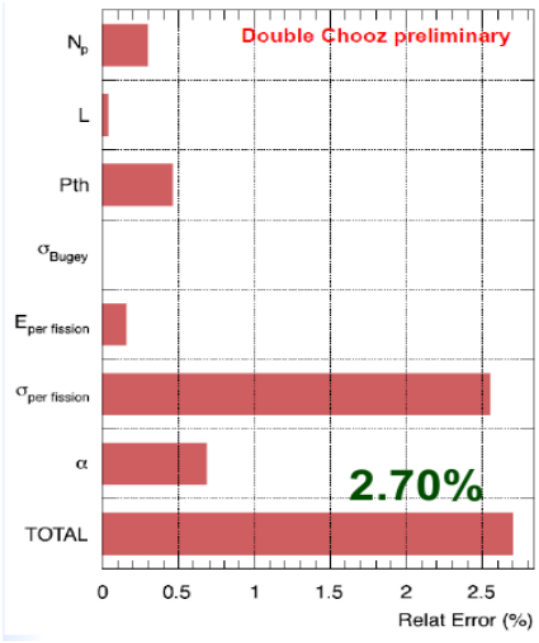

Figure 3.11: Reactor systematics from the ab initio reactor flux prediction.

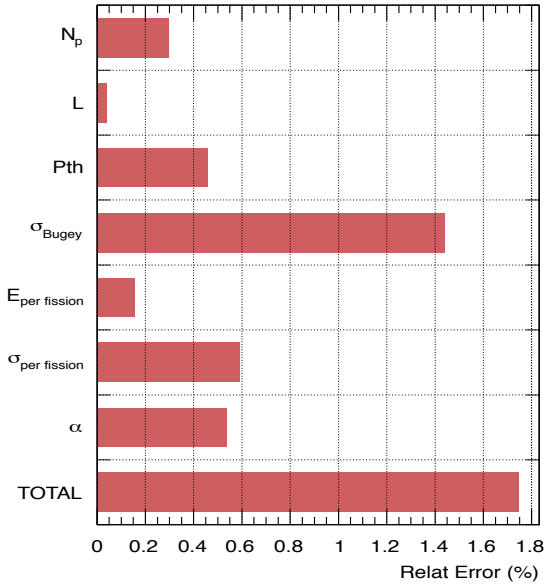

Figure 3.12: Reactor systematics with the Bougey-4 anchorage technique.

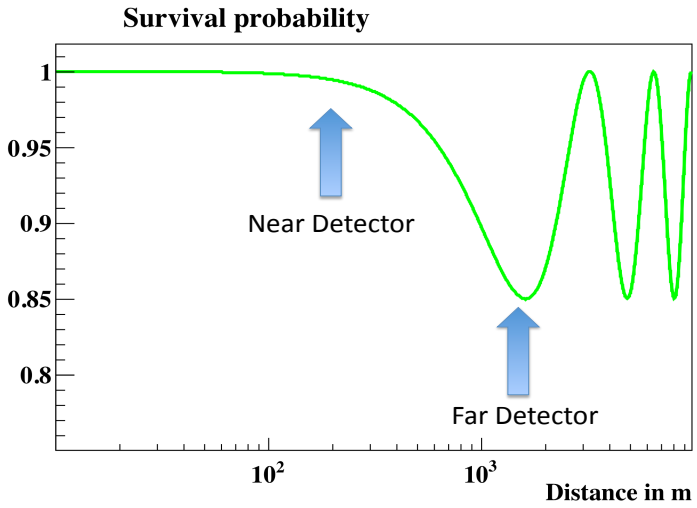

Figure 3.13: $\bar{\nu}_e$ survival probability as a function of L in a two flavor oscillation formalism.

The second way to remove the dominant systematics arising from the reactor predictions would be to compare the reactor flux at two different distances. One way for this to happen would be to use simultaneously two or more detectors. For example, in a two flavour oscillation scenario the disappearance of electron antineutrinos is given by:

$$p(\ \nu_e \rightarrow \nu_e;\ L\ ) \simeq 1 - \sin^2(2\theta_{13}) \sin^2\left(1.27\Delta m^2_{atm}\frac{L}{E}\right) \tag{3.9}$$

where the approximation $\Delta m^2_{atm} \approx \Delta m^2_{13}$ has been used. For $< E_\nu >= 3.0$ MeV, $\Delta m^2_{atm} = 2.30\ 10^{-3}$ eV^2 and $\sin^2(2\theta_{13}) = 0.16$ the survival probability $p(\ \nu_e \rightarrow \nu_e;\ L\ )$ is plotted as a function of distance in fig 3.13. Using for example two detectors, as shown in fig 3.13, the possibility of neutrino oscillations can be investigated in a reactor-model independent way. In the language of (3.6) the ratio of $\bar{\nu}_e$ recorded from the far and near detectors is given by:

$$\frac{n_f}{n_n} = \left(\frac{L_n}{L_f}\right)^2 \left(\frac{N_{p,f}}{N_{p,n}}\right) \left(\frac{\epsilon_f}{\epsilon_n}\right) \left[\frac{p(E, L_f, \theta_{13})}{p(E, L_n, \theta_{13})}\right] \tag{3.10}$$

where $p(E, L, \theta_{13})$ is the survival probability (3.9). With the indices f, n we denote the quantities of equation (3.6) for the far and the near detectors respectively. We clearly see in (3.10) that the factor with the main error, σ_f, is now cancelled. Note also that similar decisions have been taken by

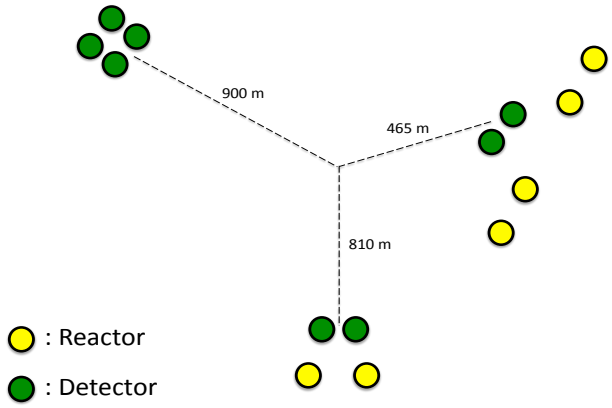

Figure 3.14: Sketch of the Daya Bay experiment layout.

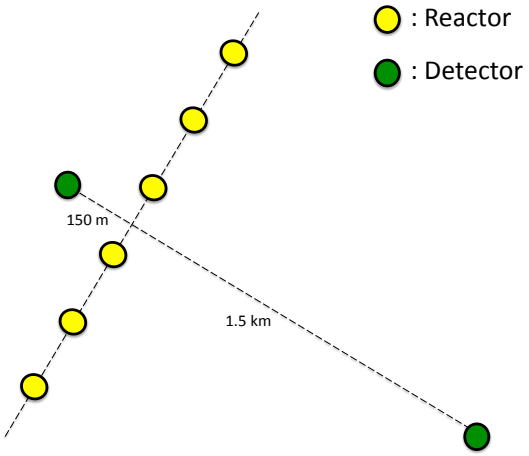

Figure 3.15: The RENO experiment layout.

accelerator neutrino experiments in order to asses the systematics from the neutrino production. MINOS and T2K for instance, use two detectors to detect ν_μ. The near ones were built with the purpose to monitor the profile of the neutrino flux.

Bougey-3 back in the 1980's used more than one detectors to tackle the uncertainties of the $\bar{\nu}_e$ source. In the 2000's the capabilities of a multi-detector reactor experiment to further scan the θ_{13} allowed region were first discussed by L. A. Mikaelyan and V. V. Sinev in [191]. Further details

are described in the so-called "Reactor White paper" [195]. This scenario was subsequently adapted by many international collaborations of neutrino physicists. Today, three experiments of this type are running in the world: Daya Bay, Double Chooz and RENO. The detector configuration scheme of Double Chooz was given in Sec. 2. The corresponding reactor-detector arrangements for Daya Bay and RENO can be found in Fig. 3.14 and 3.15. For a discussion on a unified analysis of these three efforts one might consult [196].

For the first phase of DC only the far detector was running. The calculation of the antineutrino flux was done with the help of the Bougey-4 anchorage method. This decision had the advantage to reduce the reactor systematics to 1.7 %. It also removes any complications that could arise from sterile oscillation modes like those relevant for the Reactor Antineutrino Anomaly. In the second phase of DC the near detector will be available and the reactor systematics will be further reduced in the way already described.

3.5 The Double Chooz Detector(s)

In this section we will review the main ingredients of the Double Chooz detector(s). More precisely, we will present the four-layer design concept, the Data Acquisition (DAQ) and the electronic systems of both detectors. Additionally, the main calibration systems will also be discussed. We would like to emphasize that, by the time that this thesis was written, only the far detector was operating. So, strictly speaking, we will present the Double Chooz far detector. Nonetheless, since both detectors are expected to be identical within the neutrino detection volumes, the same arguments will hold for the near detector also. Small differences between the near and far detectors are expected in the volumes necessary for background tagging or reduction (e.g. the Inner Veto or the the gamma-ray shielding).

3.5.1 Detector design

To capture the reactor anti-neutrinos, DC uses a detector that consists mainly of four concentric cylindrical volumes placed one inside the other in a way that resembles closely a four-layer russian doll. A sketch of it together with arrows pointing on its main components can be found at Fig. 3.16. The innermost cylinder is called the neutrino target (NT) and it is where the detected neutrino IBD interactions are most likely to happen. It is a 10.3 m^3 acrylic vessel filled with liquid scintillator doped with 1 gr/l of gadolinium compound (Gd). The Gd added compound is important to the detection

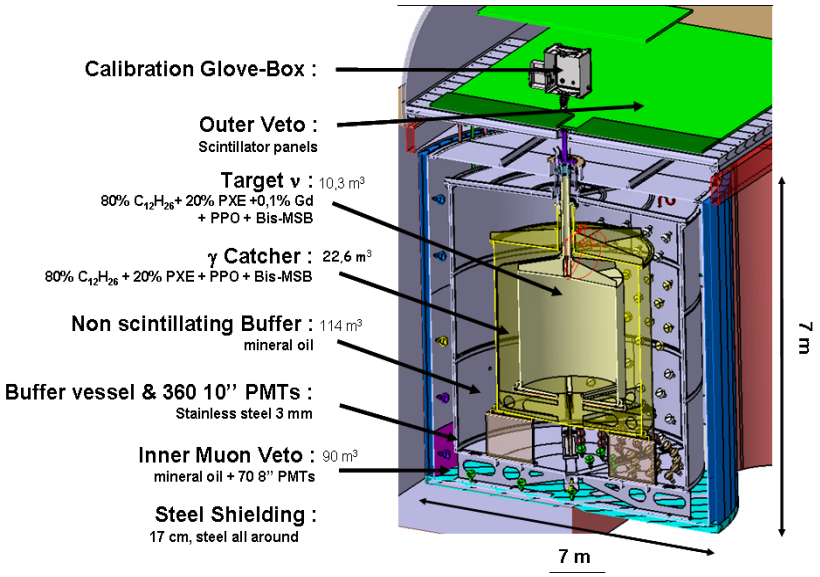

Figure 3.16: A picture of the Double Chooz detector; with arrows the main detector components are shown.

technique as we have already explained. The vessel acrylic material is transparent to light in the wavelengths relative for DC and its thickness, 8 mm, was specifically chosen to withstand the expected mechanical stretches.

Surrounding the NT there is the gamma catcher (GC); a 22.3 m^3 cylindrical region of liquid scintillator without the extra Gd doping. The thickness of GC vessel is 12 mm. Its presence is important since it was specifically designed to detect those gamma rays created at the borders of the NT that could otherwise escape detection. The dimensions of the GC were decided in order to maximize the gamma detection efficiency and extensive tests have been performed to match the scintillator light yields (LY) of the GC and the NT. Antineutrino interactions can occur at the GC as well, although their signature is expected to lack the delayed 8.0 MeV signal characteristic of the neutron absorption on Gd

Both scintillation volumes are embedded inside a 110 m^3 non-scintillating region filled with common mineral oil and called the Buffer. The vessel of the Buffer is made of stainless steel and it is 3 mm thick. Attached on the walls of the Buffer are 390 10-inches photomultiplier tubes (PMTs) that view the sensitive region in a 4π configuration giving a 14% photocathode coverage to the detector (fig. 3.17). The tube model that met the requirements set by the collaboration (good performance, low radioactivity glass, suitable weight and dimensions, etc.) was the 10-inches Hamamatsu R7081 phototube [197]. The purpose of the Buffer is to isolated the material of the PMTs from the

Figure 3.17: A view of the Buffer vessel with the PMTs attached.

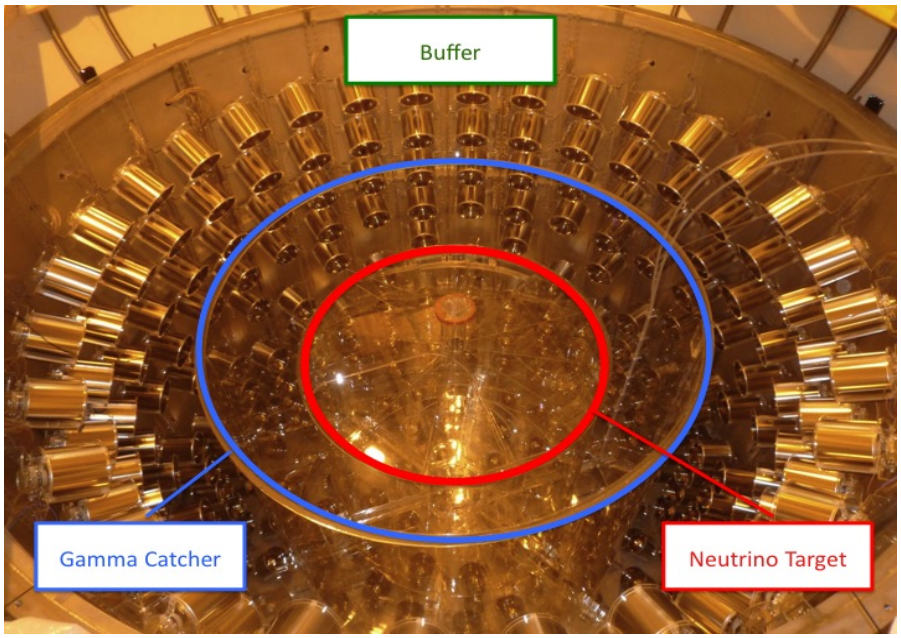

Figure 3.18: The Double Chooz Inner Detector; we denote with labels the separate regions.

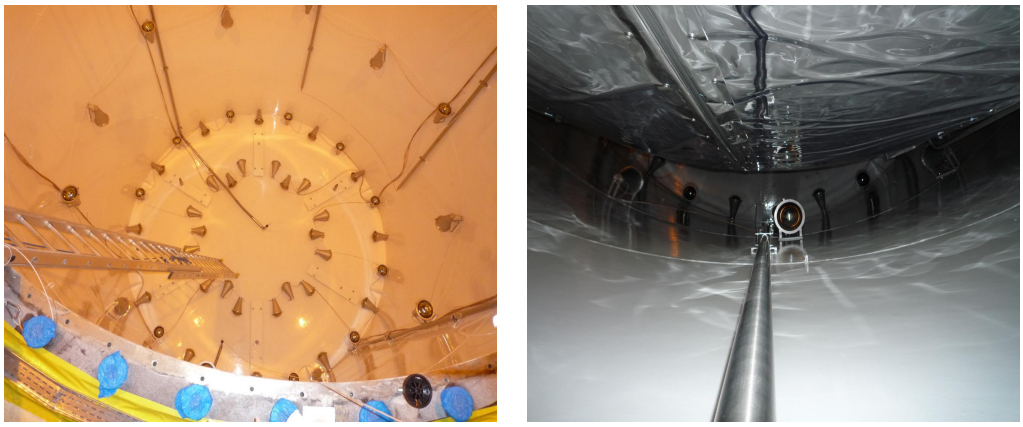

Figure 3.19: A photograph of the Inner Veto vessel (left) from the PMT installation period. A second vertical directed photograph of the Inner Veto region after the Inner Detector installation. The Buffer vessel is clearly visible.

detector scintillating region reducing thus the portion of background events arising from natural radioactivity. These three volumes together form the Inner Detector (ID). A picture of the ID denoting the three separate regions is shown in fig. 3.18.

To identify events in the ID arising from particles, or radiation, that come from the exterior, the DC detector utilizes the Inner Veto (IV). This is a cylindrical volume of 90 m^3 filled with liquid scintillator surrounding the detector's sensitive volume. The IV is instrumented with 78 8-inches PMTs (Hamamatsu R1408) while the IV walls are painted with a reflecting white dye that enhances the LY. Pictures of the IV are shown in fig. 3.19. The IV PMTs are placed in three rings. It is also interesting to quote that from the 78 PMTs of the IV the bottom rings occupies the majority of them. This was done in purpose since it was known from simulation studies that a configuration like this can contribute the most to the track reconstruction of cosmic muons.

To further shield the detector from external radiation, mainly from gamma rays coming from the rock in the laboratory cavern, 150 mm of demagnitized steel shielding was placed over the detector (fig. 3.20 left). Also three raws of plastic scintillator strips were laid on the top to further tag near-miss muons that can produce fast neutrons and other spallation products that could trigger the detector. This is the so-called Outer Veto (OV, fig. 3.20 right). The OV started taking data at July 2011 but for the first results no OV information was used.

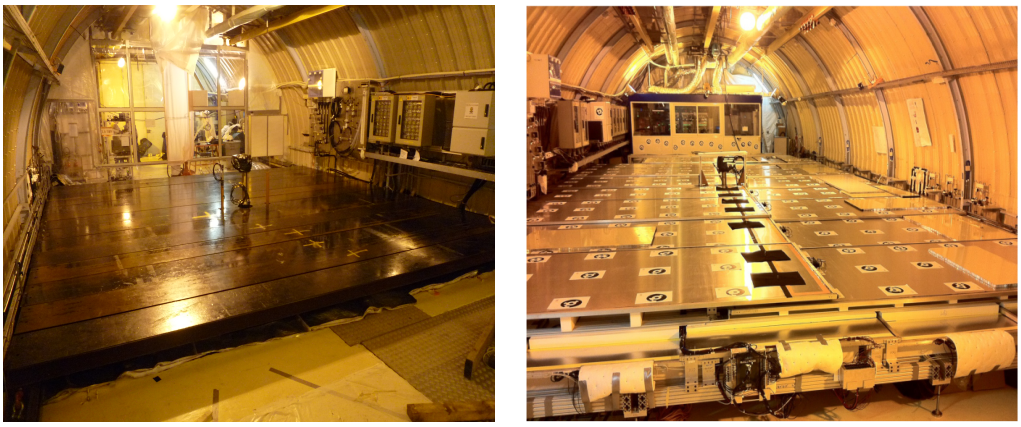

Figure 3.20: The steel plates used for shielding in DC (left) and the detectors's Outer Veto (right).

3.5.2 Liquid Scintillator, photomultipliers and light collection

Double Chooz (DC) is an homogenous detector in the sense that the agent used to induce the neutrino interactions, that is the liquid scintillator (LS), is also employed to detect the by-products of these events. LS are, in general, ideal materials for massive neutrino detectors like DC since they can be easily manufactured in large quantities and with a modest cost. The significant light yield (higher than 100 photoelectrons per MeV), the high attenuation length and the long term stability they offer, make them suitable for the construction of large-scale neutrino observatories.

When a charged particle transverses the LS it creates photons. The main mechanism for photon-production is always the scintillation light. This is the light emitted from the excitations and disexcitations of the scintillators molecules. Other processes, like:

- Čerenkov radiation
- scintillator quenching and
- bremsstrahlung

contribute to this signal but these effects are only subdominant. On the contrary, when a neutral particle enters a scintillation region it never produces light, unless it scatters a charged particle. For example, spallation neutrons created by near-miss muons in the surroundings of the DC detector can cross the Inner Veto without triggering the detector. In the particular case when

they collide with an atomic nucleus they can kick-out a bound proton. These secondary proton recoils can deposit large signals inside the detector.

For the detector target, DC uses an organic liquid scintillator composed by dodecane ($C_{12}H_{26}$) in 80 % and phenyl-o-xylylethan (PXE) in 20 %. Like this, the ratio of carbon to hydrogen molecules is roughly 1:2. This specific solvent was carefully selected because it improves the chemical compatibility with the detector materials (mainly the acrylics) and increases the number of free protons in the target. It also has a significantly high flashpoint as demanded by safety requirements.

The Neutrino Target (NT) liquid is loaded with 1 gr/l of Gd compound to enhance the neutron absorptions as already explained. To improve the Gd solubility a special metalorganic complex of Gd-β-diketone was utterly manufactured and used. This choice improves decisively the scintillator's lifetime, preserving the required attenuation length for a considerable period of time (about five years stability). As a reminder, the optical degradation of Gd-doped scintillators was a major issue in old experiments like Bougey-3 or CHOOZ. The advantage of metal-β-diketones in connection with neutrino liquid scintillator detectors was first recognized by F. X. Hartmann and R. A. Naumann in 1992 [198]. Additionally, two extra aromatic flours have been added to the target, 7 gr/l of PPO and 20 mgr/l of bis-MSB, to shift the emitted light wavelength in the range where the photomultipliers quantum efficiency peaks; that is near blue light.

The Gamma Catcher (GC) is filled with Gd-free liquid scintillator. The light yields (LY) of the GC and the NT liquids were matched with the introduction of a third solvent to the GC: the white, light-transparent medicinal oil Ondina909. Further Monte-Carlo simulations were conducted to ensure the detector's homogeneous performance. Finally, additional solvents have been added to all four volumes (including the Buffer and the Inner Veto) to equalize the liquids' densities and avoid the mechanical stretches that could otherwise damage the vessels of the detector. The attenuation lengths of all liquids are such to account for the detector dimensions.

To detect the photons produced in the scintillator from neutrino interactions and other signals, 390 10-inches PMTs (Hamamatsu R7081) have been installed on the walls of the Buffer. They are grouped in several rings of equal distance from the center of the detector and they are all directed to the center to enhance light collection. In this configuration a total of 14 % photocoverage is utterly achieved in a 4π formation. Knowing that the scintillator releases about 6500 photons per MeV and taking into account the PMTs' quantum ($\sim$ 25 %) and collection efficiencies ($\sim$ 13 %) we finally expect to observe more than 200 photons per MeV. This is enough to provide an energy resolution better than 10 % at 1 MeV.

All PMTs operate in the appropriate high voltage to provide a gain of roughly 10^7 electron-charge units in the anode. Their photocathode glasses are amply low-radioactive and their emersion in the non-scintillating liquid of the Buffer further reduces their contribution to the accidental trigger rate. All PMTs were carefully tested before their installation [197, 199, 200]. These measurements included: dark noise determination, gain measurements at the single photoelectron signals and quantification of the time-response profile or the effect of magnetic fields on the PMTs function and performance. Finally, a cylindrical mu-metal was placed around all Inner Detector (ID) PMTs to protect them from the magnetic fields arising from the earth or from other detector components; eg. the gamma-ray shielding. Some pictures of the ID PMTs, including the mu-metals, can be found in Fig. 3.17 and 3.18.

3.5.3 Electronics and DAQ

All PMTs are powered by a CAEN-A1535P system [201] at a $\sim$ 1.4 kV high voltage (HV). Like this a pulse of a few mV amplitude is observed for every photoelectron. The signals are decoupled from the power supply through a customized splitter (passive filter) [202]. With this decision, they get additionally filtered, reducing the low-frequency and pick-up noise that comes from the HV supply while the intrusive dead-volume in the detector is kept minimal. Subsequently, the separated signals are driven to the so-called Front End Electronics (FEE).

The existence of FEE is very important and has a multi-faced purpose. Primarily, the need to amplify the small amplitude neutrino-like pulses to match the dynamic range of the digital converters guided their design but they are also used to attenuate the higher muon-like pulses. Additionally, they further filter the data, minimizing distortions due to the decoupling between signal and HV, they stabilize the baseline position and they truncate high intensity signals to protect the rest of the electronics. Finally they sum, channel-wise, group of pulses providing input for the analog trigger. The FEE are implemented in a standard NIM module; they were optimized and constructed for the needs of Double Chooz [203].

Following the filtering and amplification in the FEE the recorded signals are finally directed to the analog digitizers. For the waveform digitization a customized model of Flash ADC (FADC) is employed, the CAEN VX1721 (Fig. 3.21), that was developed jointly by CAEN and APC collaborators (AstroParticule et Cosmologie, Paris). The crucial advantages of the FADC technology is the storage of all PMT pulses with a high sampling rate, 500 MHz, and an excellent charge resolution. After the digital conversion all waveforms are saved in histograms of 2 ns bins. In this way the data can be

Figure 3.21: The CAEN VX1721 FADC card.

reprocessed offline many times and refined pulse shape discrimination studies (PSD) can be conducted. The dynamical range of the FADC cards is 1000 mV with an 8-bit resolution.

Every FADC module has 8 input, analog channels and the whole readout system uses totally 64 modules. Each channel has a memory of 2 MB, divided in 1024 pages, that are (each) capable to record in real-time a time-window of 4 μs interval. The data recording occurs continuously in the same page until a trigger is asserted. Then the system writes this page and moves to the next one in a cyclic fashion graphically depicted in Fig. 3.22. The written pages are then available for readout; subsequently the next pages are being used in the same way. When page number 1024 is written, upon a trigger, the system will move to the first one if this is already readout. If not, the trigger command is ignored and a certain amount of deadtime is introduced. For every trigger a time-window of 256 ns is stored that contains most of the released scintillation light.

3.6 Trigger decisions

There are two levels of triggering in the Double Chooz (DC) detector: a hardware trigger, also called lever-1 trigger, and a software trigger. The hardware trigger is based on groups of summed PMT signals from the Inner Detector (ID) or the Inner Veto (IV), coming out from the FEE, and the decisions are taken upon estimations of the deposited energy or the PMT multiplicity. It

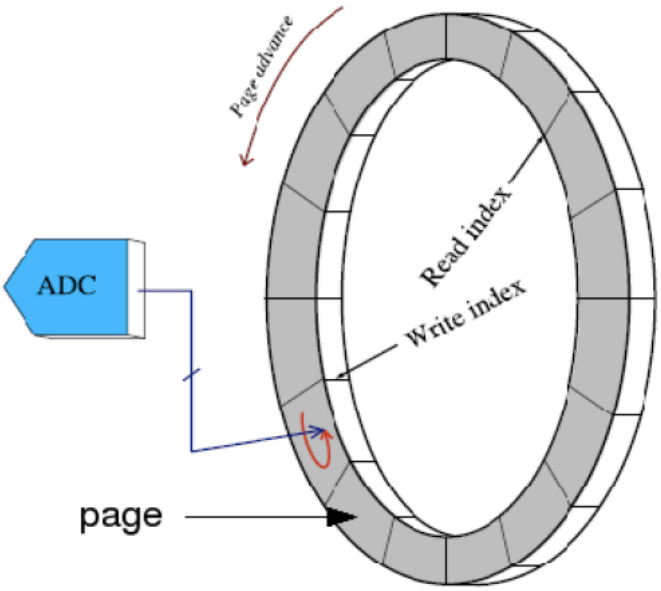

Figure 3.22: Graphical representation of the FADC card memory functioning.

is implemented on four trigger boards (TB). Two of them are used for the ID, one for the IV and the forth is the so-called trigger master board (TMB). The software trigger can be used after the level-1 trigger decision to further reduce the amount of stored data.

A graphical summary of the level-1 triggering system is shown in Fig. 3.23. The ID PMTs are separated in two groups of 195 PMTs. The separation was done evenly so that both groups observe the same volume with the same orientation and solid angle. This decision has many advantages. The signal coming from the ID PMTs is summed in the FEE in combinations of 16 and 3 channels and directed with 26 connectors on the Trigger Board A (TBA) for the first group and on Trigger Board B (TBB) for the second group PMTs. This concept is most properly depicted in Fig. 3.23.

When an event is happening inside the detector, the summed signals from both triggering group PMTs are compared with four different discriminators. The discriminator thresholds are shown in Fig. 3.24. The exact values chosen for this comparison are not based on a detailed calibration campaign but on rough estimations of the expected energy. Of course, the amplitudes of the summed signals are in first order proportional to deposited energy. When these conditions are fulfilled, for one of the two PMT groups, an 8-bit word is send to the TMB encrypting the trigger decision information.

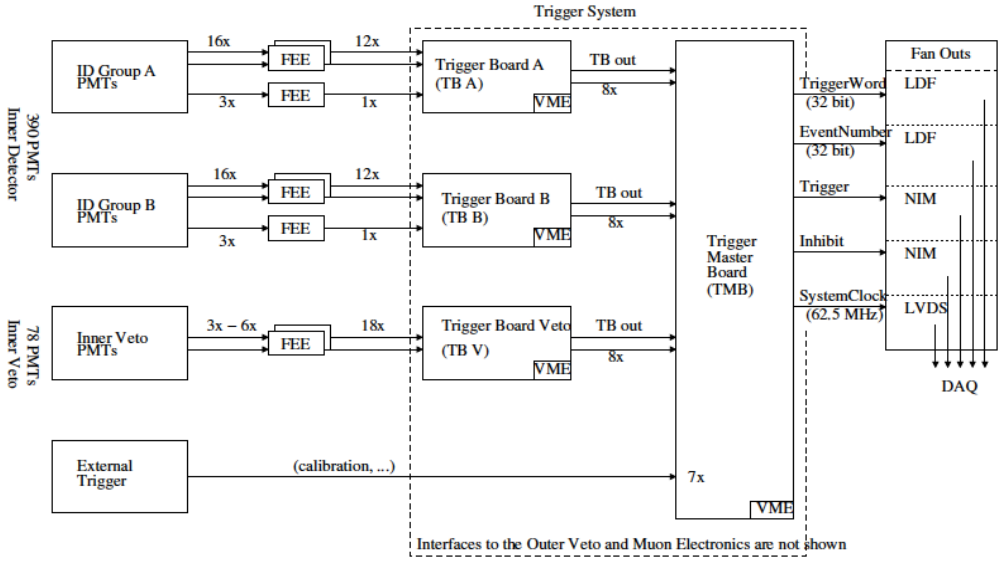

Figure 3.23: Overview of the Double Chooz triggering system [204].

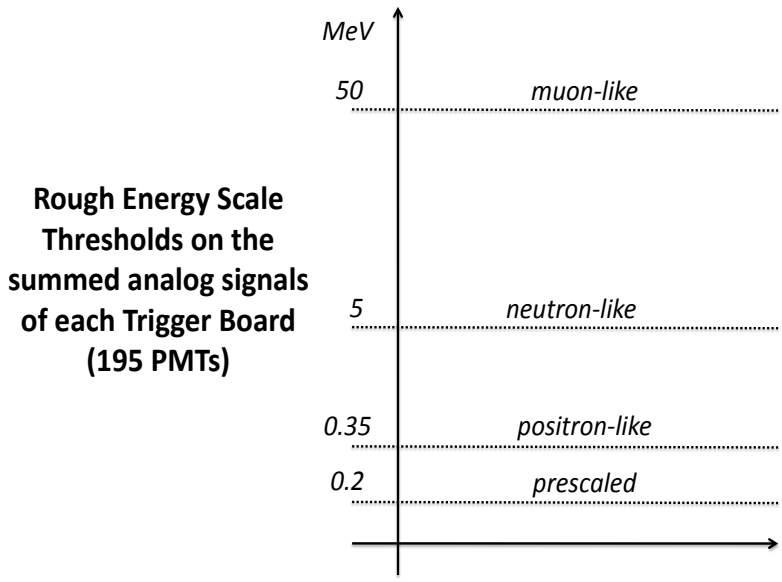

Figure 3.24: Trigger thresholds.

More information on the four discriminator thresholds is in order here. First, the muon-like threshold corresponds to the very high energy of 50 MeV and it's approximately the lowest value that one expects for ID crossing muons. As a reminder, such a high energy deposition would correspond to a 25 cm length muon track in the scintillator. The neutron-like threshold is at 5 MeV; beyond these energies we expect to observe predominantly neutron absorptions on gadolinium. The third positron-like threshold of 0.35 MeV is selected to trigger all of the $\bar{\nu}_e$ induced IBD interactions. The lowest energy initiated by a positron would be 1.022 MeV arising solely from the pair annihilation. Finally, the last trigger condition, the prescaled threshold, was chosen to monitor the detector trigger efficiency and utterly study the low-energy radioactivity background below $\sim$0.35 MeV.

Besides the amplitude trigger decisions described above, the DC detector can also trigger events on a PMT multiplicity-like basis. More precisely, low amplitude thresholds can be set on the 12 combined groups of PMT signals driven to each ID trigger board. Depending on whether or not these threshold conditions are satisfied, two multiplicity variables can be constructed that range from 0 to 12 for each trigger board. In the zero case, no signal from the 12 input 16-plets exceeds the above thresholds. On the other hand, when all PMT subgroups have signals larger than the optimized values this variable becomes 12 as it is expected. Currently, DC uses a multiplicity condition of $\geqslant$2, but only for the neutrino-like events. This choice helps to remove ab-initio some pathological events related to flashing PMTs[1].

The above discussion ends the ID trigger conditions description. The DC detector can also trigger when energy is deposited solely in the IV. This is important for the tagging of muons and muon-daughters. For this purpose all IV PMTs are grouped in the FEE and the stretcher levels in combinations of 3 to 6 PMTs as shown in Fig. 3.23. The grouping decided is shown in Fig. 3.25; five groups of IV PMTs have been chosen. Due to the high IV non-uniformity a careful trigger scan have been performed to decide on the best trigger conditions. These are (again) based on the estimated deposited energy and the PMT multiplicity patterns. Without entering the fine details, we only mention that the IV triggers at an estimated energy level of 4 MeV.

More information on the trigger conditions and logic can be found in Ref. [204]. For the first DC publication the trigger efficiency at 0.5 MeV was estimated to be >99 %. At 1 MeV, the lowest energy for IBD events, this number was fully consistent with 100 %. A detailed summary of the procedures used for the trigger efficiency determination can be found in Ref. [205].

[1]We will further elaborate on flashing PMTs on the analysis section.

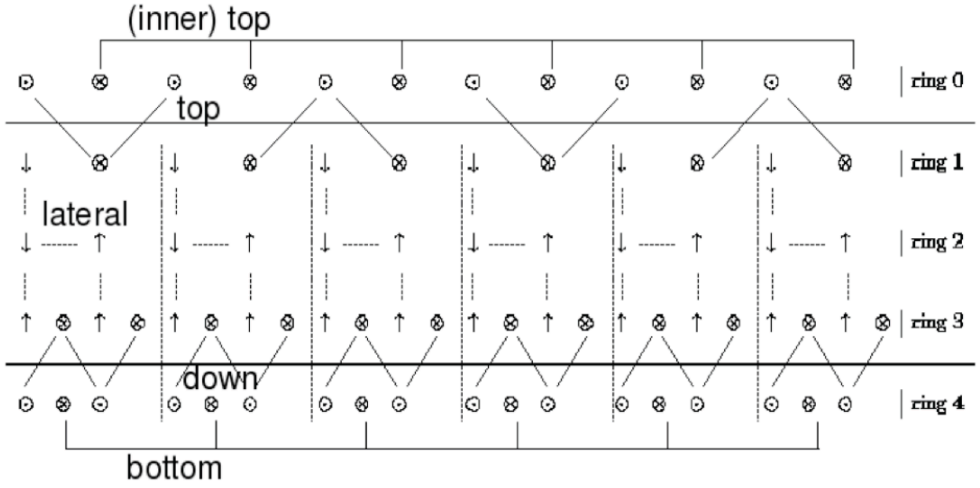

Figure 3.25: IV PMTs grouping for the corresponding triggering decisions.

3.7 Calibration systems

To understand the detector functioning and performance, while monitor as well its stability many ways can be invented. Among them, natural sources that give signals in a characteristic energy line and with a special recognition pattern are very important since clean and high-statistics samples can be isolated that follow very representatively the possible detector instabilities. Such events include natural occurring radioactivity (e.g. the U/Th decay chains), cosmic muons, michel electrons and above all else spallation neutron captures. Neutron absorptions on H or Gd give clear peaks at 2.2 and 8 MeV respectively that can be used to understand the energy scale and supervise the detector stability during time.

On the other hand, signals created by artificial sources inside the detector have the extreme advantage that their characteristics can be studied offsite and thus are, in general, well understood. Furthermore their properties can be tuned externally according to our desires and needs. For the first result, DC used light pulses from LEDs to calibrate the charge (gains) and time response (time offsets) of all ID PMTs and correct for their time variance. On the other hand the energy scale (the conversion between photoelectrons and MeV) was determined with a ^{252}Cf source in the center of the detector. The detector stability was monitored with neutron captures on Gd.

Bunches of light can be released inside the ID in totally artificial conditions through the so-called Inner Detector Light Injection system (ID-LI). The ID-LI consists of a network of optical fibers placed in the ID; more

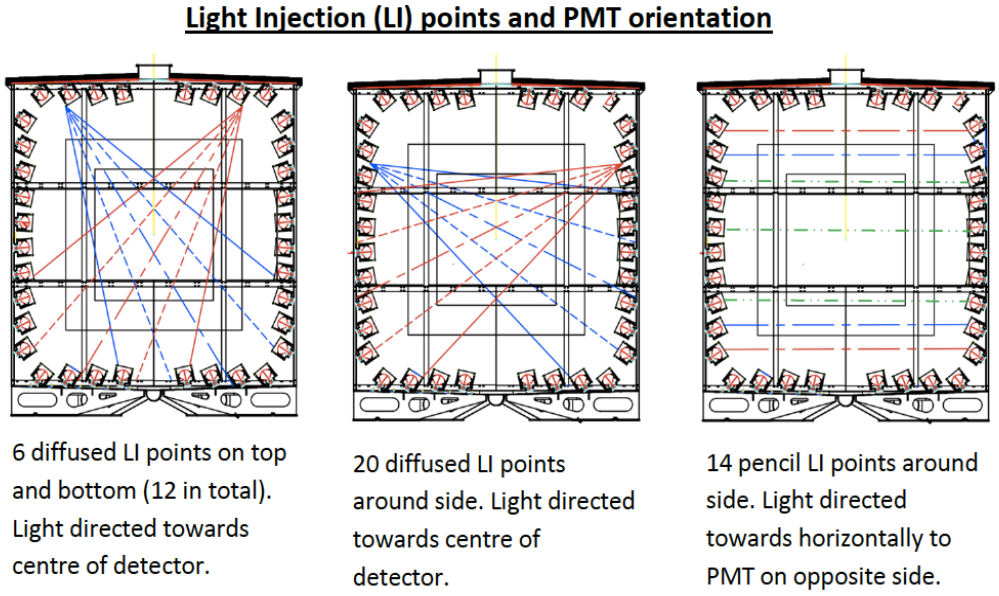

Figure 3.26: The Inner Detector Light Injection system configurations.

specifically attached on the ID PMTs. LEDs on the other side of the fibers send pulses of light of adjustable width and amplitude. Three different wavelengths can be employed: 385, 425 and 475 nm. The light is driven in the ID in two ways (Fig. 3.26):

i. with 32 teflon fibers that terminate in a diffuser (diffused light) and,

ii. with 14 quartz fibers (pencil beams)

The first configuration disperses the light inside the detector in a large angle opening and it is suitable for linearity studies and the inspection of other general properties of the detector (e.g. the optical model). The quartz fibers create a more localized beam that can be used to probe specific volumes in the detector (e.g. only the gamma cather). These ID-LI illumination schemes are shown graphically in Fig. 3.26. Thus far the ID-LI has been used to understand the detector functioning, examine its linearity and to measure PMT gains and time responses.

Radioactive sources, deployed inside the detector provide rather convenient classes of events. First the energy spectra are peaked at specific values, and second the vertices are highly localized so that an amply pure sample can be selected with a combination of energy and fiducial cuts. Furthermore,

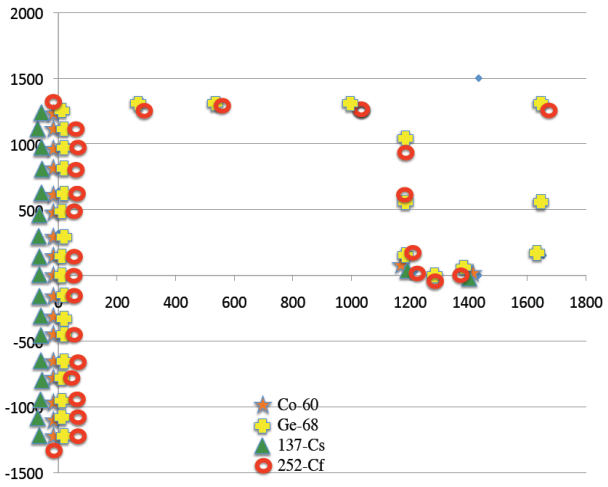

Figure 3.27: Deployed positions and sources. x-axis gives the ρ while y-axis gives the z coordinate of the source inside the DC cylindrical detector.

impurities can be easily quantified assuming that the background of physics events remains approximately constant for short periods of time.

Four sources have been deployed so far in the DC detector. These are the: ^{137}Cs, ^{68}Ge, ^{60}Co and ^{252}Cf. They have all entered the detector from the chimney via the Z-axis (ZA) and the Guide-tube (GT). As a reference we remind you that the ZA and the GT are thin tubes that allow, through a refined mechanism, to move the sources along the z coordinate of the central axis and the Gamma Cather respectively. The positions used for the moment, for source deployments are shown in Fig. 3.27. The pronounced energy peaks of the ^{137}Cs, ^{68}Ge and ^{60}Co sources are 0.662, 1.022 and 2.5 MeV respectively. The ^{252}Cf source has a continuum spectrum of gamma rays but it is also a neutron emitter; that means it gives the neutron capture peaks on H (2.2 MeV) and Gd (8 MeV).

The 2.2 MeV ^{252}Cf peak for runs at the center of the detector has been used to obtain the conversion factor of photoelectrons to MeV. The sources have been also inferred to validate the detector linearity [206] and to measure time offsets [207] and gains [208]. The detector stability has been monitored with neutron captures and the deviations were found to be smaller than 1 %. Future calibration plans include the use of the Laser Diffuser Ball [209], the Central LED Flasher [210], and the Articulated Arm [211].

3.8 Neutrino selection

An important piece for the neutrino selection is the rejection of muons and muon daughters. Cosmic muons induce, for most of the times, huge signals irrelevant for the antineutrino identification. Nonetheless, Buffer crossing muons or muons clipping the ID can produce low energy signals in the energy windows appropriate for IBD searches. Muons also produce spallation neutrons that could be absorbed several μs after, giving signals in the H (2.2 MeV) and Gd (8 MeV) absorption lines. Since muon induced neutrons like these come in high multiplicities they could fake the prompt-delayed coincidence.

To reject these events, all ID signals in a [0,1] ms window after a detected muon are rejected. This specific time interval in the muon veto corresponds to 5 times the neutron mean absorption time in H; that is 200 μs. Dedicated studies have also showed that this decision is indeed validated [212]. For the first publication of DC, muons were tagged through the ID, IV synergy:

- $Q_{IV} > 10000$ DUQ or
- $E_{ID} > 30$ MeV.

DUQ is the digitized unit of charge read-out by the data acquisition system. Also, it should be separately emphasized that for all ID signals below 30 MeV the $Q_{IV} < 10000$ DUQ condition is necessary for their selection. Like this a lot of particles or radiation that trigger the detector but coming from the outside are eliminated from the final selection.

The selection of reactor neutrinos follows, of course, closely the pattern of the IBD signature. More precisely, in the processed data corrected using all calibration constants, we first search for a signal between 0.7 - 12 MeV. This corresponds to the prompt event originating from the positron thermalization and subsequent annihilation. We then search for a second signal of 8 - 12 MeV inside the time coincidence window [2, 100] μs corresponding to the IBD delayed neutron capture on Gd. The 2 μs lower limit is there to eliminate some correlated noise. The presence of this prompt-delayed doublet is the signature of an $\bar{\nu}_e$ event. The candidate selection is also sketched in fig. 3.28 to help the reader visualize the procedure.

It is true that prompt signals originating from pure reactor $\bar{\nu}_e$ have rarely signals higher than 8 MeV. It is also true that the peak of delayed signals from Gd neutron captures has narrower resolution than the [6, 12] MeV window and this choice is somehow looser than needed. Also neutron absorptions could happen on hydrogen or after the 100 μs maximum limit of the time coincidence window. True these comments might be they are all taken

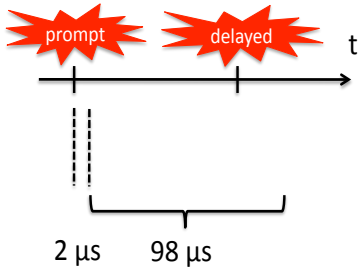

Figure 3.28: IBD prompt-delayed selection strategy in DC.

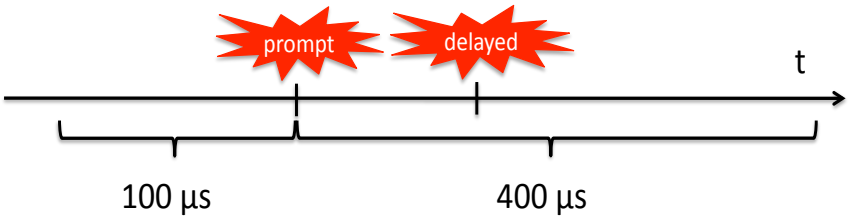

Figure 3.29: Multiplicity isolation cuts.

into account in the final oscillation analysis since the extra non-neutrino selected events are estimated and removed after the final fit, while the neutron detection efficiencies have been carefully determined through a number of important studies. For a culmination of the work done with respect to the neutron efficiencies relevant for the first publication one could have a look at Ref. [213].

Despite the software muon veto some spallation-induced neutron doublets can sneak into the signal. This is evident from the presence of an excess in the 8 MeV region of the selected candidate sample. This small bump corresponds to neutron captures tagged as prompt signals. These neutrons originate form muons that near-miss the detector or from inefficiencies related to the IV. The CHOOZ experiment dealt with these subtracting the measured background when both reactors were off. In the Double Chooz experiment to remove this contribution we employ two extra cuts. Since spallation neutrons come with high multiplicity we demand that no signal is recorded in a 100 μs window before the prompt signal and, in addition, we ask for only one signal (the delayed one) in a window of 400 μs after the prompt.

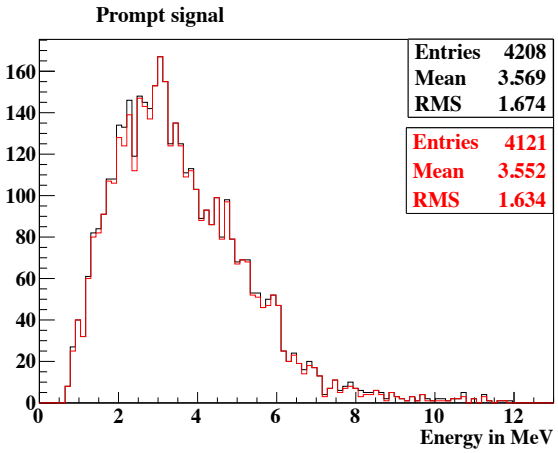

Figure 3.30: Prompt spectra before (black) and after (red) the isolation cuts.

These cuts, depicted in fig. 3.29, are called the multiplicity isolation cuts and as shown in fig. 3.30 they induce a small reduction in the 8 MeV region of the the prompt spectrum. An additional reduction is also observed in the region of hydrogen capture; around 2.2 MeV[2]. In fig. 3.30 we overlap the prompt energy before (black) and after (red) the isolation cuts. They remaining part of neutron doublets is thought to be small but additional efforts to evaluate its impact to the final fit are being pursued; see for instance [214, 215].

Finally, we include two extra rejection criteria applied to all recorded triggers during the event selection. To be more precise, it was discovered during the detector commissioning period that an unexpected source of background was present in the data. After investigation with detector data and off-site measurements it was found that the source of this extra noise was coming from some PMTs' bases that sporadically flash light that could fake the selection. Flashing PMTs of this kind are common to other neutrino detectors, say in Super-Kamiokande, and it is interesting that the other two experiments searching for θ_{13}, Daya Bay and RENO, with similar PMTs and detector designs reported on the same problem.

It is to be noted that these artificial triggers, hereafter referred as Light Noise (LN), have a very different signature from the events that excite the scintillator and so they can be identified. To handle this issue 15 PMTs were switched-off and the additional software cuts are applied to all recorded

[2]Note that setting the muon tagging cut at $E_{ID} > 30$ MeV the bump at 8 MeV is not that visible. In chapter 6, where the inefficiencies of the IV in connection with the correlated background are addressed, this issue will become even more clear.

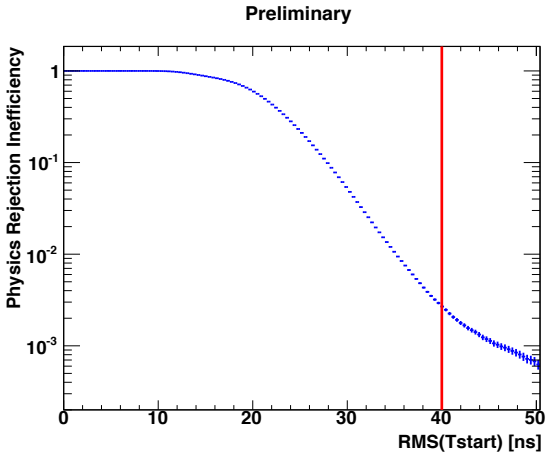

Figure 3.31: Rejection inefficiency for the RMS(T_{ST}) discrimination variable.

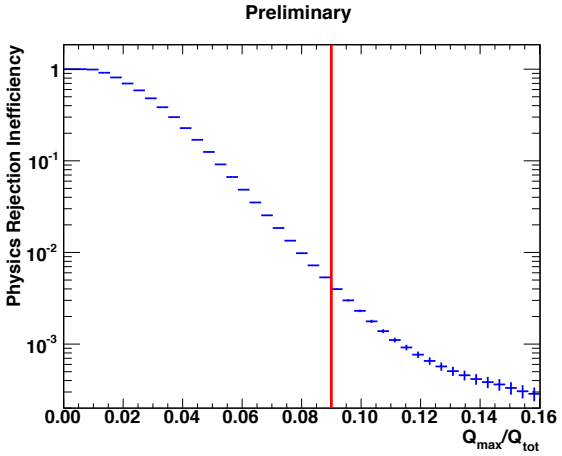

Figure 3.32: Rejection inefficiency for the several Q_{MAX}/Q_{TOT} values.

signals. First we demand that:

- The distribution of the pulses' start-times for all the channels has an RMS smaller than 40 ns for all signals, RMS(T_{ST})< 40 ns and that,

- The ratio of the highest charge recorded from all PMTs (Q_{MAX}) over the total recorded charge (Q_{TOT}) is smaller than 0.09 for prompt, Q_{MAX}/Q_{TOT}<0.09, and 0.06 for delayed signals, Q_{MAX}/Q_{TOT} <0.06.

The difference between the Q_{MAX}/Q_{TOT} cuts for prompt and delayed signals reveals an energy dependence of the Q_{MAX}/Q_{TOT} discriminating variable. This dependence is normal and well understood. In depth MC simulations

Muon veto	Q_{IV} > 10,000 DUQ or E_{ID} > 30 MeV
	1 ms dead-time after a tagged muon
Prompt signal	0.7 - 12.0 MeV
Delayed signal	6.0 - 12.0 MeV
Coincidence time window	2 - 100 μs
LN rejection (prompt signal)	RMS(T_{ST})< 40 ns and Q_{MAX}/Q_{TOT}<0.09
LN rejection (delayed signal)	RMS(T_{ST})< 40 ns and Q_{MAX}/Q_{TOT}<0.06

Table 3.1: Neutrino selection cuts

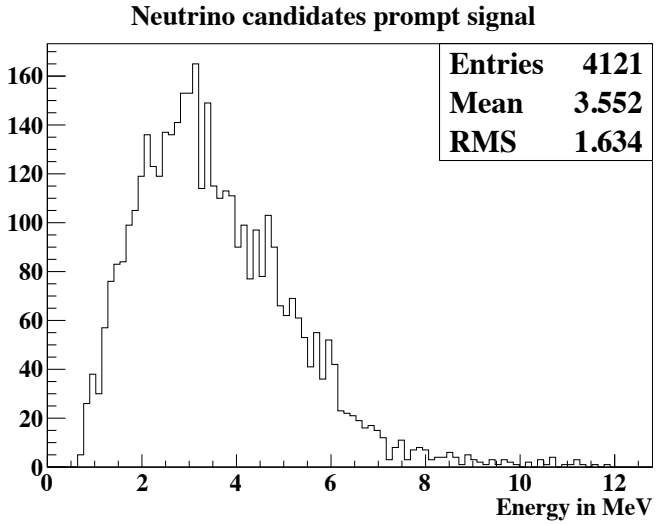

Figure 3.33: Prompt signals of the selected neutrino events.

and dedicated runs with radioactive sources deployed in the DC detector revealed that the associated inefficiencies are indeed small. In fig. 3.31 and 3.32 we include the rejection inefficiencies in terms of cumulative distributions versus the cut-off RMS(T_{ST}) and Q_{MAX}/Q_{TOT} values.

All the cuts necessary for the final neutrino selection are gathered in table 3.1. For the first phase of DC 2,594 runs taken between April 13, 2011 and September 18, 2011 were used in the analysis. The sample run-time is 101.5 days and the total muon-removed live-time is 96.8 days. Some extra corrections in the total live-time are explained in [216]. Applying the selection cuts of table 3.1 to this sample we collect 4121 prompt-delayed doublets. In fig. 3.33 we plot the selected prompt signals. The vertices of the triggered events inside the detector are plotted in fig. 3.34. The distributions inside

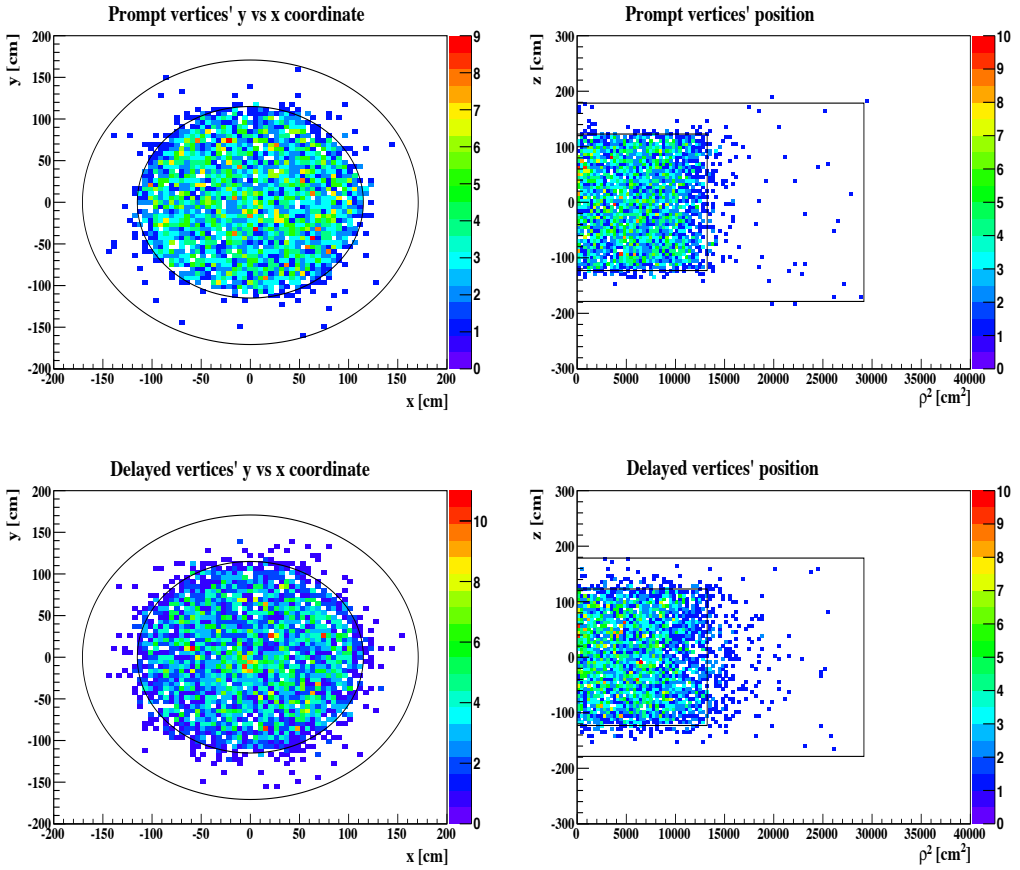

Figure 3.34: y vs x (left) and z vs ρ^2 (right) distributions, $\rho = \sqrt{x^2 + y^2}$, for the prompt (top) and delayed (bottom) events.

the neutrino target are uniform. Outside the target only a small number of events is present as it was expected. It should be again emphasized that no fiducial volume cut was applied for this analysis. The prompt-delayed distance and time difference distributions have been already given in fig. 3.7.

3.9 Backgrounds

The 4121 events already selected in the previous section consist mainly of $\bar{\nu}_e$ coming from the Chooz-B reactors. The correlation with the reactor thermal power and the reduction in the antineutrino events counted in the days when one reactor is off (fig. 3.35) is clearly visible. We know, nonetheless that a small number of background events unavoidably fakes the selection.

For counting experiments like Double Chooz these background doublets are not dangerous as long as they do not dominate the signal and are well evaluated. In terms of the signal-to-background ratio (S/B) it is a necessary precondition that S/B is high enough. Additionally, for a rate analysis, it is also extremely important to know with a good accuracy how many of these

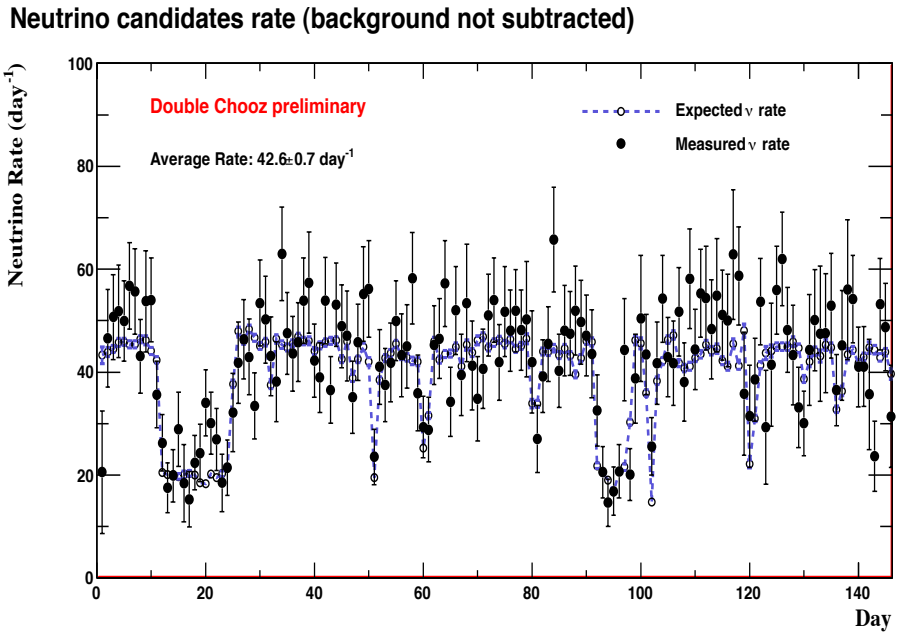

Figure 3.35: $\bar{\nu}_e$ candidates rate (dots), overlapped (dark blue line) the MC prediction.

fake events finally pass the cuts and contaminate the signal. The better the accuracy on these numbers we have the better sensitivity on θ_{13} can be achieved.

The associated background events (at least those relevant for the first phase of the experiment) can be distinguished in three major categories:

- accidentals,
- fast neutrons and stopping muons and,
- cosmogenic isotopes.

Among them, fast neutrons, stopping muons and cosmogenics could be further grouped into one category labeled as the "correlated background" (as opposed to the accidental background) because as we shall see the prompt and delayed signals of these events are caused by the same source, and thus they are entangled in the same way that it happens for antineutrinos. In the following parts of this section, we shall give a brief description for every background and we will also present how DC treated them in the first publication. We shall sketch very quickly the decisions taken pointing towards the original internal documents were these analyses could be found in more depth. Other information could be tracked in the original publication [126].

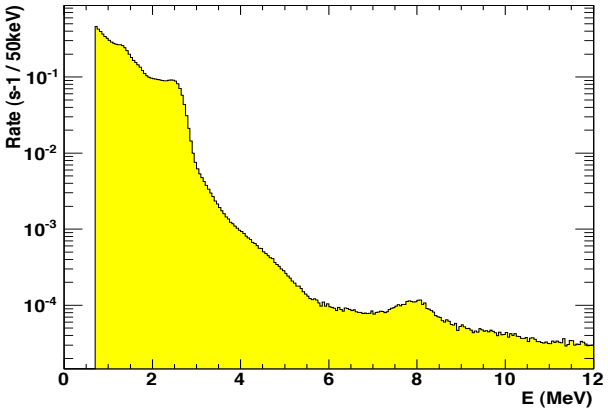

Figure 3.36: Singles spectrum in the prompt energy window.

Accidentals

In the 0.7 - 12 MeV, important for IBD searches, energy window a lot of other signals exist besides those induced by $\bar{\nu}_e$. Among them natural radioactivity, gamma rays from the surrounding rock and neutron captures on hydrogen or gadolinium are probably the most abundant. Even though the IBD coincidence window is small enough, there is always the possibility that two such uncorrelated events will happen within a small time-interval and so they will be counted as the prompt and delayed signals characteristic of IBD.

Looking at the energy of single events after the removal of Light Noise triggers with the RMT(Ts) and Q_{max}/Q_{TOT} cuts, fig. 3.36, it is clearly understood that the main source of such signals occupy the low energy part of the spectrum (below the 3 or 5 MeV limit). The clear sign of neutron captures is also present as witnessed in the small, 8 MeV peak. These neutrons arise from untagged muons that near-miss the detector. The rate originating from such accidental doublets is estimated to be:

$$R_{acc} = R_{e^+} \times (1 - e^{-R_n \Delta t_{e^+n}}) \tag{3.11}$$

where R_{e^+} is the singles rate in the prompt signal window (0.7 - 12 MeV, positron-like), R_n the rate in the delayed window (6 - 12 MeV, neutron-like) and Δt_{e^+n} the 100 μs coincidence window. Equation (3.11) is also suitable to understand, from another standpoint, the decision to dope the LS of the NT with Gd: the rate in the Gd-neutron absorption window R_n (fig. 3.37) is low enough to minimize the number of the expected accidental events. This fact combined with the prompt-delayed detection technique are really crucial for the design of the experiment.

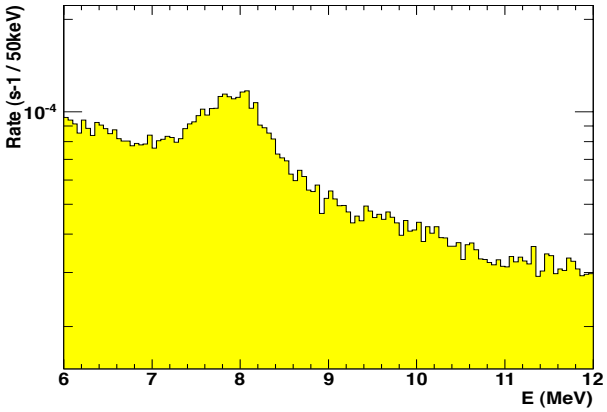

Figure 3.37: Singles spectrum in the delayed energy window.

For the fist publication, the accidental rate and spectrum were calculated through the so called "off-time" window technique. More precisely, the same selection cuts used for the neutrino sample were used but with one crucial difference: the coincidence window is now shifted from 1.002 ms to 1.1 ms. Like this only accidental coincidences are counted since we know that after 1 ms all neutron absorptions, both in H and Gd, cease to happen. Also, rate and spectrum information is available.

For the first publication the accidentals were calculated in 198 windows from 1.002 - 1.1 ms, 1.502 - 1.6 ms, 2.002 - 2.1 ms, etc... 6339 coincidences were found and as final result the mean value of all observed coincidences has been considered. The rate measured was:

$$0.332 \pm 0.004 \; events \; per \; day. \tag{3.12}$$

The shape of the spectrum found is shown in fig. 3.38. It should be remarked that using this method the accidental rate and spectrum are considered to be well-known. More information about the accidental background estimation could be found in [217].

Cosmogenic isotopes

These isotopes are the most dangerous background source for underground neutrino detectors. They are created from spallation processes induced by high energy muons on carbon nuclei. It is very difficult to treat them because they are long-lived with life-times sometimes of the order of hundreds of ms and no muon-veto could be employed without a significant physics loss. The mechanisms of their production are not well-modeled but probably the muon-induced particle showers are a precondition for their creation [218].

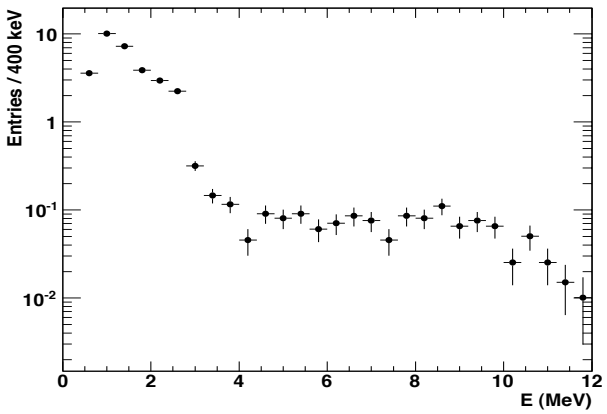

Figure 3.38: Accidentals spectrum.

Cosmogenic isotopes are also important for other neutrino experiments. The KamLAND collaboration recently published an important work on the production of cosmogenics within their detector [219] and experiments at CERN, in the past, studied the production cross-sections for the analyses purposes of the BOREXINO experiment [220]. In the case of DC two isotopes are relevant: ^{9}Li and ^{8}He. They both decay with e^{-} - n cascades and they can fake the signal selection since the β-decay Q_{β} values are around 15 MeV; that means that some electrons are emitted with energies in the 0.7 - 12 MeV window. Since the production of ^{8}He is less abundant than that of ^{9}Li, ^{8}He was not treated in the first publication. For further information on the ^{8}He/^{9}Li decay modes one might consult the relevant nuclear physics bibliography.

The sample contamination from ^{9}Li decays was treated by looking for prompt-delayed doubles after a cosmic muon. Looking at the time difference between a muon with energy deposition bigger than 600 MeV one gets the distribution of fig. 3.39. In principle one would expect this distribution to be flat since those events should be totally uncorrelated. Instead one gets this exponential shape decay at the low DT values. This contribution is indicative of the aforementioned ^{9}Li events.

To estimate the ^{9}Li events the distribution was fitted with a mathematical function having a flat and an exponential component. Using this fit a lower limit of ^{9}Li events can de deduced. The upper limit can be obtained redoing the same fit but with no E_{ID} cut. The central value is given by the average

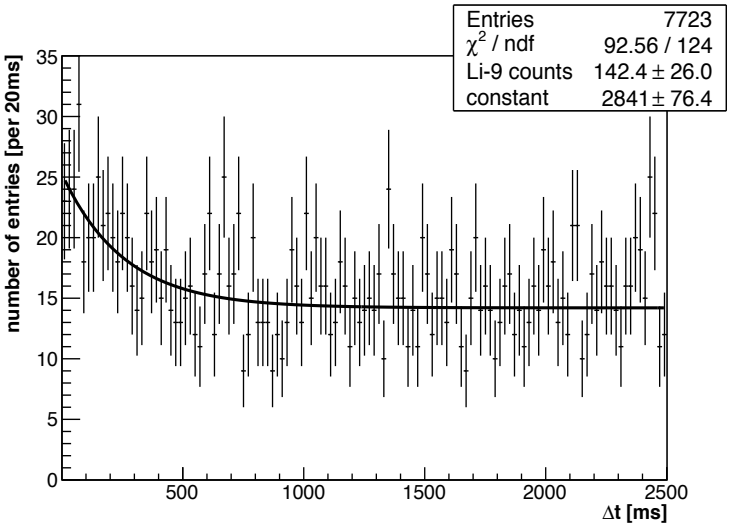

Figure 3.39: DT distribution between an E_{ID} >600 MeV and a $\bar{\nu}_e$-like event.

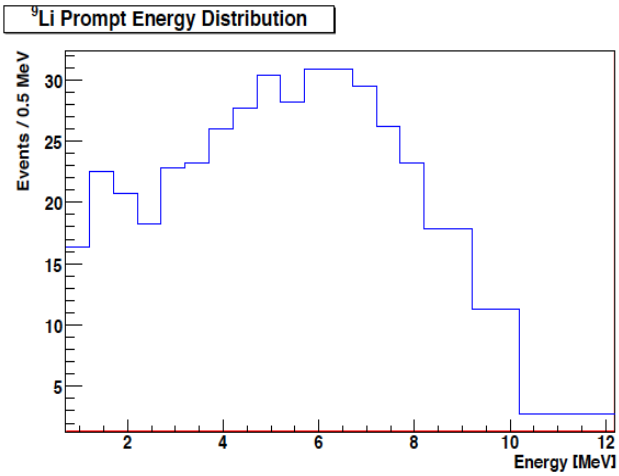

Figure 3.40: ^{9}Li spectrum (MC).

of two extremes given by the two analyses (± 1 σ). The result is:

$$2.3 \pm 1.2 \; events \; per \; day. \tag{3.13}$$

Note that the error on this estimation is big and it actually drives the main uncertainty of the θ_{13} oscillation analysis. For the spectrum information the official MC was used. The ^{9}Li spectrum is shown in fig. 3.40.

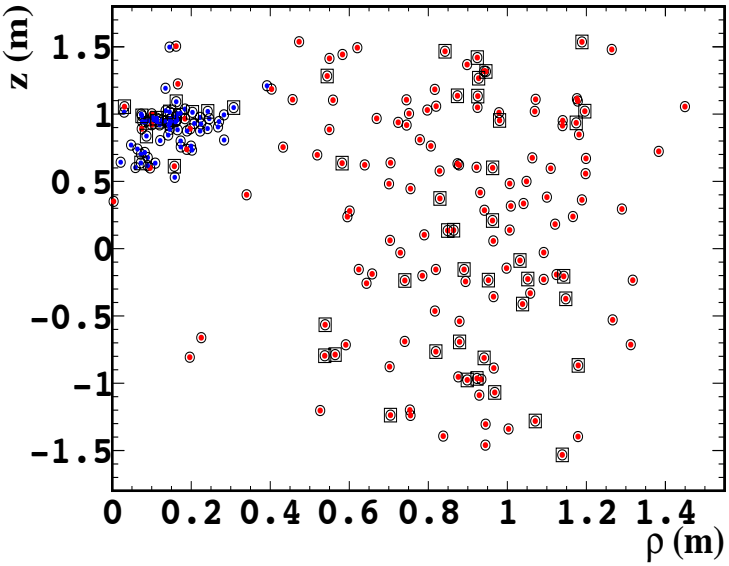

Figure 3.41: Vertices of the prompt fast neutron (red) and stopping muon (blue) events. Stopping muons are gathered below the chimney, of course, as it is expected.

Fast neutrons and stopping muons

The importance of the fast neutron background was known since the first Reines and Cowan experiment at the Hanford reactor. Neutrons, created by muons crossing the surroundings of the detector, can pass through the IV without exciting the scintillator since they carry no charge. If they are still energetic enough they can kick-out protons from nuclei inside the ID producing signals in the detector. These fast neutrons can be afterwards slowed down and captured on Gd giving the usual 8 MeV delayed signals. The described proton recoil - neutron capture doublets have the same signature as the IBD events since the fast neutron thermalization time is of the order of some μs. For reference, the first CHOOZ experiment measured 1.01 fast neutrons per day.

On the other hand, stopping muons is a background relevant only for the first DC phase when no upper Outer Veto is installed. In particular, we know that the possibility exists for a muon to enter the detector through the chimney. If this muon additionally decay inside the detector, then it will not be tagged by the IV; this is a known IV inefficiency. Furthermore, when the muon releases inside the ID energies smaller than 30 MeV it will not be

Background	Rate per day	Number of events
Accidentals	0.332 ± 0.004	32
^{9}Li	2.3 ± 1.2	223
Fast neutrons - stopping muons	0.83 ± 0.38	80

Table 3.2: Background rates

tagged by the ID as well. In these cases the Michel decay mode can fake the neutrino selection, since the muon - Michel electron signature is the same with IBD with the notable difference that the muon life-time is 2.2 μs as opposed to 30 μs that correspond to the neutron capture mean-time.

In fig. 3.41 the vertices that correspond to some selected background events of these type are shown. The vertices of stopping muons (in blue) are as expected under the chimney of the detector while fast neutrons (red) are gathered in the periphery of the NT and the GC. The fast neutron and stopping muon background was estimated to be:

$$0.83 \pm 0.38 \; \textit{events per day}. \tag{3.14}$$

The understanding and the estimation of this background was a main responsibility and contribution of the author. We will not give any further detail at this point since the whole subject will be treated in chapter 6 in more detail. Nonetheless, it should be emphasized that stopping muons are relevant only for the first analysis of DC since no OV information was used. We know that with the add of the OV data and the installation of the upper OV this background will cease to be important.

In the first period of DC, we had the privilege of roughly one day of data taking with both reactors off. The analysis of these data yielded, in the relevant for $\bar{\nu}_e$ searches energy windows, two events consistent with ^{9}Li, in accordance with our expectations. The possibility of having a substantial data set with all reactors down is a unique capability of DC.

3.10 Oscillation search

In table 3.2 we summarize the results for the background estimation. We repeat that with the selection cuts devised for the first publication we counted 4121 antineutrino-like prompt-delayed doublets. This result does include the backgrounds of table 3.2. Subtracting these numbers we are finally left with 4121 - 335 = 3786 candidates. On the other hand the official Monte-Carlo,

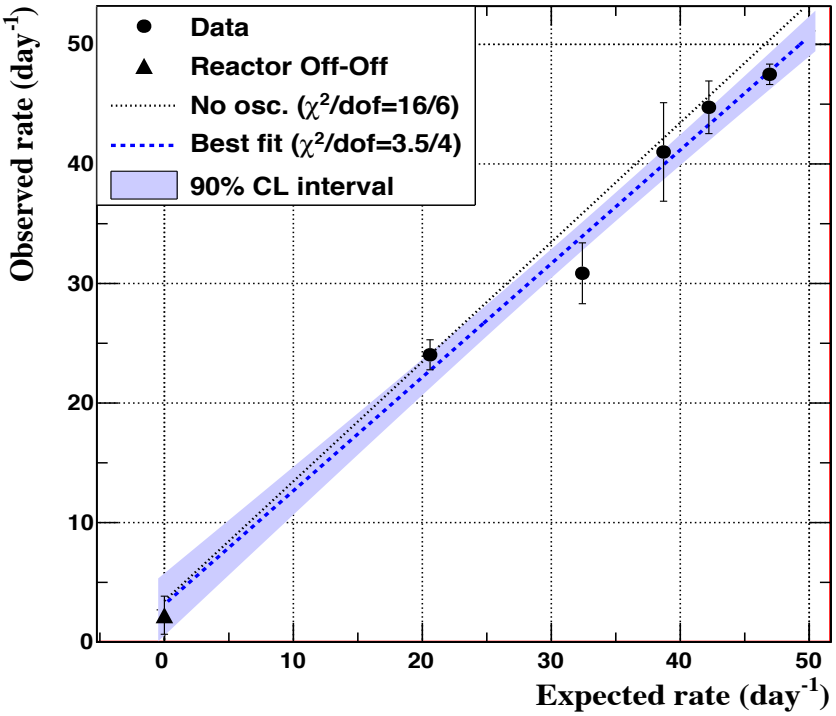

Figure 3.42: Linear fit to the observed vs the expected $\bar{\nu}_e$ rate curve.

based on reactor simulations and the incorporation of the detector response predicts 4010 $\bar{\nu}_e$ for the non-oscillation scenario; that means when $\theta_{13} = 0$. A clear deficit is seen that it is interpreted as evidence for neutrino oscillations. Even without the use of sophisticated analysis tools we could have a value for θ_{13} through a simple back-of-the-envelope calculation based solely on the usual two-flavor oscillation formula.

Probably the most straightforward way to determine the value of θ_{13} and its acceptance intervals is through a simple linear fit in the observed versus expected antineutrino rate curve. This technique has been used in the past in similar reactor experiments trying to put limits on θ_{13}. Grouping the observed and predicted $\bar{\nu}_e$ rate in a small number of periods one could fit the data points with a simple line. Like this the ratio R_{DC} between the measured and expected neutrinos is given through the slope and the background events' rate show up in the y-axis offset value. See for instance [109, 110].

The results of this analysis for the first phase of DC are shown in fig. 3.42. The whole data sample is separated in five periods. The point corresponding to the reactor off-off period is also drawn (triangle data point) and it is

included in the fit. The result of the fitter gives a ratio $R_{DC} = 0.95 \pm 0.04$ for the best fit with $\chi^2/NDOF = 3.5/4$. The y-axis line offset gives 3.2 ± 1.3 events per day for the total background. This number is not that different from the one previously estimated and it agrees with the number of events measured in the reactor off-off period. It should be also noted that the null hypothesis is disfavored with a $\chi^2 = 16.0/6$; dashed line in fig. 3.42. Using the two-flavor oscillation formula to interpret our results:

$$p(\ \nu_e \to \nu_e;\ L\ ) \simeq 1 - \sin^2(2\theta_{13}) \sin^2\left(1.27\Delta m^2_{atm}\frac{L}{E}\right), \tag{3.15}$$

we finally derive the value of $\sin^2(2\theta_{13}) = 0.093 \pm 0.065$. The value of $|\Delta m^2_{atm}|$ that we used, is $2.32^{+0.12}_{-0.08}\ 10^{-3}$ eV^2 and was taken from [221].

To obtain a better, improved estimation of $\sin^2(2\theta_{13})$ a χ^2-minimization to the data set could be performed. They are generally two ways that this could happen: one using only the rate information and another one using the combined rate and spectral informations. These are the so-called rate only and rate plus shape analyses. The χ^2 constructed for these minimizations can be factorized in the form:

$$\chi^2 = \sum_{i,j}\left(N_i - \sum_R N_i^R - \sum_B N_i^B\right)(M_{ij})^{-1}\left(N_j - \sum_R N_j^R - \sum_B N_j^B\right)^T. \tag{3.16}$$

$N_{i(j)}$ is the number of antineutrino candidates in the i(j)-th energy bin (including background). $N^R_{i(j)}$ is the $\bar{\nu}_e$ prediction from the reactor simulation for each core; the index R runs over the two Chooz-B reactor cores. $N^R_{i(j)}$ depend of course on the reactors' power and the possible value of θ_{13}. The oscillation formula used is (3.15) armed with MINOS $|\Delta m^2_{atm}|$ value.

$N^B_{i(j)}$ is the estimated background counts summed for each case separately. The sum $\sum_B$ runs over the three different categories. Finally, M_{ij} is the correlation matrix holding the total uncertainties and correlations on i-th and j-th energy bins. 18 variably sized energy bins between 0.7 and 12.2 MeV were used. The range from 0.7 to 8.2 MeV was covered in 0.5 MeV steps, from 8.2 to 10.2 MeV in 1 MeV steps, and from 10.2 to 12.2 MeV in a 2 MeV step.

M_{ij} holds the statistical uncertainties of the measurements, the uncertainties in the reactor prediction (already covered in a previous section) and the errors associated with background estimation. It also includes a component holding the errors related to the detector response as compared to the

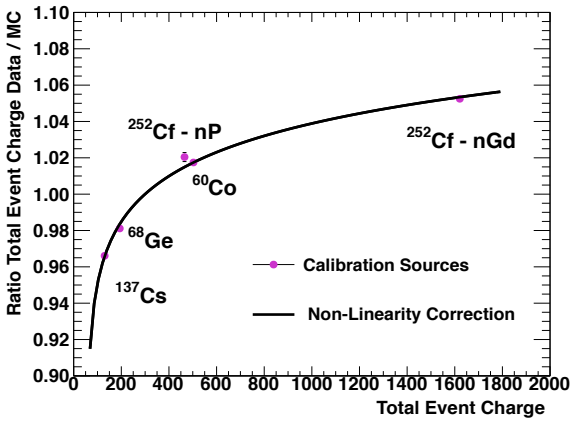

Figure 3.43: Charge data/MC ratio versus the total charge.

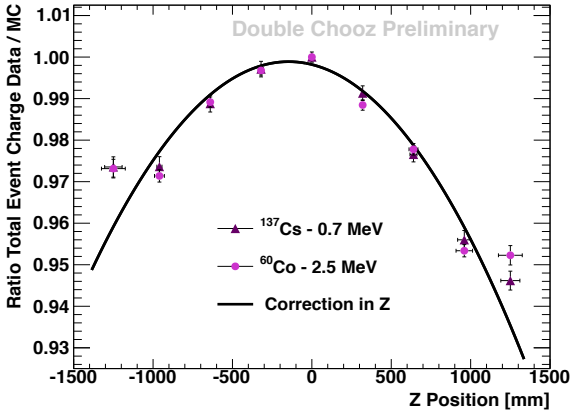

Figure 3.44: Charge data/MC ratio versus the z coordinate.

MC. This is the so-called detector covariance matrix.

$$M_{ij} = M_{ij}^{Reactors} + M_{ij}^{Detector} + M_{ij}^{stat.} + \sum_{B} M_{ij}^{B} \tag{3.17}$$

M_{ij}^{B} are the errors related to the three classes of backgrounds. For more informations one could have a look at [223].

The uncertainties connected with the detector response were evaluated with calibration data taken with the ^{137}Cs, ^{68}Ge, ^{60}Co and ^{252}Cf radioactive sources in the Z-axis of the detector. Runs with the very same conditions were simulated and the data/MC ratios in terms of the sources' energy peak positions were utterly deduced. Subsequently the dependence of these ratios with

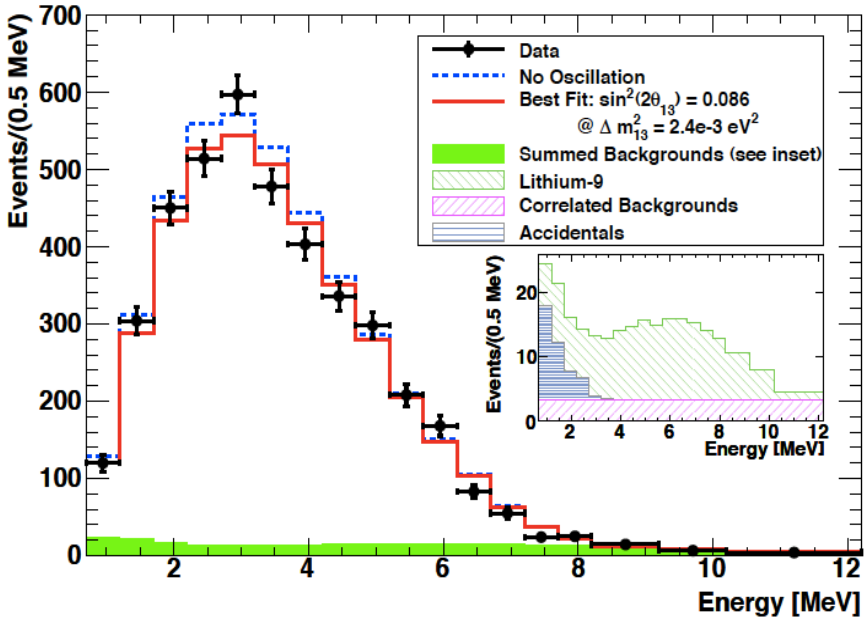

Figure 3.45: Final fit; rate plus shape analysis (prompt signal energy distribution).

energy and the z coordinate were disentangled through two empirical correction functions using totally six independent parameters. The $\rho = \sqrt{x^2 + y^2}$ dependence of the energy function was not taken into account in these correction prescriptions but work with spallation neutron captures showed that it is only subdominant. The detector covariance matrix was then determined through the mutli-sim method [222]. The uncorrected energy peak ratios versus energy and z are shown in fig. 3.43 and 3.44.

The minimization procedure constraining both the normalization and the spectrum of the signal gives a best fit for:

$$\sin^2(2\theta_{13}) = 0.086 \pm 0.041(\text{stat.}) \pm 0.030(\text{syst.}). \tag{3.18}$$

The fit is shown in fig. 3.45. The best fit has a $\chi^2 = 23.7$ and it is denoted with the red line. The non-oscillation scenario is shown in blue line. It corresponds to the weaker 26.6 χ^2 value. After 10 MeV the fit is totally dominated by the background as it was expected. The backgrounds are also shown in the box of fig. 3.45. The data minus the prediction residues are also shown in fig. 3.46. The curve that corresponds to the best fit value is shown in blue color. The pattern characteristic to neutrino oscillations is clearly visible.

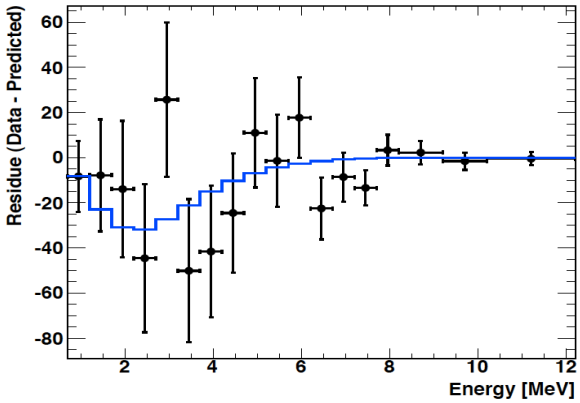

Figure 3.46: Data minus MC residues (Black points). In blue line it is overlapped the curve corresponding to the best fit.

Using a frequentist approach we find an allowed region of:

$$0.017 < \sin^2(2\theta_{13}) < 0.16 \tag{3.19}$$

at 90% C.L. and we exclude the absence of oscillations at a 94.6% C.L. Also a rate only analysis gives the result:

$$\sin^2(2\theta_{13}) = 0.10 \pm 0.04(\text{stat.}) \pm 0.08(\text{syst.}). \tag{3.20}$$

For more information and a detailed discussion on the various aspects regarding the analysis of the final fit(s) one might consult the dedicated internal note written by the final fit group [224].

And as we wind on down the road
Our shadows taller than our soul.
There walks a lady we all know
Who shines white light and wants to show
How everything still turns to gold.
And if you listen very hard
The tune will come to you at last.
When all is one and one is all
To be a rock and not to roll.

And she's buying a stairway to heaven...

Led Zeppelin

Part II

Inner Veto calibration

Chapter 4

The Inner Veto Light Injection system

4.1 Introduction, general description

As we already described in Section 3.7, the Double Chooz (DC) Inner Detector (ID) is monitored in a daily basis by the Inner Detector Light Injection system (ID-LI). The ID-LI is responsible for tracing detector instabilities and possible changes on the specific behavior of individual channels. Additionally, it can be used to further probe the detector performance and functioning. The artificial conditions under which these calibration runs are taken are very convenient from an analysis point of view as it has been frequently emphasized.

Just like the ID, the Inner Veto (IV) utilizes a similar calibration system to monitor its characteristics. Sticking to the same naming convention this device is called the Inner Veto Light Injection system (IV-LI). The hardware implementation of the IV-LI is rather different from that of the ID-LI but their conceptual designs are, in fact, quite similar. Briefly, the main purposes of both LI systems are to release light of known and tunable characteristics inside the ID and the IV respectively. The known profile of these data makes their analysis, and thus their interpretation, rather straightforward. In any case, these extra calibration runs provide us with an additional source of information for the detector of surmount importance.

The purpose and the design of the DC IV is such to identify particles or radiation that trigger the detector but originating from its exterior. This goal is not very ambitious. While the ID was optimized to reconstruct carefully the deposited energy and perform precise calorimetric measurements on the $\bar{\nu}_e$ spectrum, the IV demands a far smaller accuracy. At the underground

depths relevant for both (near and far) DC detectors the most important sources of background are cosmic muons, fast neutrons created by muons that near-miss the detector and gamma rays from the surrounding rocks. The main duty of the IV is to tag these events that could otherwise enter the detector and thus fake the neutrino selection. Loosely speaking, the IV will be used as an "on-off" system.

Nonetheless it is still extremely important, for the normal operation of the experiment, to ensure constantly that the IV is properly working in the desired level and in stable conditions. Furthermore since the IV information can be used, in the aid of the ID, to better understand some aspects of the background, e.g. to the muon track reconstruction, it is profitable to have the least a rough understanding of its response. All these objectives are fulfilled with the IV-LI.

The full list of items required from the IV-LI calibration runs is summarized below. In particular, the IV-LI is responsible to:

i. Extract the gain of every IV photomultiplier tube (PMT),

ii. Determine the offsets in the time response of all IV channels, and follow their possible changes as a function of time,

iii. Supervise the light transmission inside the liquid; namely the IV liquid scintillator, and finally,

iv. Monitor the light yield (LY) of the scintillator.

Gain measurements will be performed with weak light pulses analyzing charge liklelihoods at the so-called single photoelectron (SPE) spectrum. On the other hand, timing measurements can be most conveniently achieved with high intensity light, and like this they will be conducted. These high intensity runs will also be used to monitor the light transmission inside the liquid scintillator, comparing each time the number of photoelectrons detected. The LY of the scintillator will be probed with UV light (365 nm) that excites its molecules. Finally, through all these measurements we will be able to know whether a PMT is properly working or not.

In this chapter we will give a complete description of the hardware components, the optimization and the strategy of IV-LI system. The analysis of part of the IV-LI calibration runs will be given in the next chapter.

4.2 Inner Veto and Light Injectors

As a reminder, the IV is a cylindrical volume of roughly 7 m in height and diameter that surounds the ID in an essential way required for background re-

Figure 4.1: The Inner Veto PMT steel capsules (top) and the finally encapsulated PMT modules (bottom) [225].

jection. It is filled with liquid scintillator and it is instrumented with 78 PMTs to detect the deposited energy signals. The PMT model used in the IV is the 8-inches R1408 Hamamatsu phototube that in the past was also employed by the IMB experiment. Every PMT is placed inside a steel capsule that protects it from mechanical stresses, the earth's magnetic field and it isolates their base electronic circuits from the aggressive nature of the liquid scintillator. Some pictures of the protection capsules and the finally encapsulated PMTs are shown in Fig. 4.1(top) and (bottom). More information on the encapsulation procedure can be found in Ref. [225]. The rest of the electronics, the signal readout and digitization are those described in Section 3.5.3.

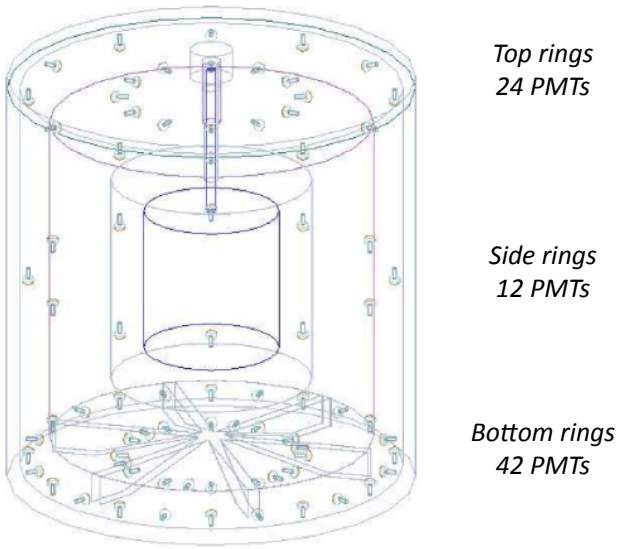

Figure 4.2: The Inner Veto PMT configuration and orientation. The three different groups of rings are labeled and clearly visible.

The IV PMTs are grouped in three different clusters of rings: the top, the side and the bottom rings, Fig. 4.2. The top rings occupy 24 of the total 78 PMTs, the side rings 12 and the bottom rings 42. This specific configuration was motivated by Monte-Carlo (MC) simulations. In particular, the excess of PMTs on the bottom of the IV was found to be rather beneficial to the muon track reconstruction, through a combination of the IV and Outer Veto (OV) information. The individual orientation of each PMT is not the same and it was also motivated by MC studies. To enhance the light collection, the IV wall was painted with a white, reflecting dye and the ID vessel exterior was covered with a VME2000 sheet.

In Fig. 4.2 the IV vessel and PMT configuration are shown. In the interior one can also see the vessels of the ID. Contrast to the ID, the IV geometry is such that would not allow us to obtain a precise calorimetric information no matter how well one could calibrate individual channels. The energy function will have a strong position dependence that is difficult to disentangle. Additionally, the reflections on the IV walls will destroy the uniform transmission of light in a very complicated way and no MC would be good enough to reproduce this. In the ID one could place a light source at the center and

Figure 4.3: The IV-LI LED board. 96 LEDs are grouped orthogonally in 8 12-plets.

illuminate all channels at once in (roughly) equal proportions. On the other hand, illuminating all channels of the IV in an equal manner, just at once, would not be so easy.

To send light evenly at all the IV channels, as required from the IV-LI, light injectors are attached on every single PMT. The light pulses necessary for these calibration runs are produced by a board of Light Emitting Diodes (LEDs, Fig. 4.3) installed outside the detector. The light is carried inside the IV through a network of quartz fibers. The LED board has 8×12 LEDs; 90 out of the 96 LEDs produce blue light (475 nm) while the remaining 6 illuminate in the UV region (365 nm). Blue light does not excite the scintillator and it will be used to study the light transmission and the attributes of individual PMTs. On the contrary, UV light excites the scintillator's molecules and will be used to survey its LY.

96 optical fibers of 25 m length are totally employed; that means that some PMTs carry more than one fiber. This is a redundancy decided clearly for safety reasons[1] but it can also serve as an additional pathway to cross-check the system's stability and proper functioning. Quartz fibers were chosen because of the plastic degradation in the liquid. The fiber model selected is the Thorlabs fiber BFH48–600 shown in Fig. 4.4 [226]. It is a high-OH,

[1]If one fiber will become somehow broken, the other one can still be utilized.

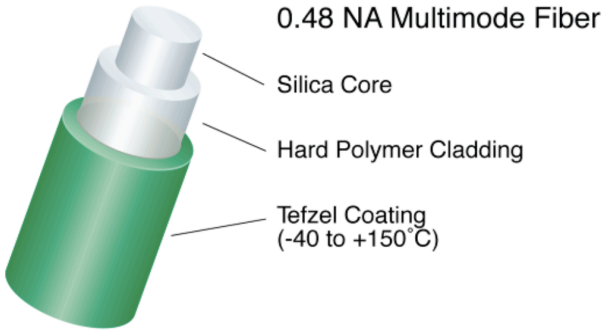

Figure 4.4: The quartz fibers utilized in the IV-LI.

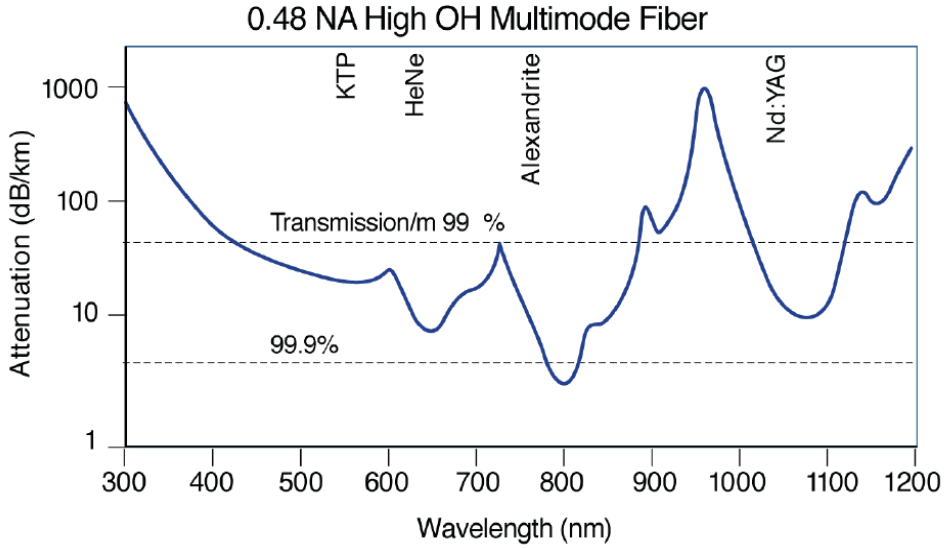

Figure 4.5: Attenuation of the quartz fibers versus the wavelength.

multimode fiber with a hard polymer cladding, that has very good transmission (around 99 % per meter in the visible region) and a large opening angle in liquid. It has an 1 mm outer diameter while the quartz core has a smaller diameter of 0.6 mm. In Fig. 4.5 we show the attenuation versus the light wavelength. The Numerical Aperture (NA) is 0.48±0.02 inducing an opening angle of 18^o in the liquid scintillator.

One of the major issues that had to be addressed was the compatibility of the decided fiber model with the IV liquid scintillator. Namely, whether the fiber's performance could be destroyed by the scintillator or vice versa. That was carefully tested and followed for more than one year without observing any degradation of the fiber or of the scintillator transmission. For instance,

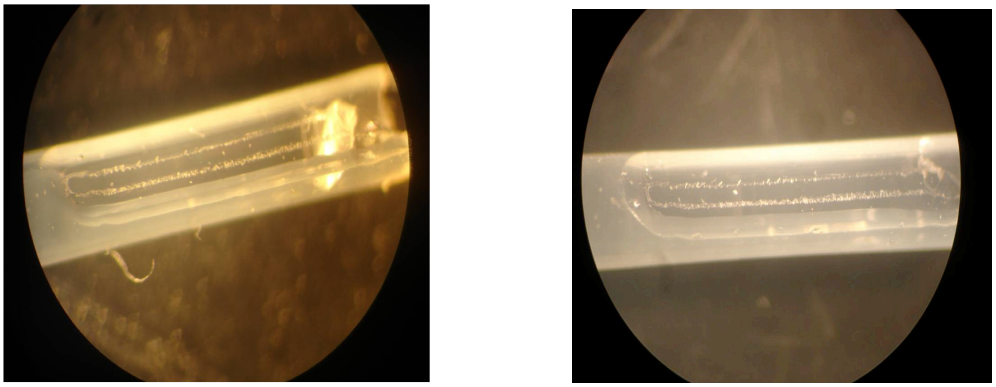

Figure 4.6: Photographs of a Thorlabs BFH48–600 fiber before (left) and after (right) its immersion in IV liquid scintillator for a period of five weeks. The cladding remained intact showing no serious effects of the scintillator on the quartz fibers.

in Fig. 4.6 one could see photographs of a fiber taken with a microscope before (left) and after (right) its immersion in liquid scintillator. The cladding remained intact signaling that no serious damages could happen on the optical fibers from the liquid scintillator. In Fig. 4.7 we also show the light transmission versus the wavelength in three samples of IV scintillator. One pure sample of liquid scintillator, another with a quartz fiber immersed in it and a last one with a wavelength-shifting fiber in it. These measurements were done with a precision spectrometer. As it is readily seen there are no serious differences between these three different curves.

4.3 Design of the Light Injection system

The LED board of the IV-LI (Fig. 4.3) necessary to create the light pulses needed for calibration is placed in a box located outside the detector between the splitter boxes, Fig. 4.8. Of course it is very important for the normal operation of the system and the detector itself this box to be light-tight since otherwise light will enter the detector through the fibers introducing noise. The 96 quartz fibers are glued onto the LED board vertically and are driven outside the IV-LI box and inside the detector. In Fig. 4.9 we show the IV-LI box open in the period where the fibers were attached on the LED board.

The quartz fibers are grouped in 6 assemblies of roughly 16 fibers each and exit the IV-LI box in two black, plastic tubes placed one inside the other.

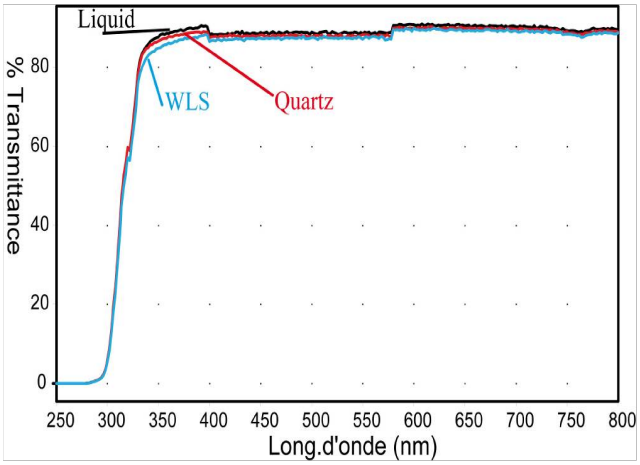

Figure 4.7: Light transmission versus wavelength in three samples of IV scintillator. One pure liquid sample used as reference (black), another with a quartz fiber immersed in it (red) and a third one with a wavelength-shifting fiber immersed in it (cyan).

Figure 4.8: The IV-LI box between splitter boxes 2 and 3.

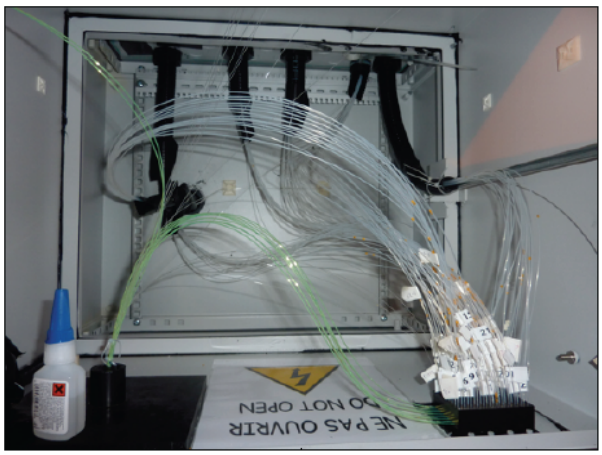

Figure 4.9: All quartz fibers are attached onto the LED board vertically and exit the detector in 6 assembled bundles through black, plastic tubes.

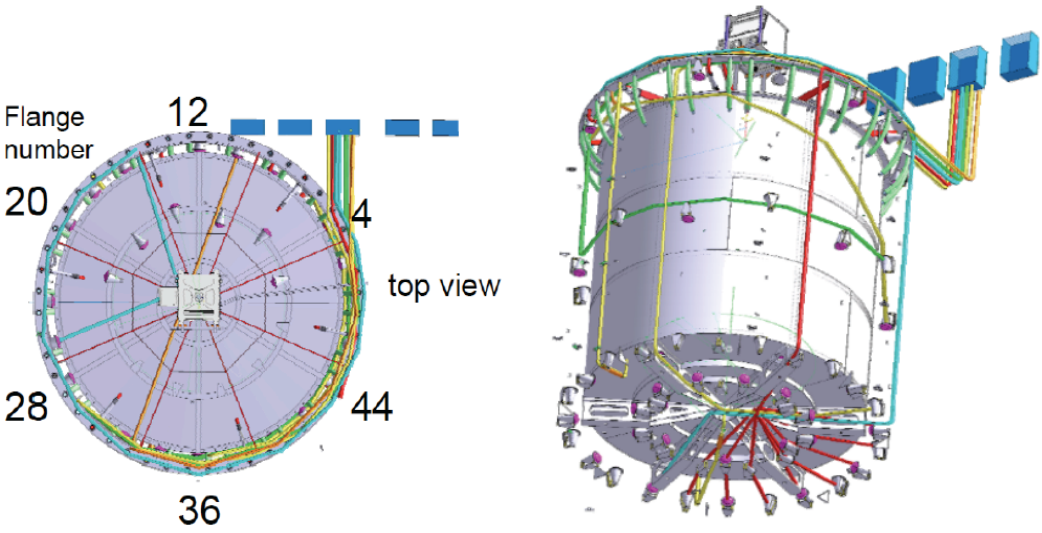

Figure 4.10: Two figures of the IV-LI fiber distribution indicating the flanges through which the fibers penetrate inside the detector.

The innermost tube with the smaller diameter is ensuring the light-tightness while the external one (more robust) protects the fibers. In Fig. 4.9 one could see the 6 bundles exiting the back of the box in the black tubes.

The plastic tubes enter the detector through the six flanges used also by the IV PMT cables. Two simulation sketches of the fiber distribution and rooting are shown in Fig. 4.10 (left) and (right). For instance, in Fig. 4.10 (left) we show a top view of the detector indicating the numbers and the po-

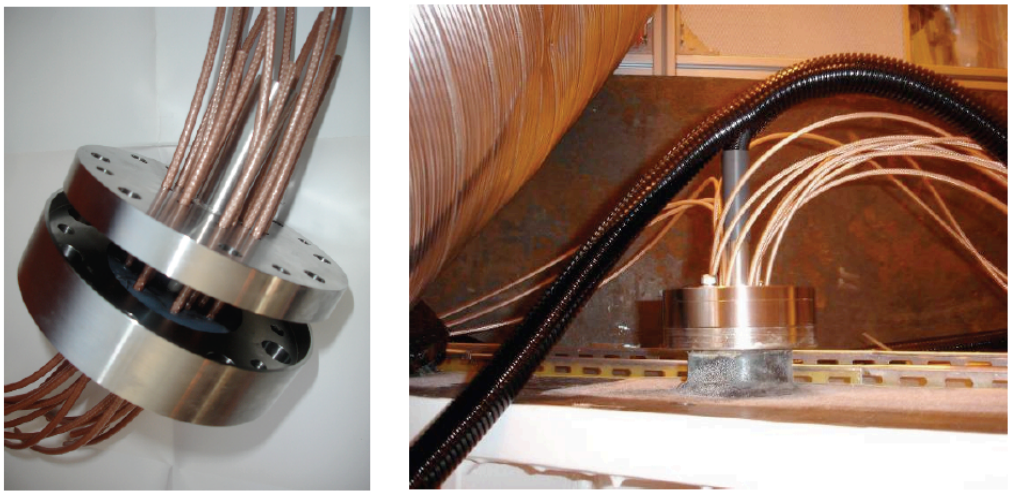

Figure 4.11: The IV flange (left). The teflon tube containing the quartz fibers is placed at the middle of the PMT cables. The fibers are protected by a double black tube (right).

sitions of the 6 IV flanges used to pass the cables and fibers into the detector. At the level of the flanges, particular care has been taken by applying black sikaflex to avoid any light leaks. Inside the flanges, the fibers pass through a narrow Teflon tube sealed with epoxy to avoid air getting inside the detector, Fig. 4.11.

Inside the IV the fibers are attached on the PMT capsules equator as seen in Fig. 4.12. For this to happen mechanical supports, made from stainless steel, have been constructed that can be screwed on the PMT capsules. The fibers are then inserted in the supports with a small teflon tube for their additional protection. In this configuration a single fiber that gets activated can illuminate the neighboring PMTs that are not that distant, but also the same PMT that carries the fiber receives some light by diffusion. The orientation of the fibers was chosen so that the performance of the IV-LI becomes maximal (A single fiber can illuminate as many PMTs as possible and all PMTs can be illuminated by at least two optical fibers). Some PMTs carry two optical fibers. In these cases the fibers can look at the same, Fig. 4.12 (left), or at opposite directions, Fig. 4.12 (right). The LED number - PMT correspondence can be found in [227].

All the LEDs are driven by a fast pulse generator Agilent 81150A through 96 switches (Fig. 4.13). The switches are controlled through a PCI bus Digital IO card Adlink 7296 implemented in a PC located next to the IV-LI box. The communication between the PC, the switches and the generator is

Figure 4.12: Fibers attached in the IV PMTs. Two examples of PMTs carrying two fibers (each) pointing in the same (left) and in opposite (right) directions.

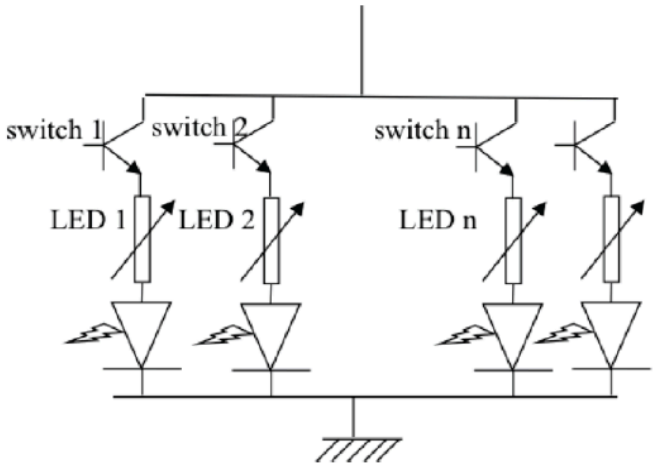

Figure 4.13: Schematic view of the IV-LI switches.

done by LabVIEW running on the IV-LI PC. The LabVIEW session communicates with the DCCALIB server which sends to the IV-LI system several parameters (pulse height, delays, pattern of LEDs to be switched on etc.).

While it is possible to switch on several LEDs, this is not recommended because, for the same generator pulse height, the amount of light emitted depends on the number of pulsed LEDs because of the limited current provided by the generator (for more than 10 LEDs switched on, no light emission is observed anymore). The LED amount of light (even if only one LED is

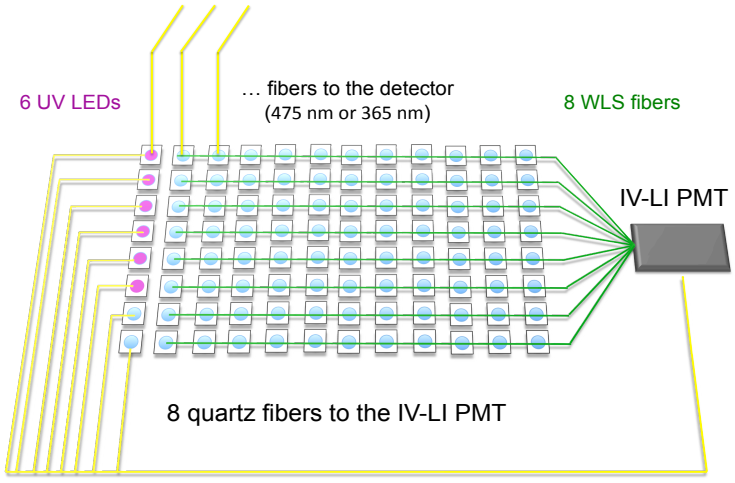

Figure 4.14: Schematic view of the IV-LI system.

switched on) depends also on the flashing rate because of the dependency of the light amount and the LED temperature. For this reason, it is strongly recommended that the IV-LI system be operated at constant rate.

To supervise the stability and the general performance of the IV-LI system a smaller, 2-inches PMT is also utilized. This extra PMT is installed inside the IV-LI box. Since, it will be used to monitor the IV-LI it is called the monitoring or reference PMT. One of its basic duties will be to cross-check the performance of the light injectors and confirm that they are functioning in the desired level. For this to happen 8 green wavelength shifting fibers (WLS, Kuraray Y11), placed over the LED board in the way shown in Fig. 4.14, are directed into the monitoring PMT. When an LED is activated by the pulse generator some light is carried inside the IV by the quartz fibers but another portion ends up to the monitoring PMT. In this way, one could tell immediately whether the LEDs are actually functioning or there is a problem in the IV. Instability issues could also be traced. Additionally, the monitoring PMT could be used for timing calibration studies.

To track possible aging effects on the WLS fibers, 8 quartz fibers are at the same time directed from the LEDs matrix to the monitoring PMT, Fig. 4.14. The green WLS fibers can also be seen in Fig. 4.9. A picture summarizing the main components in the IV-LI box is shown in Fig. 4.15.

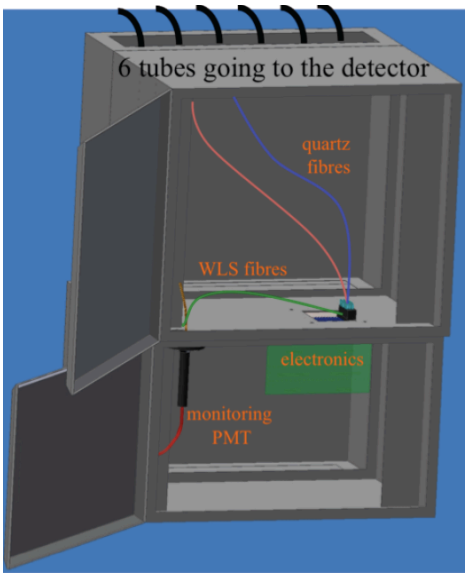

Figure 4.15: A picture summarizing the main ingredients of the IV-LI system.

4.4 Installation of the IV-LI system

The installation of the IV-LI system took place from February 2009 to June 2010 parallel with the installation of the IV itself. The positioning of the IV-LI fibers was done in two phases following the construction of the ID. First the bottom and side PMT ring fibers were placed and afterwards (after the completion of the ID) the top ring fibers were also placed. In the same periods the IV PMTs were also installed. Prior to this, all PMTs were tested with part of the IV-LI setup prepared for this purpose.

The IV-LI box containing the LED matrix, the fibers arriving from the IV, the monitoring PMT and the LED electronics is located between the splitter boxes 2 and 3. The HV of the IV monitoring PMT, having a nominal value of +1800 V, is provided by splitter 5 of splitter box 3, next to the IV-LI box. The signal of this PMT is first sent to an amplifier in the electronics hut and after to a channel of the FADCs as all other IV PMTs. The PC that controls the IV-LI and the generator that creates the light signals on the LEDs are placed on both sides of the IV-LI box. The calibration box is shown in Fig. 4.8. In this photograph one could notice the PC driving the IV-LI; the black box seen at one side of the box. The pulse generator is at the other side of the box and it is not visible.

The length of the signal cable of the IV monitoring PMT is 30.0+52.7 m in order its signal to arrive at more or less the same time than the signals of all IV PMT's and thus use the same integration gate for all IV signals. A trigger

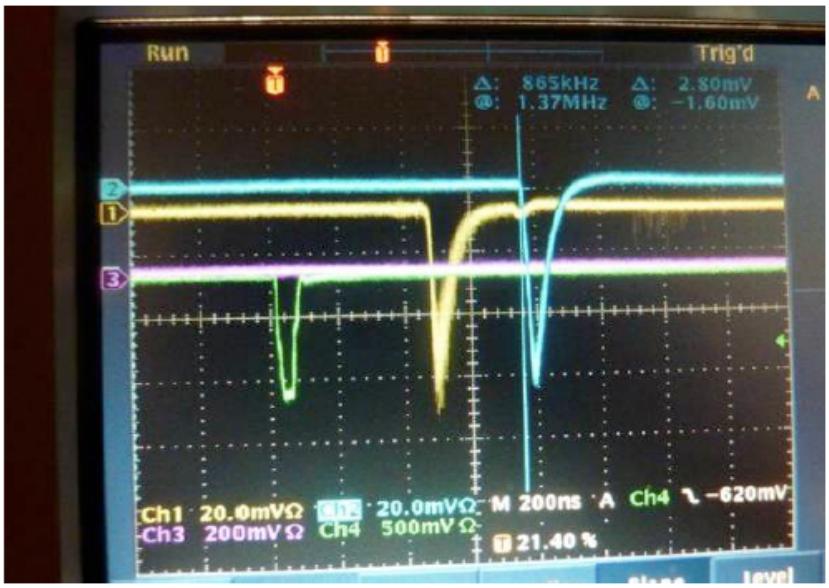

Figure 4.16: Signals observed on an oscilloscope for timing purposes. The green one is the trigger signal coming from the IV pulse generator delayed by 300 ns compared to the signal sent to the LEDs. The yellow signal is the one of the monitoring IV PMT while the blue one is the signal coming from an IV PMT. There is a delay of 300 ns between these last two signals. In order they arrive at the same time a 52.7 m cable has been added on the IV monitoring PMT.

is sent by the IV pulse generator to the DAQ through a 20.0 m cable. Fig. 4.16 presents the signals of the trigger sent by the generator, of the monitoring PMT and one IV PMT before full timing alignment. The pulse sent to the LEDs was delayed by 300 ns compared to the trigger signal. A delay of 300 ns is observed between the IV monitoring PMT signal and the one coming from the IV PMT. Adding a 52.7 m cable on the monitoring PMT signal has compensated this. The position of the pulse generator trigger can be placed anywhere by playing with the generator delay (controlled remotely). Fig. 4.17 summarizes the cable and timing situation.

4.5 Data taking procedure(s)

The data taking is controlled through a network server called DCCalibServer. The communication with the DCCalibServer is done through LabVIEW running on the IV-LI PC. The LabVIEW program runs permanently waiting to receive commands from the DCCalibServer.

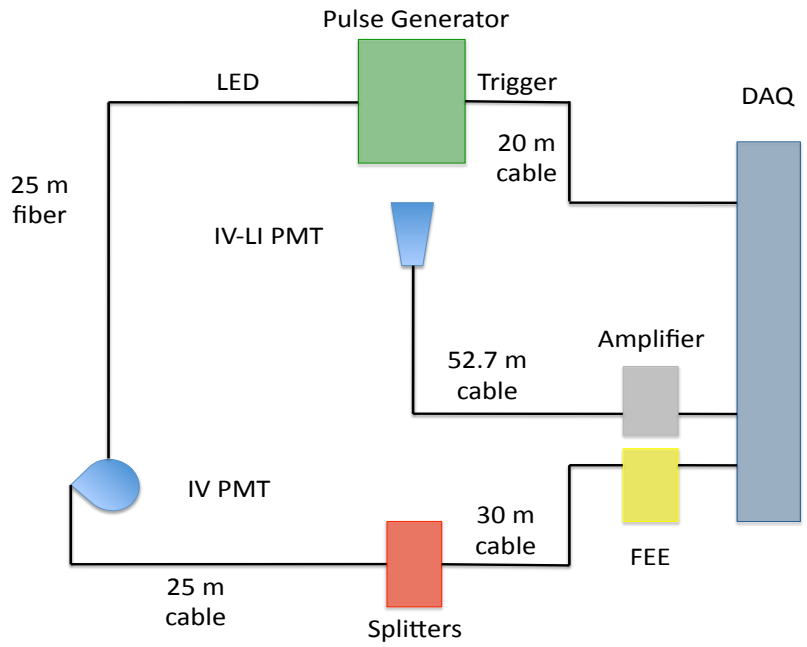

Figure 4.17: Schematic view of the IV-LI connections.

After starting the communication, the IV-LI system receives a set of parameters to be sent to the pulse generator to define the pulse height, width and rise time, the pulse delay compared to the trigger and the pulsing rate. To indicate the LED pattern to be switched on, 3 bitted words (1 bit per LED) are sent (LED1, LED2, LED3). Here is an example of the configuration file used to pulse LED 62:

```
!cd DCCALIB_RUN_IVLI_LED62_D1

RUN_DESCRIPTION :Calibration default run with IDLI (LED channel = 62)

RUN_LENGTH : 300

DCNUDAQ_ENABLE : ON

DCMUDAQ_ENABLE : OFF

DCOVDAQ_ENABLE : OFF

DCIVLI_ENABLE : ON
```

```
DCIVLI_FLASHRATE 20 #Hz

DCIVLI_DELAY 300 #nsec

DCIVLI_RISETIME 2.5 #nsec

DCIVLI_DURATION 50 #nsec

DCIVLI_HEIGHT 2500 #mV

DCIVLI_LED1 0 : 0x0

DCIVLI_LED2 1073741824 : 0x40000000

DCIVLI_LED3 0 : 0x0

!cd
```

At the start of the IV-LI system data taking LabVIEW sends to DCCalibServer "DCIVLI". When the DCCalibServer is ready to start it answers by "DCCALIBSERVER" and sends all relevant parameters. The IV-LI system enters an infinite loop and sends back "PREPARING" followed by the parameters received before for verification. The LED pattern is sent to the PCI card. DCCalibServer sends "READY" and IV-LI answers "READY" too. At that moment IV-LI waits for a "START" after which it answers "STARTING", sends the parameters to the generator and answers back "STARTED DCIVLI". The two generator outputs (channels 1 for pulsing the LEDs and channel 2 for triggering) are activated, pulse at the specified frequency and IV-LI waits a "STOP". After receiving the "STOP" it replies by "STOPPING" and by "STOPPED" after deactivating the two generator outputs.

While connecting to the IV-LI PC if LabVIEW is not running, one has to start communicationDCalibserverV1R1P1.vi (in folder chooz on the desktop) by double clicking on it. If everything goes well Fig. 4.18 must appear on the screen. This screen shows everything received by the system coming from DCCalibServer. At this moment one can start the system by running the vi. By also opening Allumage_96_leds.vi (without running it) on can better watch the status of the 96 LEDs (Fig. 4.19).

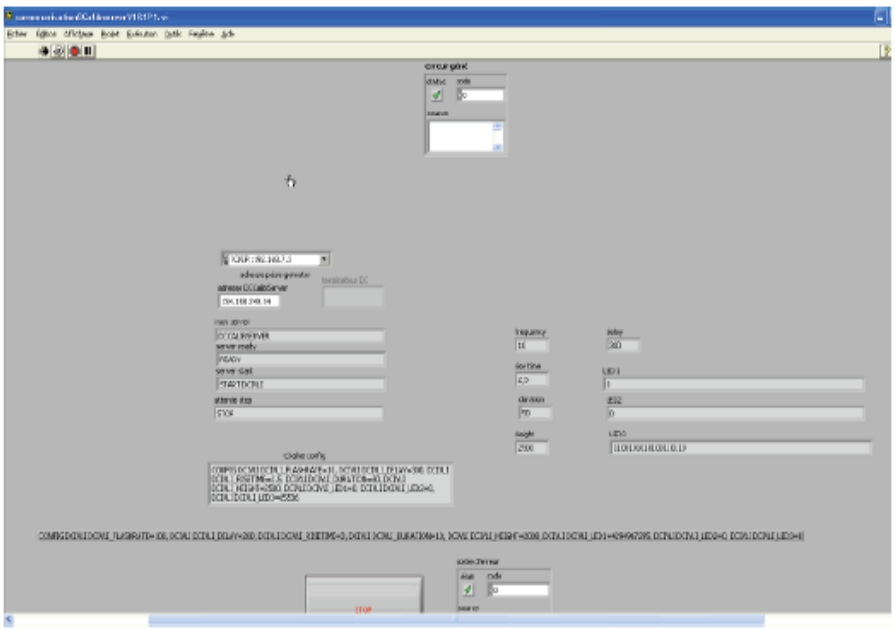

Figure 4.18: LabVIEW vi controlling the IV-LI system.

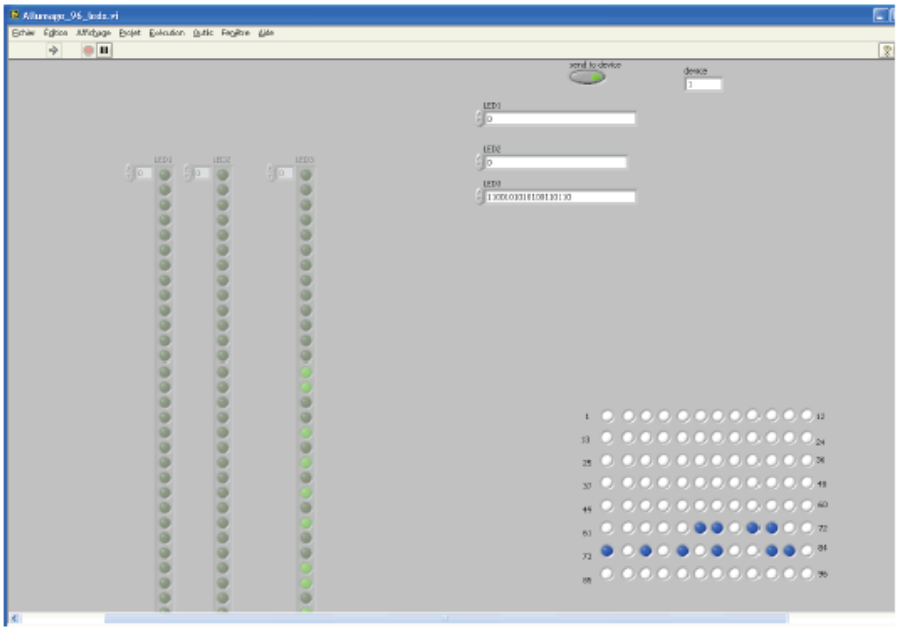

Figure 4.19: LabVIEW vi showing the status of all LEDs.

Figure 4.20: Pulse generator web control.

The pulse generator can be controlled remotely using a web browser and by going to page:

`http://192.168.7.3/index.html`

home page of windows explorer on dcfivli. To watch or modify the generator parameters one has to click on "Browser web control". At that moment one will see exactly what is in the front panel of the generator (Fig. 4.20).

4.6 Commissioning and running conditions

The IV-LI took data in August 2010 for the first time. It was the first system that operated in the DC detector. Since then it helped critically to debug the DAQ system and to understand various aspects of the detector and electronics. During the detector filling, the IV-LI was inactive since a red laser, used to monitor the liquid level of the IV, was then operating and that would have been dangerous for the PMTs.

IV-LI resumed operations after the successful detector filling in January and February 2011. In that period a big amount of data, with various LED intensities, was taken. All LEDs were exercised. From the analysis of these data sets, two running configurations were extracted; the so-called D19 and D20 configurations. The D19 configuration illuminates the IV channels in a way that most PMTs receive light of less than one photoelectron mean and they are used for gain measurements. On the other hand, D20 is a high intensity mode and it is used for timing calibration and for probing the

light transmission in the scintillator. D20 runs with UV LEDs are used for monitoring the scintillator light yield.

These two running modes are optimal in the sense that although a small number of fibers are activated the number of PMTs that receive light, in the desired regions, is maximal. Currently, the D19 and D20 calibration runs are being performed once per week.

Chapter 5

Inner Veto gain calibration

5.1 Introduction

In this Chapter we shall summarize the efforts pursued for the calibration of the charge response of the Inner Veto (IV) photomultiplier tubes (PMTs). We will elaborate on laboratory and on-site measurements. More precisely, we will present the strategy and the method chosen for the IV PMTs gain determination and we will lay down the mathematical model developed to parametrize the PMTs charge response. We will then report on the analyses of data taken at Strasbourg using an IV PMT but also on the pre-installation tests conducted at Chooz. We will conclude with the treatment of the gain calibration runs taken regularly at Chooz roughly every week.

The analysis method we shall put forward for gain determination leans on an influential paper written by E. H. Bellamy and collaborators in 1994 [228]. In this work, a refined procedure is presented that can be used to deconvolute successfully the charge distribution of a PMT in the single photoelectron mode through a simple but sophisticated statistical analysis of the photomultiplier spectra from a pulsed light source. This deconvolution gives access to the main parameters of the process as the PMT gain and the mean number of recorded photoelectrons.

What makes this approach appealing is that the actual knowledge of the light source characteristics is not at all essential to the method; they should only be fixed and square. The only ingredient required is a mathematical scheme that models, in a realistic way, the response spectra of the PMTs when illuminated with such light pulses. The model can then be applied to real spectra taken under these conditions and extract both the gain and all the relevant attributes of the light source with the use of a minimization package (for instance Minuit [229]).

The phototubes analyzed in the aforementioned publication fulfill the conditions sufficient to approximate their single photoelectron (SPE) response by a carefully weighted gaussian distribution. These cases are indeed easy to handle mainly for two reasons. First, the various photoelectron peaks are easy to discriminate since they can be very well approximated by gaussian functions displaced from the pedestal over normal steps. Second, and what is even more important, the mathematics involved are rather elementary so that the model can be solved and written down analytically. The resulting function is capable to analyze a broad spectrum of photomultipliers in a straightforward and elegant manner. The utility of the model has been explored time and again in the literature; therein lies its very success.

The fine work of Bellamy *et al.* is lucidly described in a very renowned and ever-cited publication [228]. We would like to stress from the onset that even though our approach deviates from that of Bellamy in its starting point, the gross features are common to both efforts. The resulting parametric solutions might be emphatically different but the spirit and methodology are strictly the same. In what follows we shall describe the details of our approach which are essentially those of Bellamy. The reader should not have a problem to realize that we do follow the path taken by Bellamy *et al.* modified only for our purposes.

5.2 A model for the Inner Veto photomultipliers response

5.2.1 Single Electron Charge Amplification

In modeling the response of a PMT one is usually forced to postulate a distribution function for the SPE charge deposition (the extraction of a detailed distribution taking into account all multiplication stages in the dynodes is very complicated, and assumes a very good knowledge of all multiplication parameters). That is, when an electron enters the multiplicative dynode structure the law for the charge amplification is not at all deterministic but, on the contrary, follows from a probability distribution function (pdf). This distribution is characteristic of the PMT and the voltage sharing among its dynodes. In what follows it shall be termed by $S(x)$. $S(x)dx$ gives the probability to collect an amount of charge between x and $x + dx$ in the output

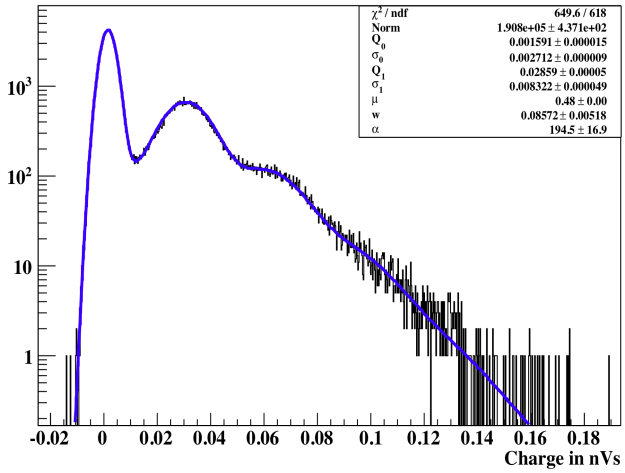

Figure 5.1: Single photoelectron (SPE) spectrum for the Hamamatsu R7081 PMT. The blue line depicts the parametric à-la-Bellamy response function.

of the PMT whenever a single electron is released from the photocathode[1]. $S(x)$ is normalized in the usual sense:

$$\int_{-\infty}^{+\infty} S(x)\, dx \;=\; 1, \tag{5.1}$$

and it is further assumed that its statistical moments are all well defined.

In calibrating and monitoring PMTs, different types of functions are used depending, each time, on the PMT under examination. For example, in the Double Chooz (DC) experiment the sensitive area of the detector is monitored by the presence of 390 PMTs distributed over a 4π solid angle. The PMT model that met the requirements set by the collaboration (good performance and charge resolution, low radioactivity glass, suitable weight and dimensions, etc.) was the 10-inches Hamamatsu R7081 phototube [197]. The gain determination of these PMTs can be done in an elementary way, based on the method presented in the Bellamy paper with essentially no modifications. The analysis is easy to carry and yields results within the desired accuracy. In Fig. 5.1 one can see how the multi-convolutioned sum of gaussians can indeed account for the low-light response of the R7801 PMT. The smallness of χ^2/ndof compel us to admit that the starting guess of the gaussian distribution as the amplification law (while not physical because it could lead to negative charges) is indeed validated.

[1]For the moment we shall ignore dark current.

In contrast to the Inner Detector (ID) PMTs, the 8-inches R1408 Hamamatsu phototubes that are used in the IV do not show a sharp peak in the SPE distributions as one would expect or even require[2] . This fact actually draws us away from the original Bellamy treatment since their response spectra cannot be modeled with the use of a simple gaussian function. Cases like these are remarkable difficult to treat since the elegant features that make Bellamy's approach so cherished are now plainly lost. More precisely:

i. the mathematics involved are, as we shall see, not at all trivial and,

ii. even if we succeed and finally tame the mathematical model, the elegant view of the various photoelectron peaks (as for example in Fig. 5.1) is now lost.

One cannot be 100% confident that the model extracts the right information or it just conspires to provide a falsified result. The big dispersion in charge for each photoelectron creates a very broad and complicated distribution.

Actually these PMTs[3] are not good for counting photoelectrons. This is not as dramatic as it sounds since for the purposes of the IV we do not want to reconstruct the deposited energy in the scintillator. The main task of the IV is less demanding: to tag the high energetic particles (mostly muons and fast neutrons) that cross the surrounding environment and enter the detector. For this aim a rough estimate is fine and adequate.

To treat these IV PMTs other techniques could be devised. Nevertheless, we shall stick to Bellamy *et al.* as much as we can even though we know that a pedantic treatment is not required nor demanded by the DC collaboration. We believe that this approach is more appropriate for the purposes of the IV calibration system. By the end of this Chapter we shall see how far can we go and whether or how we can trust our results.

We shall treat two distinct models, one based on an exponential distribution and another one based on a gamma distribution. As we shall see these schemes are inter-connected. Nevertheless we shall treat them as they were independent. Part of this decision is motivated because the final solutions we obtain are emphatically so different that it is justified to present them as they were unrelated. We would also like to compare these two models with real data so it would be convenient to have them separated in our minds. We start with the more common exponential distribution and afterwards we shall pass to the more sophisticated gamma distribution.

[2]It has been argued that this fact results from the "venetian blind" dynode structure. See for example [230].

[3]That in the past gloriously saw the Supernova 1987A in the heart of the IMB detector.

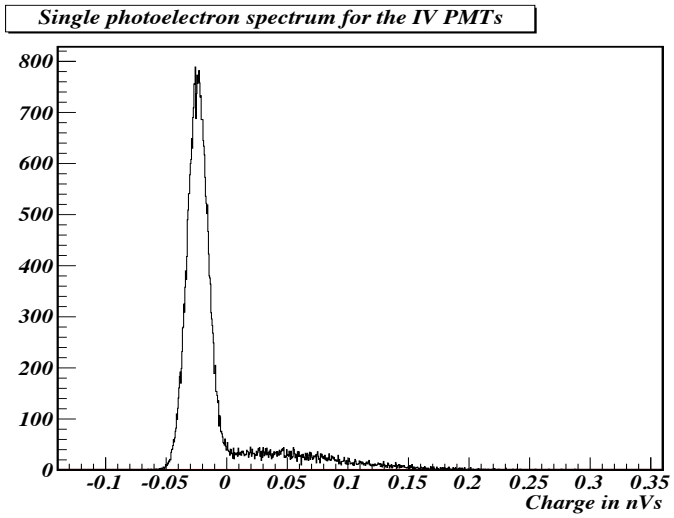

Figure 5.2: Single photoelectron spectrum of the Inner Veto Hamamatsu R1408 photomutipliers.

5.2.2 Exponential distribution

Looking at the spectrum of the R1408 PMTs around the single photoelectron (SPE spectrum), Fig. 5.2, one thing is readily understood: whatever the law of charge amplification is this can not be modeled with a simple gaussian function. Furthermore, we see that this distribution does not exhibit a clear "bump" so that one could have an idea of the SPE distribution mean value.

The signal shape (the tail after the pedestal) in Fig. 5.2 tempts us to relate the amplification process with an exponentially falling distribution. Let us try a pure exponential function of the form:

$$S(x) = \lambda\, e^{-\lambda x}\ \Theta(x), \tag{5.2}$$

where $\Theta(x)$ is the common Heavyside unit step function to avoid unphysical negative charges.

$$\Theta(x) = \begin{cases} 0, & x < 0 \quad \text{and,} \\ 1, & x \geq 0 \end{cases} \tag{5.3}$$

This function is indeed normalized and has mean value and standard deviation equal to:

$$\mu_1 = \frac{1}{\lambda}, \tag{5.4}$$

and:

$$\sigma = \frac{1}{\lambda}. \tag{5.5}$$

We shall use the symbol μ_n to denote the n-th order statistical moment. Whenever ambiguities might arise we may use the alternative symbolism:

$$E[x, S(x)] = \int_{-\infty}^{+\infty} x\ S(x)\ dx. \tag{5.6}$$

Of course, it should be obvious that:

$$\mu_n = E[x^n, S(x)]. \tag{5.7}$$

As we shall see in what follows, the model that results from (5.2) following the Bellamy analysis, is applicable to a limited number of cases and thus it is unsatisfactory since it lacks the required generality.

Nonetheless, we have moreover two important reasons for believing that the choice of an exponential distribution is inadequate for modeling the SPE amplification process. First, the choice of (5.2) assumes a specific relation between the mean value and the standard deviation of the pdf, namely that they should be equal. We believe that we have no right to assert that this specific relation holds from the onset unless this is confirmed by the data. Second, and what is even more serious, the choice of a pure exponential pdf cynically states that when an electron is subjected to the dynode system, the possibility to create zero charge, that is not to be amplified at all and just disappear, is maximal and in fact equal to the maximum of the pdf. This is, according to our belief, an empty statement.

To remedy these defects it seems almost necessary to seek for another distribution that could possibly account for the exponential-like decay tail of Fig 5.2. One tempting candidate is the gamma distribution:

$$S(x) = \lambda(1+\theta)\frac{[\lambda(1+\theta)x]^{\theta}}{\Gamma(1+\theta)}\ e^{-\lambda(1+\theta)x}\ \Theta(x) \tag{5.8}$$

In this guise, the gamma distribution is also known in the physics vocabulary as the Polya distribution. Physicists understood the utility of this function in the 60's or 70's in connection with the then newly discovered multiwire gas chambers. From (5.8) it is obvious that when $\theta = 0$ gamma distribution degenerates into a pure exponential; our initial guess. In this respect gamma distribution is more general since it automatically contains the exponential as a special case when θ is set to zero. Also it is shown to be devoid of the two defects that plague the exponential pdf.

Since the mathematical features of (5.8) are not common to physicists, as for example those of a gaussian pdf, it would be advisable to digress a little bit and describe the pure mathematical properties of the gamma distribution. We believe that a clear exposition to the mathematical facets of this latter choice will not only help us comprehend its merits but can also guide us in the interpretation of our results.

5.2.3 Gamma distribution

We might invent a number of reasons why the IMB phototubes amplify photoelectrons according to this distribution, but we shall not enter this discussion. On the contrary our attitude towards this problem shall be rather pragmatic. We shall take Eq. (5.8) as the starting point of our model and we plan to explore whether this assumption is validated by the experimental data.

With these thoughts in mind we shall lay down the pure mathematical reasons that are in favor of this latter amplification law. The first one comes from the simple observation that gamma pdf (5.8) has mean value equal to that of the exponential, Eq. (5.4),

$$\mu_1 = \frac{1}{\lambda} \tag{5.9}$$

but standard deviation modified by the the additional parameter θ.

$$\sigma = \frac{1}{\lambda\sqrt{(1+\theta)}} \tag{5.10}$$

From a pure mathematical standpoint this is highly satisfactory since we have previously argued that the exponential function-form, having equal mean value and standard deviation, is somehow restrictive. The presence of this extra θ parameter introduces additional degrees of freedom in the model and this fact is amply reflected in Eq. (5.10). Of course if some of our PMTs, due to fluctuations in their characteristics, prefer the more narrow exponential function to characterize their amplification chain then a direct application of the gamma model should result an extracted θ parameter approximately equal to zero. Again we see that gamma distribution is more flexible.

The second argument in favor of a gamma pdf comes from the fact that when $x = 0$ it returns a value equal to zero, $S(x = 0) = 0$, as is readily seen by (5.8). This is in marked difference with the exponential case. We expect on physical grounds that when an electron is driven inside the dynode structure then the possibility to produce zero charge should be small, close to

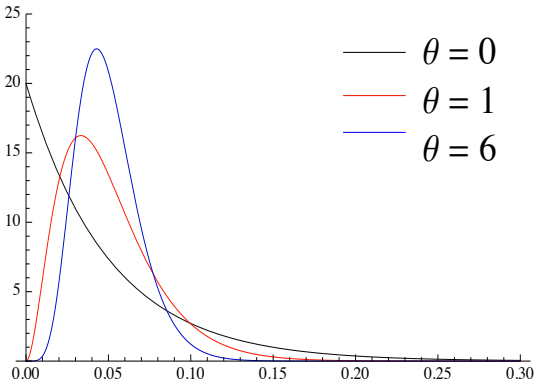

Figure 5.3: Polya distribution for three different values of θ and λ=20.

zero. Actually the inability of an exponential function to fulfill this criterion was recognized as a serious drawback for the resulting model. In this respect, we see that gamma pdf has the required mathematical properties necessary for our model business; it does not share these two defects that disfavor exponential pdf.

To get a further insight into the model that we are about to present, it would be profitable to take a few lines and examine the function-form of gamma function for some generic values of θ. Even without a detailed plot of (5.8) we can get a feeling of its shape with the help of equations (5.9) and (5.10). First, suppose that $\theta = 0$. In this case gamma pdf degenerates into an exponential as required by the analytical equations of the two models.

When θ starts to become different than zero then the variance of the distribution becomes smaller as is seen in (5.10), so that the shape of the distribution becomes narrower and taller (of course the total normalization remains equal to one). As θ grows more and more, gamma function becomes more narrower and more taller obtaining a gaussian-like peak. Nevertheless, since the mean value and the maximum of the pdf do not coincide we expect that gamma function will not be symmetrical, as for example the simple gaussian pdf. In the limiting case where $\theta \to +\infty$ the variance becomes exactly zero and the distribution becomes a Dirac delta function. All these can be verified by the plots of Fig. 5.3.

Up to now he have presented two distributions that can be used for modeling the SPE spectrum of the R1408 Hamamatsu PMTs, exponential and gamma. We of course pointed out the superiority of the gamma model for this purpose and also demonstrated its generality. In the next sections we shall treat these models in more detail. We might equally say that we only

consider one and-the-same model but with two separate sub-cases: when θ is free to move in the parametric space and when θ is fixed to zero.

5.2.4 Poisson Photoproduction

When light pulses stable in time, created for example by a laser or a light-emitting diode (LED), hit the photocathode, there is a certain probability for electrons to be produced (external photoelectric effect). This process is related to quantum efficiency (QE) and radiant sensitivity of the photocathode [231]. The probability for n photoelectrons to be created is governed by a Poisson distribution, of mean value μ, so that the probability for n photoelectrons to be released is given by the Poisson formula:

$$P(n,\mu) = \frac{\mu^n}{n!}\, e^{-\mu}. \tag{5.11}$$

$P(1,\mu)$ is the probability for a single electron emission, $P(2,\mu)$ for two, and so on. $P(n,\mu)$ is normalized in the following sense:

$$\sum_{n=0}^{\infty} P(n,\mu) = 1, \tag{5.12}$$

so that the total probability sums up to one, as one would expect from purely theoretical grounds. The probability that the light pulse will produce no electrons is different from zero and in fact equals to $P(0,\mu) = e^{-\mu}$ (just counting the "zero" cases gives a direct access to the mean value μ, the only poisson parameter).

After photoconversion, the electrons are accelerated, focused and subjected to the multiplicative dynode structure. It is a well-known fact that only a portion of the released photoelectrons survives this secondary process and finally enters the amplification chain. The probability for the photoelectrons to reach the first dynode is called collection efficiency (CE) and usually denoted as η. As is carefully explained in Chirikov-Zorin *et al.* [232] this secondary collection process follows a random binary distribution that modifies the initial Poisson mean by $\mu \to \mu \cdot \eta$. In what follows we shall attach Eq. (5.11) to the ability of a light pulse to create photoelectrons. Nevertheless, we must never forget, that μ is the modified mean according to the collection efficiency and thus characterizes jointly both the light pulse and the quantum and collection efficiencies.

With these remarks in the back of our minds let us now ask ourselves the following question: What will be the combined probability for a light pulse described by (5.11) to produce an electron that will afterwards deposit an

amount of charge between x and $x+dx$? The answer is straightforward from our previous analysis. The total probability is just the product of the two separate probabilities.

$$P(1,\mu)S(x)dx \tag{5.13}$$

Let us repeat this question but for the case of a two photoelectron emission. So, what will be the combined probability for this light pulse to produce two electrons that will afterwards deposit an amount of charge between x and $x+dx$? The answer turns out to be not that obvious at all.

To this end we shall further assume that we are well under the PMT's saturation point. In this case the whole procedure is linear and the charge we finally collect is given just by the sum of the charges that each photoelectron produces individually. In such cases the total probability is given by the convolution of the two initial pdfs. That is, the two photoelectrons are amplified according to the probability distribution $S_2(x)$ where:

$$S_2(x) = (S * S)(x). \tag{5.14}$$

Of course the convolution of two functions stems from the well-known mathematical formula.

$$(f*g)(x) = \int_{-\infty}^{+\infty} f(\tau)g(x-\tau)\ d\tau = \int_{-\infty}^{+\infty} f(x-\tau)g(\tau)\ d\tau \tag{5.15}$$

Similar arguments hold for the case of three electrons, four electrons, and so forth. The answer to our second question can be written down and is a simple generalization of our first result.

$$P(2,\mu)\ S_2(x). \tag{5.16}$$

To complete the answer $S_2(x)$ must be derived.

For the case of the gamma single electron charge distribution (5.8) the calculation of $S_2(x)$ can be done straightforward by a direct application of the convolution formula (5.15). The result is:

$$S_2(x) = \lambda(1+\theta)\frac{[\lambda(1+\theta)x]^{2\theta+1}}{\Gamma(2(1+\theta))}\ e^{-\lambda(1+\theta)x}\ \Theta(x) \tag{5.17}$$

The presence of the $\Theta(x)$ function is of course expected. By similar methods $S_3(x)$, $S_4(x)$, and so on, can be obtained so that a general formula in the case of n photoelectrons can be established:

$$S_n(x) = \lambda(1+\theta)\frac{[\lambda(1+\theta)x]^{n(\theta+1)-1}}{\Gamma(n(1+\theta))}\ e^{-\lambda(1+\theta)x}\ \Theta(x). \tag{5.18}$$

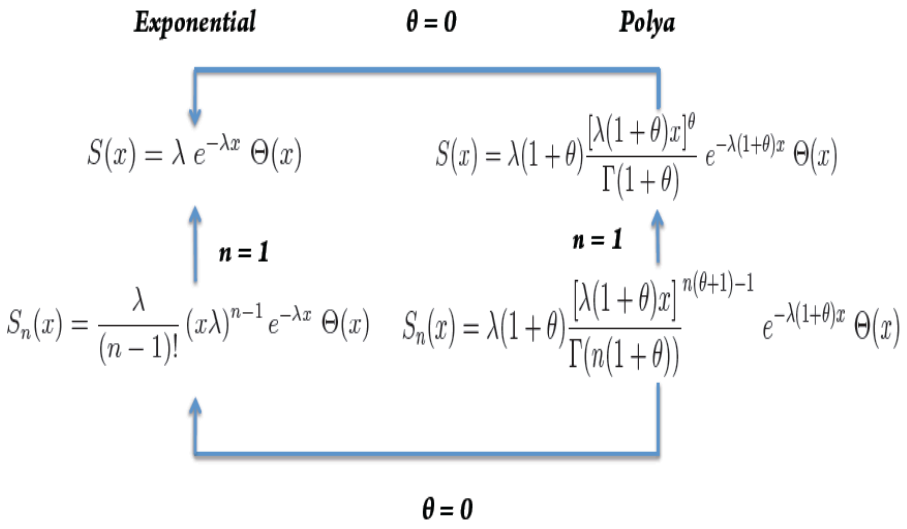

Figure 5.4: Mathematical relations for the two models

We can check that the formula (5.18) agrees with our previous considerations in the cases when n=1 or 2. Further we can prove the validity of (5.18) by means of mathematical induction. We can also prove (5.18) with the use of an integral transformation (the Fourier transform is mostly well-suited in the case of exponential or gamma distribution). The same calculations can be done for the exponential case but this is not necessary since putting $\theta = 0$ in these formulae we obtain these relations. In Fig. 5.4 we gather all the relevant equations for the two models. Notice the relations between the various formulae denoted in Fig. 5.4 with the painted arrows.

By now we must be able to recognize that the total probability for the Poisson characterized light pulse to produce charge in the vicinity of x is dictated by the probability distribution function:

$$\sum_{n=0}^{\infty} P(n,\mu) S_n(x) \tag{5.19}$$

since (5.19) is simply the sum of the individual probabilities. We also define $S_0(x)$ the zero electron charge distribution to be equal with $e^{-\mu}\delta(x)$ (defined only at x=0). This is justified because $S_0(x)$ is a pdf and is meaningful over small interval integrations.[4]

[4] When the delta function is integrated over a small interval that contains zero, then it results unit as expected.

5.2.5 Incorporating the Background

The probability distribution for charge deposition in response to a Poissonian light beam was worked out in detail in the previous section. The result was

$$S_{ID}(x) = \sum_{n=0}^{\infty} P(n,\mu) S_n(x). \tag{5.20}$$

We choose to call this pdf $S_{ID}(x)$ because it is ideal in the sence that it cannot account for any external charge fluctuation as (for instance) electronic noise. Indeed never in our previous analysis did we mention about background and the charge smearing that's responsible for. So the result of (5.20) is not at all accurate and it is only an idealization not taking into account the real data conditions.

To incorporate background effects in our formalism we must take into account the charge arising from noise. Since this signal is of chaotic character, a displaced Gaussian distribution over a mean value should be adequate.

$$B(x) = \frac{1}{\sqrt{2\pi}\sigma} e^{-\frac{(x-Q)^2}{2\sigma^2}} \tag{5.21}$$

Following the usual procedure, the final realistic output signal should follow a probability distribution given by the convolution of $S_{ID}(x)$ with the background.

$$S_R(x) = (S_{ID} * B)(x) \tag{5.22}$$

R stands for real or realistic. Our job is to derive $S_R(x)$ in a closed or, at least, in an approximate but still useful form.

At first, this seems like an extraordinary enterprise. The mathematics involved in the calculation are brute and complicated. Even the more sophisticated mathematical softwares are totally unable to provide us with an analytic expression for $S_R(x)$. To bypass this obstacle we are forced to resort to some sort of an approximation as it is usually done in such cases.[5]

Indeed if the mean value of the Poisson distribution is low enough one would expect that by ignoring terms with n greater than some value a sufficient and a handy expression can be obtained. Actually this is the case

[5]It is worthwhile to remark that C. Lane has succeeded in calculating the cumbersome sum of (5.20) with the use of the modified Bessel function $I_1(kr)$ [230]. This calculation is another manifestation of the elegance and power of pure mathematics. Nevertheless if you insist to do the final convolution with the background this step is not very convenient. Lane made this calculation for the pure exponential function but the same arguments can be applied to the gamma distribution case mutatis mutandis.

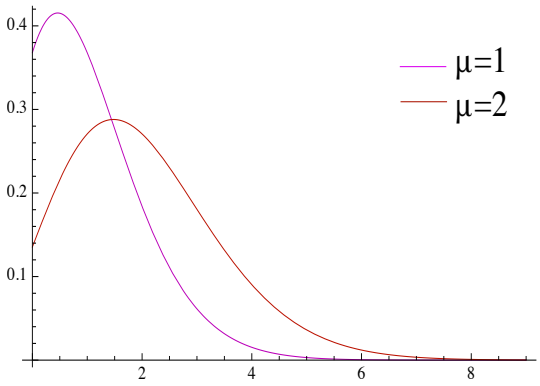

Figure 5.5: Poisson distribution

as one can readily see from the structure of the light-pulse statistics. For example, in Fig. 5.5 we show a plot of Poisson distribution for two values of μ, for $\mu = 1$ and 2. We can readily see that in both cases the Poisson distribution falls wildly after some n so that when $\mu = 1$ the values of $P(n, \mu)$ for n greater than five are small enough to be neglected. This is also the case when $\mu = 2$ but for $n \geq 8$. We now see that even though we cannot derive the expression of $S_R(x)$ in a closed form we can always approximate the full solution with:

$$S_R(x) = \sum_{n=0}^{m} P(n, \mu)\ S_R^{(n)}(x), \tag{5.23}$$

where m is an integer depending on the actual value of μ ($\sum_{n=m}^{\infty} P\ S_R^{(n)} \sim 0$), and $S_R^{(n)}(x)$:

$$S_R^{(n)}(x) = (S_n * B)(x). \tag{5.24}$$

When $\mu = 1$ then m can be chosen to be equal five while when $\mu = 2$ the first eight terms of (5.23) are just enough.

Our initial problem is now reduced to the calculation of each $S_R^{(n)}(x)$ separately. If we could obtain a formula for $S_R^{(n)}(x)$ for arbitrary n then a general formula could be obtained in terms of (5.23). This would be well-suited for plugging the (5.23) in a calculating machine since a single for–loop over the n would suffice to write the sum of the first, say, $m = 10$ terms in a relatively small and controllable code. Indeed this is the method that's been followed in most circumstances in the literature and this is exactly what is done in Bellamy *et. al.*

The last convolution integral of (5.24) is difficult for both models. This step essentially complicates the path we've taken and obscures the intuitive

features of the approach we chose to adhere. The very latest versions of Mathematica proudly penetrate this mathematical integral in terms of the confluent hypergeometric function of the first kind, ${}_1F_1(a, b, c)$[233]. Nevertheless, this solution suffers from overflows, numerical instabilities and other pathologies that complicate the use of both models. For these reasons two techniques have been devised that enable us to built the two convolution integrals relying on algebraic techniques. Since these investigations do not add to the understanding of the physical scheme and are somewhat numerical-analysis oriented we shall not present them here but the two solutions can be found at [234] and [235]. The reader interested in the fine details of these derivations could always contact the author.

In view of the final solutions, one might protest and argue that both formulas are ugly and complicated. We understand this attitude although we do not share the same concerns. The essentials of model building are deeply rooted with the mathematical intricacies of the problem under consideration and we believe that the only fair judge of a mathematical scheme is the ability or not to reproduce experimental data in the expected manner, never its mathematical difficulties. One should never forget: "make things as simple as possible, but not simpler".

Someone else might also suggest that doing the mathematics for these models is an elaborate and, as a matter of fact, unnecessary task since we could equally well penetrate the convolution integrals numerically by means of a "one of the so many" mathematical packages. For example, GNU Scientific Libraries (GSL) posses a wealth of adaptive numerical integration subroutines implemented in "`gsl_integration.h`" that could be used for these reasons [236][6]. We definitely agree in this respect but an analytical solution, if exists, presents us with a lot of merits.

For instance, for the commissioning and the calibration of the IV a large number of charge distributions at the SPE region had to be fitted[7]. Using the analytical solutions of the statistical models developed for gain extraction the minimization package could converge in a very short time-scale, usually within a few seconds, and with minimum CPU consumed. This allowed us to analyze a large number of different cases quickly and speeded-up our investigations. In any case, as is frequently emphasized it is always preferable to have the analytical solution at hand [237].

[6] Actually this was the way that we originally penetrated the integrals. Only afterwards we sought to turn the mathematical crank.

[7] For example for the extraction of the nominal HVs of all the PMTs in the IV of the Chooz-far we performed 311 fits in total.

5.3 Generated data

Before we attack real data it would be perhaps rewarding to examine how the models we have written down for gain calibration behave when applied to generated spectra. For this purpose we prepared some artificial, Monte-Carlo data and checked whether the mathematical scheme we presented reproduces the input parameters. Of course there is no physics behind these considerations. Since we were the ones that created these data we do not check the physical aspects of this problem but only the strict mathematical ones. In doing so, we shall take a rough idea about how the things work in our PMT gain-determination method and, in any case, it will be a good exercise before we move to real data.

To generate and fit the single photoelectron spectra we used `ROOT/Cint`. The events were created with `TRandom3`, the default number generator of ROOT which is the more convenient for such reasons. Pedestal was generated according to a simple gaussian and the number of photoelectrons with a Poisson distribution. For the dynode-structure chain amplification we chose an exponential and a gamma distribution respectively for the two models. With this logic we created a number of spectra, for each case, with parameters close to the ones we expect to have in realistic situations.

In all the cases the fitting functions were more than adequate to deconvolute the inserted parameters within the expected accuracy (no more than 3 or 4 σ deviations) suggesting that our models are mathematical consistent and are not plagued by undesired correlations between the extracted parameters. This of course can be checked directly through the correlation matrices. Of course, the better statistics the more accurate results you get (smaller errors). In Figure 5.6 you can see how well the two models can fit some generated spectra.

It should be mentioned that for the whole procedure to be applicable, `TMinuit` requires initial values for most of the parameters. In real data we took the pedestal values from a pedestal run we performed before every measurement using a random trigger without PMT illumination. The number of photoelectrons was also determined roughly by the ratio of the counts in the signal S_G (three σ's away from the pedestal mean) to the total number of entries in the spectrum N_{tot} through the formula:

$$\mu = -\ln(S_G/N_{tot}), \tag{5.25}$$

and the initial value of lambda was extracted for both models through a simple exponential fit over the signal. For the gamma distribution model, the value of theta was not critical to the whole procedure but its values

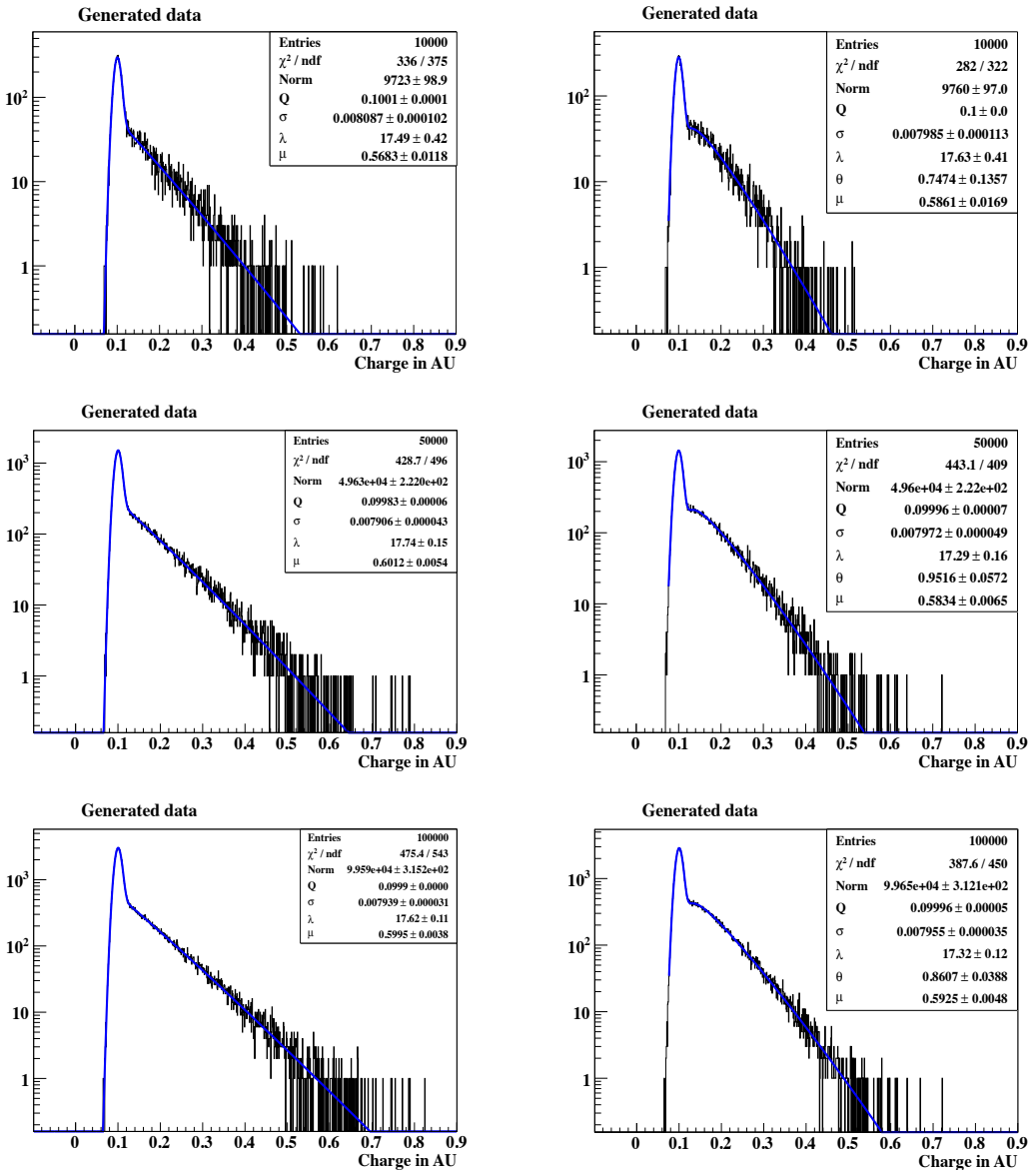

Exponential Gamma

Figure 5.6: Generated (and fitted) spe spectra for values $Q = 0.1$, $\sigma = 0.08$, $\lambda = 17.2$, $\mu = 0.6$ (Exponential and Gamma) and $\theta = 0.8$ (The gamma function extra parameter). One can see three plots for each model with entries 10000, 50000 and 100000. χ^2/ndof is always very good and as the statistics increases the errors become smaller.

should be penalized not to enter negative values since gamma function has poles in the negative real axis.

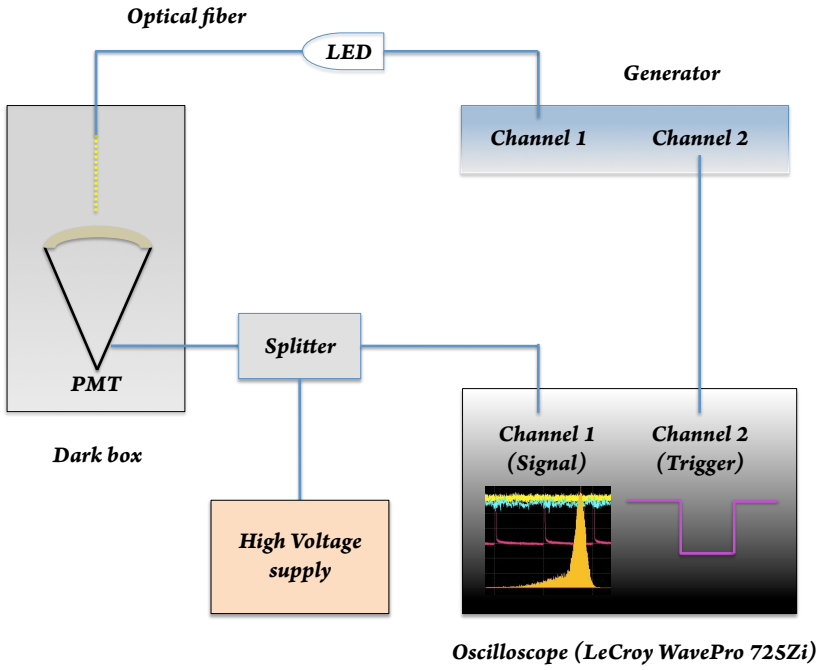

Figure 5.7: Pictorial representation of our PMT testing apparatus.

5.4 Laboratory measurements

5.4.1 Experimental setup and data

The main features of the experimental apparatus needed for the absolute calibration of PMTs are well-known and, more or less, standard. Most of the components we utilized for this purpose are graphically depicted in Fig. 5.7. As can be seen, the phototube was placed inside a dark box. Extra black silicon was used to ensure that the box is indeed light-tight and the whole setup operated inside a small air-conditioned dark room. The temperature of the room was always at 21°C.

The light pulses necessary to illuminate the phototubes were created by an LED connected to a fast pulse generator. The light was directed inside the box and onto the PMT through an optical quartz fiber, the same type that the IV Light Injection system employs. A halo-like plastic support, attached to the tube's capsule, was also used to ensure that the fiber was always on the center of the input window, just touching the photocathode (Figure 5.8). The same support can be used to change the fiber's position

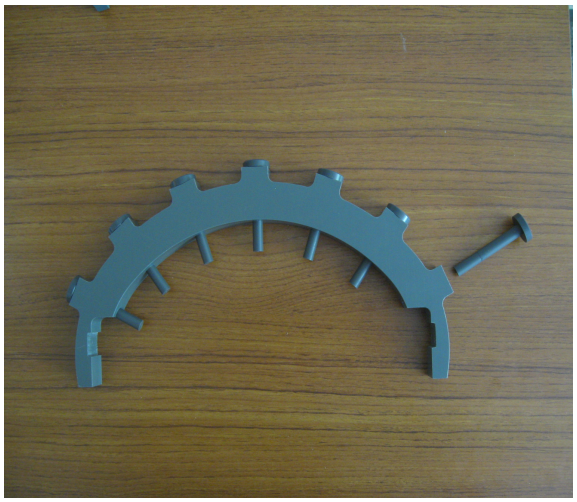

Figure 5.8: Halo-like fibers' support.

on the photocathode if needed. All of our tests were done with blue light, λ=475 nm, and the generator operated at 500 Hz (it is to be noted that due to temperature effects the LED emitted light depends on the pulsing rate). The widths of the signal pulses were 20 ns. The signal from the PMT was separated by the input High Voltage (HV) through a splitter and was driven to an oscilloscope LeCroy WavePro 725Zi (Channel 1). It should be remarked that exactly the same custom splitter units are used in the Double Chooz detector as explained in Chapter 3.

In all tests we triggered from the generator's second doublicated channel and the trigger output was send to the oscilloscope's Channel 2. In Fig. 5.9 one can see a screen-shot taken from the oscilloscope. The purple curve is the trigger sent by the generator and the cyan curve is the signal of the PMT. The two histograms, pink and yellow, denote the voltage and the charge (negative, this is why the yellow distribution is reverted) measured on the anode of the PMT respectively. In what follows we shall concern ourselves exclusively with the output charge on the oscilloscope, the yellow histogram. Of course if no additional noise is present then the two histograms are analogous as evident in Fig 5.9[8].

For the purposes of gain determination we operated the PMT at different HV values between 1300 to 1450 V; we never exceed the value of 1450 V. We also tuned the LED input voltage so that the mean value of the observed

[8]In all the measurements done in Strasbourg this was indeed the case. In contrast, during the PMT testings at Chooz-far there was sometimes an extra noise present, giving to the voltage histogram an extra exponential part.

Figure 5.9: A screen-print of the LeCroy oscilloscope.

photoelectrons would be within the range of $\mu = 0.2$ - 2.5. We always wanted to observe the pedestal clearly since then one can use it to extract information through the fit. For high values of μ, strange correlations might arise that could bias our results. In any case, it is more convenient to limit ourselves to this narrow region since the presence of the pedestal gaussian enforces strong constrains to the fitting procedure.

We have performed a significant number of measurements with the R1408 IV phototube we have here in Strasbourg. Initially we took various data to understand the PMT behaviour and validate the gamma distribution model put forward for gain determination. We subsequently cross-checked our gain determination process through data with altering HV and light input. The main results of these investigations are summarized in the following Section.

5.4.2 Gain measurements

We are now in a position to discuss the analysis of real data at the SPE region. In this section we shall describe, among others, the performance of the two fitting functions and we shall motivate the reasons we have to believe that the gamma function model is more efficient and can be used to extract the gain parameter to a very good accuracy.

To perform very accurate measurements we always let the HV on for at least one day for PMT stabilization. We also took at least $\sim 10^5$ events for each spectrum to have large enough statistics and therefore smaller errors. We did measurements with different high voltage values and different

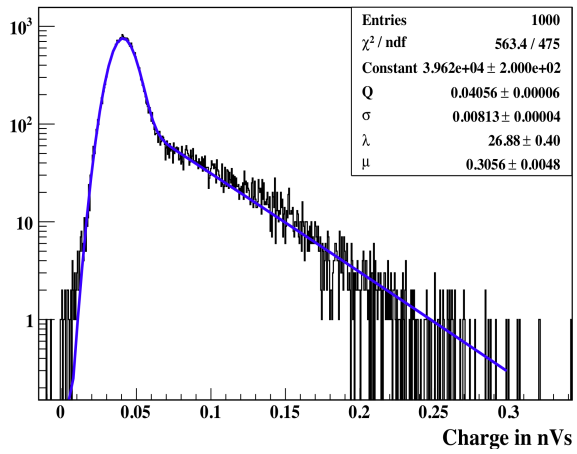

Figure 5.10: An example of a charge distribution from a PMT where the exponential based model can account for.

light input. In all cases gamma model was adequate to approximate the observed spectra in a concise and accurate manner. It is remarkable that pure mathematical considerations finally constructed a very flexible model that can parametrize the function of the R1408 PMTs for probably most of the observed cases[9].

The exponential distribution could cover some but not all cases. For instance, in Fig. 5.10 we show a PMT charge distribution taken from the DC detector where the exponential SPE charge amplification function works very well. The χ^2/ndof is really small and the model treats well the part of the signal in the distribution. On the other hand, when a "single photoelectron bump" appears the exponential model breaks down[10]. In Fig. 5.11 (top) we show such a case. In these cases the gamma model performs better as shown in Fig. 5.11 (bottom). The extra θ parameter modifies the variance on the SPE peak in the way required to account for the experimental observations.

To further check the two models and decide if we extract the right parameters we did the following test: We increased slowly the light input and tried to see if the PMT's intrinsic parameters remain the same. For example, the gain is characteristic of the photomultiplier tube and is not at all dependent to the attributes of the light pulses. The same holds for the intrinsic spread

[9]During the IV phototubes' installation we tested 82 in total PMTs. All the obtained spectra could not be analyzed according to this parametrization.

[10]Even though it can account for the gross features of the PMT's response.

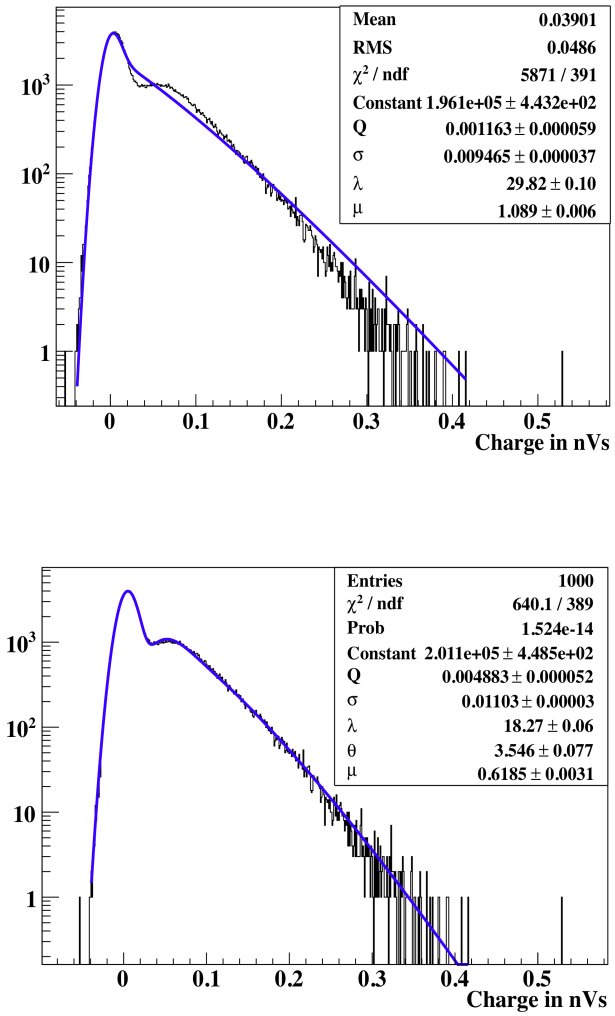

Figure 5.11: SPE fits to the charge distribution of a IV PMT. The exponential model (top) can not treat the bump in the SPE signal that is best tackled by the gamma model (bottom).

(variation) over the gain related to the θ parameter in the gamma function model. As we change the illumination and take data we should, through the analysis, find each time the same value for λ and/or θ.

The results of these tests (gathered in Table 5.1) are in favor of the gain deconvolution method. As one could see the extracted lambda in the gamma model is close enough to $\sim$ 18.0 nVs while the uncertainties never exceed the limit of five sigmas and the deviations suggest that we can estimate the gain parameter with a very good precision. θ also remains stable albeit with

Exponential Model

λ	$\pm\delta\lambda$	μ	$\pm\delta\mu$
31.0293	0.114067	0.454302	0.0026217
31.0139	0.0691134	0.566851	0.00206143
30.5115	0.0839056	0.631921	0.00275898
30.5935	0.0667552	0.731702	0.00254447
30.5241	0.0753747	0.789982	0.00312368
29.9802	0.0959648	0.888604	0.00449549
29.8176	0.104408	1.08921	0.0059518

Gamma Model

λ	$\pm\delta\lambda$	θ	$\pm\delta\theta$	μ	$\pm\delta\mu$
18.1473	0.0690661	3.77557	0.0828358	0.251455	0.00145313
18.0799	0.0423102	3.81046	0.0527141	0.313064	0.00109643
18.1389	0.0516575	3.70146	0.0622883	0.356322	0.00150365
18.1656	0.0422534	3.65092	0.0506732	0.40963	0.00140413
18.2683	0.0475186	3.56288	0.05566	0.445517	0.00168955
18.1353	0.0583767	3.60454	0.0730343	0.504144	0.00240364
18.2705	0.0649074	3.47268	0.0764942	0.620917	0.00322124

Table 5.1: Results of LED scanning for the Exponential and the Gamma model. You can clearly see that the extracted parameters, related to charge amplification, are stable for the gamma case. In the exponential function have a very specific tension.

a smaller accuracy. These results makes us confident for our gain extraction techniques.

The last cross-check we performed in our fitting model was to maintain the same light input (the same configuration in the LED) but alter the HV. In these cases the charge performance of the PMT obviously changes. More precisely the gain increases exponentially with the applied HV in a way that we shall investigate in detail in the next sections. Nonetheless, the poissonian mean μ is related with the light source and should not be affected by the changes in the HV. In Fig. 5.12 we show the dependence of μ (the mean value of photoelectrons) as a function of HV. We do clearly that indeed there is a stable plateau in μ consistent with our previous arguments. Again we see that our fitting technique is self-consistent.

To calculate the absolute PMT gain from lambda we first obtained the spe mean value, equation (5.9), and then divided by the resistance of the

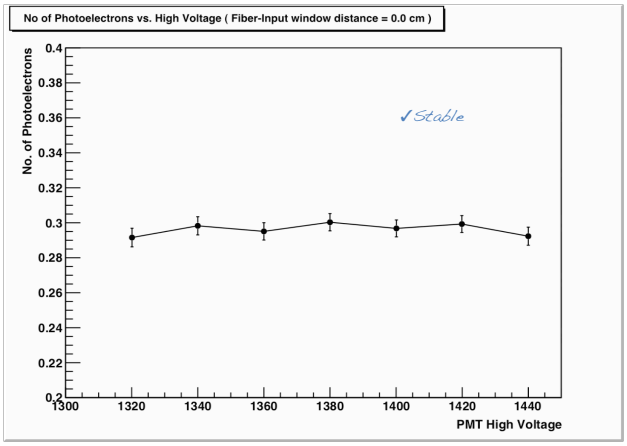

Figure 5.12: An example of a charge distribution from a PMT where the exponential based model can account for.

oscilloscope—that is 50 Ω—to convert nVs to nC. Further we divided this result by the electron charge to obtain the result in terms of electron charge units.

$$gain = \frac{1}{\lambda} \times \frac{1}{50} \times \frac{1}{e} \tag{5.26}$$

In this way our result is more transparent: Gain is the number of electrons collected in the anode of the photomultiplier tube whenever an electron is created in the photocathode. Of course the same formula applies to the variance over the gain.

5.4.3 Criticism

In closing this long discussion, and to be fair enough, we must not forget to mention that there was a small number of spectra where the gamma model could not properly account for. In these cases our fitting function was always some units above the spectrum in the region between the pedestal and the single photoelectron (Figure 5.13). These differences were small, not seen on the logarithmic scale but still there. We have good reasons to believe that these deviations are part of the PMTs signal characteristics.

Actually, adding an extra exponential tail to the gaussian "background" as done in Bellamy et al. [228] this feature can be effectively modeled. A contribution like this would probably account for pre-pulsing electrons created in the first dynode (the so-called "valley" electrons). Nonetheless, like this

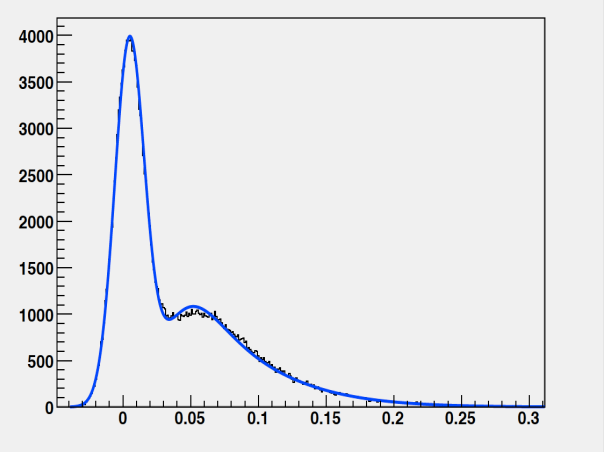

Figure 5.13: One case where Gamma model was not 100% efficient.

the number of free parameters in the PMT model will increase sufficiently and parameter correlations should be considered. Also, as of now, we were not able to show that the resulting model is indeed self consistent in the ways already explained[11]. Since we do know that this additional contribution will modify gains only in the 1 % level we decided to neglect it altogether. We know that for the precision required for the IV this is indeed a well-motivated choice. At this stage it has to be said that the model has also been tried on ID PMT signals and gave satisfactory results.

5.5 Pre-installation tests

All the R1408 PMTs were tested prior to their installation in the IV of the DC far detector. The main objective of these tests was to verify that all modules are properly working, tracing damages through their transportation, and to identify possible changes in their performance. Data with both low and high intensity light were taken. The low intensity runs were used for gain determination while the high intensity runs stimulated timing studies in the usual strategy of the IV-LI system.

The measurements were performed at the Chooz-far laboratory with part of the IV-LI already installed for this purpose. The signal from the PMTs was separated by the same splitter (splitter 310) and the HV was provided through the 20 m cables utilized in the experiment until the splitters level. For the light pulses a single LED in the board had been tacked together and a quartz fiber exiting the LI box had been assembled. The length of the testing

[11] That it passes the criteria of gain and μ independence established previously

Figure 5.14: The PMT "hat" used in all tests to block external light. The fiber cable is also visible.

fiber was 25 m as those employed by the IV-LI. At the other end of the fiber (outside the IV-LI box) a customized "hat structure" was attached to allow the blinding of the PMTs from external light while the fiber was entering the coverage from a hole at the top of the hat, Fig. 5.14. The monitoring PMT was operating inside the LI box and the rest of the IV-LI was controlled with a laptop remotely connected to the IV-LI PC.

After the placement of the testing hat, black nylon sheets were used in addition to further reduce the possibility of unwanted light leaks. The IV PMT, the monitoring PMT signal and the external trigger of the generator were readout by the LeCroy WavePro oscilloscope. The equipment needed to coordinate and perform these measurements was compact enough to fit in a working bench, Fig. 5.15. We tested 82 PMTs totally; 78 of them are now in the IV. Some problematic pieces were found and they were not installed. Normally, when no problems occurred, we spent 17 - 20 min for the tests of each module.

The low-intensity tests were performed with the LED voltage configured at a value were all PMTs received light at the SPE level; poissonian mean smaller than one photoelectron in all cases. From all these data sets, the IV PMT gains were determined with the fitting procedure described previously based on the gamma model that is most satisfactory. Data were taken with four different PMT HV configurations starting from the value of 1300 V and rising in steps of 50 V. Subsequently, the dependence of the gain with the applied HV was obtained for each PMT by fitting the four data points with an

Figure 5.15: A picture taken during the PMT pre-installation tests conducted at Chooz. Leonidas N. Kalousis is shown while taking notes on the data running conditions.

exponential function. This dependence was used to interpolate or extrapolate the nominal HV value for each PMT; that is the value for which gain equals to 10^7 in units of electron charge, Fig. 5.16. These nominal HV values were implemented in the CAEN HV system and are now applied on the PMTs functioning in the IV of the detector ensuring that they are performing with roughly the same gain.

We will only mention that the high intensity data were used to extract the individual PMT relative time response offsets. For this purpose three different intensities were utilized. In each measurement we recorded the time where the signal amplitude exceeds a fixed threshold both for the tested and the reference PMT. The time responses were obtained event by event by the difference between the response of the each PMT with the reference PMT. The overall time offsets per PMT were obtained fitting this time response profile with a simple gaussian. While the time offsets depended strongly on the applied light intensity, the relative differences between the various PMTs were found to be the same inside the expected errors. This first set of time offsets were taken into account during the commissioning of the IV. Some further information on the PMT pre-installation tests could be found in Ref. [238, 239, 240].

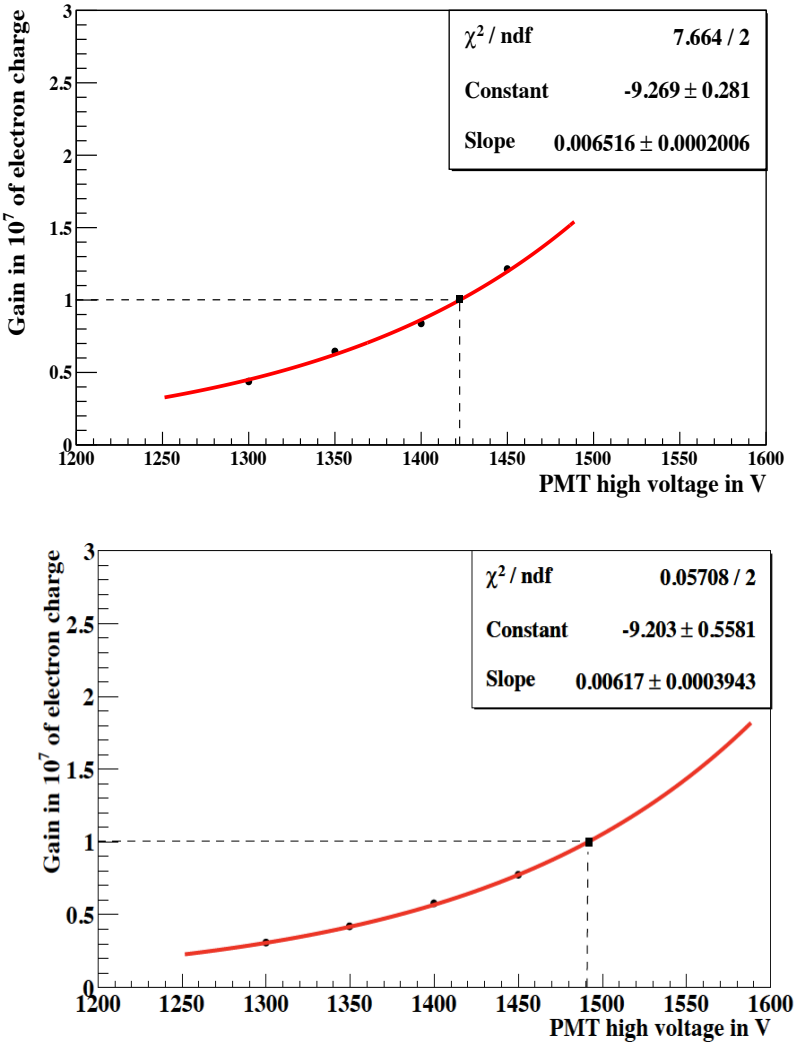

Figure 5.16: Nominal high voltages are calculated interpolating (top) or extrapolating (bottom) the exponential curves relating gain with high voltage.

5.6 "In situ" gain calibration

The installation of the IV-LI system was completed in June 2010 with the glueing of all quartz fibers in the LED matrix. In the following months, and after the parallel installation of the DAQ system, the IV-LI was commissioned with only a small pause of roughly two months necessary for the detector filling. During this period an important number of calibrations runs dedicated to gain measurements was conducted. All LEDs were exercised

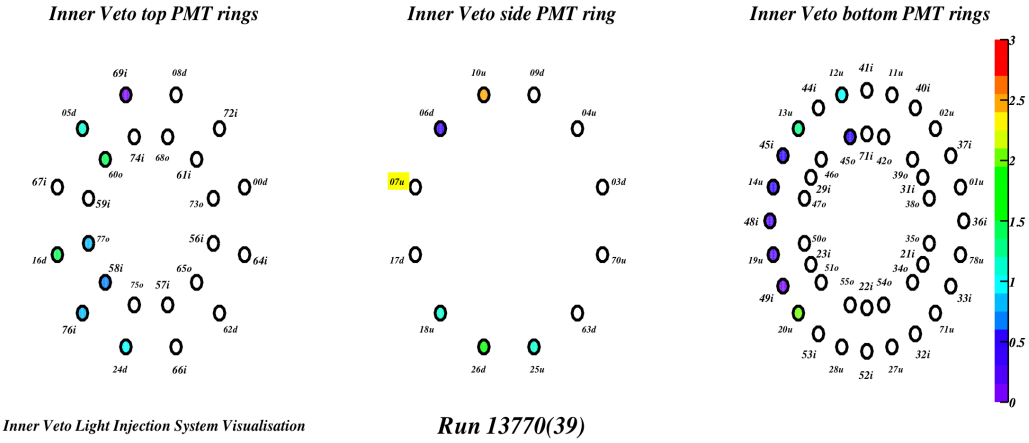

Figure 5.17: Visualization of an IV-LI calibration run taken with LED 7 (denoted with yellow). The IV channels are weighted and colored according to the poissonian mean reported by the fitting model.

with different values of applied LED voltage. The first objective was to consolidate that the IV-LI is functioning in the desired performance level that was designed for. In doing so parts of the DAQ system and the data read-out were also commissioned.

The second objective of these commissioning data was to find out the best running conditions needed for the operation of the IV-LI during the experiment. In the PMT gain calibration mode one would like to activate a relatively small number of LEDs but illuminate as many channels as possible. Since gain determination analyses will be performed, most of the illuminated channels should receive signal of weak light pulses, say $\mu < 2.5$, so that the charge spectrum model (previously described) could be applied.

For this purpose, all runs taken were analyzed through the gamma SPE parametrization function. A run configuration was written down consisting of the minimum number of LEDs and LED voltages that illuminate all PMTs with poisson mean value between 0.3 and 2.5. This is the now D19 configuration that is used for the extraction of gains[12]. For instance, in Fig. 5.17 we demonstrate visually the results of a low-light intensity calibration run taken with LED number 7. The position of the fiber inside the IV is highlighted in yellow. The PMTs are shown colored according to the poisson μ that is

[12]For redundancy some extra LED runs were added to this minimal configuration.

obtained after the analysis. One can readily see that the channels receiving light in the accepted region are in the vicinity of the activated fiber. The fiber of LED 7 is pointing upwards. Nonetheless some bottom rings PMTs record light, albeit of weaker intensity, due to reflections.

The D19 IV-LI run configuration is performed once per week. The output data are analyzed in a production-like chain with a sequence of computer code (C++, ROOT) developed for this purpose. The results are uploaded in a database created by the collaboration. We should emphasized that the charge distributions are built from the charge obtained by integrating the whole read-out window. Like this many "background" events[13] are accumulated. This contribution (the pedestal) is subtracted in an overall fashion after the fitting function minimization.

In Fig. 5.18 we show the results of those gains extracted by one random calibration run. The mean of the IV PMT gains is roughly 145 DUQ. This value is in accordance with expectations based on off-site measurements as shown in Ref. [241]. Additionally, in Fig. 5.19 we show this IV mean gain value as monitored in time. We do see that it is indeed stable within experimental errors and with the rough precision required for the IV. The gains of individual channels are stable in more or less the same way. It should be also remarked that upon detector power-cycles IV gains change in specific steps related to the detector electronic systems.

[13]That means with no pulses in the integration gate.

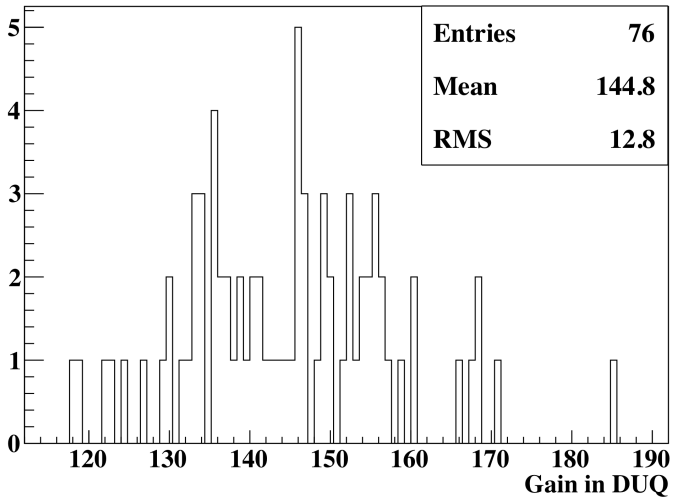

Figure 5.18: The IV PMT gain distribution as extracted from a D19 calibration run taken at 7^{th} March 2011.

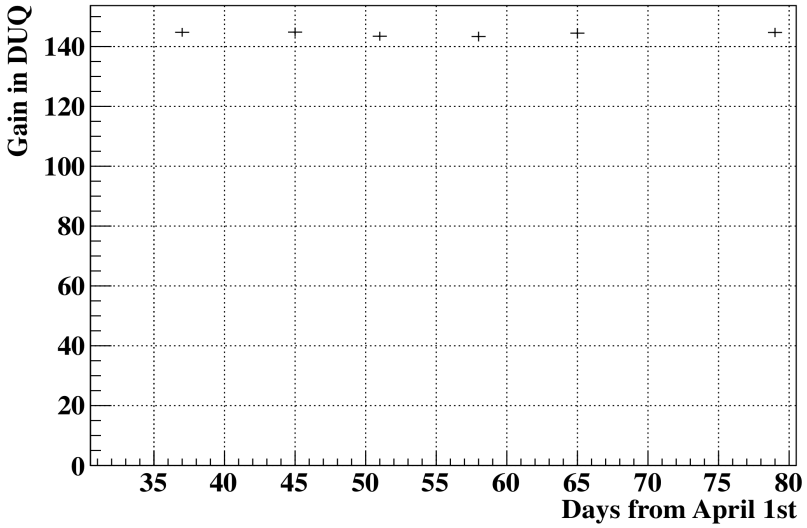

Figure 5.19: The IV mean gain monitored in time. On the y-axis gain is shown in DUQ, on the x-axis the number of days elapsed since 1^{st} April 2011.

Part III

Data Analysis

Αν μες στις φωνές που τα βράδια τρυπούνε ανελέητα τα τείχη
ξεχώριζες μία: είναι η δική του. Ανάβει μικρές πυρκαγιές,
χιλιάδες μικρές πυρκαγιές που πυρπολούν την ατίθαση νιότη μας.
Είναι η δική του φωνή που βουίζει στο πληθος, τριγύρω σαν ήλιος
που αγγαλιάζει τον κόσμο σαν ήλιος, που σπαθίζει τις πίκρες σαν ήλιος
που μας δείχνει σαν ήλιος λαμπρός τις χρυσές πολιτίες
που ξανοίγονται μπρός μας λουσμένες στην Αλήθεια και το αίθριο φως

Μανώλης Αναγνωστάκης, Χάρης 1944

If in the screams, that at night, penetrate merciless the defensive lines
you could identify one: it's his voice. He lights up small fires
myriads of tiny little flames that burning our restless youth.
It's his voice that shouts at the crowd, all over like the Sun
that embraces the world just like the Sun
that slays the sorrows, just like the Sun
and leads us the way, like a bright shinning star
towards the golden kingdoms
that lie ahead, lit in the Truth and the morning light

Manolis Anagnostakis
(March 1925 – June 2005)

Chapter 6

Fast neutrons and stopping muons

In the first part of the thesis we presented the various backgrounds relevant for Double Chooz, in Sec. 3.9 while discussing the final oscillation analysis. Among them, the combined contribution of fast neutrons and stopping muons plays an important role. The total errors on the estimations of these populations are large enough and together with ^{9}Li drive the main uncertainty of the measurement. Both these classes of events belong to the so-called correlated background, meaning that there is a certain connection between the prompt and the delayed signals. The prompt-delayed time difference and in-between distance distributions are strongly correlated as is the case of reactor antineutrinos.

In this Chapter we will elaborate on these two sources of background. We shall discuss in more details their signatures and recognition patterns. Finally we will present how they were treated for the purposes of the first Double Chooz (DC) result.

6.1 Contaminated neutrino sample

When these investigations begun our goal was to track the possible sources that contaminate the selected neutrino events and can deposit high energy prompt signals. That would be the clean imprint of incoming particles with fast neutrons to dominate the statistics as expected. We remind you that fast neutrons is a well-known, and relatively well-understood, background for reactor experiments. It consists of high energetic neutrons created in the surroundings of the detector by cosmic muons that miss the detector. Since they are neutral, these neutrons can enter the Inner Detector (ID) without

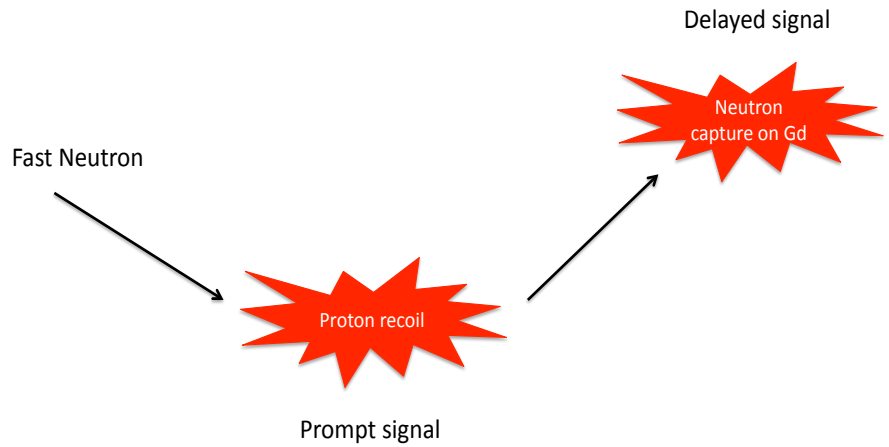

Figure 6.1: The prompt-delayed coincidences created by fast neutrons.

triggering the Inner Veto (IV) as would have been the case for the muons themselves. Inside the ID fast neutrons can induce signals while colliding with nuclear protons; proton recoils. Protons are charged and as such they do release photons in the scintillator. Subsequently these neutrons slow-down, thermalize and get absorbed in Gadolinium (Gd).

These proton recoil - neutron capture doublets, Fig. 6.1, are producing the same signature as prompt-delayed coincidences initiated by reactor antineutrinos. Our primal objective was focused on understanding fast neutrons and other similar contributions and estimating their magnitude. Then after unveiling their pattern and characteristics one could try to use this knowledge to further reduce the background contamination in an event by event basis if this needed. In doing so we identified two contributions: one arising from fast neutrons (as expected) and another produced by stopping muons.

Looking for impurities in the official antineutrino sample due to incoming particles or radiation it is almost traditional to extent the upper limit of the prompt energy window. Like this one starts to accumulate additional background events in the high energy bins that could utterly study. We did so altering the prompt energy window from 0.7 - 12.0 MeV to 0.7 - 30.0 MeV. The new positron spectrum that we found is shown in Fig. 6.2. The first thing that strikes the eye in Fig. 6.2 spectrum is the existence of a high energy tail that continues up until 30.0 MeV in an almost flat manner. Below 12.0 MeV the distribution is identical with the standard one obtained with the official

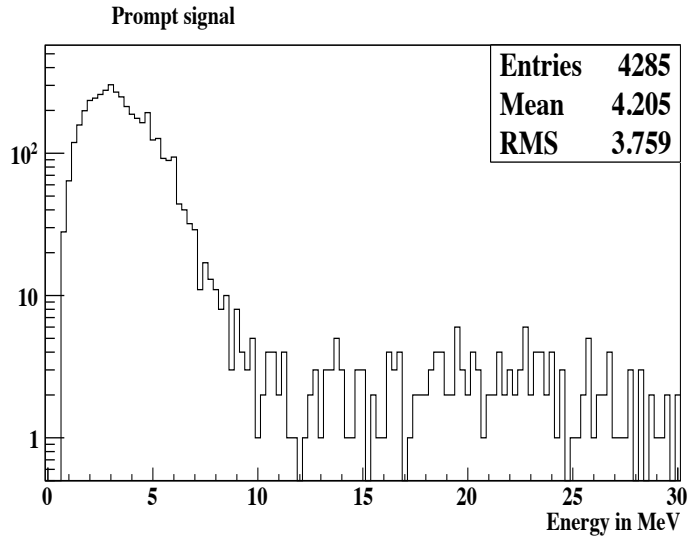

Figure 6.2: Extended energy window positron spectrum.

cuts presented in Chapter 3. There are 164 events (over a live-time of 96.8 days) in the tail and if we assume that this population does continue below the signal in the same flat manner we expect:

$$1.06 \pm 0.08 \text{ events per day} \tag{6.1}$$

of this specific background. It is of course important to try and understand what is the nature of those events beyond 12 MeV.

6.2 Events in the high energy tail

In searching for hints that could possibly guide us in comprehending the origins of the selected events in the 12 - 30 MeV range of the prompt spectrum we first note that a vertex is indeed reported for all these cases. That means that the likelihood minimization of the vertex reconstruction algorithm (`RecoBAMA`) has converged to a result. Their prompt-delayed spatial distance (ΔR, Fig. 6.3) distribution also is very correlated excluding the possibility to have selected accidental events.

Plotting the vertices of the prompt events with E $>$ 12.0 MeV (Fig. 6.4) we do see a very striking feature. It seems that there is a high accumulation of signals right under the chimney of the detector. We remind you that at the center of the detector there is a central tube, called the chimney, that was used for the liquids filling of the detector and for the deployment of

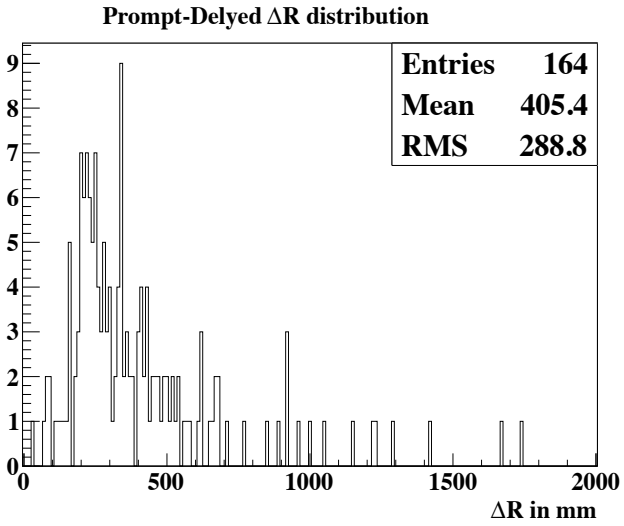

Figure 6.3: Distribution of the spatial correlation between the selected prompt-delayed doublets within the high energy tail.

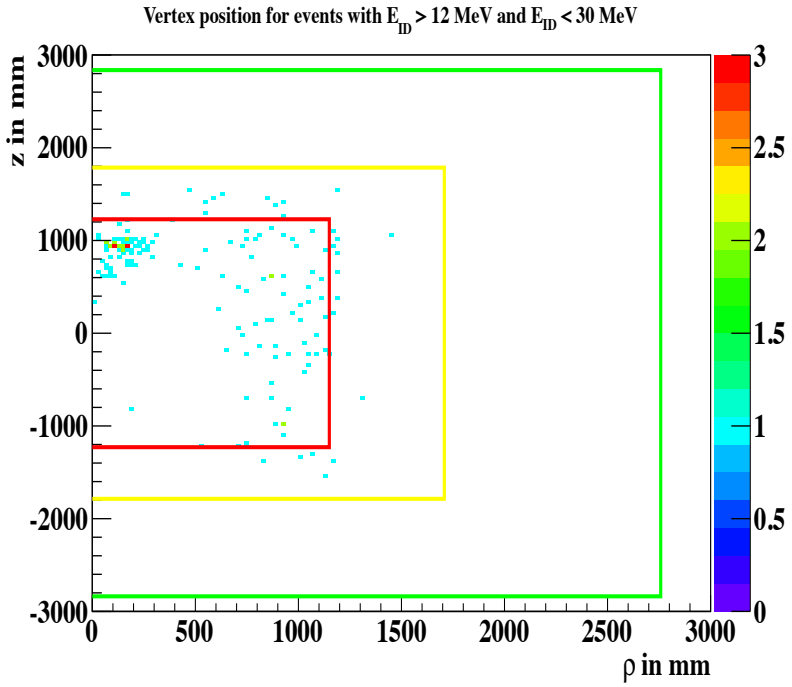

Figure 6.4: Vertices of the prompt events with 12.0 MeV $< E_{ID} <$ 30.0 MeV.

calibration sources. A second class of events distributed across the periphery of the Neutrino Target (NT) is also present.

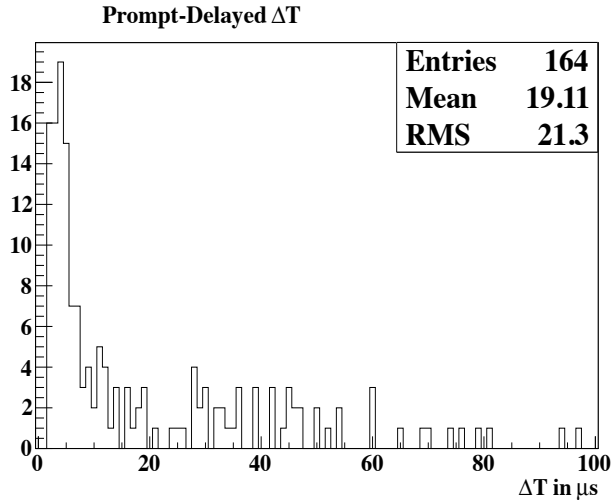

Figure 6.5: Prompt-Delayed time difference distribution for the selected antineutrino candidate events with E > 12.0 MeV.

What could be the nature of those events ? The population under the chimney could be muons that enter the detector through it and decay inside the ID. The following Michel electrons would then be the delayed signals. Certainly this is a viable possibility since stopping muons of that kind would not trigger the IV and if they deposit in the ID energies lesser than 30 MeV they are not tagged by the ID as well. We will first offer the solution to this puzzle and then present the arguments that support these statements. Indeed we do see two different classes of events. The first is stopping muons that cross the detector through the chimney and travel in the ID for a few cm depositing energies smaller than 30 MeV. The second population is fast neutrons and their vertices are distributed around the target as one would expect from intrusive particles.

To support these assertions we first show in Fig. 6.5 the time difference distribution of the events in the high energy tail of Fig. 6.2 (E > 12.0 MeV). Again we do see a striking pattern. A big portion of these selected events have ΔT smaller than ~ 12 μs. In this respect we should also remember that the decay mean-life of the muon is 2.2 μs the "endpoint" of its decay curve should be at ~ 11 μs. To complete this picture in Fig. 6.6 we show the ΔT distribution of those events with vertex coordinates inside the limits:

- z > 0 mm
- z < 1800 mm and,
- $\rho = x^2 + y^2 < 400$ mm

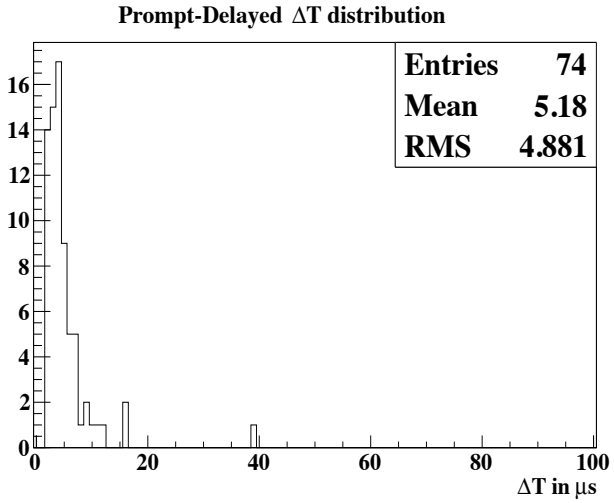

Figure 6.6: Prompt-Delayed time difference distribution for the selected antineutrino candidate events with E > 12.0 MeV and inside a small cylinder centered below the chimney.

As we see in Fig. 6.6 almost all the sample consists of events with ΔT < 12.0 μs. A small contribution of other categories of events with ΔT > 12.0 μs also exists. The position of these events and the ΔT distributions makes us confident that we see prompt-delayed doublets arising from the muon Michel decay chain:

$$\mu^- \rightarrow e^- + \bar{\nu}_e + \nu_\mu \tag{6.2}$$

The prompt signal comes from the muon that crosses the chimney while the delayed is the Michel electron releashed through 6.2. Of course the same decay with μ^+ is also possible.

The events of the second category are not gathered under the chimney but they occupy the periphery of the target. The statistics of the sample is limited but in the ΔT distribution, shown in Fig. 6.7, a clean mean of $\sim$ 30 μs is understood. As a reminder the mean capture time of neutrons in Gadolinium is also 30 μs. This answers half of the question. To complete the answer we now turn to the energy distribution of those delayed events with 12 MeV < E_{prompt} < 30 MeV. This is shown in Fig. 6.8 in black. In black we denote the whole sample of 164 events. In red we overlap the delayed energies of the those events with prompt signals inside the cylinder under the chimney denoted above and in green the rest of the events. As is evident from the green curve of Fig. 6.8 the second category of events is peaked in the Gd line, 8 MeV.

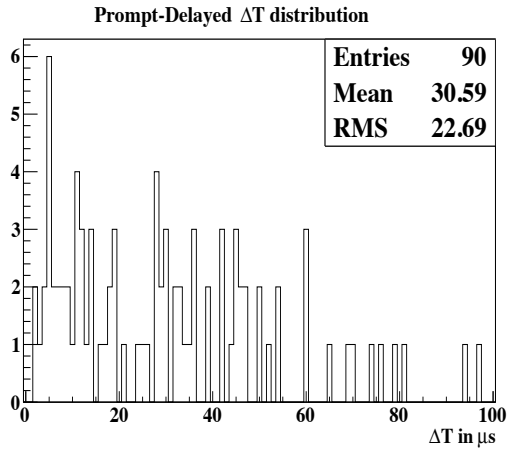

Figure 6.7: Prompt-Delayed time difference distribution for those high energy events that are not under the chimney cylinder.

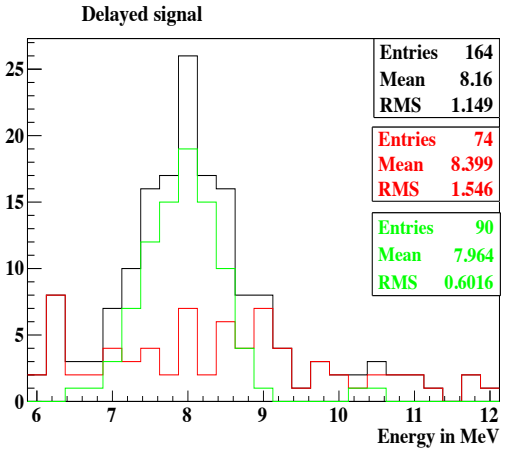

Figure 6.8: In black we show the delayed spectrum of the selected prompt events with E $>$ 12 MeV. In red we show the delayed energies of the those events with prompts inside a cylinder under the chimney and in green the rest of the events.

Obviously we do see neutron captures. Apparently these events are those fast neutrons we were originally searching for. The prompt signals are neutron collisions on protons while the delayed ones come from the absorption of neutrons on Gd. We are now able to realize why these events are in the periphery of the target, being particles coming from the exterior of the detector. These observations complete the question posed earlier in this section.

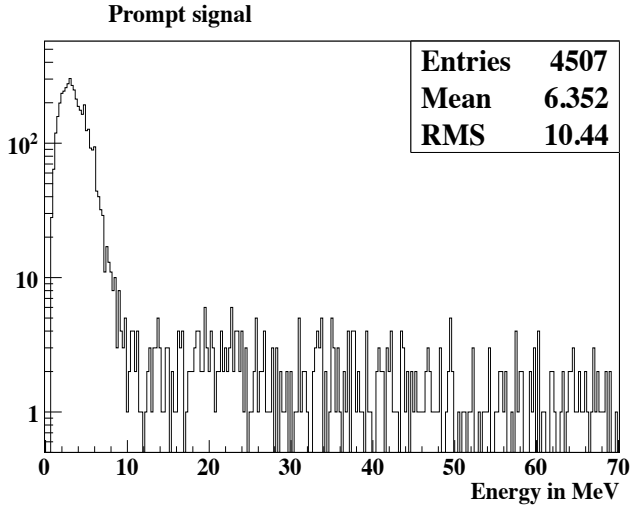

Figure 6.9: Prompt signal spectrum with the prompt energy window set from 0.7 to 70 MeV.

6.3 70 MeV muon cut-off

In this Section we will repeat the investigations pursued in the previous one but with a slight difference. We will relax the ID muon tagging cut from 30 to 70 MeV. More precisely, muons in the ID or the IV will be tagged by the following decisions:

- $Q_{IV} > 10000$ DUQ or,
- $E_{ID} > 70$ MeV.

With this muon identification strategy we will reproduce some of our previous results "mutatis mutandis". Of course, our conclusions will be the same as previously. Nonetheless we will have the opportunity to establish them with larger statistics, gaining thus more confidence on our techniques.

Firstly, we show in Fig. 6.9 the prompt signal spectrum with the upper limit set to 70 MeV. Since the ID muon cut is also at 70 MeV there is nothing that prevents us to do so. In Fig. 6.10 we show the vertices of the events with prompt signal energies greater than 12 MeV. The two populations connected with fast neutrons (FN) and chimney stopping muons (CSM) are still visible and well-understood. Nonetheless, to perform an extra check on the fast neutron part of the background we will alter the high energy upper limit of the prompt signals to see how the vertex distributions change with respect to this.

This is done in Fig. 6.11. There we show the prompt vertices for four different energy upper limits on the prompt signal. The values chosen are 60

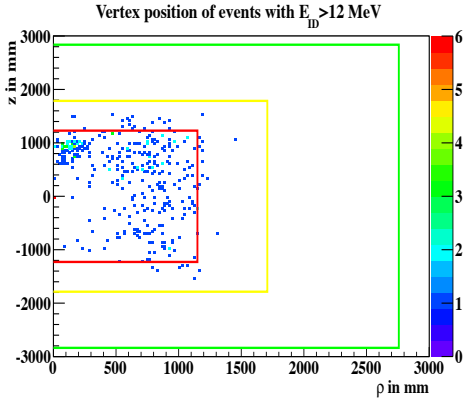

Figure 6.10: Vertices of the prompt events in the 12.0 MeV to 70.0 MeV energy window.

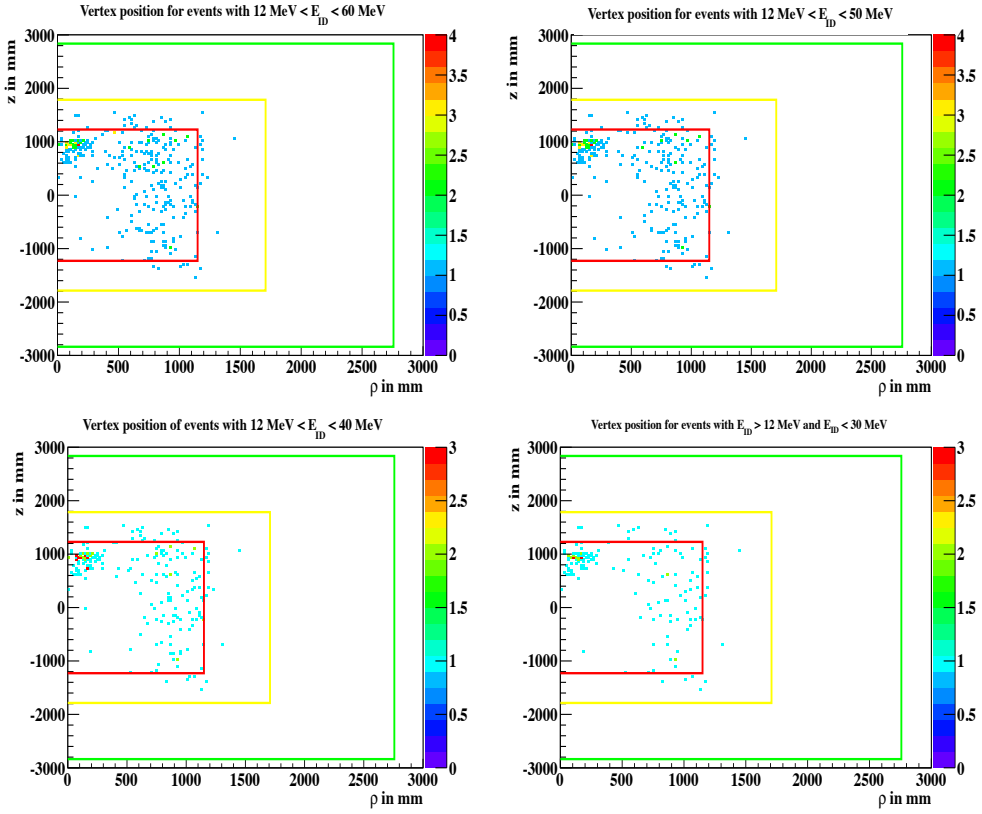

Figure 6.11: Vertices of the prompt signals for different values of the upper energy limit: 60 MeV (top left), 50 MeV (top right), 40 MeV (bottom left) and 30 MeV (bottom right).

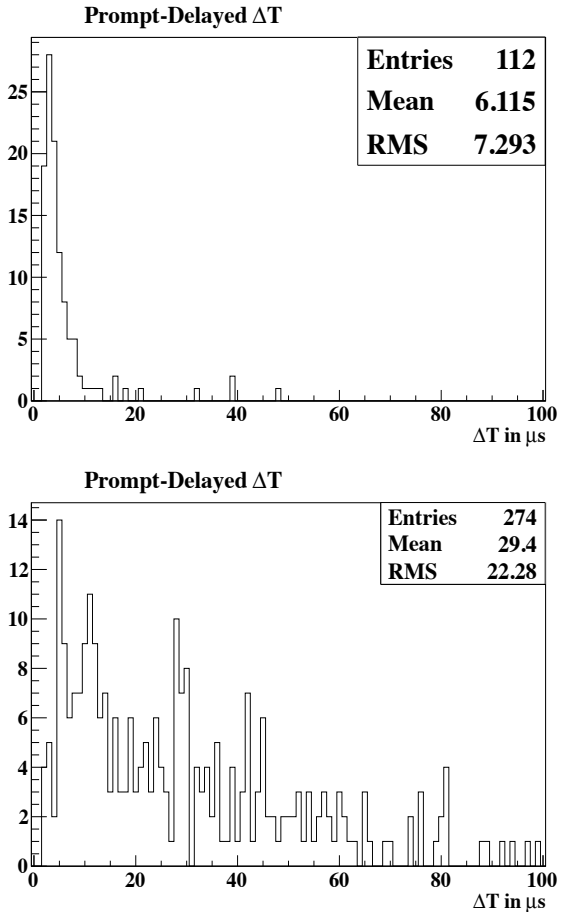

Figure 6.12: Prompt-Delayed ΔT distributions for stopping muons (top, vertices under the chimney cylinder) and fast neutrons (bottom, rest of the events).

MeV in Fig. 6.11 (top left), 50 MeV in (top right), 40 MeV in (bottom left) and 30 MeV in (bottom right). The value of 30 MeV has been already shown in Fig. 6.4 but we do include it here to facilitate comparisons. What we observe clearly in the plots of Fig. 6.10 and Fig. 6.11 is the following: as the maximum energies present in the distributions become smaller then lesser events exist in the interior region of the ID. In particular for $E_{ID} < 30$ MeV far lesser events exist with ρ smaller than 700 mm. This is, of course, the expected signature of an incoming high energetic particle: the more energetic it is the more it penetrates the main body of the detector. Finally, we should mention that in the center and bottom of the detector no events are shown as it is expected for fast neutrons.

In Fig. 6.12 (top) and (bottom) we show the ΔT distributions for stopping muon candidates (top) and fast neutrons (bottom). This rough separation

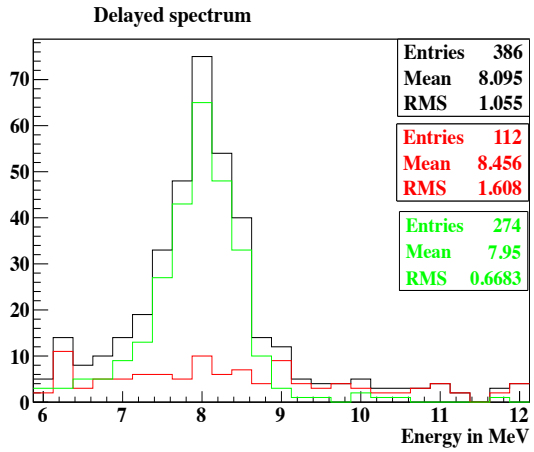

Figure 6.13: The delayed spectrum of the prompt events with 12 < E < 70 MeV. In red the stopping muon and in green the fast neutron contributions. The separation was based on the cylinder fiducial cut of Sec. 6.2.

was done with the fiducial cylinder right under the chimney that its dimensions were mentioned in Sec. 6.2. Again one sees that stopping muons have ΔT with a sharp cut-off at 12 μs while fast neutrons have the required mean ΔT value of $\sim$ 30 μs. It should be emphasized that these results are confirmed again albeit with higher statistics. Finally in Fig. 6.13 we show the delayed spectra for the events with 12 MeV < E_{prompt} < 70 MeV keeping the same color convention as in Sec. 6.2. We still see the Gd peak in the delayed events corresponding to fast neutrons as it was anticipated.

The existence of fast neutrons and stopping muons in the selected candidate sample should be by now well-understood. Nonetheless, all previous considerations also reveal another issue relevant for the first period of Double Chooz. This is an inefficiency of the IV to identify those muons that pass from the chimney. Actually this feature (this inefficiency) of the detector was known since longtime from simulation studies but the possibility for stopping muons to fake the neutrino signature in this way was only realized after our investigations were completed.

We should also mention that before this work, the ID muon cut was set in 70 MeV as was done in this section. That would have been the proper value according to estimations of the deposited energy. After these findings the muon cut on the ID was lowered to 30 MeV to treat this special case of muons and increase the possibility to tag the subsequent Michel electrons. This action also contributes in the rejection of spallation products as explained in Ref. [242].

We should also remark that the first complete picture on the fast neutron and stopping muon background along with the merits of the muon tagging improvement was presented in Ref. [242, 243]. The stopping muon background is relevant for the first stages of Double Chooz only. After the installation of the upper Outer Veto (OV) right above the chimney, they could be eliminated through an OV coincidence cut.

6.4 Separate the two contributions

To estimate the magnitude of contamination in the neutrino sample originating from fast neutrons and stopping muons we interpolated the high energy tail (E >12 MeV) below the signal. This was done assuming that both contributions continue under the neutrino spectrum in the same flat manner. Nonetheless this is only an assumption. Furthermore, since there are present in the signal two distinct contributions of background there is always the possibility that these two components will have different spectra. That would require the treatment of these two backgrounds separately.

A step before this, would be to split the two background components in the range beyond 12 MeV so that one could perform independent interpolations. To separate stopping muons and fast neutrons we will lean on their distinct characteristics. More precisely, to isolate chimney stopping muons we will use the fiducial volume cut of a cylinder under the chimney:

- z $>$ 0 mm
- z $<$ 1800 mm and,
- $\rho = x^2 + y^2 < 400$ mm

that we already employed extensively in these investigations. Additionally we will apply an extra cut on ΔT:

- ΔT $<$ 12 μs.

We know that muons decay with a mean-time of 2.2 μs and like this there is no possibility to record coincidences with ΔT $>$ 12 μs originating from stopping muons. The events that satisfy the above fiducial and ΔT cuts will be classified as stopping muons; the rest will be fast neutrons. Of course, there is expected to be a small non-purity of fast neutrons in the selected sample of stopping muons, but this amount was found to be small. To state it differently, there will be unavoidably a small part of fast neutrons under the chimney and with ΔT $<$ 12 μs but this impurity will give rise to second order corrections only.

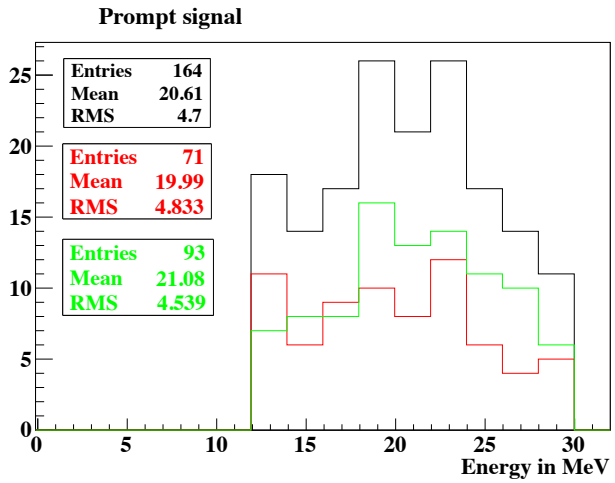

Figure 6.14: High energy spectra, E > 12 MeV, of the neutrino candidates (black). In red we overlap the separated stopping muon component and in green the fast neutrons.

Applying these cuts in the 12 - 30 MeV part of the extended neutrino candidate sample we found that 43 % of the sample consists of stopping muons while the rest 57 % are fast neutrons. The spectra of the separated sample spectra are shown in Fig. 6.14 for energies larger than 12 MeV and with a larger binning.

6.5 Spectra determination

To complete the estimation of these two sources of background we need to determine their distinct spectra; this was done in Ref. [244, 250]. The splitting of the two background components was performed (when needed) according to similar (but not identical) techniques as those presented above but the final results were identical within the expected precision.

Two methods were put forward for the spectra determination. The first [244] leans on the tagging of those events that trigger the IV depositing non-zero low energy charges, $Q_{IV} < 10000.0$ DUQ. According to the official selection criteria these events are not rejected. A soft cut on the IV PMT multiplicity was also applied ($N^{IV}_{HIT} \geq 2$) to eliminate the possibility of accumulating accidental events in the IV (e.g. natural radioactivity) with these decisions. Like this the spectra of the stopping muons and fast neutrons were inferred by the already selected sample. The stopping muon spectrum was

found to be flat and the fast neutrons spectrum appeared to rise in the low energy regime, E < 3.0 MeV.

On the other hand, in the second technique [250] the fast neutron shape was determined by the prompt-delayed coincidences that trigger the IV within the charge range of 10,000.0 DUQ < Q_{IV} < 100,000.0 DUQ. These values were found to isolate a good sample of tagged fast neutrons while rejecting cosmic muons that could induce the same signature. The stopping muon spectrum was found altering the delayed energy spectrum (this time) from 6 - 12 MeV to 12 - 30 MeV. It is true that in this high energy range we expect no neutron captures and the only coincidences recorded are due to the energetic Michel electrons. According to these investigations both spectra showed a small falling trend towards the low energy bins.

To account for these two controversial results the central value, obtained from the mean between these analyses, was used in the final oscillation fit. The total rate was:

$$0.83 \pm 0.38 \tag{6.3}$$

fast neutrons and stopping muons per day. The error was artificially augmented to cover both studies. The combined fast neutron and stopping muon spectrum that was used in the rate plus shape analysis is that shown in Fig. 6.15. One can identify the "trumpet" like shape in the low energy bins that was devised to reconcile the two contradictory approaches (the one falling and the other rising at low energies). The decision to use a more loose spectrum like this, with a bigger error seed to be conservative enough and validated. In the pull-term analysis an extra term corresponding to this background was also employed. After the minimization the central value decreased by 5 % with almost unchanged uncertainty.

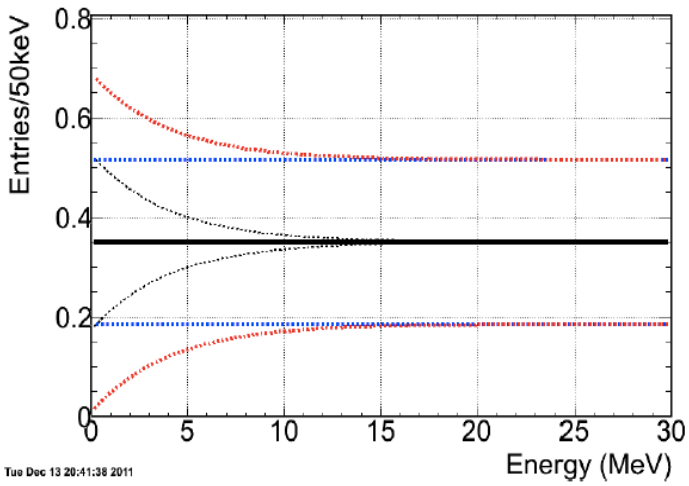

Figure 6.15: The combined fast neutron - stopping muon spectrum employed in the oscillation analysis framework. In the low energy bins the error over the central value is big to account for the different possibilities.

Chapter 7

Light Noise Rejection with Sphericity and Aplanarity

Light Noise (LN) was briefly mentioned in Chapter 3 while discussing neutrino selection. It refers to artificial, instrumental light that it is emitted sporadically from some PMT bases. Laboratory tests and on-site measurements have revealed some basic characteristics of LN [246, 247]. We now know, for example, that the wavelength of the light emitted is at the visible spectrum and that LN flashers do not excite the scintillator. For the first publication, the LN was tamed through the use of two combined cuts as it has been already described.

In this chapter we shall present yet another method to tackle LN. This work was completed during the parallel completion of the first Double Chooz (DC) publication but some of our conclusions validated the results present in that paper. Even though our algorithms were not used for the first publication, they did help the collaboration to further decipher LN.

7.1 Introduction, general arguments

The Double Chooz (DC) Inner Detector (ID) is a cylindrical volume of roughly 6 m in height and diameter instrumented by 390 photomultiplier tubes (PMTs) attached to the Buffer steal vessel. The "good" events happening in the target or the gamma catcher excite the scintillator and should illuminate the detector in a spherical fashion. How spherical an event would be depends partly on the nature of the interaction. For example, we expect neutron captures on hydrogen or gadolinium to produce clear spherical events illuminating equally all channels of the detector while LN events are

expected to lack this particular topological structure. The official Double Chooz LN rejection cuts, devised for the first publication:

- $Q_{MAX}/Q_{TOT} < 0.09$ and $RMS(TS) < 40.0$ ns for the prompt and,
- $Q_{MAX}/Q_{TOT} < 0.06$ and $RMS(TS) < 40.0$ ns for the delayed signals,

silently adhere to this logic. For example, the Q_{MAX}/Q_{TOT} discriminating variable leans heavily on the realization that for valid triggers all channels must evenly record signals. In particular, there should not be a "preferred" channel that reads-out most of the observed charge. This rational assumption is further motivated/validated by Monte Carlo simulations (MC).

In this study we tried to initiate a method to characterize the topology of the events recorded from Double Chooz. The scheme has its very beginnings to the area of pure mathematics but finds direct applications to the field of accelerator physics. In brief, we proposed the use of two new variables to distinguish physics events with "good" shape from LN triggers. The two variables proposed for this purpose are the **sphericity** and **aplanarity** discriminating variables. The way the sphericity tensor was formulated is novel and it was done for the sole purpose of DC. We will present how these considerations fit in Double Chooz and then we will directly turn them to the study and rejection of LN.

From a first look, this work seems elegant and powerful; especially when it comes to the treatment of high energy light noise events similar to those reported in [248]. The majority of our main assumptions and conclusions are quite solid and validated through calibration data, signaling that no real physics events are rejected. The scheme penetrates the LN issue of PMT 263 and confirms from another direction the decision taken by the collaboration for a harder Q_{MAX}/Q_{TOT} on the delayed signal. It is also optimistic in the sense that a better understanding towards the LN behavior can be achieved. The work thus realized depends on a specific definition of the sphericity tensor. Other variants of this framework had been pursued but they turned out to be less performant.

7.2 Highly penetrating Light Noise

The framework we are about to describe was developed as an attempt to classify the events taking place inside the Double Chooz detector according to their degree of sphericality. Initially, we started this campaign with the sole purpose to turn this edifice against LN. Nonetheless, the variables proposed should be considered as a more general frame to discriminate events according

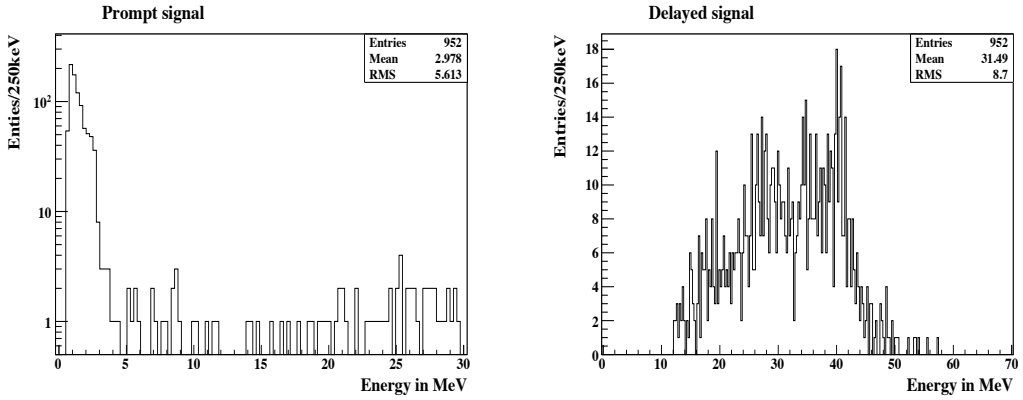

Figure 7.1: Prompt (left) and delayed (right) energy spectra for the correlated background candidate events.

to their topologies. Its first application was towards the treatment of a very specific LN pattern relevant for correlated background studies. Since this background (BG) played an important role in the gradual acceptance of the potential of these ideas we plan to describe it here to some extent. Later on we shall describe a way to tame it.

We previously demonstrated (Chapter 6) that part of the correlated BG, at least for the first phase of DC, consists of two contributions: chimney stopping muons (CSM) and fast neutrons (FN). To investigate CSM there is a clever way to isolate a pure sample by changing the delayed energy window from 12 to 70 MeV. Since single neutron captures can not release energies larger than 12 MeV we assure that we record coincidences of the muon - Michel electron chain. This conclusion came independently to many investigators including the author [249, 250].

Adhering to this logic and maintaining the official cuts for neutrino selection one obtains the energy spectra of fig. 7.1 for the prompt and the delayed events. The delayed events seem to have the desired Michel spectrum and the prompt spectrum consists of two regions: one below 3 MeV having an almost exponentially falling decay shape and another beyond 3 MeV that continues more or less flat up to higher energies. Nevertheless, as it is shown in fig. 7.2 the time and space correlation distributions cry out for another solution since for neutron captures one would expect a prompt - delayed distance smaller than 1.5 m. Also for the prompt - delayed time difference we would expect to find an exponential curve of roughly 30 μs mean.

In addition to all these, the vertex positioning of the prompt events, figure 7.3 (left), is quite puzzling since one would, in principle, expect events localized strictly under the chimney. The riddle is finally resolved looking at

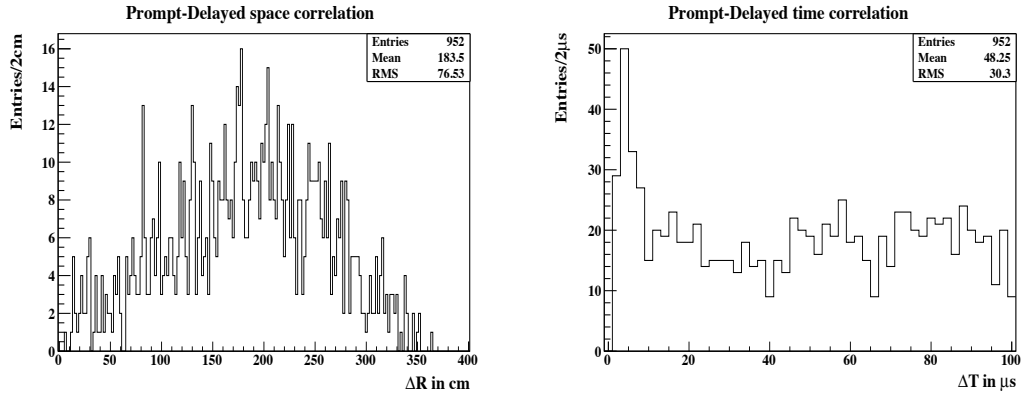

Figure 7.2: Space (left) and time (right) correlation distributions for the correlated background candidate events.

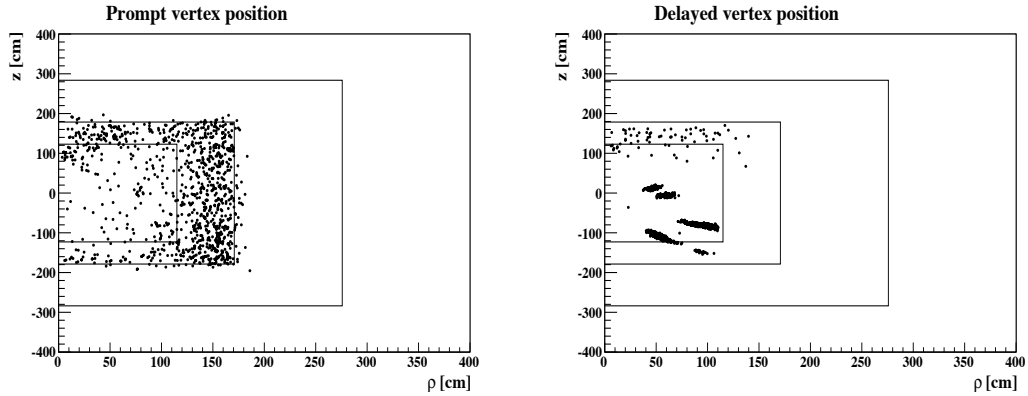

Figure 7.3: Prompt (left) and delayed (right) vertex positioning for the correlated background candidate events.

the delayed vertices, fig. 7.3 (right). It is then clear that most of the delayed coincidences are LN events of a very penetrating power (since they defy both LN tagging cuts) with the corresponding prompts to be accidentals. That was in a sense anticipated from the flat profile of the prompt - delayed time correlation distribution.

It is of course, unsatisfactory to see light noise patterns like these penetrating both our rejection cuts; even the stronger $Q_{MAX}/Q_{TOT} < 0.06$. At least the energy spectrum seems to fall quickly below 12 MeV, Fig. 7.1 (right), signaling that no significant LN contamination is present in the neutrino sample. This population becomes important when it comes to studies beyond the 12 MeV limit as it is the case for correlated background. In what shall follow we will lay down a method to tackle this unwanted LN background.

7.3 Sphericity and Aplanarity

Having a number of n three dimensional vectors $\vec{r}_i$, $i = 1, 2, 3..., n$, one can form the sphericity tensor $S^{\alpha\beta}$ defined as:

$$S^{\alpha\beta} = \sum_{i=1}^{n} r_i^a r_i^b / \sum_{i=1}^{n} |\vec{r}_i|^2, \tag{7.1}$$

with $\alpha = x, y, z$ and r_i^x, r_i^y, r_i^z the three cartesian coordinates of $\vec{r}_i$, $\vec{r}_i = (r_i^x, r_i^y, r_i^z)$. This can always be done. The importance of this mathematical abstraction lies in the fact the eigenvalues of the sphericity tensor hold essential information about the geometrical orientation of our vector set [251]. In particular with the eigenvalues $\{ \lambda_i, \ i = 1, 2, 3 \}$ of $S^{\alpha\beta}$, following the convention $\lambda_1 < \lambda_2 < \lambda_3$, one can form sphericity:

$$S = \frac{3}{2}(\lambda_1 + \lambda_2) \tag{7.2}$$

and aplanarity:

$$A = \frac{3}{2}\lambda_1. \tag{7.3}$$

These variables have been extensively used in the past for the characterization of multi-jet events in accelerator experiments like LEP or HERA. For more details one should consult references and documentation from the relevant bibliography; see for instance Ref. [252]. Accordingly for a pure spherical event sphericity must have a value close to one while non-spherical configurations have small values of sphericity, around zero. The sphericity allowed values are ranging from zero to one, $0 \leqslant S \leqslant 1$. The more close to one sphericity is the more spherical configuration we have.

Aplanarity on the other hand takes values from 0 to 0.5, $0 \leqslant A \leqslant 0.5$. It describes how aplanar the set of vectors in question is. For example, four vectors lying in the same plane will have small (close to zero) aplanarity, while four randomly oriented vectors are expected to have larger values in aplanarity. A totally random set of vectors is expected to have aplanarity close to one-half. In fig. 7.4 we demonstrate with three simple examples the logic behind these concepts.

In accelerator experiments the role of $\vec{r}_i$ is played by the various particle momenta, summing over the linear momenta of the particles created in a collision. For the purpose of DC we propose to apply the sphericity formalism to the vector set $\vec{Q}_i = Q_i \ \hat{r}_i$ with Q_i the charge recorded by the i-th channel and $\hat{r}_i$ the unit vector from the vertex of the event, as reported by `RecoBAMA`,

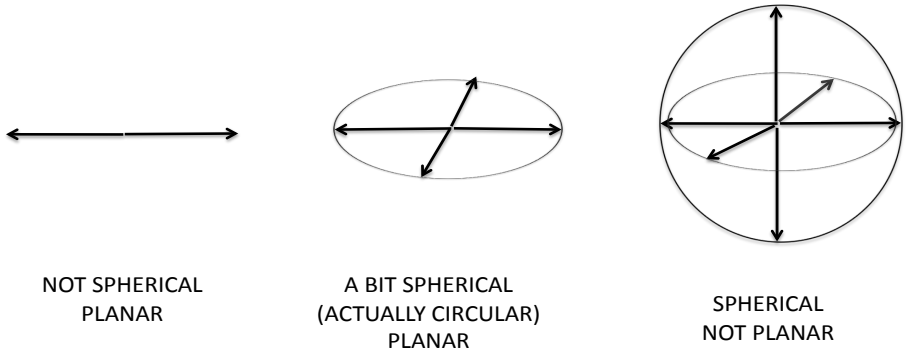

Figure 7.4: Three simple vector sets to demonstrate the ideas behind sphericity and aplanarity.

to the position of each PMT, thus $i = 0, 1, 2, ..., 391$, with channels 294 and 295 to be skipped as expected [253]. We also skip the fourteen switched off PMT since the signal recorded by them (if any) it's not to be trusted or compared with the rest of the channels. When a vertex is not reconstructed we use the point in the center of the detector (0, 0, 0)[1]. With this recipe the sphericity tensor can be written as:

$$S^{\alpha\beta} = \sum_{ch} Q_i^a Q_i^b / \sum_{ch} |\vec{Q}_i|^2, \tag{7.4}$$

with $\sum_{ch}$ as explained above. We now make the assumption (to be validated) that good physics events that happen in the target (NT) and the gamma catcher (GC) volumes should have high sphericity. We would also want them not to lay in the same plane so we also demand a big value of aplanarity. These two simple assumptions hold the essentials of what we do. In the following investigations this mathematical edifice will be further advanced in the path of data analysis formal conventions. Nonetheless, behind the formal development of our cutting strategy one should always remember this simple geometrical picture as exposed in fig. 7.4. Other discussions regarding the sphericity and aplanarity concepts could be found in [254, 255].

[1]In the below 70 MeV region cases where a vertex is not reconstructed are rare and they could be neglected for this study. This will become important in the classification of muons.

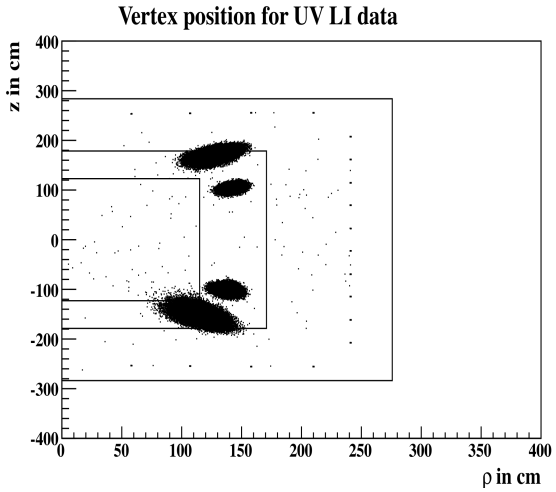

Figure 7.5: Vertex positions for the UV ID-LI runs we studied.

7.4 Calibration data

To begin with the cuts optimization, determine the efficiencies and get a further understanding of how this abstract machinery behaves with real data, we shall test sphericity and aplanarity with calibration runs that come from the ID Light Injection system (ID-LI) and from the deployed radioactive sources.

7.4.1 Light Injection data

ID-LI data have the enormous advantage of the external trigger. This by itself guarantees that only events from the light injectors are recorded, since the probability for other sources of signal to happen in the same, small sampling window (256 ns) is negligible. We decided to use for this study strictly runs with ultra-violet (UV) light since we know that this wavelength excites the scintillator and in principle should result spherical events. We studied a sufficient number of runs from different fibers but always with UV light.

The vertices, as reported by `RecoBAMA` for all these runs can be found in fig. 7.5. We clearly see different populations arising from the different fibers' activation. We also see vertices in other places in the TG and the GC and a small class of events distributed in the periphery of the buffer, from where light originates. In fig. 7.6 three plots can be found: sphericity, aplanarity distributions and a scatter plot of sphericity versus aplanarity (abbreviated as sph and apla from now on). One could clearly see and verify that our

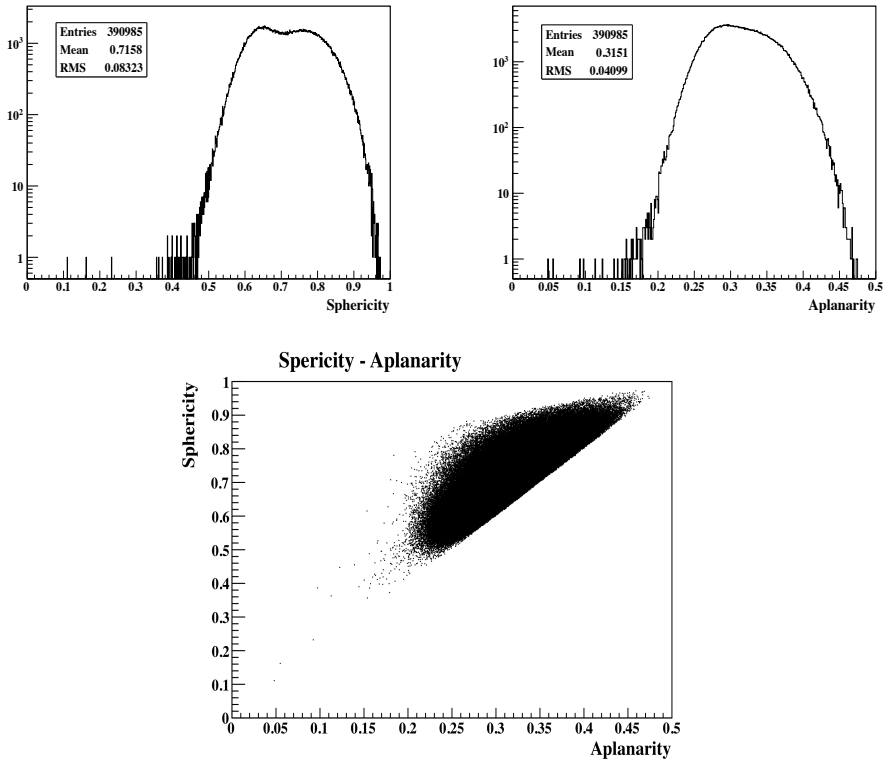

Figure 7.6: Sphericity (top left), aplanarity (top right) distributions and a scatter plot (bottom) of them.

initial premonitions on the shape of the real events are indeed vindicated with ID-LI data. We see in fig. 7.6 (top left) and fig. 7.6 (top right) that sph is far bigger than the value of 0.48 and apla is well beyond the value of 0.18. From fig. 7.6 (bottom) we see that a combined cut of sph < 0.48 and apla < 0.18 is able to create a tight box to isolate the good events. With these two combined cuts the sample is reduced at a 0.028% level.

Note that these cuts can be further strengthened so that a negligible amount of physics loss could be obtained. Nonetheless, in this section we only wanted to show that the sph and apla variables as defined through the sphericity tensor of section 7.3 can give us a handle to describe the shape of the real events. That was done through the use of UV ID-LI data. However, we know that these events come from the edges of ID and even though they do excite the scintillator the primary vertices can be at the very edges of the GC; an issue not that likely for inverse beta decay (IBD) events. This is suggesting that a more tight set of cuts relevant for IBD searches

can be obtained. To this end we used calibration data with radioactive sources to have a better understanding. It is probably hard to overestimate the importance of calibration data like these towards the understanding of efficiencies.

7.4.2 Radioactive sources

The work included in this section was strongly influenced by the initial work conducted in Ref. [256, 257] and the more in depth efforts pursued almost simultaneously in Ref. [258, 259]. Other parts of this work were motivated by arguments presented in Ref. [260, 261]. The final technique we used for this purpose is also described in Ref. [263].

For this study we used all the source deployed calibration data taken over a wide period of time, roughly from June to August 2011. The list of runs is described in Ref. [262] along with some extra details regarding the conditions to which these runs were taken. Briefly, we deal with 141 runs obtained with various sources on the Z-axis (ZA) and the Guide Tube (GT). The sources we studied are ^{137}Cs, ^{68}Ge, ^{60}Co and ^{252}Cf, and that means that we have events in a wide range of energies from, roughly, 0.5 to 12.0 MeV. A region very important for IBD searches. Further informations regarding the calibration procedure, the sources' characteristics and manufacturing can be found in [264, 265].

To select the signals arising form the sources and not those from other contributions we first discard a time interval of 1 μs after a muon, rejecting like this both muons and muon daughters. Muons are tagged from the charge depositions in the ID and the Inner Veto (IV). In particular, we call a muon an event that satisfies at least one of the conditions:

- $E_{ID} > 30$ MeV,
- $Q_{IV} > 10000$ DUQ.

After this first reduction, two extra sets of cuts are applied in the observed energies and the DR distance between the vertex of the event and the source positioning:

- Tight energy cuts around the energy peaks.
- DR < 700 mm.

The peaks related to the energy lines of the radioactive sources are clearly visible looking at the data so that one can have a firm idea where to set the required cuts. For example in fig. 7.7 we draw the energy distribution for

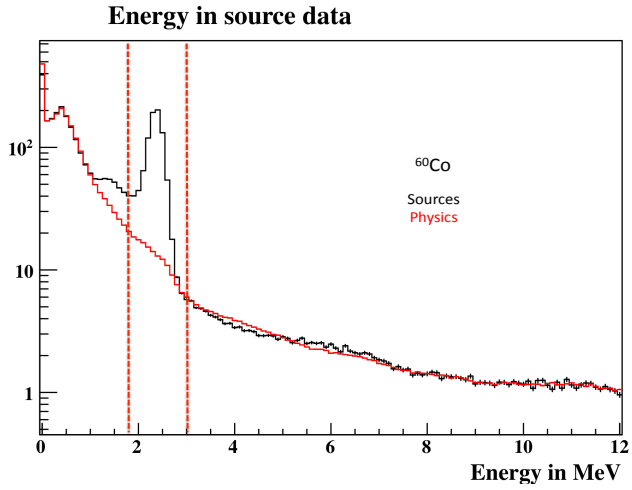

Figure 7.7: Energy spectrum of the ^{60}Co radioactive source. The selection cuts around the source signal are shown with the red vertical lines.

all the ^{60}Co runs, both in the ZA and the GT. In red we overlap also what would be expected using physics runs. Of course the excess related to the presence of the source signal is absent in the red histogram. The cuts around the source's energy line are also depicted with the dashed, red vertical lines.

The DR cut optimization was influenced by arguments given in [260]. More precisely, the DR distributions for the source data were drawn, overlapped with the expected distributions coming from neutrino physics runs. This is done in fig. 7.8 where the DR distribution arising from the ^{60}Co calibration runs (black) is overlapped with the one expected from physics runs (red). The contribution coming from the ^{60}Co source is evident. The DR cut value finally chosen was that of 700.0 mm. It should be emphasized that this optimal DR distance is different for the various sources. We did, nonetheless, stick to the same DR = 700.0 mm cut for all the sources.

Only these two cuts were used for the isolation of the source signal. We could have also used one or more of the many LN tagging cuts to further reduce the expected pollution coming from LN. This was actually done in our initial works [254, 255]. In this study we decided not to apply any LN rejection cut, accumulating thus as much LN as possible. Like this we gain in the background LN statistics. We believe that this is more appropriate since it is after all our purpose to study the LN rejection ability of our discriminating variables.

To continue we chose an equal number of physics runs as reference. The runs chosen were carefully selected so that their creation dates match closely

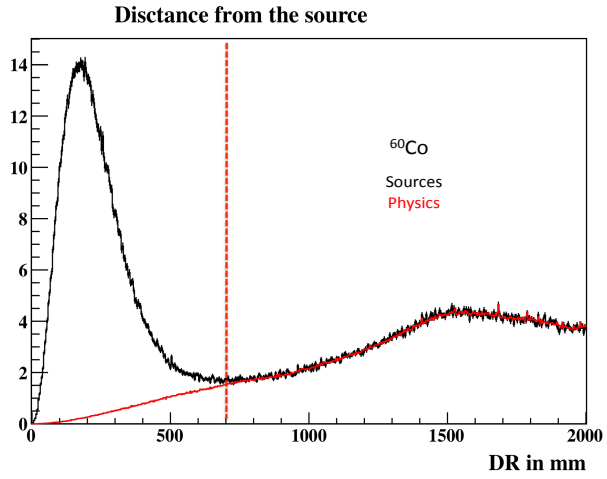

Figure 7.8: DR cut optimization.

in time with those of calibration runs. Note that this is critical to the method we shall lay down. Then, normalizing both calibration and physics runs to their total live-time we obtain the plots of fig. 7.9. The black lines show the data for the four different sources while the overlapped red lines represent the reference runs. In this technique the position of the optimum cut that prevents the loss of physics events is revealed from the place where both curves start to diverge, signaling the presence of source data.

From these plots another set of cuts for sph and apla can be devised; namely sph > 0.5 and apla > 0.2. This new set is not very different from the one devised from UV data but it is more tight as it was anticipated. We shall call these cuts the *loose shape discrimination cuts* and they are, we believe, the minimum we can do to insure no physics loss. We state them clearly:

- $sph > 0.5$ and,
- $apla > 0.2$.

One comment should be done: in our initial attempts to apply this method of calibration data to the optimization of the sph and apla cuts, small deviations were seen between the black and red histograms in the low shp ~ 0.2 and apla ~ 0.05 regions [254, 255]. These differences were then ascribed to changes in the LN patterns. Choosing carefully the calibration and reference runs to be taken in close periods of time we see that this disagreement vanishes.

Now, to further strength our selection we plan to devise another set of cuts for the region inside the NT. These would be the *strict shape discrimination*

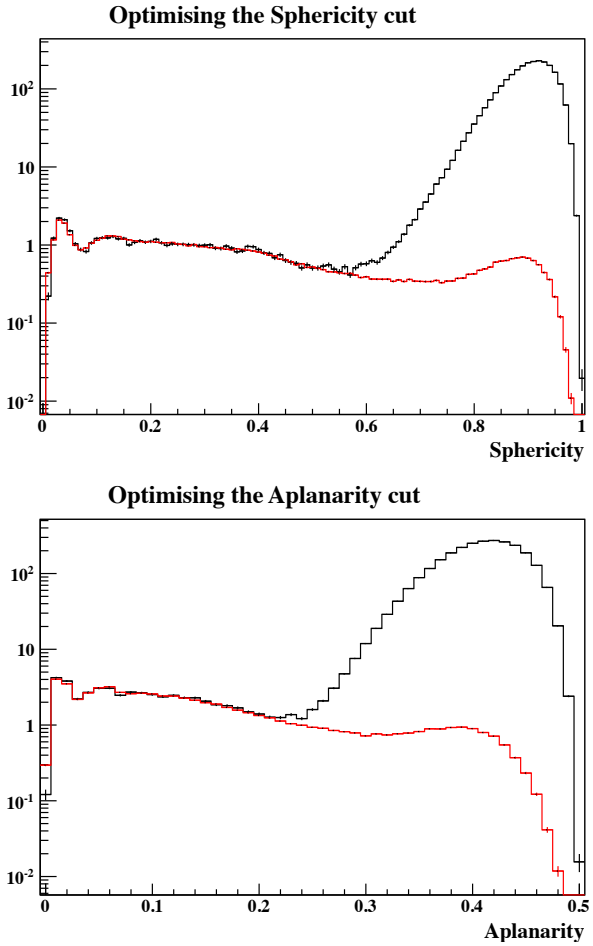

Figure 7.9: Sphericity (top) and aplanarity (bottom) distributions with black lines. Overlapped on them the corresponding normalized distributions for physics runs are shown (red lines).

cuts. We chose to do so, knowing a priori that the shape variables must have more spherical character when it comes to events originating from the center of the ID, as opposed to those arising from the edges of GC. In doing so we redraw the distributions of fig. 7.9 with the additional cut of demanding the recorded vertices to lie inside the NT. The distributions we get (fig. 7.10) are indeed indicative that a more tighter approach can be thus obtained. We see that the combined cuts on:

- sph > 0.62 and,
- apla > 0.22.

do the same job as the relaxed ones for the rest of the volume. Even if we are far away from the final optimization of our cuts suitable for neutrino

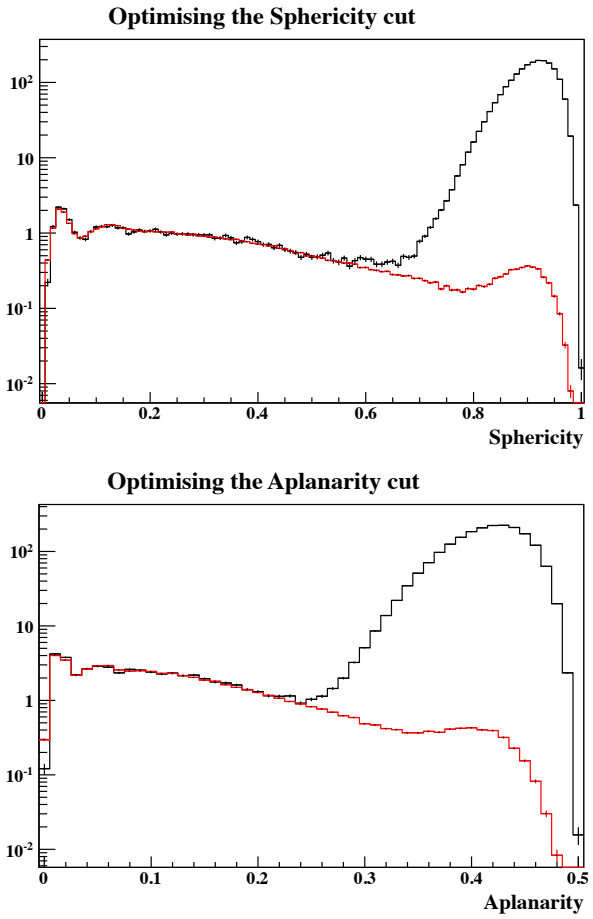

Figure 7.10: Sphericity (top) and aplanarity (bottom) distributions (black). Overlapped on them (in red) the corresponding normalised distributions for physics runs are shown. Only events inside the target are considered.

selection, we do see that a distinct approach for events inside and outside the NT shares a lot of merits, since it allows us to use harder cuts inside the target region.

One final comment is also important: from the sph distribution of fig. 7.10 (top) we clearly see that the deviations between the two curves start a bit before the 0.62 selected cut. This is true and it is related to the ^{137}Cs source and the energy dependence of both sph and apla. We shall nevertheless hold this 0.62 sphericity cut for the NT knowing that the associated rejection inefficiencies are indeed small. More information on this feature will be given in the next section.

7.5 Energy and position dependencies

The results derived in the previous section were determined by the aid of calibration data with radioactive sources deployed inside the Inner Detector. All source calibration data were used; this allowed us to enhance the statistics and minimize the associated statistical errors. It also permit us to have an overall picture regarding the minimal cuts on sph and apla that insure no significant loss of real, physics events. The large number of runs used for this study washed out most of the systematic errors coming from possible changes in the physics background of the reference runs.

Nonetheless, it is important to emphasize that treating all calibration runs on an equal footing, as we did, we are still sensitive to second order corrections arising from possible energy and position dependencies in the ID. State it differently, the method we chose to follow is sufficient to give us a first idea on the optimal cutting strategy that minimizes systematic biases but further refinements are still possible. For example, if the sph distributions are narrower beyond, say, 2.0 MeV then bigger inefficiencies are expected to be seen with ^{137}Cs data. To this end, let us mention that we are aware of the possible position dependences in the ID (energy also changes, Ref. [261]) and we expect from general arguments high energy events to be more spherical and aplanar since they fire more PMTs and the energy scale is such that threshold effects related to reconstruction are small.

In this section we tried to give affirmative answers to these concerns. Firstly, the variation patterns of sph and apla with the deposited energy were worked out using data in the center of the detector. Then the inefficiencies were derived treating this time each source separately. For this work we used data in different positions but always with the same source. The sph and apla dependences as we move along the Z-axis were also deduced separately for each source. Finally, the rejection inefficiencies were inferred examining single runs with sources on specific positions in the detector. In these cases, the limited statistics dominates systematic and statistical errors but the final results are in good agreement with previous considerations.

7.5.1 Disentangling the energy dependencies

The first question we tried to answer was the sph - apla dependence as a function of energy. For this purpose we used data in the center of the detector taken with the four ^{137}Cs, ^{68}Ge, ^{60}Co and ^{252}Cf radioactive sources. All available runs were used and the technique to isolate signals and to subtract the physics background was essentially the one presented in the previous

Radioactive source	Energy (MeV)
^{137}Cs	0.662
^{68}Ge	1.022
^{60}Co	2.5
^{252}Cf	8.0

Table 7.1: Energies peaks of the radioactive sources that were used for these analyses.

section. For consistency we include in Table 7.1 the energy peaks associated with each source. More informations on the calibration sources should be searched in Ref. [264, 265].

The results are shown in fig. 7.11 (top) and fig. 7.11 (bottom) for sphericity and aplanarity respectively. They are presented in terms of the ratios of sph and apla with reference the corresponding values at the ^{252}Cf 8.0 MeV neutron peak. The obvious conclusion read-out by both plots is that sph and apla increase as a function of energy. That was of course anticipated. The overall differences are of the order of 6 % for sph and 12 % for aplanarity in the 0.5 - 8.0 MeV range. Note that energy dependencies like these can be the case for every discriminating variable. In this study we used single runs of roughly one hour for most of the sources; this limits somehow the statistics but our final conclusions are, of course, solid.

Following the previous results on the energy dependence, it should be evident that the optimal cuts on sph and apla might be slightly different for the various energy regions. Stated differently, the rejection inefficiencies for a sharp cut on sph and/or apla will have a certain energy dependence. Note that this is a feature probably present to all other LN tagging variables. Remember, for instance, that the Q_{MAX}/Q_{TOT} cuts relevant for neutrino selection are different for the prompt and delayed signals and the tighter $Q_{MAX}/Q_{TOT} < 0.06$ cut on the 6.0 - 12.0 MeV range reflects this dependence. Mixing all data coming from different energy peaks this energy dependence it somehow washed out and hidden.

To avoid this complication, the ideal would be to have an equal number of events in the whole 0.5 - 12.0 MeV window. Nonetheless, this is not the case. Previously, in order to enhance the sample statistics we mixed all the calibration data. In this section each source will be treated separately regardless to its position inside the ID. The position dependencies will be treated subsequently. Note that there is still enough statistics for the investigations we need to pursue.

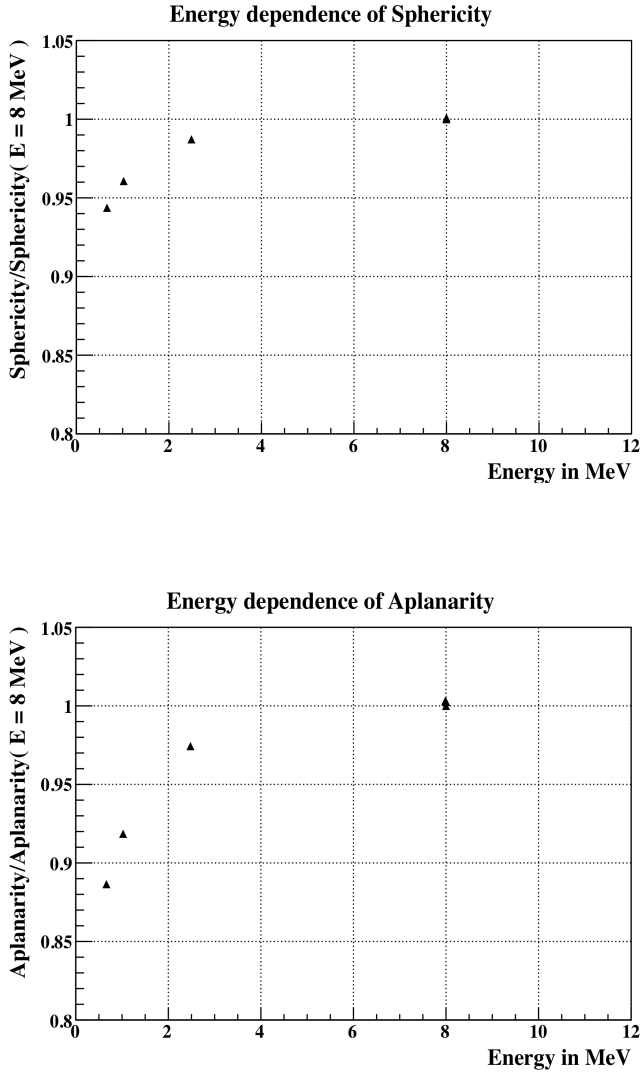

Figure 7.11: Sphericity (top) and aplanarity (bottom) dependence with energy. In both plots the ratios with respect to the 8.0 MeV neutron peak are shown.

First, we show the results obtained with the ^{60}Co source in fig. 7.12 (top left) and fig. 7.12 (top right) for sph and apla. In the bottom plots of fig. 7.12 we show the same plots for the NT. In this case we decided to present our results in cumulative distributions following Ref. [259]. In particular we draw the rejection inefficiencies regarding the possible values on the sph and apla

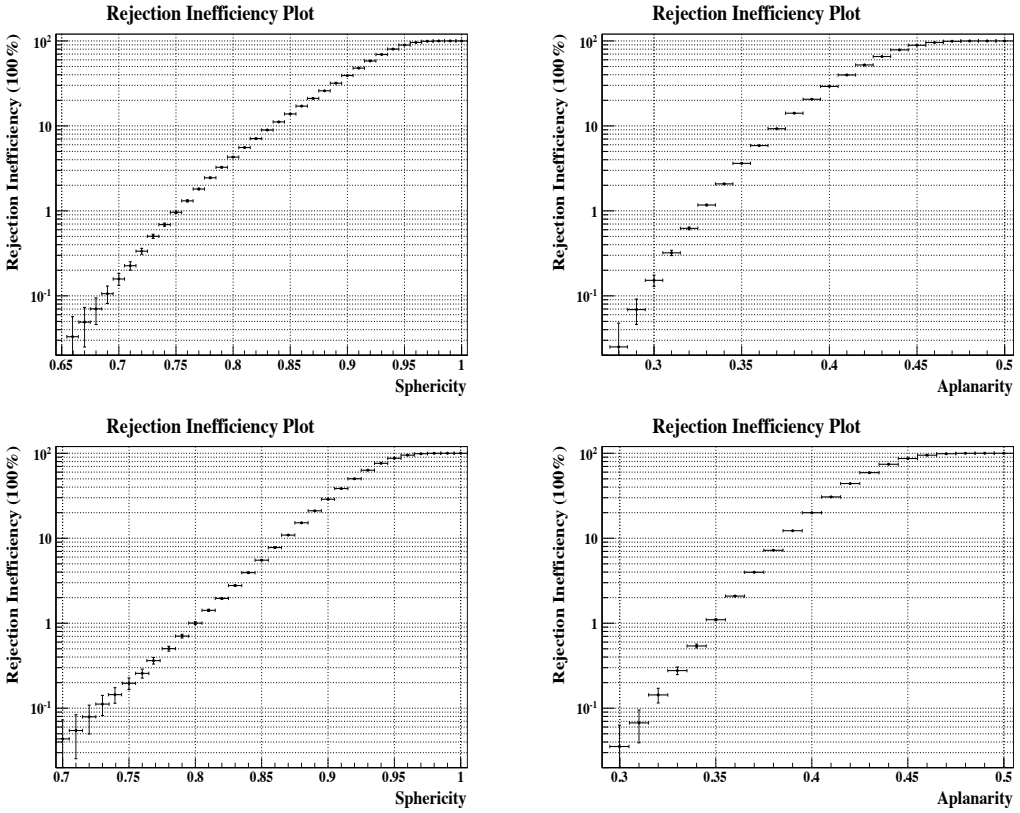

Figure 7.12: Rejection inefficiency plots for sph (top left) and apla (top right) as obtained with the ^{60}Co source. In the bottom plots the same distributions are shown for events in the NT.

cuts. In all plots the per cent ratio of the integrated difference between sources (black histograms) and physics events (red histograms) with respect to the total difference is shown:

$$\frac{\text{Integrated: } (Sources) - (Physics)}{\text{Total: } (Sources) - (Physics)} \quad \% \tag{7.5}$$

From all plots we do see that the cuts already devised for sph and apla are sound and we further do observe that when treating events in the 2.5 MeV line they could have been even more tight. For example, if we accept to lose 1 % of our signal in the NT we can apply a cut at 0.8 for sphericity and 0.35 for aplanarity.

In fig. 7.13 we show exactly the same plots as taken from the ^{252}Cf source data. In top we show the results for the ID and in the bottom plots separately those for the NT only. Again our overall considerations are confirmed and all plots are in good agreement with the ^{60}Co case. What it is strange is that

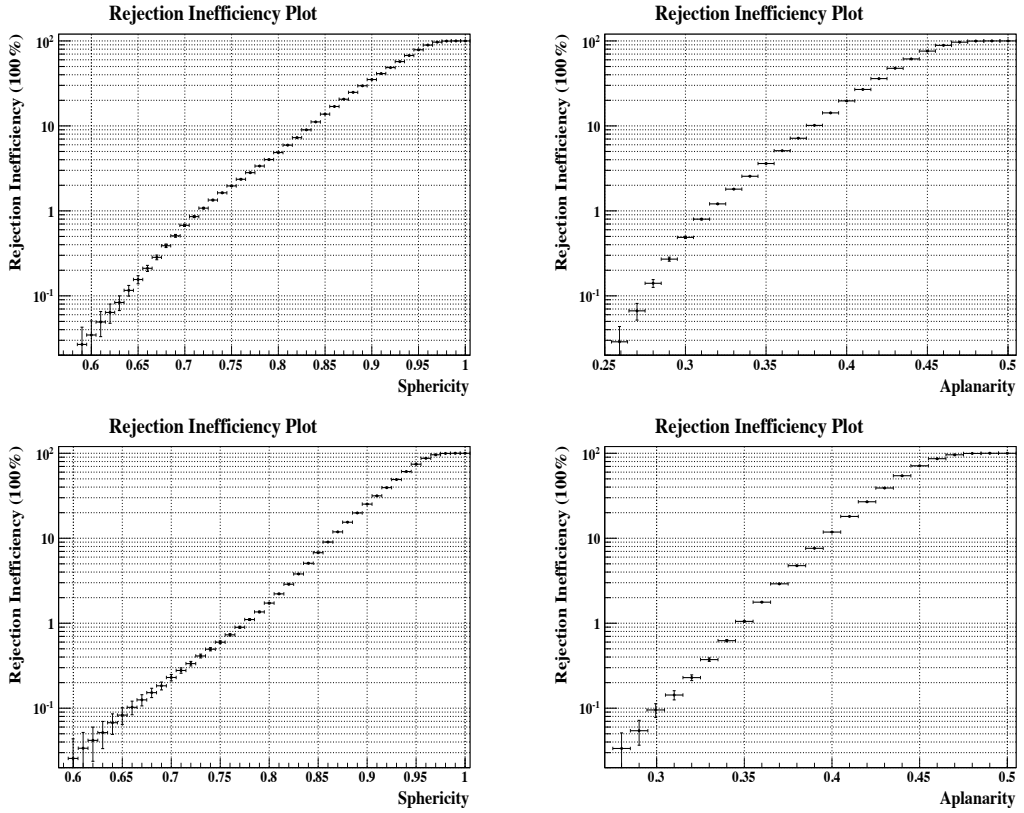

Figure 7.13: Rejection inefficiency plots for sph (top left) and apla (top right) as obtained with the ^{252}Cf source. In the bottom plots the same distributions are shown for events in the NT.

the cuts suggested from both the above sources corresponding to the 2.5 and 8.0 MeV peaks are tighter than those devised previously in Sec. 7.4.2. The source of this discrepancy is to be investigated in the data coming from the low energy ^{137}Cs source.

For instance, in fig. 7.14 we include the sph and apla rejection inefficiency cumulative distributions as obtained with ^{137}Cs data in the usual way; in the top for the ID and in the bottom for the NT. We do see that both for sph and apla, the inefficiencies are starting early, from small values in both variables. In all cases the cuts necessary to ensure no losses of physics events are different from those devised in Sec. 7.4.2. These differences reflect the dependence of sph and apla on energy, already observed in the previous section. Nonetheless, it should be noted that the loss is still small and affordable. Additionally, these small inefficiencies vanish above 1.0 MeV as seen with Germanium data and are not expected to show up in IBD searches. Finally,

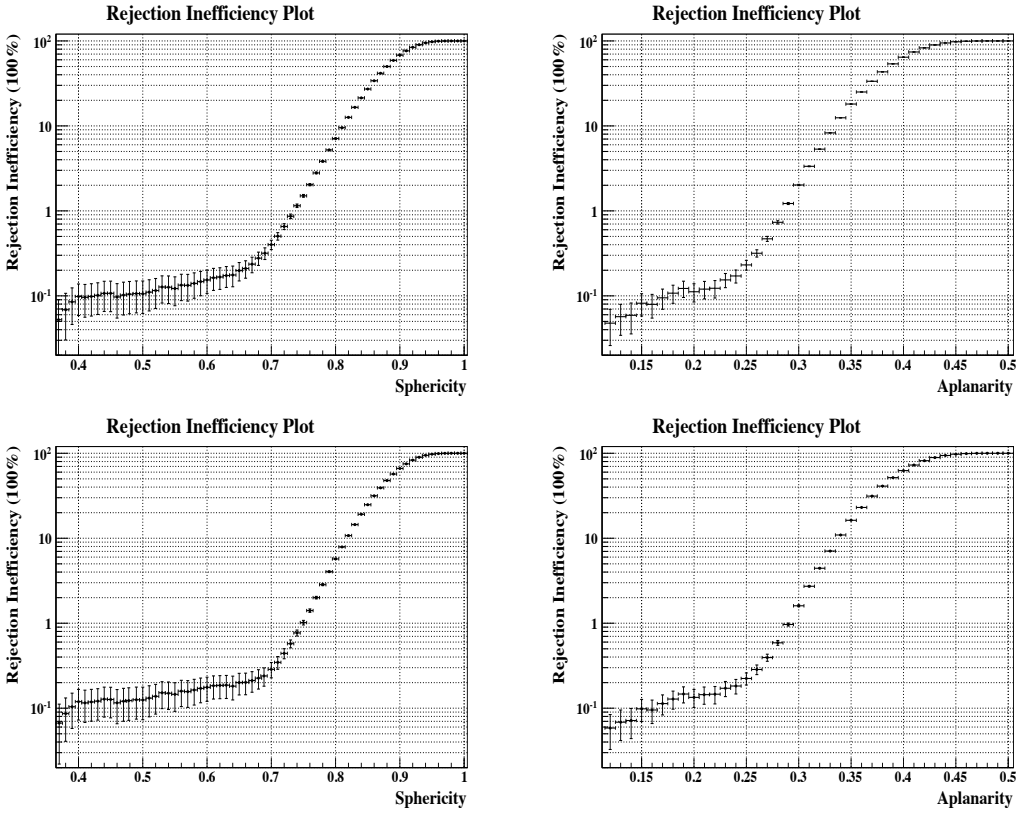

Figure 7.14: Rejection inefficiency plots for sph (top left) and apla (top right) as obtained with the ^{137}Cs source. In the bottom plots the same distributions are shown for events in the NT.

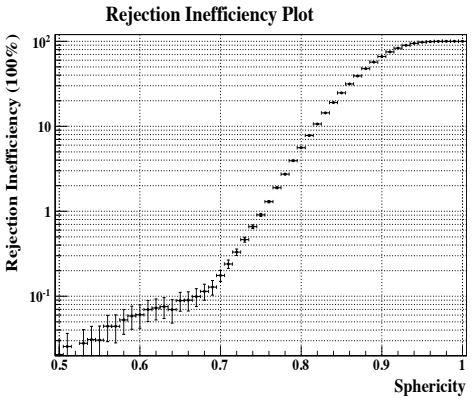

Figure 7.15: Rejection inefficiencies induced by sph in the NT. Data taken with ^{137}Cs; a $Q_{MAX}/Q_{TOT} < 0.09$ cut was also applied.

we should mention that applying an extra on $Q_{MAX}/Q_{TOT} < 0.09$ these low sph and apla events disappear as seen in Fig. 7.15 where the inefficiency plot in the NT is shown for sph with the addition of this extra cut. This is signaling that these events are somehow pathological. Note also that adding a RMS(Ts) < 40 ns cut this tail totally disappears and the inefficiencies show up beyond the 0.60 limit. For all these we shall retain the overall cuts we obtained in Sec. 7.4.2.

7.5.2 Position dependencies along the Z-axis

In this section the way that sph and apla vary with the respect to the position in the ID was investigated. For this purpose only data along the Z-axis (ZA) were considered.

The isolation of the source signals follow the lines already described, with the combined energy and position cuts. In addition to that strategy we add the soft cuts on sph > 0.5 and apla > 0.2; our conclusions are essentially unaffected with the addition of these two extra cuts. The results of this analysis are shown in Fig. 7.16 where the ratios of sph (top) and apla (bottom) are plotted with respect to the corresponding values at the center of the detector; in the x-axis the values of the z coordinate are denoted.

The first thing to notice from both plots in Fig. 7.16 is an obvious dependence with the z coordinate. More precisely, we see that both sph and apla decrease as we move away from the center of the detector. That was of course something anticipated. What it is even more interesting is that we observe a clear combined energy - position dependence since sources like ^{60}Co or ^{252}Cf have a stronger position dependence from this seen with ^{137}Cs and ^{68}Ge. In this respect we can now understand why the ID and NT inefficiencies previously calculated, showed similar patterns for the ^{137}Cs case.

A second interesting feature to note is that both sph and apla variables show an intriguing rise as we approach the z $= \pm$ 750.0 mm points in the ZA. This is surprising since we would expect from general arguments the maximum values in apla and sph to occur in the center of the detector where, from symmetry considerations, all channels should receive light in a totally isotropic way. Nevertheless, data show that this is not the case. After careful examination we confirmed that this feature is unlikely to be an artifact created by our method to isolate signals. Actually, a quick Monte-Carlo study showed that these rise patterns are also present in simulated ^{252}Cf data (Fig. 7.17). It is also important to utter that similar tensions are seen with the energy function; see for instance Ref. [261].

To avoid this extra position dependence enter (and bias) our results concerning the rejection inefficiencies we will finally examine each source (energy)

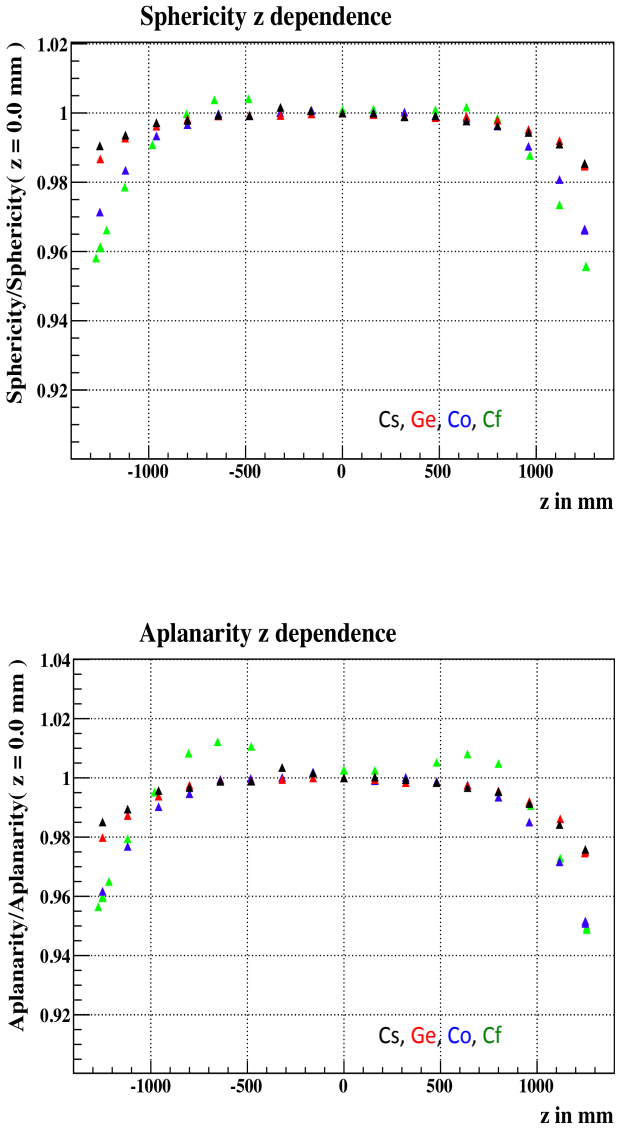

Figure 7.16: Sphericity (top) and aplanarity (bottom) dependence with the z coordinate in the Z-axis. In both plots the ratios with respect to the value in the z = 0.0 mm point are considered. In black we show ^{137}Cs data, in red ^{68}Ge, in blue ^{60}Co, and in green ^{252}Cf.

and position separately. To this end we will analyze individually one run at a time with a source at a specific position. Of course, our analysis technique will be the same as previously.

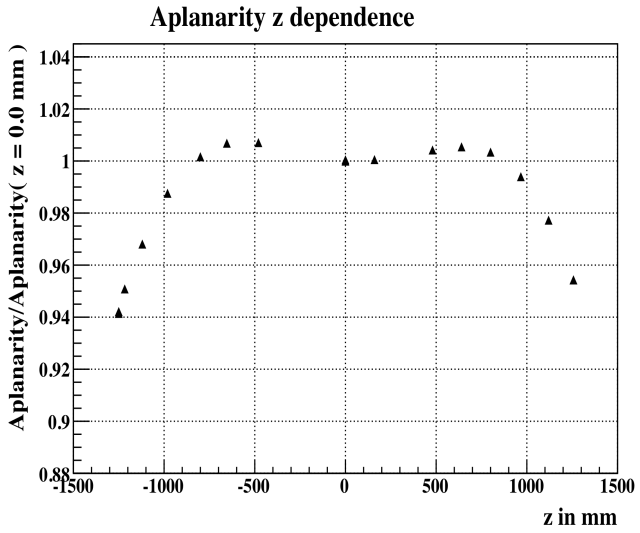

Figure 7.17: The aplanarity dependence along the Z-axis as taken with MC ^{252}Cf data. The "spikes" observed with data at roughly z = ± 750.0 mm are clearly visible.

The results from this analysis are shown in Fig. 7.18 where we draw the rejection inefficiencies as a function of the energy itself. The various energy points were taken as usual with the four deployed sources of Table 7.1. We present the results for two positions in the ZA, at z = 0.0 mm and z = 1250.0 mm. In Fig. 7.18 (top) we show sph and apla for the z = 1250.0 mm point and in Fig. 7.18 (bottom) for z = 0.0 mm. Three differeent cuts of sph and apla are shown. In green for sph > 0.68, in blue for 0.72 and in red for 0.76. Also in green for apla > 0.26, in blue for 0.28 and in red for 0.30.

Even though in this treatment we are dominated by statistical errors and we are sensitive to possible changes in the normalized physics reference runs. We again see that these conclusions (Fig. 7.16) are in good agreement with previous considerations.

7.6 Dependence on the reconstructed vertex

The point of the reconstructed vertex plays an important role in the calculation of both sph and apla in this implementation of the sphericity tensor. In this connection, we should mention that we deliberately decided to chose the interaction location as the starting point of the vectors that build sphericity

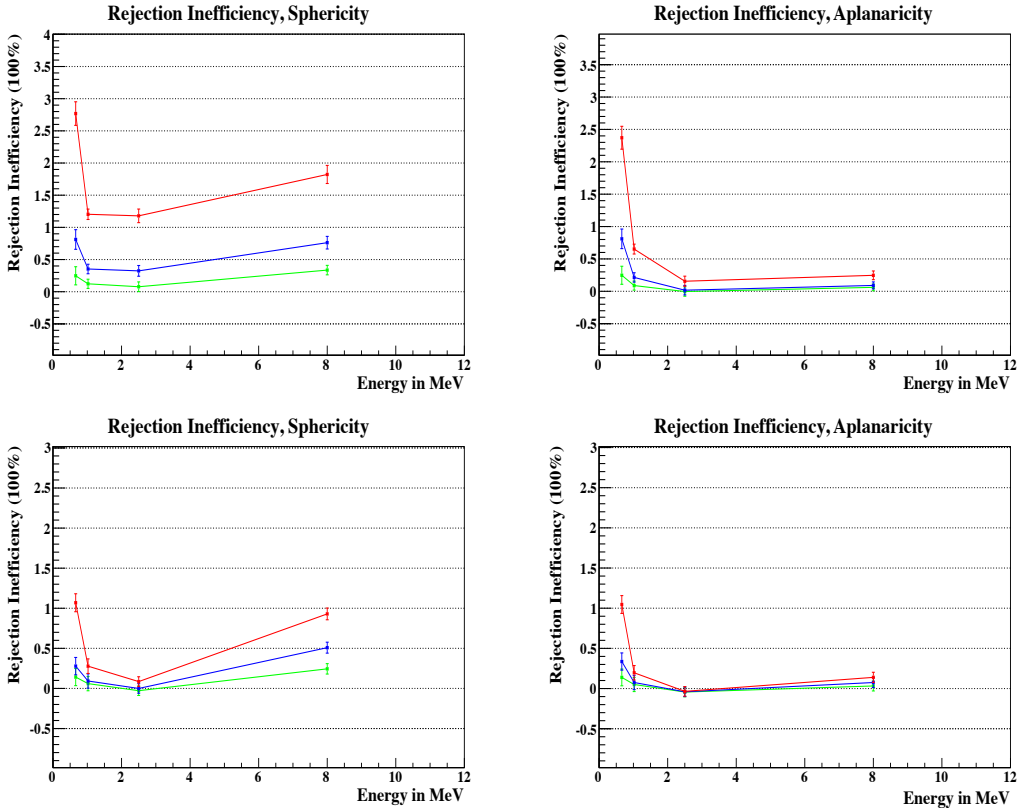

Figure 7.18: Rejection inefficiency plots for sph (left) and apla (right) versus the energy. In the top we show the results for the z = 1250.0 mm point in the Z-axis and in the bottom those for z = 0.0 mm. The cuts values in sphericity are 0.68 (green), 0.72 (blue), 0.76 (red) and in aplanarity 0.26 (green), 0.28 (blue) and 0.30 (red).

tensor since we knew a priori that this choice is going to give us narrower distributions in the sph and apla variables. Many other variants of this framework have been tested but, as of now, this version turned out to be the most performant.

Remember that other LN discrimination variables lean on the position of the reconstructed vertex to correct for the time of flight and improve the resolutions of the calculated distributions. Nonetheless, some could look at this dependence with a tone of suspicion. In this short section we tried to investigate this vertex dependence and its possible effects.

First of all, we should mention that studies performed with generated MC data revealed that the differences in calculating sph and apla from the truth MC vertex and the reconstructed one are not important. Also, MC studies

in cases where the vertex is a priori known (such as a spherical photon pulse at the center of the detector) showed again that the results are not affected by the process of the reconstruction. This is of course by-product of the fact that `RecoBAMA` works very well with simulated data.

In addition to all these, we should utter that it has been demonstrated, beyond any doubt, that `RecoBAMA` works quite well when it comes to detector data. This has been shown with calibration data [260]. Also, the optimization of our cutting decisions was done with real data and that means that any systematical bias (if any) should have been taken already into account. State it differently, the resolutions of the obtained variables should have absorbed this effect. Finally, the sph and apla variables were calculated in cases were the vertices are roughly known (as in the case of calibration data with a source at a specific point) and the results were in all cases in good agreement with the ones obtained by the use of the reconstruction algorithm.

Nevertheless, as an extra check we calculated sph and apla hacking artificially the output of `RecoBAMA`. Initially, we altered the output of each coordinate x, y and z according to a random number picked up from a gaussian with zero mean value and standard deviation $\sigma_i = 300.0$ mm[2] for each coordinate, $i = x, y, z$. In these cases the total change can become very big but still no significant differences are observed.

In Fig. 7.19 we show three random examples from this study. They were calculated with calibration data from radioactive sources at the detector. In all cases, we can verify that the real distributions (black distributions; vertex taken from `RecoBAMA`) match closely with the "haked" ones (red distributions). Of course, if you exaggerate with the hacking, say if you input $\sigma_i = 1000.0$ mm to the random number generator, then clear differences are seen, Fig. 7.20. We nevertheless do not believe that such a huge error can be induced systematically by `RecoBAMA`.

In our previous investigations, the vertices of the events were altered in a totally random way using a number generator. We also went further and investigated the effect of a constant systematic bias. Two options were examined: systematic shifts in the $\hat{r}$ and $\hat{z}$ directions. In both cases the possibility for a plus and minus effect was investigated; positive and negative shifts in r and z. The value of the bias induced was picked to be 400.0 mm but further investigations with larger biases confirm our conclusions.

In the Fig. 7.21 and 7.22 we show some random examples from this exercise. In Fig. 7.21 a bias of 400.0 mm is induced in the $-r$ direction and

[2]According to measurements with radioactive sources the total resolution of the vertex reconstruction algorithm is 320.0 mm for the worse case, the Cs source. The value 300 mm chosen individually for each coordinate is high enough to render our results well-motivated.

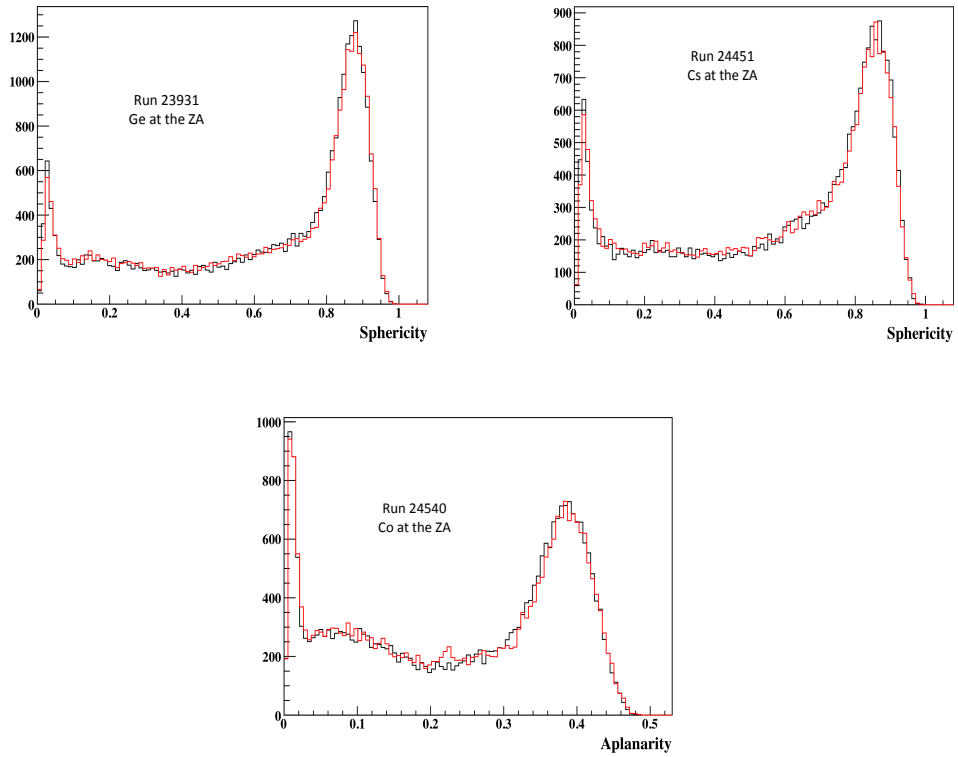

Figure 7.19: Real (black) and "faked" (red) sph and apla distributions. The vertex coordinates were faked with random numbers taken from a gaussian centered at zero and $\sigma = 300.0$ mm.

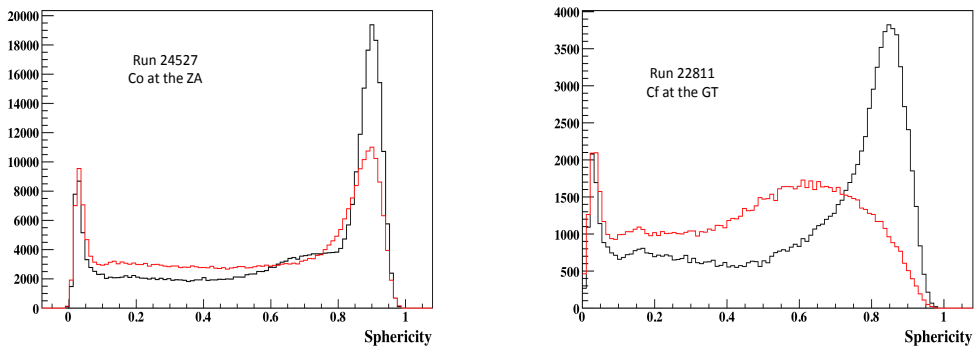

Figure 7.20: Real (black) and "faked" (red) sph and apla distributions. The standard deviation of the gaussian number generator was chose to be 1000.0 mm. We observe clear differences between the two curves.

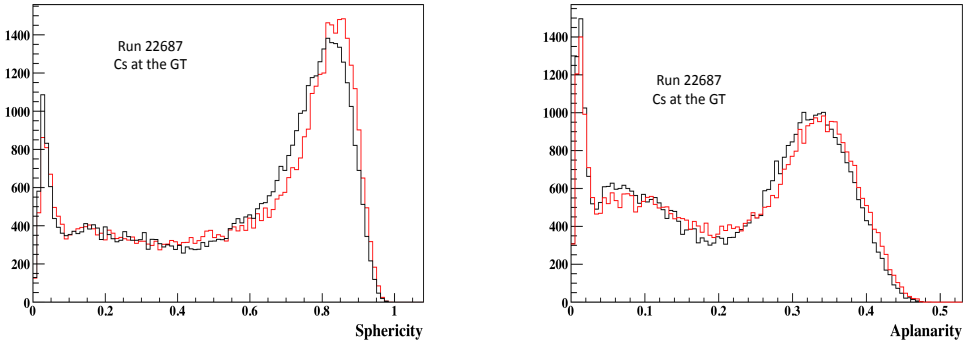

Figure 7.21: Real (black) and "faked" (red) sph and apla distributions. A constant bias of 400.0 mm was inserted in the -r direction.

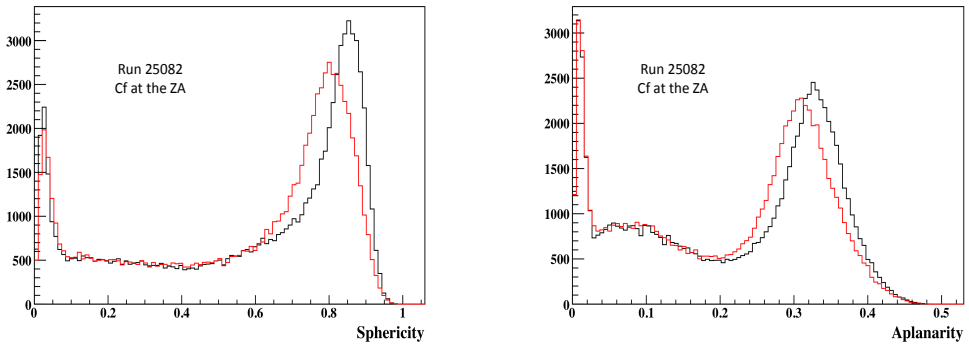

Figure 7.22: Real (black) and "faked" (red) sph and apla distributions. A constant bias of 400.0 mm was inserted in the -z direction. Changes in accordance with the position dependencies of sph and apla are seen.

in Fig. 7.22 in the $-z$ direction. Differences can be seen according to the position dependence of each variable but in every example the distributions are all inside the limits already deduced. Additional tests could be found in Ref. [263]. For all these we believe that the choice of building the sphericity tensor from the vertex of the event is well-motivated since we improve the resolution, while a strong dependence of sph and apla on the reconstructed vertex has not been observed.

7.7 Light Noise treatment

In this section we will show how all these previous considerations fit to the tagging and rejection of LN. We will first investigate separately the rejection

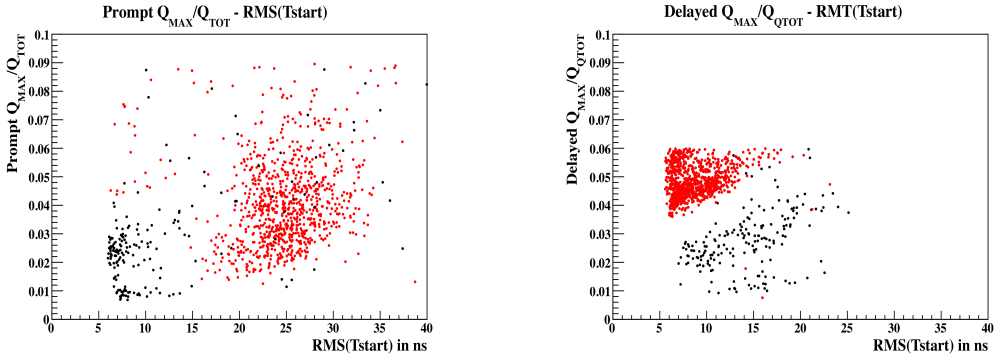

Figure 7.23: Q_{MAX}/Q_{TOT} vs RMS(Tstart) scatter plots for prompt (left) and delayed (right) events. In black we draw the events with $z(delayed) > 50$ cm and with red those with $z(delayed) < 50$ cm. LN patterns are clearly seen in the delayed events plot.

of two selected LN samples and then we will turn to the study of the neutrino selection. In this course we will also test the standard cuts decided for LN identification.

7.7.1 LN patterns relevant for correlated background searches

We now turn to the study of the LN events described in Section 7.2. To separate a clean LN sample one could ask for a delayed vertex z coordinate smaller than 50 cm, since as it is seen from the delayed vertex distribution, Fig. 7.3 (right), LN occupies this region (as opposed to CSM delayed events that are spread beyond 50 cm). To see how this BG manifests itself in terms of the official DC LN taggers we draw, in Fig. 7.23, scatter plots of Q_{MAX}/Q_{TOT} vs RMS(Tstart) for the prompt and the delayed correlated BG candidates. In black are the events with $z(delayed) > 50$ cm and in red those with $z(delayed) < 50$ cm. We clearly see in the scatter plot for the delayed signals, Fig. 7.23 (right), that the points corresponding to LN are clearly separated from the rest of the events. One could isolated them with a further combined cut in the Q_{MAX}/Q_{TOT} - RMS(Tstart) plane but we shall do otherwise; we will apply the formalism of shape variables developed thus far.

As explained before, we will use the relaxed and the strict cuts for outside and inside the NT volume respectively. In Fig. 7.24 we plot *sph* vs *apla* for

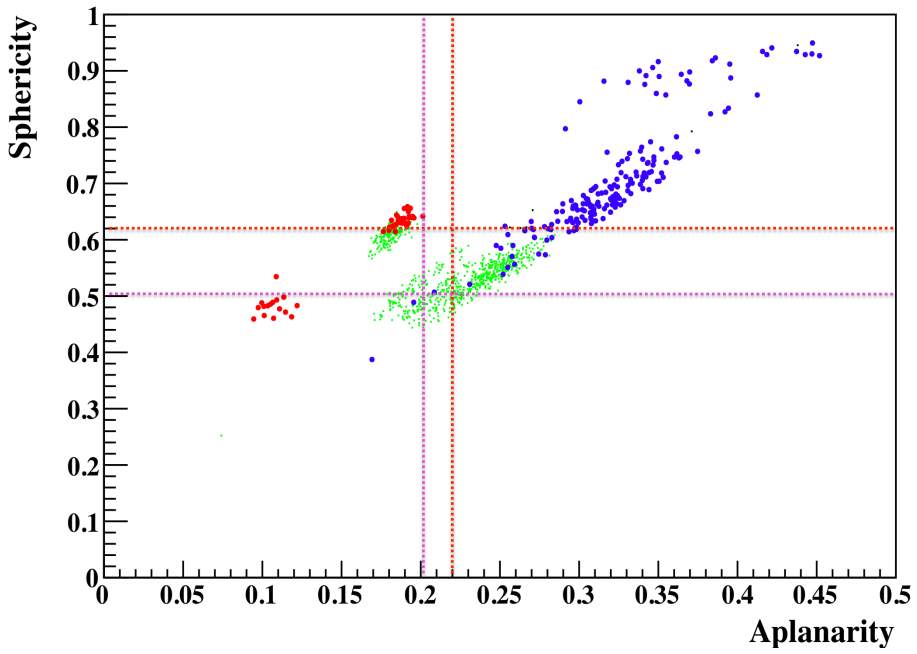

Figure 7.24: *sph* vs *apla* plot for correlated BG candidate events. Blue color for the events with $z(delayed) > 50$ cm, green for the events with $z(delayed) < 50$ cm and inside the NT and red those with $z(delayed) < 50$ cm and outside the NT.

the delayed signals[3] of the correlated BG candidates. In blue color are the events with $z(delayed) > 50$ cm (mostly Michel electrons), in green the events with -120 cm$< z(delayed) < 50$ cm (mostly LN inside the NT) and with red those events with $z(delayed) < -120$ cm (mostly LN outside the NT). Applying the combined relaxed (purple lines) and strict (red lines) cuts as shown in Fig. 7.24 the LN events can be rejected. From the totality of the 890 LN events below $z(delayed) = 50$ cm only 7 events pass this treatment, 99.2% reduction. These events lie on the limits of our rejection cuts.

It is true that these cuts reject also some stopping muon–Michel electron events as can be seen from the blue dots lying outside the selection cuts. The loss is indeed small but it is still there. This is, nevertheless, not fatal since our cuts have not been made to treat muon daughters. What is important is that a high energy profile LN can be treated easily in the framework described in the previous sections.

[3]There is where LN lurks.

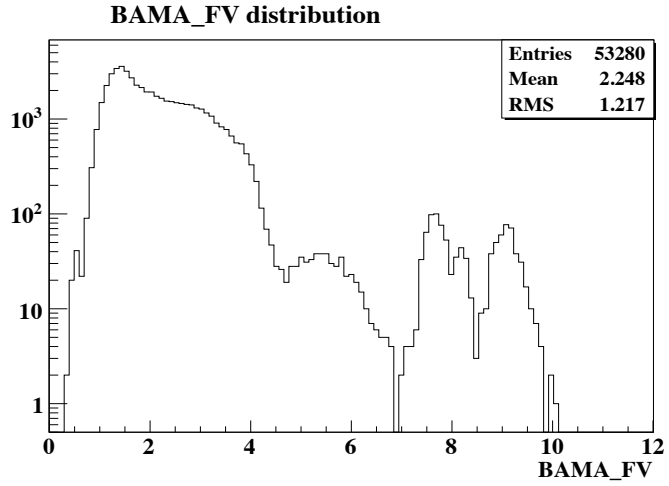

Figure 7.25: BAMA_FV distribution for the events that pass the official LN tagging criteria. For BAMA_FV > 4.5 the events are less spherical and are candidates of LN.

7.7.2 RecoBAMA functional value

Another way to select a sufficiently pure LN sample is through the functional value of the vertex reconstruction algorithm, `RecoBAMA` (BAMA_FV). `RecoBAMA` is tracing the point in the detector where light is created, that is the vertex, through a likelihood minimization exploiting the event's channel-wise hit charge and time information. The underlying model assumes that the events should be isotropic. Consequently, for spherical events this minimization procedure will converge for most of the times and this fact is reflected in the functional value returned by the fitter.

As a rule of thumb, events with BAMA_FV > 4.5 are less spherical and they are candidates of LN. In Fig. 7.25 we show the distribution of BAMA_FV after the application of the official DC LN rejection cuts. Beyond the value of 4.5 we see the peaks of events that are suspicious of being LN. In Fig. 7.26 (left) we draw the vertices of those events[4] that pass the official LN cuts but have BAMA_FV > 4.5 and energies greater than 12 MeV. One can obviously observe the pathological vertex structures characteristic of LN. In Fig. 7.26 (right) we also show the sph - apla scatter plot of those events. Both variables values occupy regions in that two-dimensional plane that are rejected by the spherical cuts of previous sections. Events with a bad quality vertex reconstruction are less spherical and this is reflected in the eigenvalues of the sphericity tensor. Applying the combined sph and apla cuts the sample

[4]Rejecting muons and muon daughters.

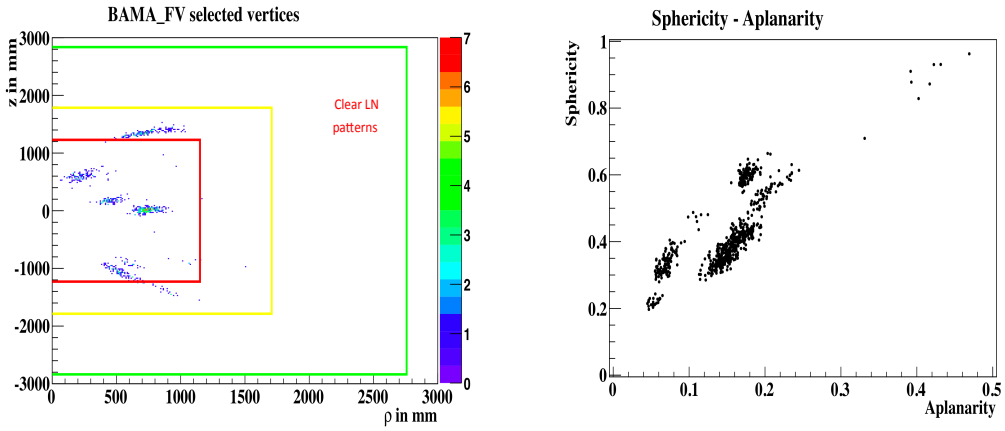

Figure 7.26: Vertices of the events selected with a BAMA_FV > 4.5 cut (left) and the corresponding sph - apla scatter plot (right).

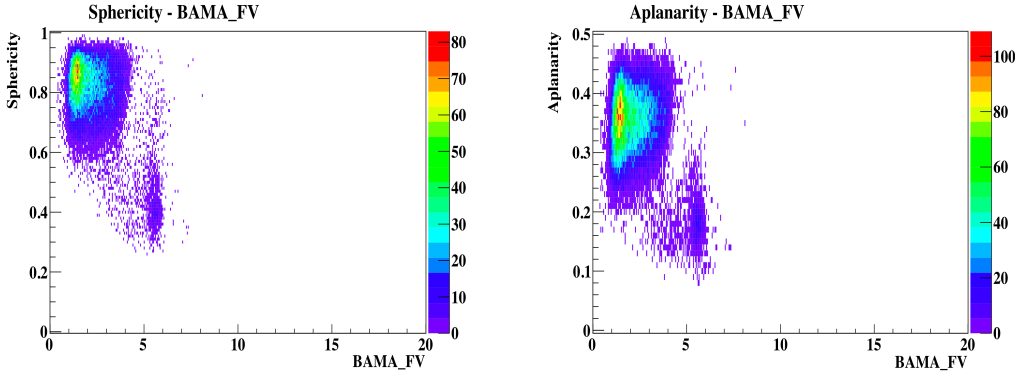

Figure 7.27: BAMA_FV vs shp (left) and BAMA_FV vs apla (right). LN events are clearly separated in these two-dimensional plots having low sph and apla but relatively large BAMA_FV values.

is reduced in a 98 % level. Again we see that sph and apla have indeed a very good discrimination power.

Another way to understand all this, is to draw scatter plots of BAMA_FV vs sph and BAMA_FV vs apla. This is done in Fig. 7.27 (left) and (right). One could easily see that low sph or apla values correspond to large values in BAMA_FV (larger than 4.5) in accordance to our previous considerations. For some extra information concerning the correlation between sph, apla and BAMA_FV one can have a look at Ref. [266].

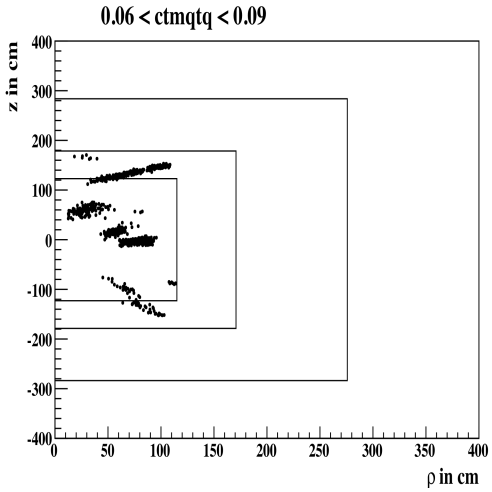

Figure 7.28: Vertices of the delayed correlated BG candidate events with Q_{MAX}/Q_{TOT} between 0.06 and 0.09.

7.7.3 Q_{MAX}/Q_{TOT}(delayed) < 0.06

To further examine the ability of this scheme to tag LN we go one step further and relax the strict $Q_{MAX}/Q_{TOT} < 0.06$ cut on the delayed signals. Since the $Q_{MAX}/Q_{TOT} < 0.06$ events have been already treated we now turn to the BG candidates with $0.06 < Q_{MAX}/Q_{TOT} < 0.09$. To look for the existence of LN in the selected sample we draw, as usual, the vertices of the delayed events, Fig. 7.28. Indeed we see similar thick spots that correspond to LN. These bad events were all removed by the tighter Q_{MAX}/Q_{TOT} criterion. In what follows we will see their rejection inside the *sph – apla* scheme.

In Fig. 7.29(top) we draw the usual *sph – apla* scatter plot with purple dots for the events outside the NT and with red for those inside NT. In Fig. 7.29(bottom) are the vertices of these events with the same coloring convention. It is clear from Fig. 7.29(top) that almost all of these events fail to pass the combined shape cuts (in purple lines are the relaxed and in red the strict shape discrimination cuts). Only 3 events pass these cuts but from the vertex positioning and the prompt-delayed time difference it turns out that they should be Michel electrons. This result is very important since it does not only demonstrates the capability of our method to track LN but it validates from another direction the $Q_{MAX}/Q_{TOT} < 0.06$ cut chosen for extra LN suppression. We consider this as a very important cross-check.

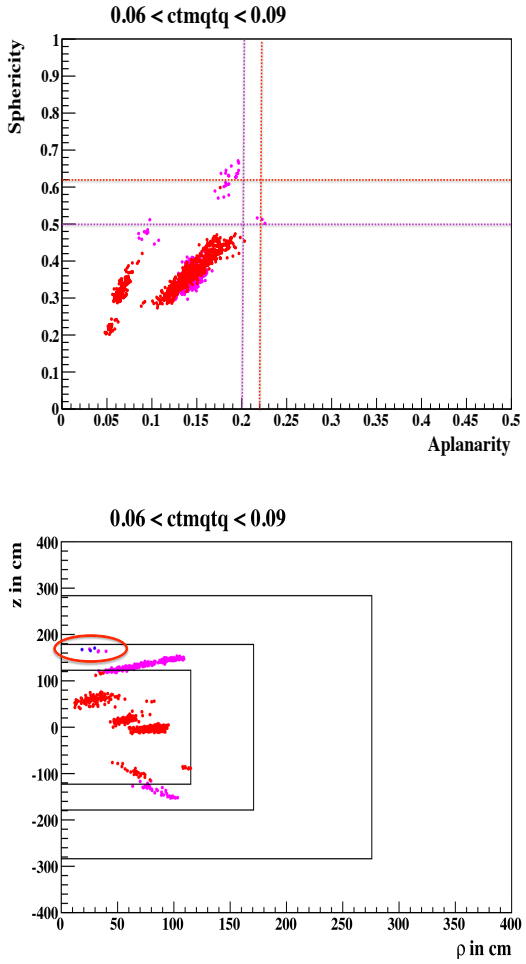

Figure 7.29: *sph* vs *apla* scatter plot (top). With purple color we denote the events outside the NT and with red those inside the NT. With the same colors we mark the relaxed and strict shape cuts. The delayed vertices (down) are displayed with the same color convention and we further indicate (in blue and inside a red circle) the events that pass both cuts.

7.7.4 Accidentals and neutrino candidates

We now turn, in this short section, to describe how these ideas could fit on the neutrino candidates selection. It is *not* our intention to find the most efficient and flexible scheme to signal selection in this section. We will do the minimum required to show that the scheme presented in this report is self-consistent and that it can solve the problem of the "noisy" PMT 263 in an elegant manner. We will first use the shape variables for the estimation of accidentals.

The rate of accidental events in DC has increased by a factor of $\sim$ 20 from 8^{th} of August 2012 [267]. After investigation it was found that the source for this large augmentation was LN events identified with PMT 263. To tackle this extra noise, the flasher PMT 263 was switched off and a new Q_{MAX}/Q_{TOT} was proposed for the delayed signals. Namely, the $Q_{MAX}/Q_{TOT} < 0.06$ cut for delayed events assured most of us that the issue of PMT 263 will not affect neutrino selection [268, 269]. In this section we will remove this extra cut adding the relaxed and strict shape cuts only on the delayed events. We will then test three sets of cuts for LN rejection on the calculation of accidentals. These three sets will be:

1. $Q_{MAX}/Q_{TOT} < 0.09$ on the delayed,
2. $Q_{MAX}/Q_{TOT} < 0.06$ on the delayed,
3. $Q_{MAX}/Q_{TOT} < 0.09$ plus the shape cuts on the delayed.

with the rest of the LN rejection criteria being the official ones.

The rate of accidentals (R) has been calculated using the recipe:

$$R = R(0.7, 12) \times R(6, 12) \times 100\mu s \tag{7.6}$$

and the results are shown in Fig. 7.30 in a day by day fashion. R(0.7, 12) is the rate of events between 0.7 - 12 MeV and R(6, 12) the same rate in the delayed energy window of 6 - 12 MeV. In black are shown the results of the accidental rate for the first loose selection. The rate[5] equals to 0.53 events/day and the jump associated with the activity of PMT 263 is visible. In red the results with the second set of cuts are shown. The rate is 0.39 events/day and it is indeed stable even in the period where the abnormal change in the accidentals was observed. That was the chief argument to incorporate this tighter Q_{MAX}/Q_{TOT} cut for the neutrino selection. Finally in blue we plotted the rates for the third set of cuts. One can see again that the jump in the rates is not observed if we relax the tight Q_{MAX}/Q_{TOT} cut on the delayed but we include the shape cuts. The rate found is 0.38 events/day in a very close agreement with the previous analysis. What it is even more interesting is that the daily rate changes follow closely the same patterns as seen in the red and blue curves of Fig 7.30. This observation is really important since it validates from another point of view the official DC strategy for accidental suppresion.

Using this scheme on the neutrino selection ($Q_{MAX}/Q_{TOT} < 0.09$ plus the shape cuts on the delayed) we count 4118 anti-neutrinos and a rate

[5]This rate is just the mean of the day-by-day rate distribution.

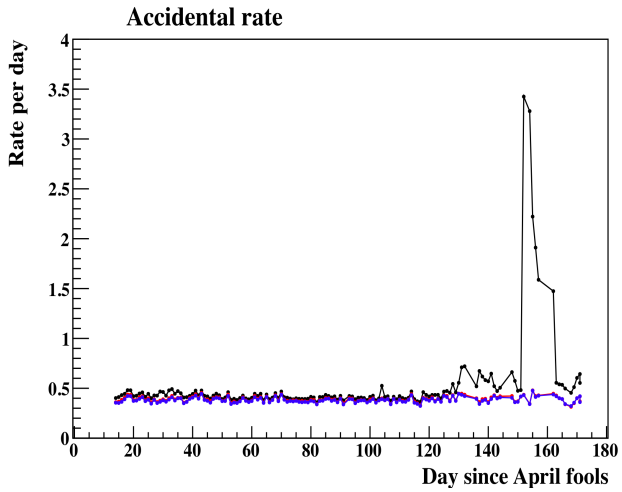

Figure 7.30: Day by day accidental rate. Cuts on the delayed events: in black with $Q_{MAX}/Q_{TOT} < 0.09$, in red with $Q_{MAX}/Q_{TOT} < 0.06$ and in blue with $Q_{MAX}/Q_{TOT} < 0.09$ plus the shape cuts.

42.5 $\bar{\nu}_e$/day; a number close to the official one. Remember that with the official cuts, one has 4121 anti-neutrinos and a rate 42.6 $\bar{\nu}_e$/day. We can not confirm that these three rejected events are LN but this is not important. What matters is that these two numbers are in a very good agreement indicating that our decisions for the neutrino selection are indeed solid and that high energy light noise as the one presented in section 7.2 does not enter our signal. We believe that this is a very important cross-check.

7.8 Special High Voltage runs

In this final section we will further present how our LN rejection framework works with a set of special High Voltage (HV) runs taken deliberately for LN studies. As we already mentioned, the 15 "hottest" PMTs of the DC detector were switched off to reduce LN radically in the hardware level. Nonetheless in the September 17^{th}, 2011 a set of runs were taken with all PMTs on. In this configuration the accidental rate is far higher than the one measured for the first publication as a result of the 15 extra hot PMTs. Analyzing these runs, one can acquire an additional feeling of how software cuts perform and more important whether it is possible to return to the old PMT configuration.

In this analysis, the most important thing (among others) is the observed rates in the prompt and the delayed energy windows. These quantities control

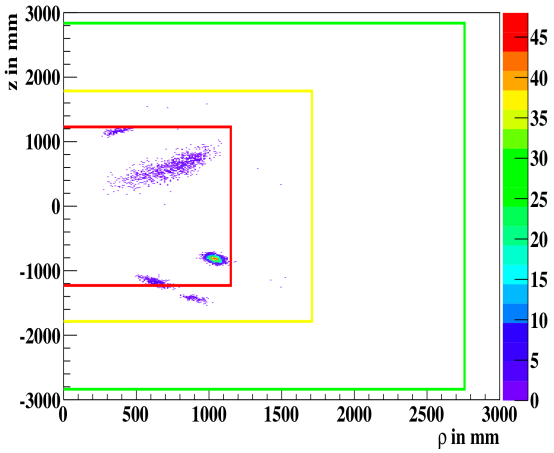

Figure 7.31: Vertices of those events in the 6 - 12 MeV range that evade the standard LN cuts.

the number of accidental doublets that contaminate the neutrino sample as explained in Section 7.7.4. For the neutrino selection only the window of 0.7 to 12 MeV is relevant. In this section we will analyze these special HV runs and we will compare them with an equal amount of data taken in the same period but with the nominal configuration (15 PMTs off). We will show that a single additional cut in sphericity is enough to remove the LN contribution of the 15 noisy PMTs. The accidental rate will then be comparable to the one measured in the detector when all PMTs are on.

We first utter that the accidental rate for the currently running nominal HV configuration is:

$$0.32 \pm 0.03 \text{ events per day.} \tag{7.7}$$

From this rate 7.48 ± 0.03 Hz consist in signals in the prompt energy window and 0.005 ± 0.001 Hz in signals in the delayed. On the contrary when all PMTs are activated the accidental rate becomes:

$$4.82 \pm 0.13 \text{ events per day.} \tag{7.8}$$

The rate of prompt signals is 8.33 ± 0.02 Hz. In the delayed window the event rate becomes 0.067 ± 0.02 Hz. We clearly understand that the enhancement in the rate of accidentals when all PMTs are switched on comes from the higher rate (almost an order of magnitude) in the delayed window.

As an illustration we draw the vertices of those events in the 6 - 12 MeV range that evade the standard LN criteria, Fig. 7.31. We do see islands of

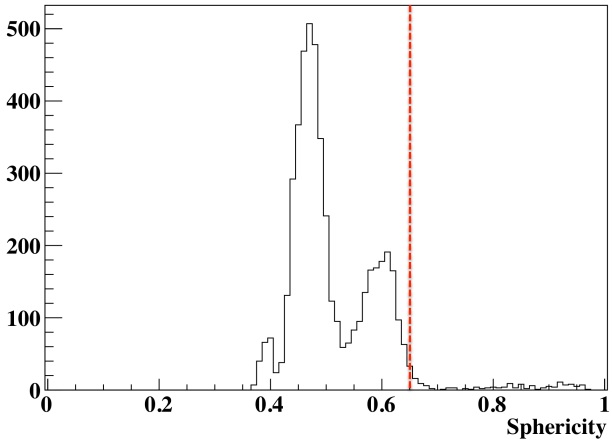

Figure 7.32: Sphericity distribution of the 6 - 12 MeV events that pass the standard LN cuts.

vertices corresponding to the emission of light from different PMTs. These are the events responsible for the observed enhance on the accidental rate. To understand how to treat with this issue we show in Fig. 7.32 the sphericity distribution for this category of signals. We readily observe that this distribution is concentrated around relatively low values of sph. An extra cut in sph at 0.65 would be enough to remove most of this signal. At that sph value the rejection inefficiency is around 0.3 %.

Applying the additional cut of sph > 0.65, the rate in the delayed energy window becomes 0.006 ± 0.01 Hz and the accidental rate reduces now at the value of:

$$0.46 \pm 0.04 \text{ events per day.} \tag{7.9}$$

We (again) believe that this result is very important in the understanding of LN and the battle against it.

Chapter 8

Muon selection

8.1 Introduction

Muons, created from the collisions of primary cosmic ray particles in the upper levels of the atmosphere, are a main source of background for underground neutrino detectors. When they travel through the scintillation region of the Double Chooz (DC) Inner Detector (ID) they release large amounts of energy so that their signature could be easily identified. But, even when they do not enter the ID they often initiate showers of particles that can trigger the ID and contribute to the observed accidental rate.

In the particular case of scintillation detectors like DC, muons can also create spallation neutrons that are absorbed on hydrogen or gadolinium producing signals several μs after the prompt muon. Bearing in mind that the mean absorption-time for thermal neutrons on hydrogen is roughly 200 μs an interval of 1 ms dead-time seems to be necessary and appropriate to prevent all these subsequent signals to fake the neutrino selection. The neutron absorption peaks are also very pronounced so that their positions could be used to understand the detector performance and determine its energy scale. In Fig. 8.1 the two peaks corresponding to the hydrogen and gadolinium neutron absorption are shown from the analysis of data in narrow time intervals that follow the muon passage.

Through going muons also provide a window of opportunity to a better understanding of the way a detector performs since for most of the time their signal is very clean and the physics behind it is simple and well understood. They can be used to keep track of the detector stability or to monitor the quality of the liquid scintillator in the ID or the Inner Veto (IV). In the past, large-scale underground experiments took advantage of the very clean muon signals to calibrate and control their detectors [270].

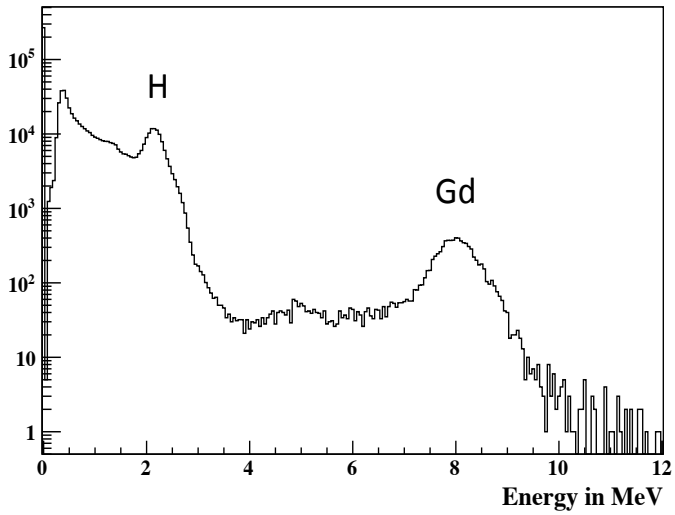

Figure 8.1: Neutron absorption peaks on hydrogen and gadolinium produced after a muon passage.

For all these it seems necessary to have at hand a solid and equally well-understood grasp on the signature that muons leave in the detector. In the ideal case, one would like to have a sound frame that disentangles the various classes of energy depositions initiated by cosmic ray muons.

In this chapter, a number of methods that could be used towards muon selection are presented. Among them, the most primitive, is the one based on the use of sharp charge cuts to identify the muons that activate the ID and the IV. These cuts are based on estimations and analytical simulations of the expected energy depositions assuming that muons behave like Minimum Ionizing Particles (MIP). In this study, they are also motivated through a rough comparison between data and Monte-Carlo (MC).

Furthermore, two additional techniques towards muon identification are also presented. It is has to be noted that all these methods converge to a common result. The additional consistency of our considerations with the results from various reconstruction algorithms makes them elegant and again well-motivated. The techniques summarized in this chapter were developed by the author building on earlier work done by A. Tonazzo et al. [271].

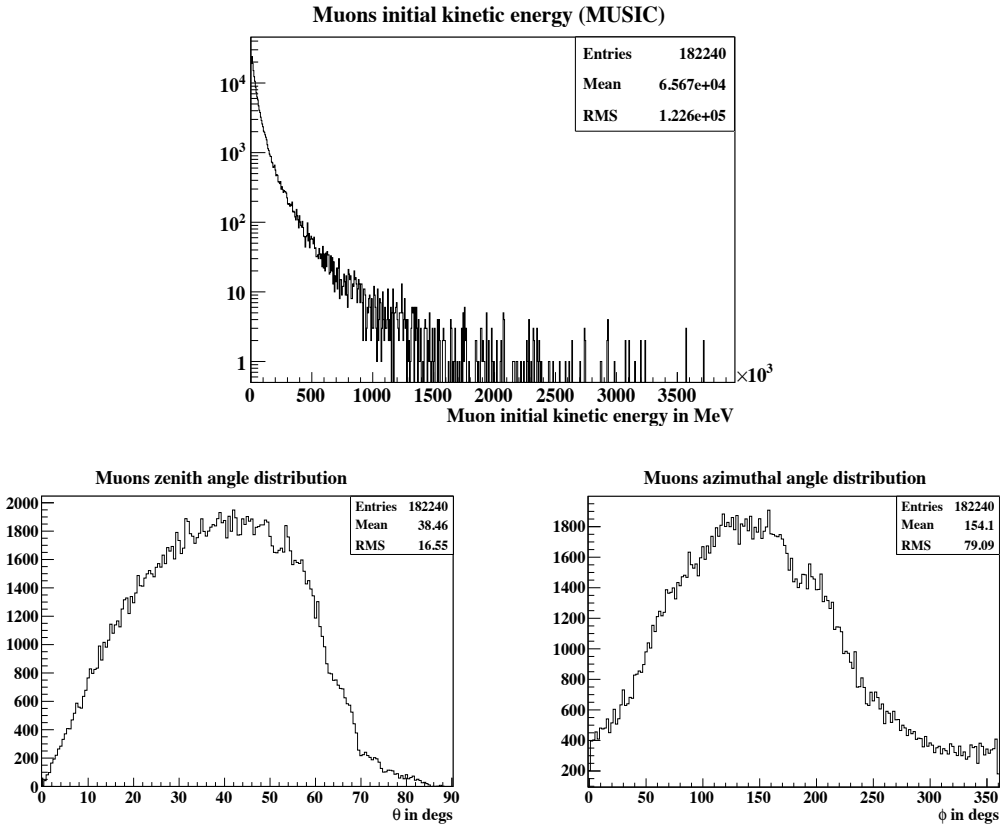

Figure 8.2: Initial energy distribution (top) of the generated muon events. Also the zenith (bottom left) and azimuthal (bottom right) angular distributions.

8.2 MUSIC generated sample

For the aid of our investigations we used a sample of muons passing through the cavern of the DC far detector laboratory. The initial energies and angular distributions of the simulated muons were produced by the MUSIC (MUon SImulation Code) generator [272]. The particles starting points where distributed in a volume above the DC detector and for the rest of the simulation the official DC software packages (DOGS) were used.

In fig. 8.2 (top) the initial particle energies are shown. The zenith θ and azimuthal ϕ angular distributions for the muons are shown in fig. 8.2 bottom left and bottom right respectively. To help the reader, two simple two-dimensional cartoons depicting these angles are included in fig. 8.3. A few comments are in order here. Firstly, as it is shown from the zenith angle distribution, muons have for most of the time incoming angles of roughly 45

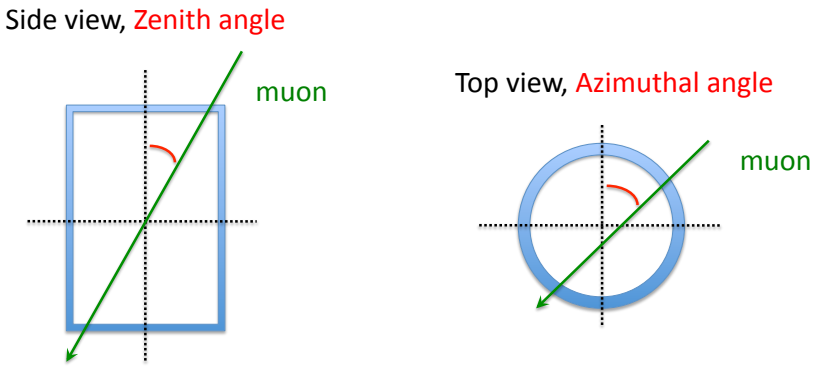

Figure 8.3: Zenith and azimuthal angles.

deg directed from upwards to downwards. With zenith angles bigger than 90 deg we do expect only a small portion of cosmic muons. On the other hand, the azimuthal distribution shows significant variations in the muon flux while one would, in principle, expect a perfect rotational symmetry. This is because the MUSIC code takes the expected muon flux from the sea level and propagates it through the overburden rock topology. The differences from uniformity in fig. 8.2 (bottom right) arise from the hill profile of the Chooz-far site. The MUSIC algorithm has been validated with muon data from the CHOOZ experiment. A more detailed exposition of the MUSIC package along with some extra informations on the expected fluxes in the Chooz and Kamioka sites can be found elsewhere [272].

The charge distributions of the generated events for the ID and the IV are shown in fig. 8.4 (top left) and (top right) respectively. For the collected charge the 14 switched off photomultipliers (PMT) of the ID and the two channels of the IV that malfunction were neglected on purpose. These plots should be contrasted with the plots of fig. 8.4 (middle left) and (middle right) prepared with real physics data. The similarity between the two patterns is evident with the IV simulated spectrum to lack the exponential decay shape at low energies that it is related to natural radioactivity not present in the MC sample. The IV data spectrum possesses also two peaks at around 15000.0 and 38000.0 DUQ, fig. 8.4 (bottom). Their origin is connected to natural radioactivity and the trigger conditions of the detector [273].

Some extra comments are in order. 97.7 % of the events initial generated are finally registered; this was taken from the MC truth particle tracking

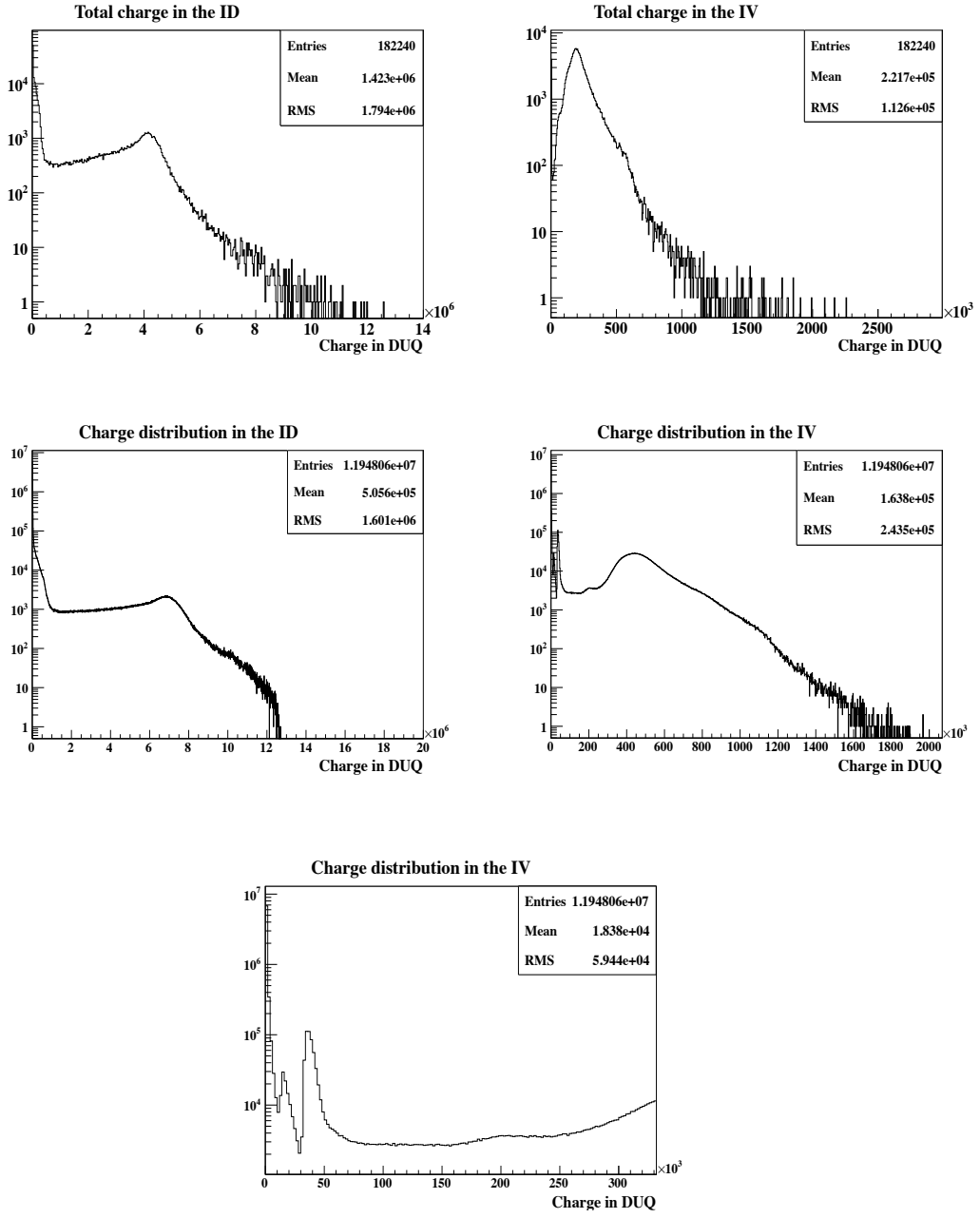

Figure 8.4: The deposited charge distributions for the Monte-Carlo muon sample in the ID (top left) and the IV (top right). The same distributions for the ID (middle left) and the IV (middle right) are also shown for real data. The low energy region of the IV data spectrum is also shown (bottom).

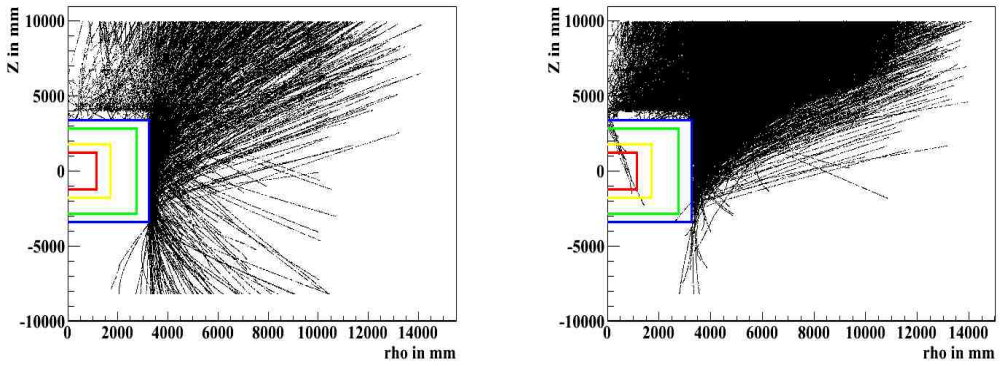

Figure 8.5: Muon tracks for those muons that do not cross the detector but the IV records signal (left) and those that do not deposit charge in the IV crossing or not the detector (right).

information. On the other hand, the IV has non zero charge for 98.1 % of the total cases. The origin of this difference is twofold. To understand it the z *vs.* ρ two-dimensional projections of the three-dimensional (x, y, z) muon tracks as given by MC were plotted for two specific cases. With ρ the radius $\sqrt{x^2+y^2}$ is denoted following the common notation used for cylindrical coordinates.

In fig. 8.5 (left) the muon tracks are shown for those events where the muon itself does not enter the detector but nonetheless charge is indeed read-out in the IV. It is clearly seen that the muons are passing just outside the borders of the detector. In these cases particles from shower cascades enter the detector. These cascades usually deposit small charges in the IV around the magnitude of natural radioactivity. The events where significant energy depositions are induced by muon spallation products are rare and they can be neglected when discussing muon selection.

At the second plot, fig. 8.5 (right), the cases where the IV records no charge at all are shown. Two event categories are clearly present. First there are those events where the muon do not enters detector or clips the IV so that the energy deposition is small to trigger the detector. The second class of events is striking. A small number of muons can sneak in the ID through the chimney without being tagged by the IV; this is an expected inefficiency of the IV. The total number of chimney muons are only a small fraction of the whole sample. In the following investigations the systematics induced to the muon selection due to muon showers are totally ignored. We shall also put forward a combined ID - IV approach to ID muon selection demanding that each ID muon should necessarily trigger the IV. This approach, of course,

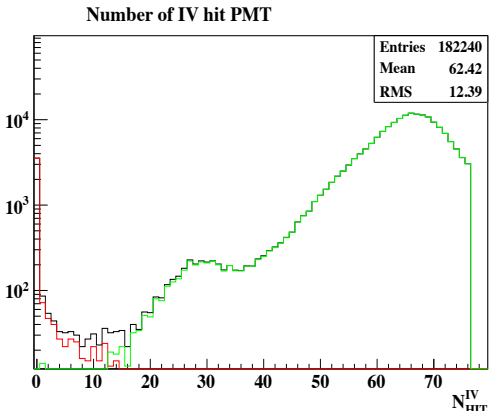

Figure 8.6: MC distribution of IV PMT multiplicity. In green are the events when a muon crosses at least the IV and in red when the muon does not enter the detector.

will not account for chimney crossing muons. We decided to do so with the knowledge that the induced efficiency losses are indeed negligible.

8.3 Muon selection: sharp charge cuts

The minimum charge depositions for a muon crossing the ID or the IV are sufficiently well understood. One could in principle use these values to tackle muon selection applying sharp cuts on the recorded charges. This strategy has been pursued by many investigators within the DC collaboration. See for instance [271, 274]. In this section the values of the charge cuts we decided to use will be motivated. For this reason, we used extensively the MC sample but not in an absolute way. We will also lay down some elements that we are going to further develop in the next stages of this work.

First, the distribution of IV PMT multiplicity for the MC muon sample is shown on fig. 8.6. In red are shown the events when a muon do not crosses the IV and in green are depicted the muons that cross at least the IV. In black we overlap all the events. From this plot we realise that setting a cut on the PMT multiplicity bigger than 11, $N^{IV}_{HIT} > 11$, we hold most of the IV muons and only a small fraction of "good" events is rejected. According to MC this cut does not remove IV muons at the level of 0.05%.

In fig. 8.7 we plot the charge distributions for data (left) and MC (right) before (black) and after the $N^{IV}_{HIT} > 11$ cut. In the bottom plots of fig. 8.7 we zoom at the low energy region. After this selection, a reduction of 60% is induced on the data in the low energy part where the singles spectrum is

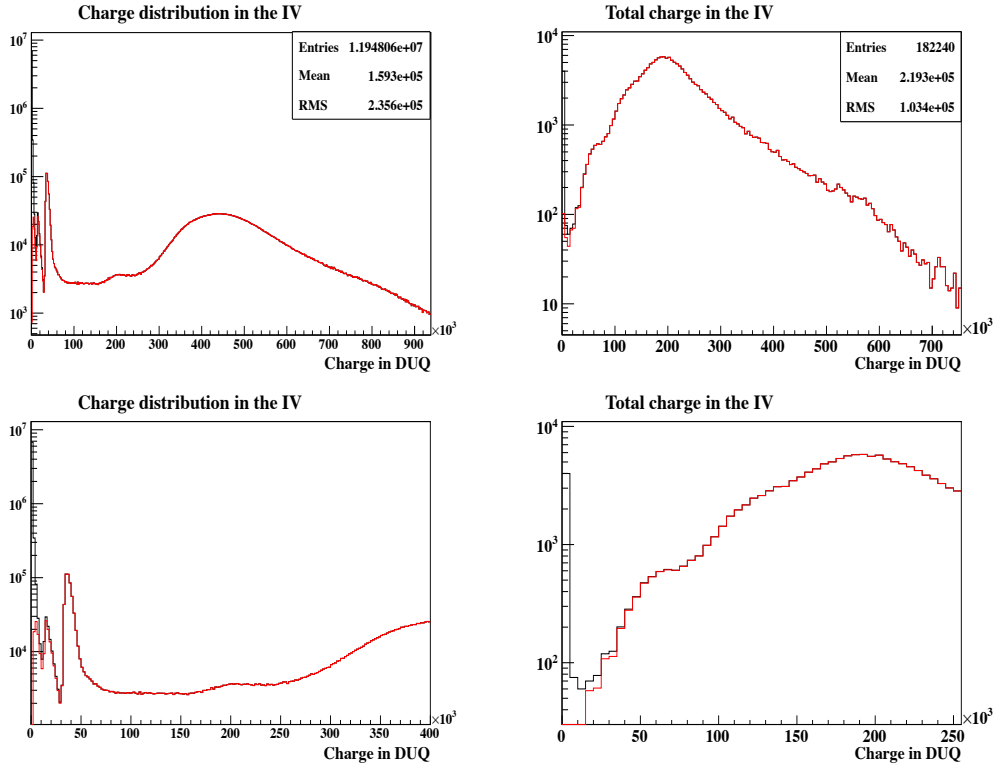

Figure 8.7: IV charge distributions before (black) and after (red) the first $N_{HIT}^{IV} > 11$ cut for data (left) and MC (right). In the bottom plots we zoom at the low energy part of the corresponding distributions.

expected. To further continue with the IV muon selection we compare figures 8.7 (left) and 8.7 (right). A common feature is witnessed in both plots. This is the clear presence of a bump around 200000.0 DUQ and 60000.0 DUQ in the data and MC respectively[1]. These bumps are related to the presence of stopping muons in the DC detector [275]. We clearly see that putting a charge cut just below the stopping muon bump it is enough to keep a clean muon sample. We shall exploit this geometrical feature for IV muon selection.

Looking at the data spectrum it is understood that the most perfect value to place this cut in the data would be at 100000.0 DUQ. Nonetheless, it is a fact that we cannot tell clearly whether the "plateau" in the data spectrum between 50000.0 and 100000.0 DUQ corresponds or not to muons. We also know that a sharp cut like this is expected to allow some other non-muon

[1]The differences between the charge values in data and MC originate from the fact that the latter was not fully tuned to match the detector response.

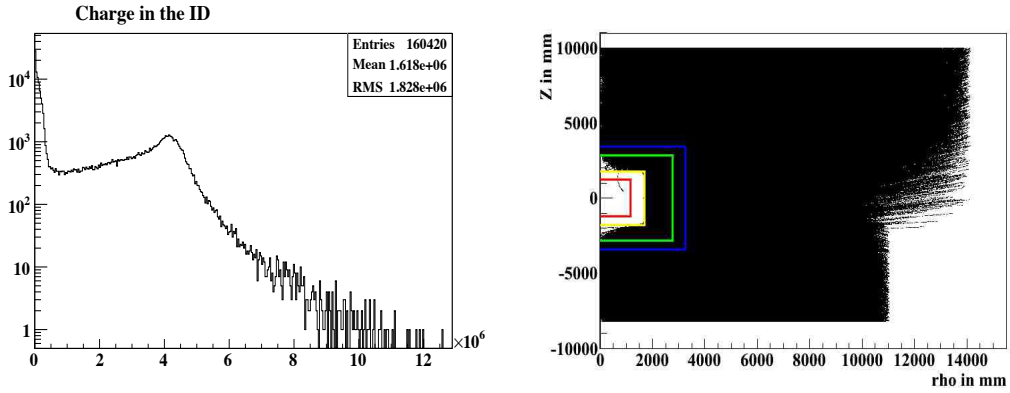

Figure 8.8: MC charge distributions for the IV selected ID muons (left) and the muon tracks for those events with $Q_{ID} < 50000.0$ (right).

events pass the selection criteria. Truth this might be, we shall stick to this cut knowing a priori that the expected systematics could be of the order of 3 - 6 %[2]. We state clearly the cuts for IV muon selection:

- $N_{HIT}^{IV} > 11$ and,
- $Q_{IV} > 100000.0$ DUQ.

According to a rough Monte-Carlo comparison the induced inefficiency to the IV muon sample is around 0.15 %.

For the ID we shall use a combined approach using both the ID and IV information. More precisely we decided to call "ID muons" those muons that necessarily trigger the IV. With this recipe we know a priori that we will reject those muons that cross the chimney, but as it has been already demonstrated these are only a small fraction of the total sample. So, the starting point for selecting ID muons are the cuts for the IV selection. Applying these cuts to the MC sample, and demanding also non zero charge in the ID as well, we obtain the spectrum of fig. 8.8 (left).

It is interesting to try to understand the various regions of this plot. Roughly we observe two contributions with a boundary around 500000.0 DUQ. The events below the 500000.0 DUQ limit can have really small energies and we expect them to be highly entangled with other backgrounds (BG). To understand their origin it is sufficient to draw the muon tracks for those events where $Q_{ID} < 500000.0$ DUQ. This is done in fig. 8.8 (right). We clearly see that all this contribution comes from Buffer crossing muons. These

[2]The systematic error was estimated by varying the Q-cut values at the two extremes.

muons produce Cerenkov radiation and can give spallation products that excite the scintillator (for instance proton recoils or neutron captures). Their contribution is highly entangled with the various low energy BG sources so that their selection is far from trivial. In the first part of this work we will neglect them totally focusing only on the treatment of muons that pass the Gamma Catcher (GC) and the Neutrino Target (TG) volumes; collectively referred hereafter as scintillation volume muons. In the second part of this work we will present arguments about their signature in our detector but we will again neglect their contribution to the muon rate.

To further attack ID muon selection we now draw in fig. 8.9 (top) and (bottom) the distributions for Q_{MAX}/Q_{TOT} and N_{HIT} for the ID as taken from the MC sample; N_{HIT} is the ID PMT multiplicity. In black are all the events. In red we denote those events where the muon do not enters the ID. In blue we depict the Buffer muons and finally in green those that make it to the scintillation region. From both plots we confirm the conclusions already drawn from fig. 8.8 (left). The values of Q_{MAX}/Q_{TOT} and N_{HIT} for Buffer muons span the whole allowed region, making difficult to seperate them from the lurking background without the disadvantage of inducing high inefficiencies. Nevertheless, we see that scintillation volume muons have more narrow distributions and that the combined cuts $N_{HIT} > 150$ and $Q_{MAX}/Q_{TOT} < 0.15$ do not remove essentially any scintillation volume muons. The estimated inefficiency according to MC is 0.2 %.

Applying these cuts to real data we have a reduction of 81% on the initial sample. The remaining events for data and MC are shown at fig. 8.10 (top) and (bottom) respectively following the usual color convention for the MC sample. Before motivating the cut for ID muons it is again profitable to have a look at the various regions of both distributions. Buffer muons are clearly separated from TG and GC muons with the latter having higher energy deposition as it is expected. What is surprising is the presence of yet another contribution in the data sample at the low energy part where the Buffer muon contribution begins. Since this contribution is not present in the MC sample we might be tempted to say that these events are not muons. Nonetheless, this is not 100% certain. On the other hand, since we also ask the IV to be fired in our selection scheme it seems that this population must originate from particles coming from the outside of the detector. The possibilities that they could be fast neutrons (FN) or gamma rays coming from the exterior has been investigated but our conclusions are not decisive. For the moment we shall ignore this tail of events but later on we do plan to argue about its possible origins.

To conclude with ID muon selection we will put our last cut in the charge value were the Buffer muon contribution ends. Looking again at the fig. 8.10

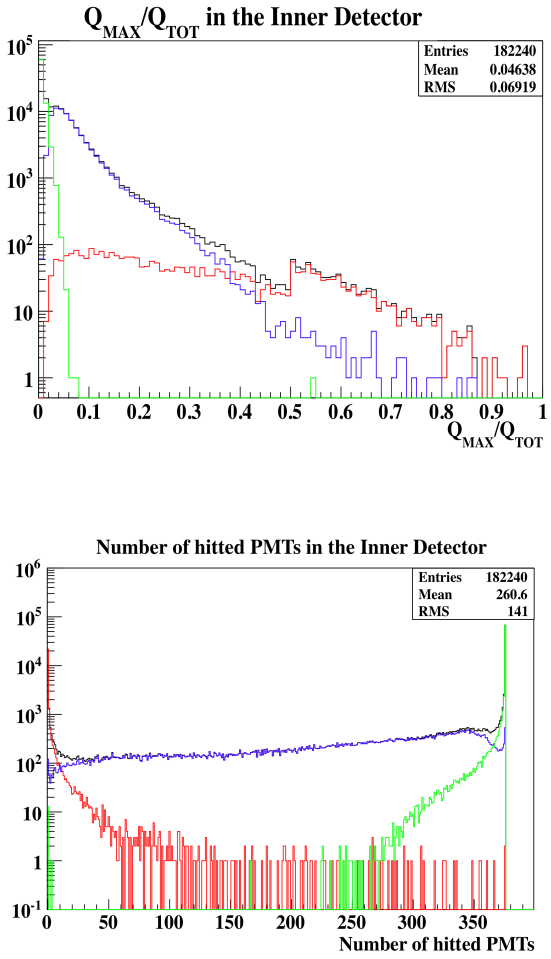

Figure 8.9: MC distributions for Q_{MAX}/Q_{TOT} (top) and for N_{HIT} (bottom). Color conventions: in black are depicted all the events, in red those that the muon crosses only the IV and in blue are shown the Buffer muons and in green the scintillation volume muons.

(bottom) we see that this value is at 9000000.0 DUQ. In a rough energy scale this corresponds to 60 MeV; close enough to the energy expected from theoretical considerations assuming that muons are MIPs. This last cut completes our muon selection strategy. We summarize our ID muon cuts:

- $Q_{IV} > 100000.0$ DUQ
- $N_{HIT}^{IV} > 11$

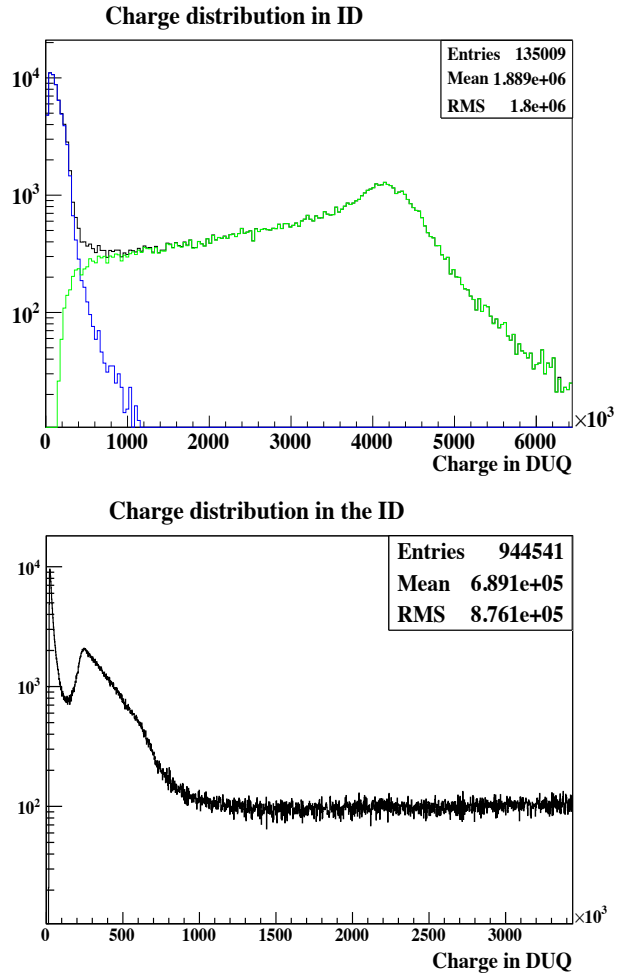

Figure 8.10: Charge distributions after the second set of cuts for MC (top) and data (bottom). In blue are shown the Buffer muons and in green the scintillation muons.

- $N_{HIT} > 150$
- $Q_{MAX}/Q_{TOT} < 0.15$
- $Q_{ID} > 900000.0$ DUQ

According to the muon simulation all these cuts can induce a loss of ID scintillation muons at the order of 2.3 %. This number corresponds to the accuracy that this method can achieve. We have now developed all the machinery necessary for IV and ID muon selection. In the following parts we shall present two more approaches for the isolation of ID muons.

8.4 Muon rates

Having decided the cuts required for muon selection we are now in a position to determine the rates with which muons trigger the ID and the IV. These are quantities interesting for many studies and more important to supervise the detector performance and its stability. The output of these analyses can serve us to cross-check the results of various simulation packages.

For the muon rate we lean on the primitive method, to determine its value from the number of selected events divided by the total run-time. Another solution would be from the mean value of the time-difference distribution of two adjacent muon events (ΔT distribution). The mean is usually taken from an exponential fit to the data. Both techniques have been exploited so far in the DC collaboration and a predilection is shown towards the latter. We decided, nonetheless, to follow the most straightforward method and calculate the muon rates from the entries of the selected sample. It should be emphasized that in all cases the resulting numbers arising from the ΔT distribution fit were extracted and they were found to be in close agreement with our results.

Applying the IV muon selection to the data set of DC first publication and knowing that the total run-time of the sample is 101.5 days we are then left with a muon rate of:

$$39.400 \pm 0.002\ (stat.)\ Hz$$

in the IV. Only the statistical error is quoted. It should be noted that the dead-time associated with the selection of antineutrino events uses different, looser cuts for the IV triggering.

In fig. 8.11 (top) and (bottom) we plot our results as obtained in a day by day fashion. For each day we summed all runs beginning after 0:00 in that day and ending before 23:59. In fig. 8.11 (top) is shown the IV muon rate vs the raw day number starting from April the 1st; the zeroth day is the 1st of April, 2011. In fig. 8.11 (bottom) the distribution of rates per day is also shown. Its mean value is 39.41 Hz very close to the result already taken from the whole sample.

For the ID, our selection scheme yields a muon rate equal to:

$$10.929 \pm 0.001\ (stat.)\ Hz.$$

Again no systematical error was calculated. On fig. 8.12 (top) are shown the ID muon rates vs the raw day number following exactly the same conventions for the day numbering and the sample grouping as it was done for the IV. On fig. 8.12 (bottom) the associated ID rate distribution is shown.

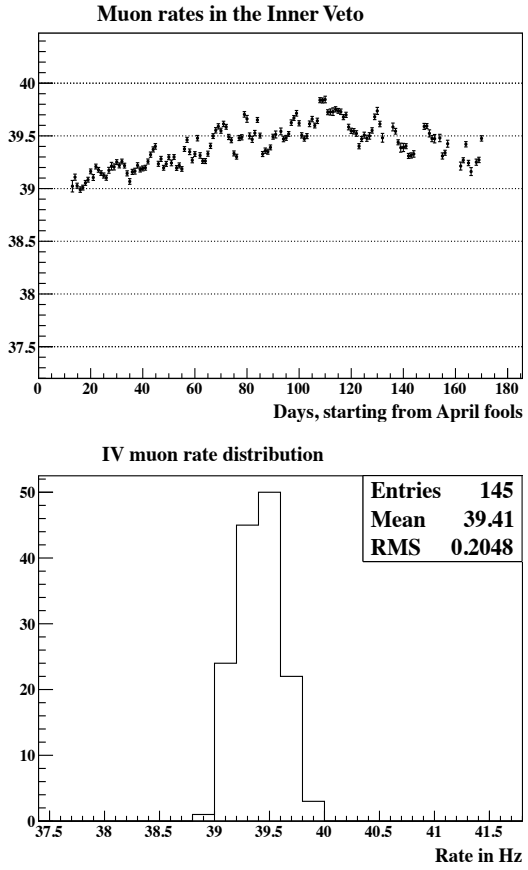

Figure 8.11: IV muon rate per day (top) and the associated muon rate distribution (bottom).

What is indeed interesting to note, is that in both rate vs day plots, both for the IV and the ID, a common rise is readily observed. After investigation one could see that the rise patterns for the IV and ID are very similar in magnitude. Arguments have been given within the DC collaboration (see for instance [274]) that both patterns are consistent with seasonal changes related to variations in the atmospheric temperature and pressure. We will very briefly elaborate on this rise in a following section.

8.5 Understanding the ID muon signature

In the remaining part of this work we plan to investigate more thoroughly the selection of ID muons studying in detail their signature. An approach has been already given but we do plan to elaborate more on ID muons. The

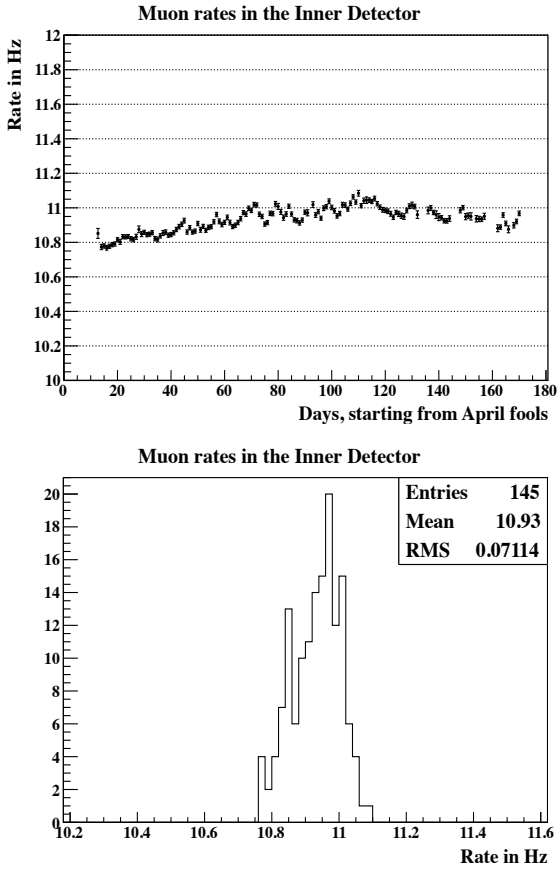

Figure 8.12: ID muon rate per day (top) and the associated distribution (bottom).

purpose of this work is twofold. Firstly, we would like to validate the existing approach and secondly try to gain, if possible, a better understanding on the way our detector responds to muons. To this end we plan to exploit also the timing information of the IV and ID responses. It should be emphasized that all approaches up to now have focused solely on the event-wise charge information only.

To do so we introduce, grouped in pairs, four new variables that we shall call wtime[0,1] and wtimeIV[0,1][3]. They correspond to the mean values (0th component) and the RMS (1th component) of the histograms obtained by filling the pulse start times for each channel weighted by the read-out channel's charge for every event. wtime[0,1] are taken from the ID channels and wtimeIV[0,1] from those in the IV as the name suggests. Note that

[3]The names of the variables arise from the abbreviation of weighted time. Note that the distributions from where wtime and wtimeIV stem are similar but not identical to the usual pulse shape discrimination distributions.

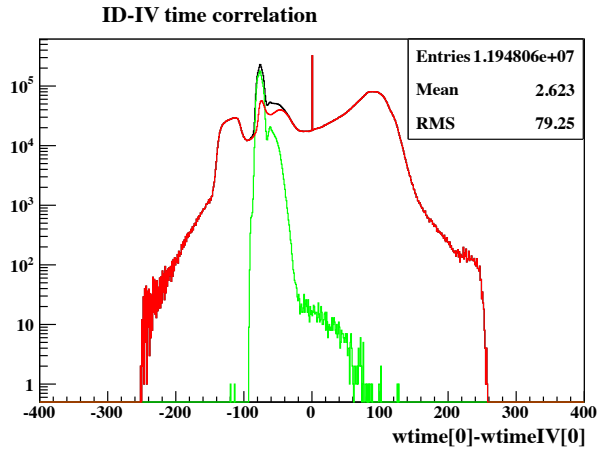

Figure 8.13: wtime[0] - wtimeIV[0] distribution with real data. The color conventions are explained within the text.

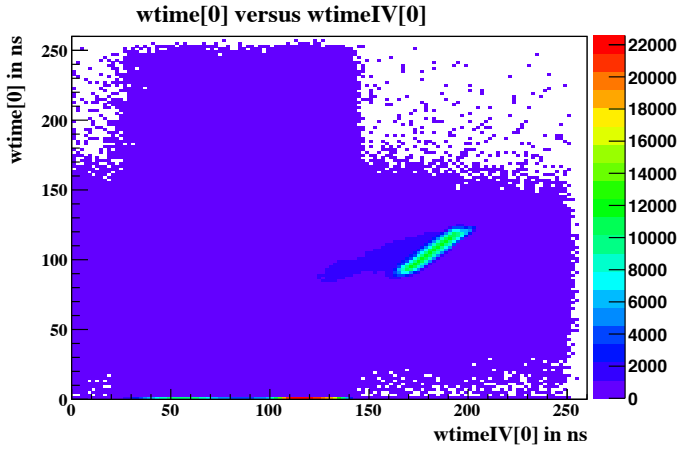

Figure 8.14: wtime[0] versus wtimeIV[0] scatter plot with real data.

wtime[1] is similar but not identical to the official DC discriminating variable RMS(Ts). Some parts of the analysis we put forward with wtime[1] could have been done with RMS(Ts) while some other points are more transparent through wtime[1].

The reason we invented these variables was because we wanted to look for correlations between the time-responds in the IV and the ID. To see this in fig. 8.13 we plot, in black, the distribution of wtime[0] - wtimeIV[0] and wtime[0] versus wtimeIV[0] in fig. 8.14. In fig. 8.13 we do see a peak at 90 ns floating over a background of uncorrelated events. The specific position of the

peak is connected with issues related to the trigger [205]. The peak of course corresponds to incoming particles with muons to dominate the statistics as expected. Other particles like fast neutrons should be included under this peak but muons consist of the majority. To further clean the sample we apply the following cuts:

- $N_{HIT}^{IV} > 11$
- $N_{HIT} > 150$
- $Q_{MAX}/Q_{TOT} < 0.15$

we already know that they remove essentially no scintillation muons. We draw this latter plot, obtained with the cuts above, in green in fig. 8.13 while in red we superimpose the rejected events. We clearly see the presence of a bump at the red histogram signaling that some correlated events were rejected. That was anticipated, since we know that some Buffer muons are rejected through the combined $Q_{MAX}/Q_{TOT} < 0.15$ and $N_{HIT} > 150$ cuts.

Three regions in the selected wtime[0] - wtimeIV[0] distribution catch the eye. First there is a pronounced peak that corresponds evidently to ID muons. Then there is a second peak slightly separated from the main contribution and a third region that spans a wide interval, equal almost to the whole sampling window, suggesting that some BG was not properly subtracted. To see this, one could plot RMST(start) or ctt2tot[3] observing that these events occupy regions that should be rejected through the Light Noise (LN) tagging cuts. We remind that ctt2tot[3] is a common tail-to-total variable originating from the usual corrected for the time of flight Pulse Shape Discrimination (PSD) distribution [276]. Adding the extra $Q_{IV} > 100000.0$ DUQ cut this population disappears.

The most challenging part would be to interpret the two IV - ID correlated peaks in the wtime[0] - wtimeIV[0] distribution. For this purpose a lot of paths could be followed; we plan to take the most radical. In fig. 8.15 we draw the distribution of wtime[1] in normal (left) and logarithmic (right) scale. The structure revealed is very interesting and suggesting. We clearly observe the presence of three separate regions with approximate limits at 11.5, 26 and 52 ns. Note that without the Q_{IV} >100000.0 DUQ a forth region of LN events with wtime[1] bigger than 52 ns would have been present.

To see where these three regions correspond in the energy spectrum we draw in fig. 8.16 the charge distribution for the ID with the already applied preselection. We superimpose the various regions in red for 26 ns < wtime[1] < 52 ns, blue for 11.5 ns < wtime[1] < 26 ns and green for wtime[1] < 11.5 ns. It is indeed a very interesting feature that the wtime[1] regions are well

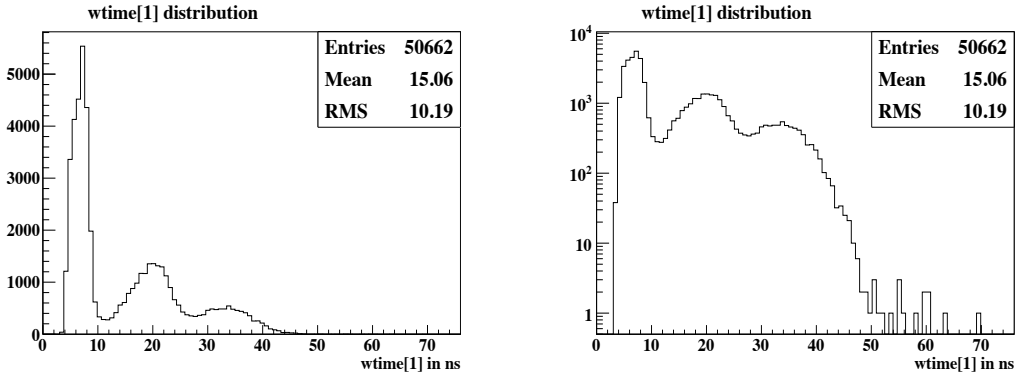

Figure 8.15: wtime[1] distribution in normal (left) and logarithmic (right) scale.

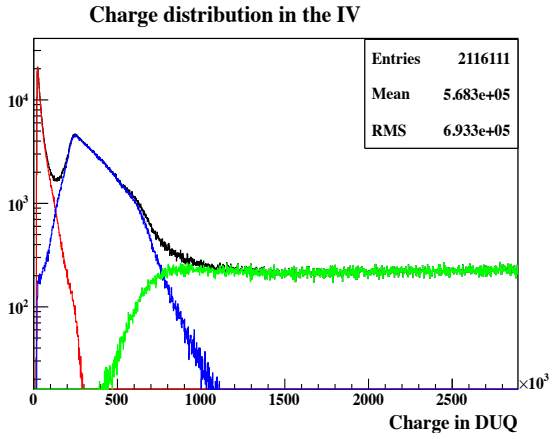

Figure 8.16: Charge regions for the various values of wtime[1]. In red for 26 ns $<$ wtime[1] $<$ 52 ns , in blue for 11.5 ns $<$ wtime[1] $<$ 26 ns and green for wtime[1] $<$ 11.5 ns.

separated in energy. Totally leaning on a rough MC comparison one could assume that the wtime[1] $<$ 11.5 ns region corresponds to ID scintillation muons, that the second region between 11.5 and 26 ns corresponds to Buffer muons while for the third only assumptions could be made. In the following we shall focus on these regions in much greater detail.

Region I: 26 ns $<$ wtime[1] $<$ 52 ns

The first interesting point to utter is that for this region the muon tracking reconstruction algorithm `RecoHam` does not report any tracks at all. Also, the events present in this class have different time signatures than those in

the other classes corresponding to the smaller displaced peak of fig. 8.13. This can be shown drawing the fig. 8.13 selected sample overlapping in green the events within the wtime[1] region above. This is done in fig. 8.17. We also observe that the vertices as reported by `RecoBAMA`, the standard vertex reconstruction algorithm, (fig. 8.18) are gathered at the edges of the TG. Then, if one takes also into account that for most of the cases a huge amount of charge is measured in the IV (see fig. 8.19) it is easy to conclude that these events correspond to particles coming from the exterior. In this respect it is interesting to know why their time stamp, as seen in the wtime[0] - wtimeIV[0] distribution, is different from the rest of the cases.

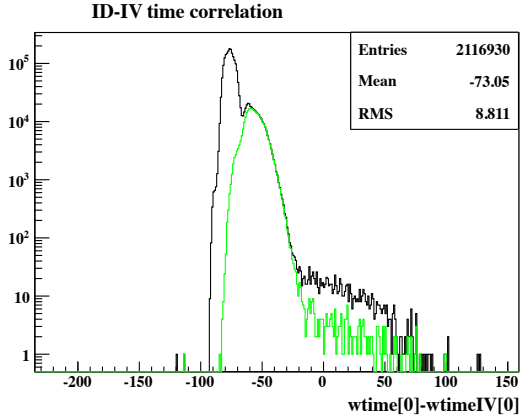

Figure 8.17: wtime[0] - wtimeIV[0] distribution; in green we overlap those events with 26 ns $<$ wtime[1] $<$ 52 ns.

The possibility that we are treating LN was seriously examined but it was soon rejected since: (i) The vertices do not show the pathological structures characteristic of LN (ii) The ID - IV time-responses are correlated, in contradiction with what would be expected if one dealt with LN (iii) The ID vertex positioning and the charge collected in the IV suggest that we see particles coming from the outsides of the detector (iv) All known LN tagging variables were tested but none of these shown any pattern similar to LN. See for instance fig. 8.20 (left) and (right) where the Q_{MAX}/Q_{TOT} and RMS(Ts) variables are plotted. Finally, we should also mention that for the majority of these events an Outer Veto (OV) coincidence is reported.

All the above arguments are enough to persuade us that we do see ID - IV correlated events, to wit external particles or radiation. Since the events in this region are not present in the MC muon sample and since no muon tracking information is available in the data one would tent to think that they do not correspond to cosmic ray muons. The second possibility for them to

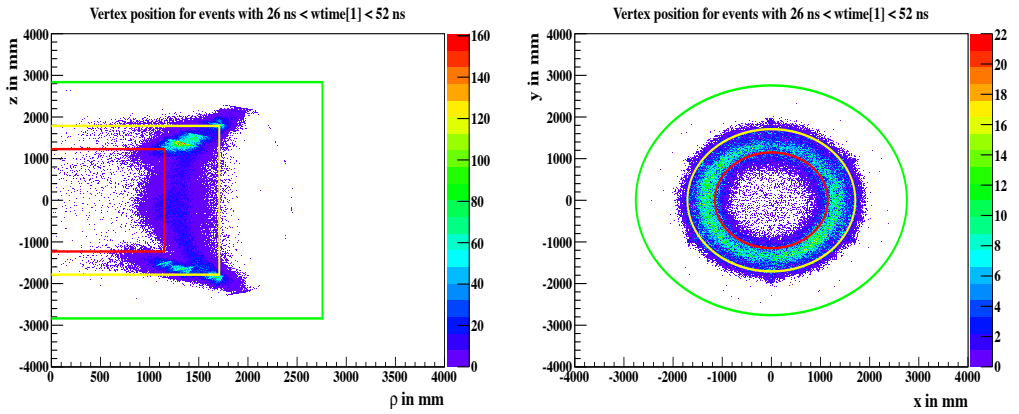

Figure 8.18: Vertices for the events with 26 ns $<$ wtime[1] $<$ 52 ns. We draw the z versus ρ (left) and y versus x (right) distributions. The borders or the several ID regions are included.

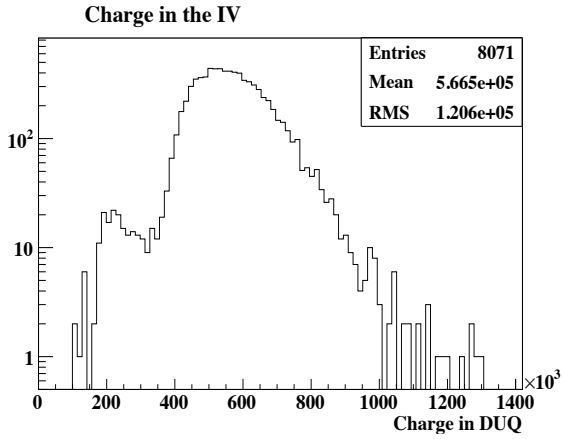

Figure 8.19: Collected charge in the IV for the 26 ns $<$ wtime[1] $<$ 52 ns events.

be fast neutrons (FN) was examined but it was also disfavored since: (i) The reconstructed vertices are gathered at the very edges of the GC, not in its periphery as one would expect from FN (ii) A look at the neutrino candidates for the first publication run list (fig. 8.21) reveals that no such population is present in the sample while one expects a FN contamination of roughly 0.5 events per day (iii) an examination of tagged FN following the considerations of [277, 278] showed that FN prefer the wtime[1] $<$ 26.0 region.

Even though the possibility to observe rock gammas is always relevant, we have a predilection to believe that these events are muons entering only the Buffer and releasing photons primarily through Cerenkov radiation. We

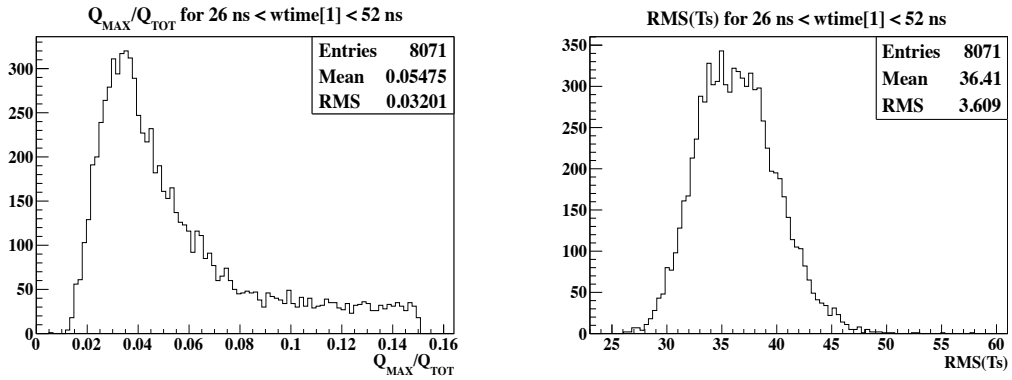

Figure 8.20: Q_{MAX}/Q_{TOT} (left) and RMS(Ts) (right) for the 26 ns < wtime[1] < 52 ns events.

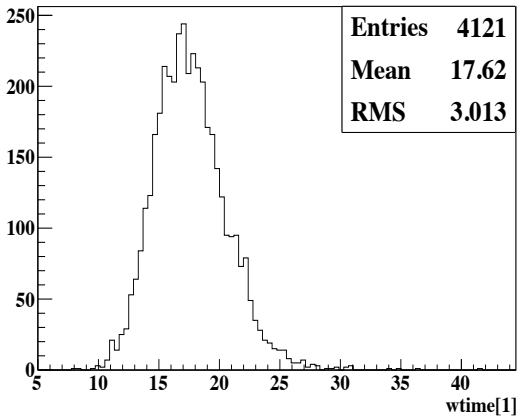

Figure 8.21: wtime[1] for the selected neutrino candidates. No significant excess exists at 26 ns < wtime[1] < 52 ns that could be connected with FN.

believe that the reason why this effect is not seen in the MC stems from an improper treatment of the Cerenkov radiation component in our simulations. In this respect this work could also help us to better understand and thus tune the MC behaviour. Nonetheless, despite personal prejudices, we should bear in mind that the origins of this contribution are still obscure and more work is indeed needed.

Region II: 11.5 ns < wtime[1] < 26 ns

Let us now concentrate on the region with 11.5 ns < wtime[1] < 26 ns. From the ID - IV time correlation and the energy spectrum we expect them to be Buffer muons that give cascades of particles, Cerenkov radiation and

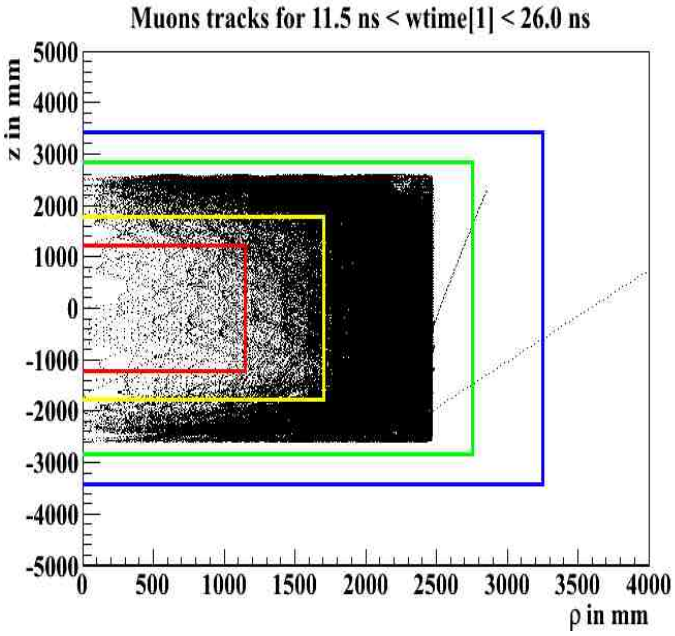

Figure 8.22: Muon tracks for those events with 11.5 ns $<$ wtime[1] $<$ 26 ns. Plot prepared with real data, the tracking information was taken from RecoHam.

that sometimes maybe clip the GC. The reason that these cases have more narrow wtime[0] - wtimeIV[0] and wtime[1] distributions arise probably from the fact that they travel more inside the detector with higher probability to create light through the associated showering particles.

To test this assumption we show in fig. 8.22 the muon tracks for those selected cases within this region. This plot was prepared with real data and the tracking information was taken from `RecoHam`. We indeed see most of the tracks to populate the Buffer region. Of course there are some orbits that do enter the GC. Taking into account that these cases are only a small fraction of the total sample and bearing in mind the errors and biases inherent to every reconstruction algorithm we believe that these observations are strong indications pointing towards our hypotheses.

Region III: wtime[1] $<$ 11.5 ns

The last part of our assumption is that the wtime[1] $<$ 11.5 ns cases are muons that enter at least the GC region. Again one could use the tracking algorithm to further confirm this hypothesis and again this is validated as seen in fig. 8.23 where we plot the minimum of the cylindrical radius ρ_{min} for

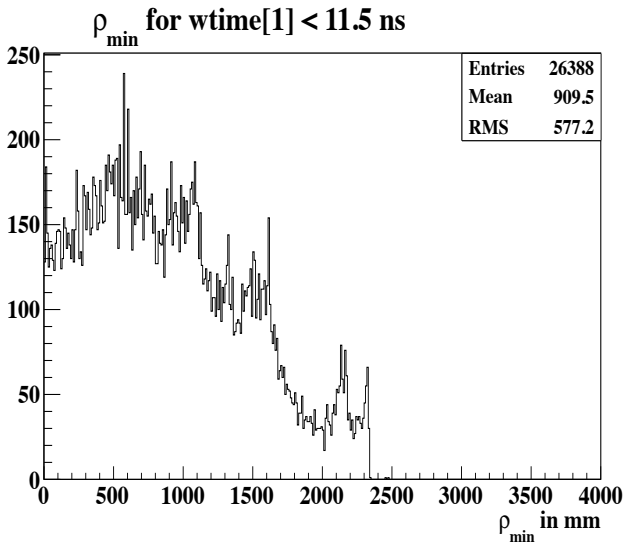

Figure 8.23: The distribution of minimum ρ for the events with wtime[1] smaller than 11.5 ns.

these tracks. We see clearly that most of the cases have ρ_{min} smaller than 1700 mm, the value that corresponds to the radius of the GC. In addition we observe that the energy spectrum we find (fig. 8.16) fits well to the expected one for scintillation muons. Motivated by these observations we shall initiate another approach to ID muons based on these features.

8.6 ID muon rates; revisited

Following our previous considerations we shall finally put forward a measurement of the cosmic muon flux relating ID muons with the region III of the wtime[1] discriminating variable. We summarize the decided cuts:

- $Q_{IV} > 100000.0$ DUQ
- $N_{HIT}^{IV} > 11$
- $N_{HIT} > 150$
- $Q_{MAX}/Q_{TOT} < 0.15$
- wtime[1] < 11.5 ns

Note that the selection perceived is very different from the mainstream approaches already pursued in DC.

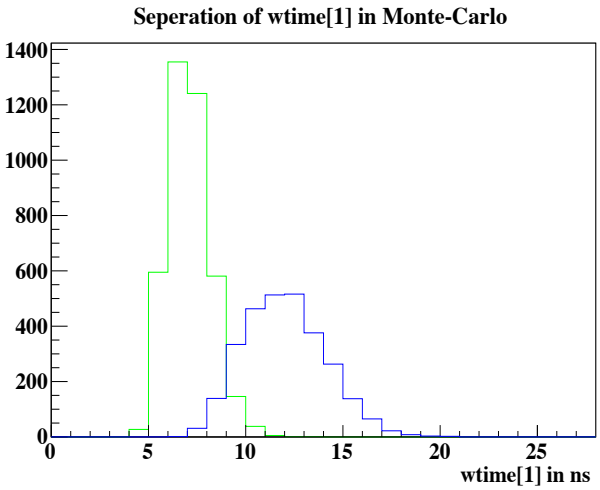

Figure 8.24: wtime[1] distributions for scintillation (green) and Buffer (blue) muons. Plots derived with the Monte-Carlo sample.

To further motivate this selection we show in fig. 8.24 the wtime[1] distributions for Buffer (blue) and scintillation muons (green) obtained with the MC sample. It is satisfactory to see that MC predicts the separation we did witness previously. The exact limits of the two regions do not match and the space between the two peaks is not identical, but we already knew that the MC might not be perfect regarding these issues. Also note that the first 26 ns $<$ wtime[1] $<$ 52 ns peak is not present in MC. That was, in fact, anticipated since the corresponding energy region was also absent in the MC energy spectrum. According to the MC the wtime[1] $<$ 11.5 ns cut removes ID muons in the order of smaller than 1 %.

With this selection recipe the ID muon rate could be determined. The result is:

$$11.177 \pm 0.001 \ (stat.) \ Hz.$$

No systematical error was again calculated. On fig. 8.25 (top) and fig. 8.25 (bottom) are shown the ID muon rates vs the raw day number, following the usual conventions, and the ID muon rate distribution. It is very important that the results of the two methods for ID muon selection agree to an accuracy of roughly 2 %. We feel that this is an important cross-check.

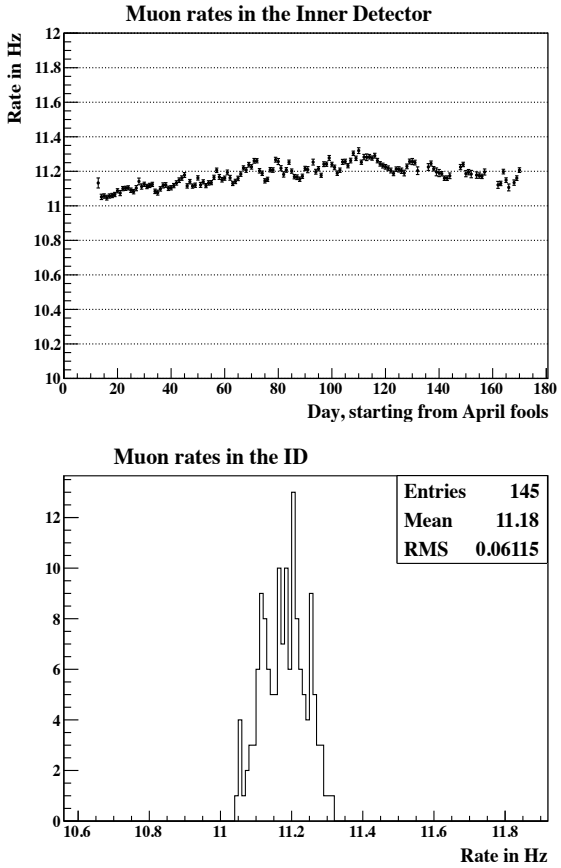

Figure 8.25: ID muon rate per day (top) and the associated distribution (bottom).

8.7 The aplanarity formalism

In this section we shall motivate yet another formalism to attack ID muon selection. The considerations we are about to describe, were derived while investigating the origins of the 26 - 52 ns region in wtime[1]. More precisely, we found very convenient the use of another variable (originally devised for the tagging of LN) that we shall name central aplanarity. The sample selection will follow the lines already presented in previous sections but for the final separation of scintillation and Buffer muons central aplanarity will be exploited. It is gratifying that the aplanarity approach, we will put forward, agree with that based on wtime[1] in less than 1 % accuracy. Also, both strategies show the same improvement in the low energy part of the selected ID sample; a feature not present in a sharp cuts approach.

As a reminder, aplanarity has been defined as the 1.5 of the smaller eigenvalue of sphericity tensor, S^{ab} . The vectors required for the construction of the sphericity tensor are taken from the reconstructed vertex of the event. In the cases were a vertex is not reported, the decision taken is to use the centre of the detector (0, 0, 0). Note that this is very important for muons since in these cases a vertex is not available for most of the times. But in any case, an aplanarity variable can always be defined from a tensor built from the center of the detector. This variable will be called central aplanarity. Of course, central sphericity also exists. Note also, that the cuts relevant for central aplanarity and sphericity will be very different from those already devised for common aplanarity and sphericity.

In fig. 8.26 central aplanarity (capla) is shown for Monte-Carlo (top) and data (bottom). In the MC plot we overlap in blue the contribution of Buffer muons and in green that from scintillation muons. The similarity of the two capla distributions is in general evident but with a notable difference at the very low capla regime. This difference originates from the presence of the low energy part in the spectrum that's not present in the MC. What it is indeed convenient is that according to the MC, Buffer and scintillation muons are well separated in the aplanarity space. A simple cut at 0.08 in central aplanarity seems enough to remove a lot the Buffer muons, but note that the data - MC similarity with respect to capla is not perfect. If we trust MC the inefficiencies induced to the scintillation muon sample are smaller than 1 %. The actual shapes of the two distributions differ a lot but the population in low capla values originating from Buffer muons is indeed present.

Motivated by these observations we apply the following combined cuts to the data sample:

- $N_{HIT}^{IV} > 11$
- $Q_{IV} > 100000$ DUQ
- $N_{HIT} > 150$
- $Q_{MAX}/Q_{TOT} < 0.15$
- capla > 0.08

Like this, we find the distribution of fig. 8.27 for the charge deposition. Remember that, as it has been already demonstrated, the first four cuts do not remove significantly any scintillation muons exactly as the fifth cut in capla. Looking at the resulting spectrum of fig. 8.27, it is very intriguing to see that

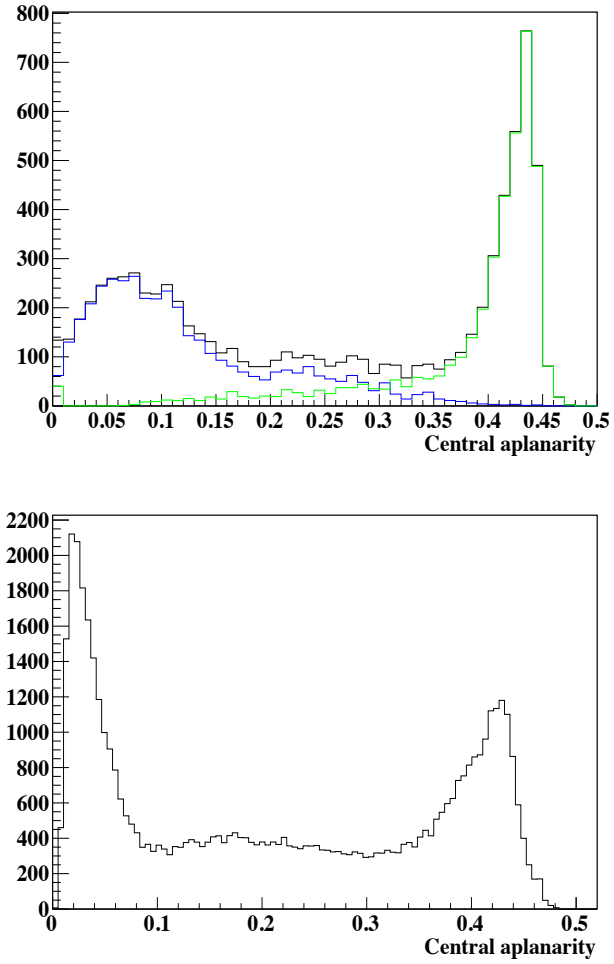

Figure 8.26: Central aplanarity distributions for MC (top) and data (bottom). In the MC distribution Buffer muons are depicted in blue and ID scintillation muons are shown in green.

it has been separated in two split regions with a loose border somewhere around 400000.0 DUQ. Judging alone from the shape of the distribution it seems that most of the Buffer muons have been totally abolished from the sample. This is of course what MC suggested us.

Another way to see this clean separation is by looking the capla distribution of the 11.5 ns $<$ wtime[1] $<$ 26 ns region. This is shown in fig. 8.28. Remember that this region in wtime[1] was previously interpreted as Buffer muons and it is very gratifying that those observations are independently confirmed through capla; to wit 11.5 ns $<$ wtime[1] $<$ 26 ns events have

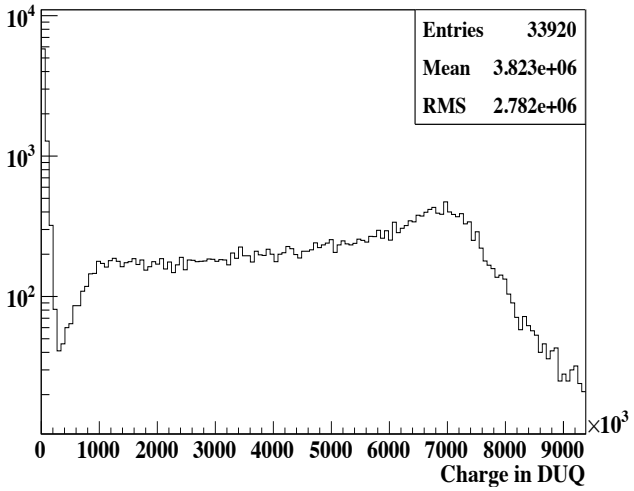

Figure 8.27: ID charge deposition after the five decided cuts.

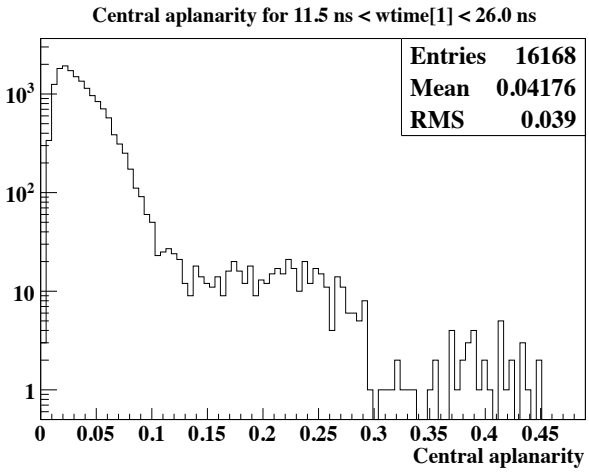

Figure 8.28: Central aplanarity for 11.5 ns $<$ wtime $<$ 26.0 ns.

small capla as expected for Buffer muons. From the spectrum in fig. 8.27 it is also observed that the first wtime[1] region, 26 ns $<$ wtime[1] $<$ 52 ns, is still there. In this respect it is interesting to understand why this class of events have relatively high values of capla. In fig. 8.29 the capla distribution for the events in the 26 ns $<$ wtime[1] $<$ 52 ns region is shown.

The actual reason for this separation of Buffer - scintillation muons seen in fig. 8.27 is still not fully clear to us. Nonetheless, all of the arguments fit well to the observations and they are further confirmed through MC. To finalize the ID muon selection one additional cut is needed to remove the low energy

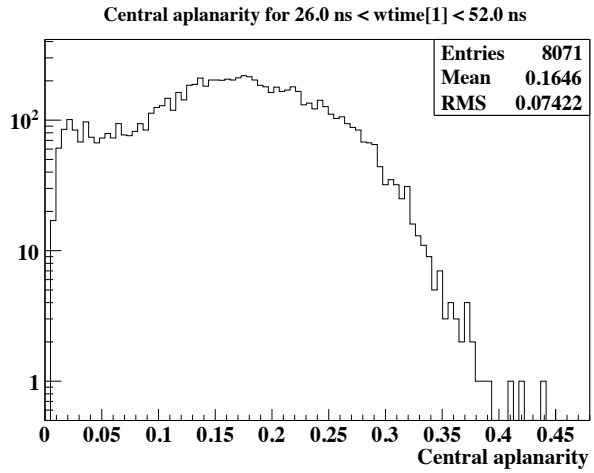

Figure 8.29: Central aplanarity for 26.0 ns < wtime < 52.0 ns.

part in fig. 8.27 . This will be the ID charge cut $Q_{ID} > 400000.0$ DUQ. This is somehow looser than the $Q_{ID} > 900000.0$ DUQ cut we previously used, owing to the $capla > 0.08$ condition. We now summarize the cuts devised for ID muon selection in this section:

- $Q_{IV} > 100000.0$ DUQ
- $N_{HIT}^{IV} > 11$
- $N_{HIT} > 150$
- $Q_{MAX}/Q_{TOT} < 0.15$
- capla > 0.08 ns
- $Q_{ID} > 400000.0$ DUQ

With this selection the inefficiencies are expected to be roughly 0.3 % in magnitude.

Before we turn to the ID muon rate calculation, it will be interesting to compare the energy spectra provided by the wtime[1] and capla approaches. This is done for the data in fig. 8.30. In green we denote the wtime[1] selected sample and in blue those events selected according to capla. It is very important that both distributions agree to a remarkable degree in shape. The most important feature is the consistency observed in the low energy region, the part that all sharp charge cuts approaches are expected to reject. The number of events finally selected with the two methods utterly agree to a better than 0.5 % level.

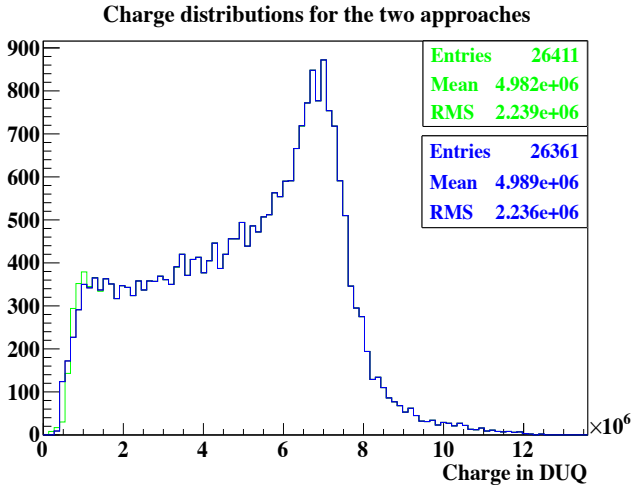

Figure 8.30: Charge distributions (data) as obtained with the wtime[1] (green) and the capla (blue) approaches.

Using the aforementioned technique to ID muon selection we obtain a rate of:

$$11.149 \pm 0.001 \ (stat.) \ Hz.$$

for the ID. The relevant day by day plots for this selection are gathered in fig. 8.31. The result is in accordance with previous considerations in an astonishing level. Especially the wtime[1] and capla techniques agree to an unprecedented level. See for instance fig. 8.32 were the ID muon rates are plotted, in black for the wtime[1] based approach and in red for that through capla. It is also important that both data points show the same variation patterns.

8.8 Final remarks

Both IV and ID muon rates, as calculated through the various techniques, show several interesting modulations with the passage of time. Even though we reported in these variation patterns we deliberately postponed to give arguments about their origins. This will be rectified in this short section.

Firstly, we should mention that what we see is unlikely to be an issue related to the detector's response. In other words, we do see a real effect, not an artifact caused by changes in the detector's performance. The chief reason for believing so is that the ratio between IV and ID rates (say those calculated through the sharp charge cuts approaches) is roughly constant for

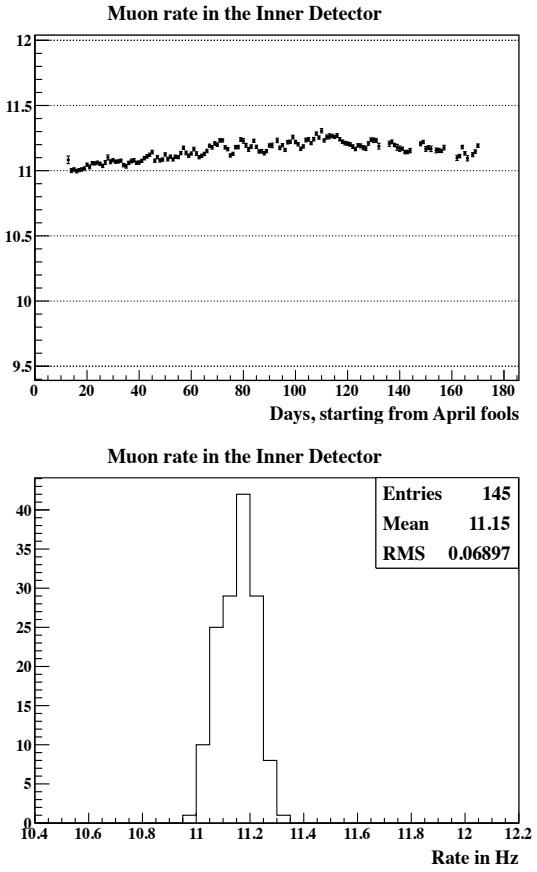

Figure 8.31: ID muon rate per day (top) and the associated distribution (bottom).

the period of data taking (fig. 8.33)[4]. Actually evidence have been reported within the DC collaboration that these modulations follow closely the changes observed in the atmospheric temperature and pressure. For a summary of these efforts one could have a look at [274]. It has to be noted that, in the past, similar modulations in the muon flux have been observed but other underground experiments like MACRO [279], ICECUBE [280] or MINOS [281] for instance. For a recent work on this subject the reader might consult an important paper published lately by the BOREXINO Collaboration [282].

[4]Here we shall neglect small, second order modulations of this ratio arising from the accuracy of our analysis methods.

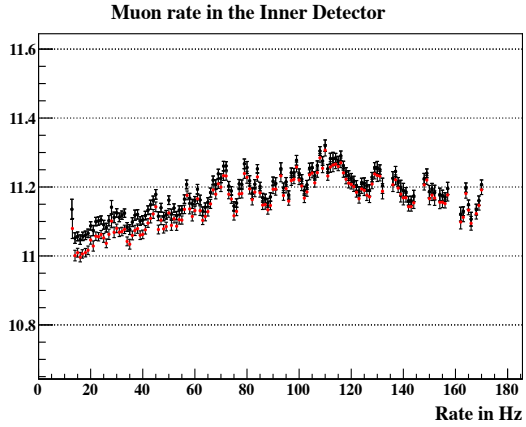

Figure 8.32: ID muon rates per day for the wtime[1] (black) and capla (red) techniques.

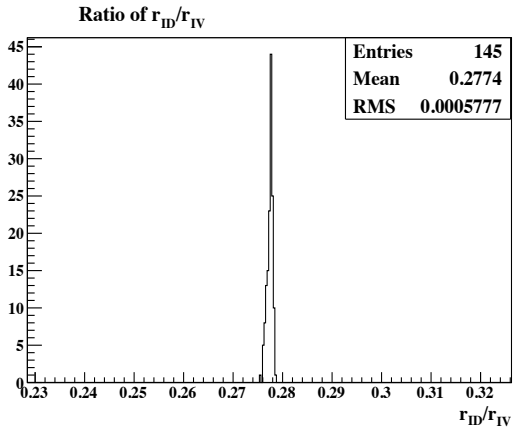

Figure 8.33: Ratio of the muon rate in the ID over the rate in the IV.

Πάντα στον νου σου να ᾽χεις την Ιθάκη.
Το φθάσιμον εκεί είν΄ ο προορισμός σου.
Αλλά μη βιάζεις το ταξιδι διόλου.
Καλλίτερα χρόνια πολλά να διαρκέσει·
και γέρος πια ν΄ αράξεις στο νησί,
πλούσιος με όσα κέρδισες στον δρόμο,
μη προσδοκώντας πλούτη να σου δώσει η Ιθάκη.

Η Ιθάκη σ΄ έδωσε τ΄ ωραίο ταξίδι.
Χωρίς αυτή δεν θα βγαινες στο δρόμο.
Άλλα δεν έχει να σου δώσει πια.

Κι αν φτωχική τη βρείς, η Ιθάκη δεν σε γέλασε,
Έτσι σοφός που έγινες με τόση πείρα,
ήδη θα το κατάλαβες οι Ιθάκες τί σημαίνουν.

Κ. Π. Καβάφης, Ιθάκη

Always remember Ithaca.
To arrive there is your final destination.
But take your time, don't speed this journey.
You'd rather want this trip to last for years;
and aged one day to settle in the island,
rich and mature with all the lessons that you learned,
without expecting Ithaca to give you treasure chests.

Ithaca gave you this notorious journey.
Without her you would not have started this adventure.
But nothing more she haves to give you.

And if you find her poor, Ithaca never tricked you.
Wise as you are, with all these memories to haunt you,
you should already know Ithaca's meaning.

C. P. Kavafy, Ithaca

Conclusions

Double Chooz (DC) is one of the leading experiments setup to measure the neutrino mixing angle θ_{13} leaning on the disappearance of reactor electron anti-neutrinos at a baseline of roughly 1 km away from the reactor cores. Throughout the thesis we presented the experimental concept and the hardware implementation of DC emphasizing the importance of this experiment from a general perspective. The main notions of neutrinos and neutrino oscillations were presented clearly so that the reader could profit and understand the significance of DC in the global picture. This was done in particular with a detailed discussion of the most recent, precise measurements of the various oscillation parameters.

The work conducted in the course of this thesis was instrumental to the construction and the operation of the DC detector; the "eye" of the experiment. The proper functioning of the detector, the understanding of its performance and the monitoring of its stability are all aspects, vital to a precise determination of θ_{13}. The author contributed to the construction and the optimization of the Inner Veto (IV) of the DC far detector. A device necessary for the rejection of several dangerous backgrounds.

We tested all the IV photomultiplier tubes (PMTs) prior to their installation ensuring that they are properly operating and we investigated their behavior before their placement inside the detector. Additionally we were involved in the construction and the operation of the Inner Veto Light Injection system (IV-LI). The calibration in terms of the time and the charge response of all the IV PMTs is performed through the IV-LI and so the monitoring of the IV is intimately connected to the IV-LI. We analyzed the pre-installation data providing to the collaboration the necessary input for the configuration of the IV (eg. the nominal PMT high voltage values).

We also analyzed the first large-mass data taken during the commissioning period to probe the detectors performance and setup the IV-LI optimal running conditions. During the course of the experiment we were responsible for the analysis of the calibration sequences taken once per week with the IV-LI for gain determination.

We were also strongly involved in the analysis studies performed by the DC collaboration towards the first publication result. We concentrated on the estimation of various categories of backgrounds. We succeeded in providing the first concise treatment of the combined fast neutron and stopping muon background proving unequivocally that the high energy class of events that contaminate the signal consists of two populations. The tools and the notions developed were instrumental to the final estimation. Accordingly we traced (through this work) a dangerous inefficiency of the IV improving the muon tagging decisions. All this work was very important for the first measurement of θ_{13} reported by the DC collaboration.

An instrumental background relevant for this generation of θ_{13}-searching liquid scintillator detectors was also studied and an interesting frame was put forward for its identification. The algorithms written were tested with calibration data and the rejection inefficiencies were studied in some extent. The final machinery advanced, helped the collaboration to further decipher the behavior of this noise and it validated form another point of view the decisions and selection criteria devised for neutrino events. Additionally our algorithms seem to have a better performance in the high energy regime.

Finally we contributed significantly in the Inner Detector muon identification strategy. Besides the already existing approaches to attack muon selection with the use of sharp cuts on the charge (or energy) we formulated two further techniques to select muons that cross the Inner Detector: one based on the pulse shape information and another leaning on the hit topology patterns. The degree at which these approaches agree in the calculation of the muon rates is rather satisfactory.

The understanding of muon tagging and the signals that muons deposit in the detector are very important for a thorough understanding of the detector itself. In this respect this study will play an important role in future investigations. Furthermore a precise measurement of the muon rate could help us to comprehend the output of many cosmic ray simulation packages and validate their performance. Last, the seasonal variation/modulation of the muon flux seen with these investigations could help us examine and test many models associated with the production and the propagation of particles in the upper levels of the atmosphere.

Bibliography

[1] G. J. Neary, "The β-Ray Spectrum of Radium E", Proc. R. Soc. Lond. A 1940 175, 71-87

[2] http://en.wikipedia.org/wiki/Polonium

[3] J. Chadwick, Verh. d. Deutschen Phys. Ges. 16 (1914) 383.

[4] C. D. Ellis and W. A. Wooster, "The Average Energy of Disintegration of Radium E", Proc. Roy. Soc., A, 117, 109 (1927).

[5] Winter K., "Neutrino Physics", Cambridge Monographs on Particle Physics, Nuclear Physics and Cosmology.

[6] W, Heitler and G. Herzberg, Naturwiss., 17, 673 (1929).

[7] P. Ehrenfest and R. J. Oppenheimer, Phys. Rev. 37, 33, (1931).

[8] J. Chadwick, "The Existence of a Neutron", Proc. Roy. Soc. A, 136, p. 692-708, (1932).

[9] E. Fermi, Z. Phys. 88, 161 (1934).

[10] F. Hoyle, "Concluding remarks", Proc. Roy. Soc. (London) A 301, 171 (1967).

[11] F. Reines, "The neutrino: From Poltergeist to particle", Nobel lecture 1995.

[12] H. Bethe and R. Peierls, Nature 133, 532, (1934).

[13] http://library.lanl.gov/cgi-bin/getfile?25-02.pdf

[14] G. Feinberg, Phys. Rev. 110, 1482 (1958).

[15] J. Leites Lopes, "Forty years of the first attempt at the electroweak unification and of the prediction of the weak neutral boson Z", Braz. J. Phys. vol.29 n.3 Sao Paulo Sept. 1999

[16] G. Danby et al., "Observation of High-Energy Neutrino Reactions and the Existence of Two Kinds of Neutrinos", Phys. Rev. Lett. 9, 3644 (1962).

[17] M. Perl, "Evidence for Anomalous Lepton Production in e^+ - e^- Annihilation", Phys. Rev. Lett. 35, 14891492 (1975)

[18] K. Kodama et al. (DONUT Collaboration), "Observation of tau neutrino interactions", Phys. Lett. B 504 (2001).

[19] LEP Collaborations and the LEP Electroweak Working Group "A Combination of Preliminary Electroweak Measurements and Constraints on the Standard Model", arxiv.org/0612034v2.

[20] C. S. Wu et al., "Experimental test of parity conservation in beta decay", Phys. Rev., 105, 4 (1957).

[21] T. D. Lee and C. N. Yang, "Question of Parity Conservation in Weak Interactions", The Physical Review, 104 (1956).

[22] R. H. Dalitz, "Decay of τ Mesons of Known Charge", Phys. Rev. 94, 1046 - 1051 (1954).

[23] Garwin, R.L., Lederman, L.M., Weinrich, M., "Observations of the failure of conservation of parity and charge conjugation in meson decays : the magnetic moment of the free muon", Physical Review, 105(4), 1957.

[24] Friedman, J. I. and Telegdi, V. L., Phys. Rev. 105, 1681 (1957).

[25] M. Goldhaber, Lee Grodzins and A. Sunyar , "Helicity of neutrinos", Phys. Rev. Lett., 109, 1015-1017, 1958.

[26] E. C. G. Sudarshan and R. E. Marshak , New York"Chirality Invariance and the Universal Fermi Interaction", Phys. Rev. 109, 18601862 (1958)

[27] R. P. Feynman and M. Gell-Mann, "Theory of the Fermi interaction", Phys. Rev. 109 193-198 (1958).

[28] J. J. Sakurai, Nuovo Cimento 7 (1958) 649.

[29] A. Salam, "On Parity Conservation and Neutrino Mass" Nuovo Cim. 5 (1957) 299.

[30] L. D. Landau, Nucl. Phys. 3, 127 (1957).

[31] Lee, T. D. and Yang, C. N., Phys. Rev. 105, 1671 (1957).

[32] T. Thummler, "Introduction to direct neutrino mass measurements and KATRIN", XXIV International Conference on Neutrino Physics and Astrophysics, Athens, Greece, June 14 - 19, 2010.

[33] K. Nakamura and S.T. Petcov, "Neutrino mass, mixing and oscillations", Particle Data Group (2010).

[34] F.J. Hasert et al, Observation of neutrino-like interactions without muon or electron in the Gargamelle neutrino experiment, Nucl. Phys. B73 (1974) 1

[35] R. Davis, D. S. Harmer, H. C. Kenneth, "Search for neutrinos from the sun", Phys. Rev. Lett. 20, 1205-1209 (1968).

[36] T. J. Haines et al., "Calculation of Atmospheric Neutrino-Induced Backgrounds in a Nucleon-Decay Search", Phys. Rev. Lett. 57, 1986 - 1989 (1986).

[37] K.S. Hirata et al., "Experimental study of the atmospheric neutrino flux", Phys. Lett. B 205, 416 (1988).

[38] C. F. von Weizsacker, "Uber Elementumwandlungen im Innern der Sterne. I", Physikalische Zeitschrift, vol. 38, 176 - 191 (1937).

[39] C. F. von Weizsacker, "Uber Elementumwandlungen im Innern der Sterne. II", Physikalische Zeitschrift, vol. 39, 633 - 646 (1938).

[40] H. A. Bethe, "Energy production in stars", Phys. Rev. 55, 434 - 456 (1939).

[41] E. G. Adelberger et al. , "Solar fusion cross sections. II. The pp chain and CNO cycles", Rev. Mod. Phys. 83, 195245 (2011).

[42] J. N. Bahcall and C. Pena-Garay, "Solar models and solar neutrino oscillations", New J. Phys., 6, 63 (2004).

[43] J. N. Bachall, R., "Solar neutrinos. I: Theoretical", Phys. Rev. Lett. 12 (1964) 300-302.

[44] R. Davis, "Solar neutrinos. II: Experimental", Phys. Rev. Lett. 12 (1964) 303-305.

[45] Cleveland, Bruce T. et al., "Measurement of the solar electron neutrino flux with the Homestake chlorine detector", Astrophys. J. 496 (1998) 505-526.

[46] J. N. Bahcall, M. H. Pinsonneault, and S. Basu, "Solar models: current epoch and time dependences, neutrinos, and helioseismological properties", Astrophysical J. 555, 990-1012 (2001).

[47] Fukuda, Y., et al. 1996, Phys. Rev. Lett., 77, 1683 (Kamiokande Collaboration)

[48] J. N. Abdurashitov et al. (SAGE), "Measurement of the solar neutrino capture rate by SAGE and implications for neutrino oscillations in vacuum", Phys. Rev. Lett. 83 (1999) 4686-4689

[49] GALLEX solar neutrino observations: Results for GALLEX IV, Hampel, W. et al. (GALLEX), Phys. Lett. B447 (1999) 127-133.

[50] GNO solar neutrino observations: Results for GNO I, Altmann, M. et al. (GNO), Phys. Lett. B490 (2000) 16 - 26.

[51] `http://www.sns.ias.edu/~jnb/`

[52] Suzuki, Y. 2001, Nucl. Phys. B, 91, 29

[53] `http://www-sk.icrr.u-tokyo.ac.jp/sk/physics/solarnu-intro-e.html`

[54] T. K. Gaisser, "Atmospheric Neutrinos", arxiv.org/0612274.

[55] F. Reines et al., Phys. Rev. Letters 15, 429 (1965).

[56] C. V. Achar et al., Phys. Rev. Letters 18, 196 (1965).

[57] T. K. Gaisser, "Atmospheric Neutrino Fluxes", arxiv.org/0502380

[58] T. K. Gaisser and M. Honda, "Flux of Atmospheric Neutrinos", arxiv.org/0203272

[59] T. Kajita, "Discovery of neutrino oscillations", Rep. Prog. Phys. 69 (2006) 1607 - 1635.

[60] K. S. Hirata et al., "Observation of a small atmospheric ν_μ/ν_e ratio in Kamiokande", Phys. Lett. B, 280, 146 - 152 (1992).

[61] K. S. Hirata et. al, "Atmospheric ν_μ/ν_e ratio in the multi-GeV energy range", Phys. Lett. B, 335, 237-245 (1994).

[62] D. Casper et al., "Measurement of atmospheric neutrino composition with the IMB-3 detector", Phys. Rev. Lett., 66, 2561 - 2564,(1991).

[63] R. Becker-Szendy et al., "Search for muon neutrino oscillation with the Irvine-Michigan-Brookhaven detector", Phys. Rev. Lett., 69, 1010-1013 (1992).

[64] T. Kajita, "Experiments with Atmospheric Neutrinos", II International Neutrino Summer School 2010 (Yokohama and Tokai, J-PARC), 23 - 31 August 2010.

[65] M. Gell-Mann and A. Pais, "Behavior of neutral particles under charge conjugation", Phys. Rev. 97 (1955).

[66] N. Cabibbo, "Unitary symmetry and leptonic decays", Physical Review Letters, 531533 (1963).

[67] S. L. Glashow, J. Iliopoulos and L. Maiani "Weak Interactions with LeptonHadron Symmetry", Physical Review D2, 1285 (1970).

[68] M. Kobayashi and T. Maskawa, "CP-Violation in the Renormalizable Theory of Weak Interaction", Progress of Theoretical Physics 49, 652 - 657 (1973).

[69] E. Kh. Akhmedov and A. Yu. Smirnov, "Paradoxes of neutrino oscillations", Phys. Atom. Nucl. 72 (2009) 1363-1381

[70] M. Zralek, "From kaons to neutrinos: Quantum mechanics of particle oscillations", Acta Phys. Polon. B29 (1998) 3925

[71] B. Pontecorvo, "Mesonium and antimesonium", Sov. Phys. JETP 6 (1957) 429.

[72] Z. Maki, M. Nakagawa, and S. Sakata, "Remarks on the unified model of elementary particles', Prog. Theor. Phys. 28 (1962) 870.

[73] Neutrino astronomy and lepton charge, Gribov, V. N., Pontecorvo, B., Phys. Lett. B28 (1969) 493.

[74] Neutrino experiments and the question of leptonic-charge conservation, Pontecorvo, B., Sov. Phys. JETP 26 (1968) 984-988. [Zh. Eksp. Teor. Fiz. 53, 1717 (1967)].

[75] A. Strumia and F. Vissani, "Neutrino masses and mixings and...", arxiv.org/0606054

[76] B. Kayser, "Neutrino Oscillation Phenomenology", arxiv.org/0804.1121

[77] L. Wolfenstein, "Neutrino oscillations in matter, Phys. Rev. D17, (1978) 2369-2374.

[78] S. P. Mikheyev and A. Yu. Smirnov, "Resonance enhancement of oscillations in matter and solar neutrino spectroscopy, Sov. J. Nucl. Phys. 42 (1985) 913 - 917.

[79] S. P. Mikheyev and A. Yu. Smirnov, "Resonance amplifications of ?? oscillations in matter and solar neutrino spectroscopy, Nuovo Cimento C9 (1986) 24.

[80] S. P. Mikheyev and A. Yu. Smirnov, "Neutrino oscillations in variable-density medium and ?-bursts due to gravitational collapse of stars, Sov. Phys. JETP, 64 (1986) 4 - 7.

[81] S. P. Mikheyev and A. Yu. Smirnov, Proc. of the 6th Moriond workshop on "Massive neutrinos in astrophysics and particle physics, Tignes, France, eds. O Fackler and J. Tran Thanh Van, (1986) p.355.

[82] Boris Kayser "Neutrino Mass, Mixing, and Flavor Change", arxiv.org/0211134v1

[83] S. F. King, "Neutrino Mass Models", arxiv.org/0310204

[84] Fukuda, Y. et al. (Super-Kamiokande), "Evidence for oscillation of atmospheric neutrinos", Phys. Rev. Lett. 81 (1998) 1562 - 1567.

[85] Y. Itow, "Atmospheric neutrinos - Results from running experiments", The XXV International Conference on Neutrino Physics and Astrophysics, June 3 - 9 2012, Kyoto, Japan.

[86] The Super-Kamiokande Collaboration, "Evidence for an oscillatory signature in atmospheric neutrino oscillation", Phys. Rev. Lett. 93, 101801 (2004).

[87] M. H. Ahn et al. (K2K Collaboration), "Measurement of neutrino oscillation by the K2K experiment", Phys. Rev. D 74, 072003 (2006).

[88] Stanley Wojcicki, "Accelerator Experiments with Conventional Beams", II International Neutrino Summer School 2010 (Yokohama and Tokai, J-PARC), 23 - 31 August 2010.

[89] P. Adamson et al. (MINOS Collaboration), "Measurement of the Neutrino Mass Splitting and Flavor Mixing by MINOS", Phys. Rev. Lett. 106, 181801 (2011).

[90] R. Nichol, "Final MINOS Results", The XXV International Conference on Neutrino Physics and Astrophysics, June 3 - 9 2012, Kyoto, Japan.

[91] D. Beavis et al. (E889 Collaboration), Physics Design Report BNL 52459 (1995).

[92] K. Abe et al. (T2K Collaboration), "The T2K Experiment", arxiv.org/1106.1238

[93] K. Abe et al. (T2K Collaboration), "First Muon-Neutrino Disappearance Study with an Off-Axis Beam", arxiv.org/1201.1386

[94] OPERA: An appearance experiment to search for oscillations in the CNGS beam. Experimental proposal, Guler, M. et al. (OPERA), CERN-SPSC-2000-028, 2000.

[95] Nicoletta Mauri, "Highlights from the OPERA experiment", International Conference on New Frontiers in Physics, 10-16 June 2012 Kolymbari, Crete, Greece.

[96] SNO Collaboration, J. Boger et al., Nucl. Instrum. Meth. A449, 172 (2000), nucl-ex/9910016.

[97] H. H. Chen, "Direct Approach to Resolve the Solar-Neutrino Problem", Phys. Rev. Lett. 55, 15341536 (1985).

[98] Alain Bellerive, "From SNO to SNOLAB", The 10th ICATPP Conference, Villa, Como, 8-12 October, 2007.

`http://vali.physics.carleton.ca/~alainb/ABellerive_SNO_como2007.pdf`

[99] Q. R. Ahmad et al., "Direct Evidence for Neutrino Flavor Transformation from Neutral-Current Interactions in the Sudbury Neutrino Observatory" Phys. Rev. Lett. 89, 011301 (2002).

[100] S. Fukuda et al., Phys. Rev. Lett. 86, 5651 (2001).

[101] B. Aharmim et al. (SNO Collaboration), "Combined Analysis of all Three Phases of Solar Neutrino Data from the Sudbury Neutrino Observatory", arxiv.org/1109.0763

[102] J. Busenitz et al., "Proposal for US Participation in KamLAND", http://bama.ua.edu/~andreas/ps_files/kamland_prop.pdf

[103] K. Eguchi et al. (KamLAND collaboration), "First Results from KamLAND: Evidence for Reactor Anti-Neutrino Disappearance", Phys. Rev. Lett. 90, 021802 (2003).

[104] S. Abe et al. (KamLAND collaboration), "Precision Measurement of Neutrino Oscillation Parameters with KamLAND", Phys. Rev. Lett. 100 (2008).

[105] S.T. Petcov, M. Piai, "The LMA MSW Solution of the Solar Neutrino Problem, Inverted Neutrino Mass Hierarchy and Reactor Neutrino Experiments", arxiv.org/0112074.

[106] G. Alimonti, et al. (Borexino Collaboration), "The Borexino detector at the Laboratori Nazionali del Gran Sasso", NIMA Volume 600, Issue 3, 11 March 2009, Pages 568-593.

[107] M. Pallavicini, "Results from Borexino", The XXV International Conference on Neutrino Physics and Astrophysics, June 3 - 9 2012, Kyoto, Japan.

[108] P. F. Harrison, D. H. Perkins and W. G. Scott, "Tri-Bimaximal Mixing and the Neutrino Oscillation Data", arxiv.org/0202074

[109] M. Apollonio et al., "Search for neutrino oscillations on a long base-line at the CHOOZ nuclear power station", Eur. Phys. J. C27, 331(2003).

[110] F. Boehm et al., "Final results from the Palo Verde Neutrino Oscillation Experiment", hep-ex/0107009

[111] "The CHOOZ experiment: Proposal to Search for Neutrino Vacuum Oscillations $\Delta m^2 = 10\ eV^2$ Using a 1 km Baseline Reactor Neutrino Experiment."

http://duphy4.drexel.edu/chooz_pub/

[112] http://en.wikipedia.org/wiki/Chooz_Nuclear_Power_Plant

[113] http://en.wikipedia.org/wiki/Palo_Verde_Nuclear_Generating_Station

[114] From discussions with many past CHOOZ members.

[115] Bemporad, C. and Gratta, G. and Vogel, P., "*Reactor-based Neutrino Oscillation Experiments*", Rev. Mod. Phys. 74 (297), 2002.

[116] T. Schwetz, M. Tortola and J. W. F. Valle, "Global neutrino data and recent reactor fluxes: status of three-flavour oscillation parameters", arxiv.org/1103.0734

[117] M. Mezzetto and T. Schwetz, "Theta_13: phenomenology, present status and prospect", arxiv.org/1003.5800

[118] P. Adamson et al. (MINOS), "New constraints on muon-neutrino to electron-neutrino transitions in MINOS", Phys. Rev. D82 (2010) 051102.

[119] K. Abe et al. (T2K), Indication of Electron Neutrino Appearance from an Accelerator-produced Off-axis Muon Neutrino Beam, Phys. Rev. Lett. 107 (2011) 041801.

[120] C. Giganti, "New results from the T2K experiment" , International Europhysics Conference on High Energy Physics (EPS/HEP), 21 - 24 July 2011, Grenoble, France.

[121] P. Huber, M. Lindner, T. Schwetz, and W. Winter, "Reactor neutrino experiments compared to superbeams", Nucl. Phys., B 665, 487 (2003).

[122] P. Adamson et al. (MINOS), "Improved search for muon-neutrino to electron-neutrino oscillations in MINOS", Phys. Rev. Lett. 107 (2011) 181802

[123] A. Holin, "New Results from the MINOS Experiment" , International Europhysics Conference on High Energy Physics (EPS/HEP), 21 - 24 July 2011, Grenoble, France.

[124] G. L. Fogli, E. Lisi, A. Marrone, A. Palazzo and A. M. Rotunno, "Evidence of $theta(13) > 0$ from global neutrino data analysis", arXiv:1106.6028

[125] Th. Schwetz, M. Tortola and J. W. F. Valle, "Where we are on θ_{13}: addendum to Global neutrino data and recent reactor fluxes: status of three-flavour oscillation parameters", arXiv:1108.1376

[126] Y. Abe et al., "Indication for the disappearance of reactor electron antineutrinos in the Double Chooz experiment", hep-ex/1112.6353.

[127] F. P. An et al. (DAYA-BAY), "Observation of electron-antineutrino disappearance at Daya Bay", Phys. Rev. Lett. 108 (2012) 171803.

[128] http://en.wikipedia.org/wiki/Daya_Bay_Nuclear_Power_Plant
http://fr.wikipedia.org/wiki/Centrale_nuclaire_de_Ling_Ao

[129] S.-B. Kim et al. (RENO), "Observation of Reactor Electron Antineutrino Disappearance in the RENO Experiment", arxiv.org/1204.0626, 2012.

[130] T. J. C. Bezerra, H. Furuta and F. Suekane, "Measurement of Effective Δm^2_{31} using Baseline Differences of Daya Bay, RENO and Double Chooz Reactor Neutrino Experiments", arXiv:1206.6017

[131] P. A. N. Machado, H. Minakata, H. Nunokawa, R. Zukanovich Funchal, "Combining Accelerator and Reactor Measurements of θ_{13}; The First Result", arXiv:1111.3330

[132] http://www.youtube.com/watch?v=r6_WXC44q58

[133] D. Ayres et al. (NOvA), "Letter of Intent to build an Off-axis Detector to study numu to nue oscillations with the NuMI Neutrino Beam", arXiv:hep-ex/0210005, 2002.

[134] Ambats, I. et al. (NOvA), "NOvA proposal to build a 30-kiloton off-axis detector to study neutrino oscillations in the Fermilab NuMI beamline", arXiv:hep-ex/0503053, 2005.

[135] J. Cao, "Observation of electron antineutrino disappearance at Daya Bay", nuTURN 2012 - Neutrino at the Turning Point, 8 - 10 May 2012, INFN - Laboratori Nazionali del Gran Sasso

[136] H. Nunokawa, S. Parke and R. Zukanovich Funchal, "Another possible way to determine the Neutrino Mass Hierarchy", arXiv:hep-ph/0503283

[137] O. Mena and S. Parke Phys. Rev. D 69, 117301 (2004).

[138] W. Buchmuller, P. Di Bari, M. Plumacher, hep-ph/0401240 (2004).

[139] Patrick Huber, "Neutrino facilities – comparison of performance", European Strategy for Neutrino Oscillation Physics May 14-16, 2012, CERN

[140] J. Alonso et al., "Expression of Interest for a Novel Search for CP Violation in the Neutrino Sector: DAEdALUS", arXiv:1006.0260

[141] KATRIN: A next generation tritium beta decay experiment with sub-eV sensitivity for the electron neutrino mass

[142] Theory of neutrinoless double beta decay, J. D. Vergados, H. Ejiri, F. Simkovic, arXiv:1205.0649, 2012.

[143] A. Barabash, "Double beta decay experiments: past and present achievements", arXiv:hep-ex/0608054

[144] S. R. Elliott, "Introduction to the Double-Beta Decay Experimental Program", arXiv:nucl-ex/0609024.

[145] Klapdor-Kleingrothaus HV, Dietz A, Harney HL, and Krivosheina IV, Mod. Phys. Lett. 16 2409 (2001).

[146] C. E. Aalseth et al., Comment on "Evidence for Neutrinoless Double Beta Decay", arXiv:hep-ex/0202018

[147] M. Auger et al. (EXO-200), "Search for Neutrinoless Double-Beta Decay in ^{136}Xe with EXO-200", arXiv:1205.5608

[148] KamLAND-Zen Collaboration, "Measurement of the double-β-decay half-life of ^{136}Xe with the KamLAND-Zen experiment", arXiv:1201.4664

[149] J. J. Gomez-Cadenas, J. Martin-Albo, M. Mezzetto, F. Monrabal, M. Sorel, "The search for neutrinoless double beta decay", arXiv:1109.5515

[150] C. Athanassopoulos et al. (LSND Collaboration), Phys. Rev. Lett. 77, 3082 - 3085 (1996).

[151] C. Athanassopoulos et al. (LSND Collaboration), Phys. Rev. Lett. 81, 1774 - 1777 (1998).

[152] A. Aguilar et al. (LSND Collaboration), Phys. Rev. D64, 112007 (2001).

[153] E. D. Church, K. Eitel, G. B. Mills, M. Steidl, "Statistical Analysis of Different Muon-antineutrino $\rightarrow$ Electron-antineutrino Searches", arXiv:hep-ex/0203023

[154] E. Church et al., "A letter of intent for an experiment to measure ν_μ to ν_e oscillations and ν_μ disappearance at the Fermilab Booster (BooNE)", arXiv:9706011

[155] A. A. Aguilar-Arevalo et al. (The MiniBooNE Collaboration), Phys. Rev. Lett. 98, 231801 (2007).

[156] A. A. Aguilar-Arevalo et al., Phys. Rev. Lett. 102, 101802 (2009).

[157] Zelimir Djurcic, "MiniBooNE Oscillation Results 2011", arXiv:1201.1519

[158] G. Karagiorgi, Toward solution of the MiniBooNE and LSND anomalies. Neutrino 2010, XXIV International Conference on Neutrino Physics and Astrophysics, Athens, Greece

[159] G. Karagiorgi, "*Confronting Recent Neutrino Oscillation Data with Sterile Neutrinos*", hep-ph/1110.3735.

[160] P. Huber, "Light Sterile Neutrinos: A White Paper", arXiv:1204.5379

[161] F. Ardellier et al., "Letter of Intent for Double-CHOOZ: a Search for the Mixing Angle θ_{13}", hep-ex/0405032.

[162] S. Berridge et al., "*Proposal for U.S. participation in Double-CHOOZ: A New θ_{13} Experiment at the Chooz Reactor*", hep-ex/0410081.

[163] F. Ardellier et al., "*Double Chooz: A Search for the Neutrino Mixing Angle θ_{13}*", hep-ex/0606025v4.

[164] `http://www.dchooz.org/DocDB/cgi-bin/public/ShowDocument?docid=3393`

[165] J. K. Ahn, et al.," *RENO: An Experiment for Neutrino Oscillation Parameter θ_{13} Using Reactor Neutrinos at Yonggwang*", hep-ex/1003.1391.

[166] Daya Bay Collaboration, *"A Precision Measurement of the Neutrino Mixing Angle θ_{13} Using Reactor Antineutrinos At Daya Bay"*, hep-ex/0701029.

[167] J. C. Anjos et al., "*Angra Neutrino Project*", hep-ex/0511059.

[168] P. Vogel and J. F. Beacom, "Angular distribution of neutron inverse beta decay, $\bar{\nu}_e + p^+ \rightarrow e^+ + n^0$", Phys. Rev. D 60, 053003 (1999).

[169] G. Mention, Ph.D. thesis (2005), url:
`http://tel.archives-ouvertes.fr/tel-00010528/fr/`

[170] K. Terao, "*Neutrino Search Using n-H Capture Signal*", Double Chooz internal document 3667-v2.

[171] F. von Feilitzsch et al., Phys. Lett. B 118, 162 (1982)

[172] K. Schreckenbach et al., Phys. Lett. B 160, 325 (1985)

[173] A.A. Hahn et al., Phys. Lett. B 218, 365 (1989)

[174] Y. Déclais, "*Neutrino Oscillation search at Reactors*", Nuclear Physics B (Proc. Suppl.) 70 (1999) 148-154.

[175] Y. Déclais, "*Short Baseline reactor experiments*", Sterile neutrinos at the crossroads, VirginiaTech. 2011.

[176] O. Meplan et al., in ENC 2005: European Nuclear Conference ; Nuclear power for the XXIst century: from basic research to high-tech industry (2005).

[177] NEA-1845/01 (2009), documentation for MURE.

[178] G. Marleau et al., Report IGE-157 (1994).

[179] K. Suyama et al., Nuclear Technology 138, 97 (2002).

[180] C. Jones et al., "*Reactor Simulation for Antineutrino Experiments using DRAGON and MURE*", nucl-ex/1109.5379.

[181] V. Kopeikin et al., *Reactor as a source of antineutrinos: Thermal fission energy (2004)*, hep-ph/0410100v1.

[182] Jeff and eff projects: `http://www.oecdnea.org/dbdata/jeff/`

[183] Th. A. Mueller et al., "*Improved Predictions of Reactor Antineutrino Spectra*", hep-ex/1101.2755.

[184] P. Huber, "*On the determination of anti-neutrino spectra from nuclear reactors*", hep-ph/1106.0687

[185] G. Mention et al., "*The Reactor Antineutrino Anomaly*", Phys. Rev. D 83, 073006 (2011).

[186] C. Giunti, M. Lavender, "*First Double-Chooz Results and the Reactor Antineutrino Anomaly*", hep-ph/1111.5211.

[187] A. Palazzo, *An estimate of θ_{14} independent of the reactor antineutrino flux determinations*,

[188] M. Cribier et al., *"A proposed search for a fourth neutrino with a PBq antineutrino source"*, hep-ex/1107.2335.

[189] T. Lasserre, Proceedings of the EPS-HEP 2011 conference, "*The Reactor Antineutrino Anomaly*" , Grenoble 2011.

[190] G. Ranucci, "*Borexino Source Experiment*", SNAC11 2011.

[191] L. A. Mikaelyan and V. V. Sinev, Phys. Atomic Nucl. 63 (2000) 1002, hep-ex/9908047.

[192] Y. Déclais et al, Phys. Lett. B 338(1994)383.

[193] V. Kopeikin, L. Mikaelyan,V. Sinev IAE-5980/2 (Kurchatov Institute).

[194] V. Kopeikin, Y. Déclais, I. Machulin, L. Mikaelyan, V. Sinev IAE6026/2 (Kurchatov Institute).

[195] The White Paper, *"A new nuclear reactor experiment to measure θ_{13}"*, arxiv.org/040204.

[196] G. Mention et al., *"A unified analysis of the reactor neutrino program towards the measurement of the θ_{13} mixing angle"*, hep-ex/0704.0498.

[197] E. Calvo et al., *"Characterization of large area photomutipliers under low magnetic fields: design and performances of the magnetic shielding for the Double Chooz neutrino experiment"*, arxiv:0905.3246v1.

[198] F. X. Hartmann, R. A. Naumann, " ", Nucl. Instrum. Meth. A 313 (1992) 237.

[199] T. Matsubara et al., Nucl. Instrum. Meth., A661, 16, 2011.

[200] C. Bauer et al., JINST, 6, P06008 (2011).

[201] CAEN Corporation, http://www.caen.it/. The device was co-developed with APC.

[202] A. Verdugo, Double Chooz internal document 530-v1.

[203] E. Caden and C. Lane, "Front End TroubleShooting Documentation", Double Chooz internal document DC-doc-2407-v2.

[204] Anselm Stuken, "Overview of the NuDAQ trigger system", Double Chooz internal document

[205] S. Lucht, "Trigger Efficiency Task Force - Summary', Double Chooz internal document 3247-v1 (Presentation at the Rio collaboration meeting, October 2011).

[206] P. Novella, B. Reinhold and K. Terao "Linearity studies with calibration data", Double Chooz internal document 2996-v1.

[207] I. Stancu, "Time Offsets from the Ge-68 Data", Double Chooz internal document 3018-v1.

[208] Y. Sun, "Gain measurement using radioactive source data", Double Chooz internal document 3109-v2.

[209] J. Goon, "Laser System Integration Readiness Review", Double Chooz internal note 2414-v6

[210] D. M. Kaplan, J. E. Kaplan, H. A. Rubin, and D. Underwood, Double Chooz LED Flasher Prototype, Double Chooz internal note 1721-v1

[211] J. Maricic, E. A. Damon, "Articulated Arm System Integration Readiness Review", Double Chooz internal note 2519-v2

[212] A. Remoto, "*Muon identification: synthesis and EU++ proposal*", Double Chooz internal document 3230-v1 (Presentation at the Rio collaboration meeting, October 2011).

[213] Z. Djurcic et al., "*Neutron Efficiency Task Force Summary*", Double Chooz internal document 3268-v1 (Presentation at the Rio collaboration meeting, October 2011).

[214] J. Losecco, "*Soft Neutrons II*", Double Chooz internal document 3646-v4 (Presentation at the Sendai collaboration meeting, October 2012).

[215] J. Losecco, "*Fit with Soft Neutron and* ^{9}*Li Background*", Double Chooz internal document 3851-v1.

[216] G. Horton-Smith, "*Fine corrections to live time*", Double Chooz internal document 3288-v1.

[217] K. Crum, "Multiplicity cuts on IBD and off-time searches", Double Chooz internal document 3279-v2.

[218] M. Cribier, "On the cosmogenics background: ^{8}He and ^{9}Li", Double Chooz internal document 144-v1.

[219] The KamLAND Collaboration, "Production of Radioactive Isotopes through Cosmic Muon Spallation in KamLAND", hep-ex/0907.0066

[220] T. Hagner, et al., "Muon-induced production of radioactive isotopes in scintillation detectors", Astropart. Phys. 14 (2000) 33.

[221] P. Adamson et al. (MINOS Collaboration), Phys. Rev. Lett. 106, 181801 (2011).

[222] I. Ostrovskiy, "Detector covariance matrix", Double Chooz internal document 3301-v4.

[223] I. Ostrovskiy, Ph.D. thesis, Double Chooz internal document 3872-v1.

[224] A. Franke et al., "Double Chooz Neutrino Oscillation Fit Results - first DC publication", Double Chooz internal document 3519-v16.

[225] D. Dietrich et al., "Summary of Inner Veto PMT replacement", Double Chooz internal document 1609-v1.

[226] `http://www.thorlabs.de/thorproduct.cfm?partnumber=BFH48-600`

[227] D. Dietrich et al., "Grouping and Orientation of Veto PMTs after Replacement", Double Chooz internal document 1546-v4.

[228] Bellamy et al., "Absolute Calibration and Monitoring of a spectrometric channel using a photomultiplier", NIMA 339 (1994) 468-476.

[229] F. James, "MINUIT Tutorial: Function Minimization", 1972 CERN Computing and Data Processing School, Pertisau, Austria, 10-24 September, 1972.

[230] C. E. Lane, Gain Determination for R1408 PMTs, Double Chooz internal note, `DC-doc-2-v1`.

[231] Hamamatsu, *Photomultiplier tubes and assemblies for scintillation counting & High Energy Physics*. Revised Jun. 2009.

[232] I. Chirikov-Zorin *et al*, *Method for precise analysis of the metal package photomultiplier single photoelectron spectra.* NIMA456(2001) 310-324.

[233] M. Abramowitz & I. A. Stegun, *Handbook of Mathematical Functions*. New York: Dover Publications (1972), ISBN 978-0-486-61272-0.

[234] L. N. Kalousis, *"The Inner Veto Calibration System"*. `DC-doc-1375-v1`.

[235] L. N. Kalousis, *"A model for the Inner Veto PMTs"*. `DC-doc-1465-v1`.

[236] `www.gnu.org/software/gsl/manual/html_node/Numerical-Integration.html`

[237] *Analytical versus numeric convolution*, in W. Verkerke & D. Kirkby, *RooFit Users Manual v2.07*

[238] L. N. Kalousis et al., "Inner Veto Calibration System", Double Chooz internal document 1375-v1.

[239] L. N. Kalousis et al., "The Inner Veto Light Injection System", Double Chooz internal document 1772-v3.

[240] L. N. Kalousis et al., "IV-LI commissioning", Double Chooz internal document 1824-v.

[241] L. N. Kalousis et al., "Gain measuremenets for IV and ID", Double Chooz internal document 2040-v1.

[242] L. N. Kalousis, "Background Studies", Rio meeting, DocDB-3264

[243] EU++ results at 2nd comparison stage, DocDB-3199.

[244] A. Cabrera, "Correlated Background Analysis for DC1stPub", Double Chooz internal document 3471.

[245] K. Nakajima, "Technical note and spectrum of a stop muon and fast neutron analysis at 1st publication stage", Double Chooz internal document 3631

[246] F. Suekane, "Light Noise", Double Chooz internal document 2565-v1 (Presentation at the APC collaboration meeting, May 2011).

[247] I. Gil - Botella et al., "Towards a better understanding of the glowing: a possible explanation of the light emission process", Double Chooz internal document 3234-v1.

[248] D. Greiner, "High Energy Light Noise", Double Chooz internal document 2511-v2.

[249] M. D'Agostino, "Additional Fast Neutron and Michel Studies", Double Chooz internal document 3356-v1.

[250] K. Nakajima, "Analysis of Stop Muon and Fast Neutron", Double Chooz internal document 3355-v7.

[251] James D. Bjorken and Stanley J. Brodsky, Phys. Rev. D1, 14161420 (1970).

[252] http://cepa.fnal.gov/psm/simulation/mcgen/lund/pythia_manual/pythia6.3/pythia6301/node213.html

[253] J. Maeda, "PMT and Channel number in DOGS", Double Chooz internal document DC-doc-2139-v3.

[254] L. Kalousis, "New Framework for Light Noise Rejection", Double Chooz internal document 3503-v1.

[255] L. Kalousis et al., "Event Shape Discrimination", Double Chooz internal document 3509-v1

[256] S. Perasso, "Light Noise from PMT #263 and Light Noise Rejection Cuts", Double Chooz internal document 3053-v2.

[257] S. Perasso, "First Evaluation of the Light Noise Rejection Efficiency with the t2tot variables", Double Chooz internal document 3072-v1.

[258] D. Franco, "Light noise cut test with calibration data", Double Chooz internal document 2900-v1.

[259] D. Franco, "Light noise plots (TO BE BLESSED)", Double Chooz internal document 3384-v2.

[260] I. Stancu, "The Performance of RecoBAMA in Light of the First Calibration Data", Double Chooz internal document 2918-v1.

[261] I. Stancu, "Position Dependence of the Energy Function: Data vs MC", Double Chooz internal document 3499-v1.

[262] Z. Djurcic and J. Reichenbacher, "Deployed Radioactive Calibration Source Info", Double Chooz internal document 3202-v2.

[263] L. Kalousis, "Selected topics on Sphericity and Aplanarity", Double Chooz internal document 3739-v1.

[264] J. Busenitz et al., "Proposal for early deployment of calibration sources", Double Chooz internal document 2049-v2.

[265] J. Busenitz et al., "First source calibration", Double Chooz internal document 2946-v1.

[266] L. Kalousis, "LN rejection", Double Chooz internal document 4065-v1.

[267] C. Palomares, DC-doc-2969-v2.

[268] C. Palomares, DC-doc-3255-v2.

[269] M. Toups, DC-doc-3258-v1.

[270] R. Becker-Szendy et al., Calibration of the IMB detector', NIMA 352 (1995) 629-639.

[271] J. Dawson et al., "*Preliminary muon analyses in the EU++ cluster*", Double Chooz internal document 2567-v1 (Presentation at the APC collaboration meeting, May 2011).

[272] A. Tang et al., Muon Simulations for Super-Kamiokande, KamLAND and CHOOZ", hep-ph/0604078.

[273] M. Rohling, "Inner Veto trigger studies", Double Chooz internal document 3769-v1.

[274] D. Dietrich, "*Muon rate @ DC-far and atmospheric effects*", Double Chooz internal document 3223-v2 (Presentation at the Rio collaboration meeting, October 2011).

[275] M. D' Agostino, "*Michel Electrons in Early Physics Data*", Double Chooz internal document 2564-v1 (Presentation at the APC collaboration meeting, May 2011).

[276] D. Franco, "Light noise cut test with calibration data", Double Chooz internal document 2900-v1.

[277] E. Conover, "IBD candidates vetoed by the OV", Double Chooz internal document 3716-v1

[278] A. Meregaglia, "FN tagging with PSD", Double Chooz internal document 3786-v1.

[279] M. Ambrosio et al. (MACRO coll.), "Seasonal variations in the underground muon intensity as seen by MACRO", Astropart. Phys. 7 (1997) 109.

[280] P. Desiati (for the ICECUBE coll.), "Seasonal Variations of High Energy Cosmic Ray Muons Observed by the IceCube Observatory as a Probe of Kaon/Pion Ratio", in Proc. of the 32nd ICRC (2011).

[281] P. Adamson et al. (MINOS coll.), "Observation of muon intensity variations by season with the MINOS far detector", Phys. Rev. D81 (2010) 012001.

[282] BOREXINO Collaboration, "Cosmic-muon flux and annual modulation in Borexino at 3800 m water-equivalent depth", hep-ex/1202.6403